Ministério da
Ciência, Tecnologia e Inovação

sid.inpe.br/mtc-m19/2013/09.17.14.26-TDI

OCEAN COLOUR VARIABILITY ACROSS THE SOUTHERN ATLANTIC AND SOUTHEAST PACIFIC

Natália de Moraes Rudorff

Doctorate Thesis Course Graduate in Remote Sensing, guided by Drs. Milton Kampel, and Robert Frouin, approved in August 19, 2013.

URL of the original document:
<http://urlib.net/8JMKD3MGP7W/3ERLCSE>

INPE
São José dos Campos
2013

PUBLISHED BY:

Instituto Nacional de Pesquisas Espaciais - INPE
Gabinete do Diretor (GB)
Serviço de Informação e Documentação (SID)
Caixa Postal 515 - CEP 12.245-970
São José dos Campos - SP - Brasil
Tel.:(012) 3208-6923/6921
Fax: (012) 3208-6919
E-mail: pubtc@sid.inpe.br

Ministério da
Ciência, Tecnologia e Inovação

sid.inpe.br/mtc-m19/2013/09.17.14.26-TDI

OCEAN COLOUR VARIABILITY ACROSS THE SOUTHERN ATLANTIC AND SOUTHEAST PACIFIC

Natália de Moraes Rudorff

Doctorate Thesis Course Graduate in Remote Sensing, guided by Drs. Milton Kampel, and Robert Frouin, approved in August 19, 2013.

URL of the original document:
<http://urlib.net/8JMKD3MGP7W/3ERLCSE>

INPE
São José dos Campos
2013

Cataloging in Publication Data

Rudorff, Natália de Moraes.

R835o Ocean Colour Variability across the Southern Atlantic and Southeast Pacific / Natália de Moraes Rudorff. – São José dos Campos : INPE, 2013.

xxxii + 289 p. ; (sid.inpe.br/mtc-m19/2013/09.17.14.26-TDI)

Thesis (Doctorate in Remote Sensing) – Instituto Nacional de Pesquisas Espaciais, São José dos Campos, 2013.

Guiding : Drs. Milton Kampel, and Robert Frouin.

1. bio-optical variability. 2. uncertainties. 3. ocean colour radiances. 4. Southern Atlantic. 5. Southeast Pacific. I.Título.

CDU 528.8:351.463.5

Aprovado (a) pela Banca Examinadora em cumprimento ao requisito exigido para obtenção do Título de *Doutor(a)* em

Sensoriamento Remoto

Dr. João Antonio Lorenzzetti

Presidente / INPE / SJCampos - SP

Dr. Milton Kampel

Orientador(a) / INPE / SJCampos - SP

Dr. Robert Frouin

Orientador(a) / UCSD / Estados Unidos - USA

Dra. Evlyn Márcia Leão de Moraes Novo

Membro da Banca / INPE / SJCampos - SP

Dra. Aurea Maria Ciotti

Convidado(a) / USP / São Sebastião - SP

Dra. Vivian Lutz

Convidado(a) / INIDEP / Argentina - ARG

Este trabalho foi aprovado por:

( ) maioria simples

(✓) unanimidade

Aluno (a): *Natália de Moraes Rudorff*

São José dos Campos, 19 de Agosto de 2013

“A maravilhosa disposição e harmonia do universo só pode ter tido origem segundo o plano de um Ser que tudo sabe e tudo pode. Isto fica sendo a minha última e mais elevada descoberta”.

Issac Newton

Dedico sobre tudo a Deus, minha família, em especial meus pais Bernardo e Heloisa, amigos e professores que me acompanharam nesta caminhada, construindo meu ser.

AGRADECIMENTOS

Agradeço primeiramente a Deus por sua Divina Providência em minha vida e ter me dado a oportunidade e a condição de realizar o doutorado. Por todo crescimento pessoal e pessoas maravilhosas que Ele colocou em meu caminho me ajudando e sustentando nesta jornada - professores, colegas, familiares e amigos. Agradeço muito a todo apoio e amor incondicional dos meus pais, meus irmãos, avó, tios e primos. De modo muito especial a meus pais – Bernardo e Heloisa que sempre me apoiaram, consolaram e me animaram em meio às lutas. A meus irmãos e cunhadas – Fred e Lucélia, Conrado e Camila e meu sobrinho Rafael, por todo apoio, ajuda, companheirismo e alegria. Aos amigos e amigas, em especial à Laura e Francisca – tesouros de Deus que levarei por toda vida – muito obrigada pelo ombro amigo, ajuda, carinho, partilhas e ânimo. Aos meus orientadores Milton e Robert, por terem acreditado em mim, por dar a oportunidade de realizar o doutorado, por todo aprendizado, suporte e valiosas discussões científicas, e pela amizade. A todos que me ajudaram no trabalho de forma direta e indireta na ajuda das coletas e processamento dos dados, em especial à Mayza – grande amiga que não poupou esforços mesmo em meio às suas dificuldades – agradeço a todo apoio e acolhida. Ao Brian Schieber – por toda solicitude e prontidão em sempre ajudar. De modo muito especial também à Vivian Lutz por toda a ajuda, acolhimento, atenção e amizade. Ao João e toda sua família e amigos que me apoiaram e alegraram nesta jornada. À Fátima e Dona Maria que são grandes exemplos de humildade, alegria e garra. À Chiara – grande amiga e orientador de vida. À Charleen pela acolhida em San Diego. Pela graça de ter conhecido tantas pessoas especiais e lugares maravilhosos e por todas as experiências vividas que levarei com muito carinho no coração.

Agradeço ao Programa de Pós-Graduação no INPE e todos os professores pela oportunidade do doutorado e aprendizado valioso. À Coordenação de Aperfeiçoamento de Pessoal de Nível Superior (CAPES) que proveu a bolsa de estudos. Ao *Partnership for Observation of the Global Ocean* (POGO) e *International Ocean Colour Coordinating Group* (IOCCG), pelos excelentes cursos de formação e pela oportunidade de experiência de doutorado no exterior. Ao Robert pela oportunidade do cruzeiro e confiança no trabalho. À NASA que viabilizou o cruzeiro e análises. A todos os representantes e técnicos dos laboratórios que possibilitaram as análises – Salvador Airton Gaeta (Instituto Oceanográfico da Universidade de São Paulo, IO-USP), Rodolfo Paranhos (Universidade Federal do Rio de Janeiro, UFRJ), Vivian Lutz, Riki e Rubens (*Instituto Nacional de Investigación y Desarrollo Pesquero*, INIDEP), Greg Mitchell e Brian (*Scripps Institute of Oceanography*), Xavier e Loisel (LOG – *Laboratoire d'Océanologie et de Géosciences, Université du Littoral-Côte d'Opale*). A todos da tripulação do R/V Melville que tornaram esta viajem fantástica e inesquecível.

ABSTRACT

Ocean colour radiometry (OCR) provides essential information for studies of primary productivity, heat fluxes, and biogeochemical cycles in the upper ocean. Generalized OCR models relating satellite radiometric data to biogeochemical variables are developed using global *in situ* data sets. However, when applied to specific regions these models commonly give results with significant deviation from *in situ* measurements, mainly due to field and satellite measurement uncertainties and model underrepresentation of ocean colour variability. Hence to improve OCR products further understanding of the sources of measurement uncertainty and bio-optical variability across different oceanic regions is needed. This work was focused on the Southern Atlantic and Southeast Pacific Oceans encompassing important biogeochemical provinces with highly distinct optical waters. *In situ* data was collected during a summer campaign on board the research vessel Melville (MV1102 cruise). The first part of the investigation was an uncertainty analysis of the radiometric and bio-optical data with three main objectives: (i) test different radiometric techniques with above and in-water approaches (ii) apply closure analyses with forward modeling of remote sensing reflectance (R_{rs}); and (iii) analyze the impacts of the uncertainties on operational OCR models. The uncertainty analysis revealed moderate to high levels associated with the various techniques, with 12 to 26% relative differences (RD) for the ocean-colour bands (412- 555 nm) and 3-12% for the reflectance ratios (412-510/555). The use of a merged R_{rs} (Instruments, INS) reduced uncertainties since each individual technique was subject to different instrumental and environmental biases. Complete closure was not obtained, especially for the stations with more adverse environmental conditions (with winds, waves and clouds), with 18-34% RD compared to modeled R_{rs} bands. Nonetheless, the impact of INS uncertainties on retrieved OCR products for empirical and semi-analytical (SA) models was still generally smaller than the intrinsic errors of the inversion schemes. Hence, the approaches applied to obtain more accurate measurements were effective in reducing the main sources of uncertainties. Significant sources of deviations of the OCR models were related to the optical variability of the study region and intrinsic model errors. The second part of the investigation analyzed the sources of bio-optical variability and their relations to biogeochemical variables across distinct provinces. The bulk inherent optical properties (IOPs) were in first order associated with the chlorophyll *a* concentration (Chl*a*) gradient. Second order variations were explained by specific IOPs linked to the phytoplankton community structure, composition and size distribution of the particle assemblage and variability of the coloured dissolved and particulate organic matter (CDM). To synthetize the first and second order optical variations across the study region, a Regional Specific Optical Water Type (R-SOWT) classification was proposed by defining 5 classes that integrate the specific IOPs and bio-optical indices, i.e., a phytoplankton Size Index, CDM index, the specific backscattering coefficient (b_{bp}/Chl*a*) and spectral slope (η). The R-SOWT significantly improved the performance of SA models by using class-specific parameterizations, especially for the b_{bp} retrieved by the GSM (Garver-Siegel-Maritorena) model, reducing from 35 to 9% RP, and the CDM absorption coefficient of

the QAA (Quasi-Analytical Algorithm) model, reducing from 30 to 23 % RD. For more optically complex waters the improvements of the retrievals were much more significant. Further analysis of spatiotemporal variations of the optical relations and applicability of the R-SOWT for different seasons (and regions) are recommended for future studies. This approach has potential to improve OCR satellite products and be used as a new product that integrates relevant information for biogeochemical studies.

VARIABILIDADE DA COR DO OCEANO NO ATLÂNTICO SUL SUBTROPICAL E PACÍFICO SUDESTE

RESUMO

A radiometria da cor do oceano oferece informações essenciais para estudos de produtividade primária, fluxos de calor e ciclos biogeoquímicos na superfície dos oceanos. Modelos generalizados de cor do oceano que relacionam dados radiométricos de satélite com variáveis biogeoquímicos são desenvolvidos com bases de dados globais *in situ*. No entanto, quando aplicados a regiões específicas estes modelos apresentam desvios significativos que estão relacionados a incertezas nas medidas *in situ* e satelitais, e sub-representações da variabilidade da cor do oceano. Portanto, para a melhoria de produtos de cor do oceano é preciso conhecer melhor as fontes incertezas das medidas e a variabilidade bio-óptica em diferentes regiões oceânicas. O presente trabalho teve como foco os Oceanos Atlântico Sul Sub-tropical e Pacífico Sudeste abrangendo importantes províncias biogeográficas com águas opticamente distintas. Dados *in situ* foram coletados durante uma campanha de verão a bordo do navio de pesquisa R/V Melville (MV1102). A primeira parte do trabalho compreendeu análises de incertezas dos dados radiométricos e bio-ópticos com três objetivos principais: a) a comparação de diferentes técnicas de amostragem com instrumentos emersos e submersos; b) comparações com a reflectância de sensoriamento remoto (R_{sr}) modelada; e c) análises dos impactos das incertezas em modelos operacionais de cor do oceano. As análises de incertezas revelaram níveis de altos a moderados associados às diferentes técnicas, com diferenças relativas (DR) de 12 a 26% para as bandas de cor do oceano (412-555 nm) e 3 a 12% para as razões de bandas (412-510/555). O uso de uma medida de R_{sr} integrada (Instrumentos, INS) reduziu as incertezas já que cada técnica individual estava sujeita a diferentes erros instrumentais e ambientais. O ajuste perfeito com a R_{sr} modelada não foi obtido, principalmente para as estações com condições ambientais mais adversidades (de vento, ondas e nuvens), com 18-34% DR para as bandas espectrais. Ainda assim, o impacto das incertezas do INS foi de modo geral, menor que os erros intrínsecos aos modelos empíricos e semi-analíticos (SA) de cor do oceano. Dessa forma, os métodos empregados para obter medidas mais acuradas foram razoavelmente eficazes em reduzir as incertezas. Desvios significativos dos modelos de cor do oceano foram relacionados à variabilidade óptica da região de estudo e erros intrínsecos aos modelos. A segunda parte da investigação compreendeu análises das fontes de variabilidade bio-óptica e suas relações com as variáveis biogeoquímicas nas diferentes províncias. A distribuição dominante das propriedades ópticas inerentes (POIs) esteve associada ao gradiente de concentração de clorofila *a* (Cl*a*). Variações de segunda ordem foram relacionadas a POIs específicas associadas à estrutura da comunidade fitoplanctônica, a composição e distribuição do tamanho das partículas e à variabilidade da matéria orgânica dissolvida e particulada (MODP). Para sintetizar as variações de primeira e segunda ordem na região de estudo, uma classificação Regional de Tipos Específicas de Águas Ópticas (R-TEAO) foi proposta para definir 5 classes,

integrando as POIs específicas e índices bio-ópticos, i.e., o Índice de tamanho do fitoplâncton, índice de CDM, o coeficiente especifico de retroespalhamento das partículas (b_{bp}/Cl*a*) e o parâmetro de variação espectral (η). O R-TEAO melhorou significativamente o desempenho de modelos SA com parametrizações especificas para cada classe, reduzindo a DR do b_{bp} do modelo GSM01 (Garver-Siegel-Maritorena) de 35 a 9 % e o coeficiente de absorção do MODP de 30 a 23 % para o modelo QAAv5 (Quase Analytical Algorithm). Para águas mais opticamente complexas a melhoria dos modelos foi ainda mais significativa. Análises das variações espaço-temporais das relações ópticas e a aplicabilidade do R-TEAO para estações sazonais diferentes e outras regiões oceânicas, são recomendadas para pesquisas futuras. O método tem potencial de ser aplicado para a melhoria de produtos de cor do oceano por satélite e ser usado como um novo produto integrando informações importantes para estudos biogeoquímicos.

LIST OF FIGURES

LIST OF TABLES

LIST OF ABBREVIATIONS

ACC – Antarctic Circumpolar Current

AOP – Apparent Optical Property

ASD – Analytical Spectral Devices

B04 SI – Bricaud et al. (2004) Size index

BENG - Benguela Current Coastal Province

BGCP – Biogeochemical Provinces

BMCZ – Brazil-Malvinas Confluence Zone

CDM – Colored Dissolved Organic Matter + Detritus

CDOM - Colored Dissolved Organic Matter

Chl*a* – Chlorophyll a concentration

CZCS – Coastal Zone Colour Scanner

CB06 SI – Ciotti and Bricaud (2006) Size index

CP – Cape Peninsula Upwelling Cells

CTD - Conductivity-Temperature, Depth

FKLD - Southwest Atlantic Shelves Province

GSM01- Garver-Siegel-Maritorena version 01

GSFC – Goddard Space Flight Center

GIOP – Generalized IOP model

HPLC – High Performance Liquid Chromatography

HNLC – High Nutrient Low Chlorophyll

HS6 – HydroScat-6

HOCR PRO II – Hyper spectral Radiometer

HUMB - Chile-Peru Current Coastal Province

IOP – Inherent Optical Property

IOUSP – Instituto Oceanográfico da Universidade de São Paulo

INPE – Instituto Nacional de Pesquisas Espaciais

INIDEP - Instituto Nacional de Investigación y Desarrollo Pesquero

IRD - *Institut de Recherche pour le Développement*

LM - Levenberg Marquardt

LOG – *Laboratoire d'Océanologie et de Géosciences, Université du Littoral-Côte d'Opale*

MC – Malvinas Current

MBR – Maximum Band Ratio

MODIS - Moderate Resolution Imaging Spectrometer

MERIS - MEdium Resolution Imaging Spectrometer

MG09 – CDOM index

NASA – National Aeronautical and Space administration

NOMADv2 - NASA bio-Optical Marine Algorithm Data version 2

NIR – Near Infrared spectral range

NAP – non algal particles

OCR – Ocean Colour Radiances

OPP – Oceanic Primary Production

OAC – Optically Active Constituents

ODV – Ocean Data View software

OC3M – Chl*a* empirical model for MODIS bands

OC4 - Chl*a* empirical model for SeaWiFS bands

OWT – Optical Water Types

OB – Ocean Basins

PL – Punta Lavapies Upwelling Cell

PLME – Patagonian Large Marine Ecossystem

PAR – Photosynthetically Active Radiation

PFT – Phytoplankton Functional Types

PRR – Profiling Reflectance Radiometer

PSD – Particle Size Distribution

QAA - Quasi-Analytical Algorithm

R-SOWT – Regional Specific Optical Water Types

RMSE – Root Mean Square Error

RPD – Relative Percent Difference

RPD* - Absolute Percent Difference

SeaWiFS - Sea-viewing Wide Field-of-view Sensor

SATL - South Atlantic Gyral Province

SASW – Subantarctic Surface Water

SACW – South Atlantic Central Water

SSTC - South Subtropical Convergence Province

SANT - Subantarctic Water Ring Province

SA – Semi-analytical models

SACW – South Atlantic Central Water

SASW – Subantarctic Surface Water

SIO – Scripps Institute of Oceanography

SD – Standard Deviation

STF – Subtropical Front

SAF – Subantarctic Front

TriOS – TriOptical Sensors

UFF – Universidade Federal do Rio de Janeiro

UPD – Unbiased Percent difference

UCSD – University of California San Diego

UV – Ultraviolet radiation

VSF – Volume Scattering Function

VIS – visible spectral range

LIST OF SIMBOLS

a	absorption coefficient, m^{-1}
a_p	particulate absorption coefficient, m^{-1}
a_s	coloured dissolved organic matter absorption coefficient, m^{-1}
a_d	detritos absorption coefficient, m^{-1}
a_{cdm}	coloured dissolved and particulate organic matter absorption coefficient, m^{-1}
a_{phy}	phytoplankton absorption coefficient, m^{-1}
a_{phy*}	phytoplankton specific absorption coefficient, $m^2.mgCla^{-1}$
$a_{*<micro>}$	microplankton specific absorption coefficient, m^{-1}
$a_{*<pico>}$	picoplankton specific absorption coefficient, m^{-1}
a_w	pure seawater absorption coefficient, m^{-1}
a_{nw}	non-water absorption coefficient, m^{-1}
b_b	backscattering coefficient, m^{-1}
b_p	particle scattering coefficient, m^{-1}
b_{bp}	particle backscattering coefficient, m^{-1}
$\sim b_{bp}$	particle backscattering probability ratio
b_w	pure seawater backscattering coefficient, m^{-1}
β_v	volume scattering function, $m^{-1}sr^{-1}$
C	chlorophyll *a* concentration, mgChl*a*. m^{-3}
$Chla$	chlorophyll *a* concentration, mg Chl*a*. m^{-3}
D	diameter, μm
E_d	downwelling solar irradiance, W. m^{-2}
E_u	upwelling solar irradiance, W. m^{-2}
f	Environmental factor
F_0	mean solar flux at the top of the atmosphere, W. m^{-2}
g_i	geometrical parameters relating remote sensing measurements to IOPs
K_d	downwelling attenuation coeficiente, m^{-1}
L_T	total radiance measured by the sensor, W. $m^{-2}.sr^{-1}$
L_u	upwelling radiance, W. $m^{-2}.sr^{-1}$
L_w	water-leaving radiance, W. $m^{-2}.sr^{-1}$
L_{sky}	sea surface reflected sky radiance, W. $m^{-2}.sr^{-1}$
L_{pl}	plaque radiance, W. $m^{-2}.sr^{-1}$

η backscattering spectral slope

n_w^2 seawater refractive index

N concentration number, particles.m^{-3}

Q bidirectional correction fator, sr

Q_{bb} backscattering efficiency fator

R_{rs} remote sensing reflectance, sr^{-1}

r_s spearman correlation coefficient

r^2 determination coefficient

S_{cdm} colour organic matter spectral slope , nm^{-1}

S_f size index adjustment fact

μ_d mean cosine of the downwelling irradiance

μ_u mean cosine of the upwelling irradiance

t air-water interface factor

t time, hours, minutes or seconds

u proportional factor for the absorption and backscattering coefficients

$0-$ below-water 0 m depth

$0+$ above-water 0 m depth

z depth, m

ξ Particle size distribution spectral slope

ξ ratio between the coloured organic matter absorption coefficient at 410 and 440 nm

ζ ratio between the phytoplankton absorption coefficient at 410 and 440 nm

θ_s zenith solar angle, ^{o}

θ_v zenith sensor-viewing angle, ^{o}

δ first optical depth

λ wavelength, nm

λ_o reference wavelength, nm

ρ_{pl} reflectance factor of the plaque

ρ_{sky} sea surface reflectance factor of the sky radiance contribution

χ maximum band ratio (440, 490, 510)/555, in log scale.

τ_a atmospheric optical thickness, m^{-1}

φ_s azimuthal solar angle, ^{o}

φ_v azimuthal sensor-viewing angle, ^{o}

R diffuse reflectance

Φ factor accounting for reflection and refraction at the air-water interface

σ_{bb} particle backscattering cross section, m^2

SUMMARY

1 INTRODUCTION

Ocean Colour Radiometry (OCR) is a technology that has developed rapidly since the launch in the late 1970's of the first ocean colour satellite sensor, the Coastal Zone Colour Scanner (CZCS). With more sophisticated sensors onboard the subsequent satellites: Sea-viewing Wide Field-of-view Sensor (SeaWiFS), Moderate Resolution Imaging Spectroradiometer (MODIS) and Medium Resolution Imaging Spectrometer (MERIS), among others; generating an enormous volume of data across the global ocean, the impetus has been strong to develop and provide high quality ocean-colour products for applications in various fields of biogeochemistry, oceanography, and atmospheric sciences. Within the list of products routinely distributed by satellite ocean-colour project offices are, among others: the chlorophyll *a* concentration (Chl*a*) (MARITORENA et al., 2002; O'REILLY et al., 2000), the phytoplankton and coloured dissolved and particulate organic matter (CDM) absorption coefficients (a_{phy} and $a_{cdm,}$ respectively) and the particle backscattering coefficient (b_{bp}) (LEE et al., 2002; MARITORENA et al., 2002). Besides these, higher level products, such as the oceanic primary production (OPP) and phytoplankton functional types (PFTs), have also been developed and provided by specialized OCR groups (NAIR et al., 2008; RUDORFF; KAMPEL, 2012). These products have served as a great data source for worldwide researches, since satellite sensors provide a unique tool to access synoptic data over extensive areas, with global coverage and frequent temporal revisit (MCCLAIN, 2009).

A major challenge for the OCR community is however, to obtain accurate ocean colour products across different regions and seasons, as the uncertainties will depend on the performance of the correction algorithms for the satellite radiometric measurements and the performance of the bio-optical models used to derive the biogeophysical parameters. The indirect radiometric measurements obtained by the satellite sensors are highly influenced by various sources of noises and biases associated with the atmospheric interference, sea surface roughness, sensor-sun geometry and sensor calibration. Many improvements have been made on correction algorithms to obtain more accurate radiometric measurements from space, but this is still a great challenge for the ocean colour community (IOCCG, 2010). Hence, the development and maintenance of OCR satellite programs, still rely heavily on *in situ* radiometric measurements (HOOKER et

al., 2002; BAILEY; WERDELL 2006). *In situ* radiometry is used for a series of applications regarding the analysis of the relations between apparent and inherent optical properties (AOPs and IOPs, respectively), the development and validation of bio-optical models, the validation of satellite products, and vicarious calibration of satellite sensors. *In situ* measurements are subjected to minor sources of noises, but there may still be some significant levels of uncertainties on both the radiometric and bio-optical data, if not adequately treated.

Regarding the radiometric *in situ* measurements, there are two main approaches currently used: one using above-water instrumentation and the other using coupled in-water and deck sensors. There are well defined protocols for the measurement procedures and data processing schemes for each approach (MUELLER et al., 2003). Nevertheless, many issues are still open for discussion and further improvements are needed. Uncertainties may range from a few percent (> 5 %) to several tens percent (over 50 %), with the highest generally associated with above-water measurements, optically complex waters and adverse environmental conditions (regarding the sea state and illumination conditions) (TOOLE et al., 2000; HOOKER et al., 2002; HOOKER; MOREL, 2003; HOOKER et al., 2004; KOWALCZUK et al., 2006). The above-water approach has a more simple logistic and can obtain measurements from a moving platform without requiring ship time to stop, taking thus advantage of opportunity cruises (DESCHAMPS et al. 2004). The in-water approach, on the other hand, is not affected by surface reflection effects, but is affected by other sources of uncertainties related to the fluctuations of the in-water light field (ANTOINE et al., 2008).

Bio-optical measurements are also highly sensitive to various sources of uncertainties which need careful attention, especially regarding the CDOM absorption (a_s) and particle backscattering (b_{bp}) coefficients. CDOM is usually in very low concentrations in open ocean waters and the low signals are challenging to obtain accurate measurements with the appropriate optical instrumentation (BRICAUD et al., 1981; MUELLER et al., 2003). Backscattering measurements are even a greater challenge as the signals are also very low and the optical configuration for such measurements is not simple (TWARDOWSKI et al., 2007; STRAMSKI et al., 2008; ANTOINE et al., 2011). Another important bio-optical variable that despite of being extensively measured

across the oceans, still has significant levels of uncertainty (>30%), is the Chl*a*. With the incoming of the *High Pressure Liquid Chromatography* (HPLC) technique, enabling a much more precise determination of the pigment composition of the phytoplankton assemblage, this method has become a standard reference for OCR analysis in place of the fluorometric methods (O'REILLY et al., 2000). Nonetheless, if not adequately treated the HPLC may also have some important biases (HOOKER et al., 2009).

The challenges in obtaining accurate *in situ* radiometric and bio-optical measurements are so serious that strong efforts have been concentrated in determining the sources and levels of uncertainties, as well as their impacts on ocean colour modeling. Besides knowing the technical limitations of the measurements, such studies aim to define adequate standard protocols (MUELLER et al., 2003b; MUELLER et al., 2003) The *in situ* global data bases used for the development and validation of ocean colour products, are provided by different laboratories that apply different approaches, with diverse instruments and data processing schemes. Thus, the integration of such data set is a great challenge and may account for high uncertainties in OCR programs (BAILEY; WERDELL, 2006). The NASA bio-Optical Marine Algorithm Data (NOMAD) base is an attempt to integrate these sets with high quality control schemes (WERDELL; BAILEY, 2005). Global bio-optical models have used this base for their tuning and up-dates (e.g. OC4 and Quasi-Analytical Algorithm - QAA). The NOMAD however, also has some significant levels of uncertainty and despite that it covers a higher Chl*a* dynamic range (0.012-72 $mg.m^{-3}$), the points are unequally distributed in the global ocean mostly concentrated near coastal systems (WERDELL; BAILEY, 2005).

Recent studies however, have shown that there may be significant bio-optical variability within the oceans causing deviations in the "globally" tuned bio-optical models (MOORE et al., 2009; SZETO et al., 2011). The empirical and semi-analytical (SA) models are parameterized using global mean relations between the remote sensing reflectance and IOPs, which are governed by a first order variability related to the Chl*a* gradient (MOORE et al., 2009). Second order variabilities associated with the specific IOPs, e.g., the biogenic absorption capacity and the particle backscattering efficiency and spectral dependency, may cause significant deviations in relation to the global mean relations. Such variability may be linked to important biogeochemical properties such as

the phytoplankton and microbial community structure, the dissolved and particulate coloured organic matter cycles and the composition and size distribution of the particle assemblage (LOISEL et al., 2010; SZETO et al., 2011). Hence, the detection of such second order variations across different oceanic regions may provide means to enhance OCR modeling and obtain important biogeochemical information (SZETO et al., 2011).

For instance, the CDM content in the surface layers of the ocean was previously thought to have a tight covariation with the present and past phytoplankton biomass (BRICAUD et al., 1998). More recent studies revealed however, a rather high variation in the proportions of the CDM in respect to the bulk biogenic (non-water) absorption (a_{cdm}/a_{nw}), which may be related to different processes regulating the sources and losses of the CDM, such as upwelling sources and photodegradation losses (SIEGEL et al., 2002; MOREL; GENTILI, 2009). Morel and Gentili (2009) proposed an index that tracks the deviations of the CDM content in respect to the global mean relation with Chl*a*, namely CDOM index, which became a standard ocean colour product. Such variability has implications on the empirical OC4 model (O'REILLY, 2000), but may also provide relevant information on processes regulating the phytoplankton growth (being CDOM both a light competitor and protector in the surface layer) and transfer flux of organic and inorganic carbon within the deep ocean and ocean-atmosphere interface (SIEGEL et al., 2002).

The specific phytoplankton absorption coefficient (a_{phy}*, a_{phy}/Chl*a*) also varies within the oceans, related especially to changes in the phytoplankton size structure. Pico (micro) cells tend to have higher (lower) a_{phy}* due to the intracellular composition and concentration of primary and accessory pigments (SATHYENDRANATH et al., 1987; CIOTTI et al., 2002). The variability in the a_{phy}* may cause significant impacts on ocean colour retrievals, and may provide important information on the phytoplankton size structure (CIOTTI et al., 2002; CIOTTI; BRICAUD, 2006). Another important source of second order bio-optical variability is related to the particle backscattering coefficient (b_{bp}) amplitude and spectral variations (η slope) (BROWN et al., 2008; LOISEL et al., 2010). Such variations are known to be dependent on the composition and size distribution of the particle assemblage (particle size distribution, PSD). However, the actual sources ocean b_{bp}, i.e., particle types and size ranges, are still far

from being well understood. Some authors have related the specific b_{bp} (b_{bp}*, b_{bp}/Chl*a*) to the presence of particles with a higher or lower b_{bp} efficiencies (e.g., smaller/high index particles and larger/low index particles, respectively) (LOISEL et al., 2010), while others have related the variations in η to changes in the size structure of the particle assemblage and co-varying phytoplankton community (KOSTADINOV et al., 2009). Such studies however, have relied mainly on radiative transfer modeling that does not adequately explain complex optical relations, and only on a few *in situ* data. Moreover, there are contradictory works that show the role of different sources regulated the variability of oceanic b_{bp}, and this topic has become a major OCR research subject, with important implications on ocean colour modeling and relevant information regarding carbon cycling and trophic flux (LOISEL et al., 2006; DALL'OLMO et al., 2009; KOSTADINOV et al., 2009).

The performance of ocean colour models thus depends on the accuracy of the *in situ* data used to develop the model, and spatial-temporal variations of the specific IOPs. In this sense, to improve the model performances and adequately use OCR products to study the biogeochemical processes across the oceans, there are needs to improve the current techniques and processing schemes to obtain more accurate *in situ* radiometric and bio-optical measurements, and to characterize the sources of bio-optical variability across different regions and seasons. Novel approaches based on regional or class-specific parameterization schemes may be an alternative to enhance the performance of the models accounting for the spatial-temporal bio-optical variability (MOORE et al., 2009; SZETO et al., 2011; MOORE et al., 2012). Nonetheless, to adequately apply such schemes, one needs first to have more comprehensive and accurate *in situ* data across different regions to characterize the variability and to understand the bio-optical relations across the oceans, as there are extensive unsampled regions, especially in the open ocean and southern hemisphere (SZETO et al., 2011).

The southern Atlantic and southeast Pacific comprehend some of the extensive unsampled regions of the NOMAD base, encompassing important biogeochemical provinces (BGCP), such as the: Benguela Current Coastal Province (BENG); South Atlantic Gyral Province (SATL); South Subtropical Convergence Province (SSTC); Subantarctic Water Ring Province (SANT); Southwest Atlantic Shelves Province

(FKLD) and the Chile-Peru Current Coastal Province (HUMB) (LONGHURST, 2007). These regions are extensively unsampled due to the high challenges in navigating and sampling rough seas with strong currents and winds, promoted by the westerlies. They encompass different systems with great relevance for regional and global carbon cycling and trophic flux. The SATL, for instance, is composed of oligotrophic waters dominated by picoplankton groups. Despite of the low OPP of picoplankton groups, the subtropical gyres account for 30-50% of the global OPP, due to the extensive spatial coverage that they occupy in the oceans (KARL et al., 1996). The meso-eutrophic waters of the BENG, SSTC, SANT, FKLD and HUMB, on the other hand, are more spatially restricted, but sustain extensive phytoplankton blooms, especially during the austral spring and summer seasons. These blooms are generally dominated by nano and micro PFTs associated with new OPP (LONGHURST, 2007). The Patagonian Shelf Large Marine Ecosystem in the FKLD, is one of the most productive systems of the global ocean with high PPO, CO_2 sinking rates and fishery stocks (BIANCHI et al., 2009; FERREIRA et al., 2009; LUTZ et al., 2010).

In this context, the present work aimed to contribute with the analyses of ocean colour variability across the southern Atlantic and Southeast Pacific, using *in situ* data collected during a summer campaign in 2011, on board the R/V Melville (MV1102 campaign). The cruise encompassed all of the nine BGCP mentioned above, with highly differing systems from the open ocean oligotrophic waters of the SATL, to the mesotrophic waters of the SSTC and SANT, and more eutrophic coastal waters of the BENG, FKLD and HUMB (LONGHURST, 2007). The study was structured to attend three main goals: (i) to analyze the uncertainties of *in situ* measurement, (ii) to characterize the bio-optical variability and its relations with the distribution of the biogeophysical parameters (i.e., Chl*a*, PFTs, CDM and PSD), and (iii) to propose a class-based approach to synthetize the observed variability and enhance ocean colour products for the study region. The analyses aim to contribute for information of the ocean colour variability not only for the study region, but also for some general discussions of new venues to obtain more accurate ocean colour products elsewhere in the global ocean, as well as some insights on the relations between AOPs and IOPs, and the sources of bio-optical variability in the ocean.

2 OBJECTIVES

2.1. General

The general objective of the present work was to analyze the ocean colour variability across the southern Atlantic and Southeast Pacific, focusing on the sources of uncertainty and bio-optical variability, using *in situ* data obtained during the MV1102 cruise. The uncertainty analyses comprehended comparisons of the different approaches used for the radiometric and bio-optical measurements; closure experiments (using radiative transfer forward models); and the impacts on the retrievals of ocean colour products. The main goal was to identify the sources of uncertainty in the different approaches and define the best procedures to achieve accurate quantities for further analyses and protocol recommendations. The bio-optical variability comprehended a description of the distribution of the bio-optical properties and their relations with the biogeophysical parameters, i.e., the trophic state (indexed by the Chl*a*), the phytoplankton groups and microbial community, the CDOM and detritus content and the composition and size distribution of the particle assemblage. The ultimate purpose was to propose a class-based approach to synthetize the bio-optical variability and enhance the retrieval of ocean colour products, using class-specific parameterizations for ocean colour models. The rational of the regional scheme was to map water-types defined by the specific bio-optical properties and indices, i.e., the CDOM index (MOREL; GENTILI, 2009), the phytoplankton Size Index (CB06SI, Ciotti and Bricaud (2006)) (related to a_{phy}*), b_{bp}* and η.

2.2. Specific

The specific objectives were to:

- Analyze the uncertainties related to the *in situ* radiometric and bio-optical measurements, testing different processing schemes, comparing different approaches (e.g. above and in-water radiometry) and identifying the main sources of environmental, instrumental and methodological biases;

- Compare the measured and modeled R_{rs} in a closure experiment using forward radiative transfer models (MOREL; MARITORENA, 2001; MOREL et al., 2002);

- Describe the implications of the uncertainties for ocean colour remote sensing in the retrieval of biogeochemical products, with empirical and semi-analytical bio-optical models (OC4v6 (O'REILLY et al., 2000); GSM01 (MARITORENA et al., 2002); QAAv5 (LEE et al., 2002));

- Propose sampling and data processing schemes for the retrieval of accurate *in situ* radiometry and bio-optics, with the different approaches tested in the present work;

- Describe the distribution of the biogeochemical provinces in in the southern Atlantic and Southeast Pacific, for the austral summer of 2011;

- Describe the distribution of the bio-optical properties within the BGCP, and their relations with the CDOM and detritus content, the dominant phytoplankton group, the microbial community, and composition and size distribution of the particle assemblage;

- Analyze the impacts of the bio-optical variability on the retrieval of the Chl*a* using the OC4v6 MBR empirical model, identifying the sources of first and second order variability for the different BGCP;

- Synthetize the bio-optical variability using statistical correlation analysis (e.g. Spearman Rank, Principal Components) and propose a Regional Specific Optical Water-Types (R-SOWT) classification scheme (R-SOWT) using a K-Means Cluster Analysis and the specific IOPs i.e., CDOM index, CB06 Size Index, b_{bp}* and η

- Compare the performance of the R-SOWT with a global class-based approach of Optical Water Types (OWT) (MOORE et al., 2009), to define dynamic optical water-types associated with the trophic levels, phytoplankton distribution, PSD and biogeochemical processes;

- Evaluate the performance of the R-SOWT and OWT to enhance the retrieval of OCR products applying class-specific parameterizations for semi-analytical (SA) models, i.e., the QAAv5 and GSM01.

3 THEORETICAL BACKGROUND

3.1. Ocean Colour Radiances: fundaments, history and state of art

The aim of Ocean Colour Radiometry (OCR) is to retrieve information of the water optically active constituents (OAC) e.g. water molecules, phytoplankton pigments, CDOM, detritus, sediments, associating the inherent optical properties (IOPs) e.g. absorption and backscattering coefficients, to the apparent optical properties (AOPs) that can be remotely sensed by radiometric sensors e.g. radiances and remote sensing reflectance. The OACs have specific absorption and backscattering properties that interact with the solar downwelling irradiance (namely, E_d or E_S) within the water column. The proportion of E_d that did not suffer absorption nor forward scattering processes, and is thus backscattered to the ocean surface, corresponds to the solar upwelling irradiance (E_u). The portion of E_u that is transmitted through the ocean surface and travels in a solid angle, defined by a zenithal and azimuthal direction, is the water leaving radiance (L_w). An above-water radiometer usually measures a radiance signal contaminated by the sea surface reflection and atmospheric interference, depending on its altitude (sea level, aircraft or satellite platform), which is defined as the total radiance (L_T) and has to be corrected to obtain L_w. When normalized by E_d, the L_w retrieves the remote sensing reflectance (R_{rs}), which is an AOP that no longer depends on the instant light intensity, but solely on some geometrical aspects of the solar-sensor-viewing configuration (due to bidirectional effects of the R_{rs}), and on the IOPs of the water medium. Hence, the spectral shape and magnitude of the R_{rs} at a given sensor-solar geometry, will be mainly determined by the composition and concentration of the OACs present in the first few meters of the water column (GORDON; MCCLUNEY, 1975; MOREL; PRIEUR, 1977). One may thus, use the R_{rs} to determine the IOPs or concentration of the biogeophysical parameters, using either empirical models or radiative transfer inversion models (with analytical and semi-analytical approaches). The relation between the OACs, IOPs and AOPs is what determines the colour of the ocean, nominating this research field as *Ocean Colour Radiometry*.

The first OCR mission started in 1970 with the launch of the Coastal Zone Colour Scanner (CZCS), which was actually an experimental satellite that enabled the first

synoptic view of the global ocean. This revolutionized the research fields of oceanography and atmospheric sciences, providing new measurements that were never possibly obtained with traditional techniques from ships, buoys and even aircrafts (MCCLAIN, 2009). The success of the mission allowed efforts to be concentrated on further missions with a rapid advance of the emerging technologies and research fields. Despite of the simple radiometric characteristics of the CZCS, the images showed clear features of the distribution of phytoplankton biomass, which in sighted the first empirical bio-optical Chl*a* model. The model associated the 443/550 R_{rs} band ratio with the Chl*a* using 60 *in situ* match-up points. The rational of the model was that the chlorophyll *a* (plus its degradation products, e.g. pheophytin *a*) has an absorption peak centered at the 443 nm band, diminishing the $R_{rs}(443)$ will increasing Chl*a*, whereas the 550 nm band maintains invariable (O'REILLY et al., 1998).

The following satellite missions of SeaWiFS, MODIS and MERIS, allied to the increasing efforts to obtain globally distributed *in situ* match-ups of radiometric and bio-optical measurements, enabled further improvements for the retrieval of biogeophysical parameters (MCCLAIN, 2009). The empirical Chl*a* model evolved to the OC4 (for SeaWiFS) and OC3M (for MODIS) (O'REILLY et al., 2000) maximum band ratio (MBR) model, which are constantly up dated with new *in situ* sets collected across different provinces in the world's oceans. A diversity of other products are now obtained by empirical and semi-analytical models and routinely distributed by satellite ocean-colour project offices (e.g. Chl*a*, a_{phy}, b_{bp} and a_{cdm}). These products have served as great data sources for worldwide researches and the construction of climatological series, since satellite sensors provide a unique tool to access synoptic data over extensive areas, with global coverage and frequent temporal revisit (MCCLAIN, 2009).

Parallel to these advances, the OCR, however, also faces some important challenges regarding: the continuity of the space missions (that are expensive); merging ocean colour products from different sensors; some technical limitations for the requirements of sensor capability by the ocean colour community; needs of more specialized products for climate change monitoring (e.g. OPP and PFTs); and remote sensing of optically complex inland and coastal waters (MCCLAIN, 2009). The main challenge, however, is actually a precursor for most of the above cited, which is the retrieval of accurate

radiometric and bio-optical ocean colour products. Both satellite and *in situ* measurements may have high uncertainties, which will propagate to much higher levels for the derived biogeophysical products (MCCLAIN et al., 2004). The satellite measurements have even more uncertainties because of the atmospheric interference and radiometric calibrations challenges (IOCCG, 2010). The L_w that emerges from the ocean surface corresponds to solely 10% of the radiance signal measured by the satellite sensor, whereas 90% is from the atmosphere. The absorption and backscattering processes of the gases, aerosols and water vapor are modeled in radiative transfer atmospheric models, which are used to correct for their interference. However, the varying components, e.g., aerosols, are difficult to quantify in a pixel by pixel basis. Most models assume that the ocean is black for the near and medium infra-red bands (NIR and SWIR, respectively), with a null L_w due to the high water absorption. Thus, the NIR and SWIR bands are used to estimate the aerosol concentration (SHI; WANG, 2009). Waters with presence of sediments and phytoplankton blooms, however, may still have reliable NIR L_w values (DORON et al., 2011). Moreover, this correction scheme also fails for coastal areas with complex absorbing aerosols for which under-corrected absorption signals in the blue bands will lead to overestimations of Chl*a* (IOCCG, 2010). Regarding the radiometric calibration issue, the satellite sensors need to be constantly calibrated from space, because of the decaying sensor response function with time. There are different ways to do the calibration and a common way, has been applying vicarious calibration techniques using *in situ* match-ups as ground "truth" references. The vicarious calibration can be applied either by comparing the satellite retrievals with the *in situ* L_w or comparing the modeled top-of-the-atmosphere (TOA) radiance (with a radiative transfer code and *in situ* inputs) with the satellite signal (HOOKER, 2003).

The *in situ* radiometric and bio-optical data sets are vital for OCR missions, as they are used for the development and validation of bio-optical models, as well as for the vicarious calibration of the satellite sensors. The challenges in obtaining accurate *in situ* radiances have been addressed by several ocean colour groups with *in situ* experiments and radiative transfer modeling (MOBLEY 1999; HOOKER et al. 2002; ANTOINE et al., 2008). The above-water approach, which consists of above-water L_w and E_d, is subjected to sea surface reflection effects of sky and sun glint. Whereas, the in-water

approach consists of below-water L_u and E_d measurements coupled and above-water E_d (namely, E_S) measurements taken from deck sensors, and is subjected to effects of in-water perturbations (e.g. focus and defocusing effects of the downwelling rays) (STRAMSKA; DICKEY, 1998). Hence, the 5% uncertainty level requirement for OCR purposes of vicarious calibrations and bio-optical modeling (MCCLAIN et al., 2004) is very strict and few inter-comparison works evaluating the different approaches have obtained such success. It is actually even difficult to determine a quantity to be used as reference for inter-comparison schemes. Some works have attempted to apply closure experiments comparing the measured quantities with modeled, using forward radiative transfer models (GREEN; SOSIK, 2004; CHANG et al., 2007). The forward models use IOPs or OACs (e.g. Chl*a*) to derive the AOPs through radiative transfer functions (GORDON et al., 1988). These experiments are challenging due to the complexity of the relations between IOPs and AOPs, with needs for model simplifications. Nonetheless, it helps to better understand the relations and identify some sources of variability (e.g. bidirectional effects) (MOBLEY et al., 2002).

With all the challenges to obtain accurate radiometric data, only highly controlled monitoring sites, such as the Marine Optical Buoy (MOBY) (in the North Pacific), has been used for SeaWiFS and MODIS vicarious calibration exercises. The MOBY acquisition and data processing scheme is highly controlled, with quality filtering schemes that enable the strict maximum of 5% uncertainty. Moreover the data sets provided for such applications have strict requirements of low Chl*a* waters and hyper-spectral data (BAILEY et al., 2008). Applications for bio-optical model development and validation, on the other hand, require globally distributed data sets that come from regional and global networks with monitoring sites of time-series stations (e.g. CHLOROGIN, AERONET-OC, CalCOFI) and ship-based data sets including long-term cruises (e.g. the Atlantic Meridional transect programme – AMT) (WERDELL; BAILEY, 2005). The performance of bio-optical models is dependent on the accuracy and coverage of the radiometric and bio-optical data sets used to tune and parameterize the models. The NOMAD base, with coincident measurements of AOPs (L_w, E_S, K_d), Chl*a* and some IOPs (a and b_{bp}), is used for the OC4, OC3M and QAA (LEE et al., 2002) updates. The first version had >3,400 match-ups with a high Chl*a* range of 0.012-72 $mg.m^{-3}$ (WERDELL; BAILEY, 2005). The second version available in 2008

encompassed another 1,000 points (total of ~4,579). Nonetheless there are still extensive unsampled areas in the global ocean, which may compromise or limit the performance of ocean colour products for these regions. Moreover, even with some rigorous quality control with well-defined protocols for data collection and processing, when one applies more rigorous controls the set falls into half: from ~4,579 to 2,372 points (MOORE et al., 2009; SZETO et al., 2011). The global distribution ends up with only a few sampled regions, which are highly concentrated in coastal provinces (MOORE et al., 2009) (Figure 3.1). Hence, there is an urgent need to populate the unsampled areas with high quality radiometric and bio-optical data.

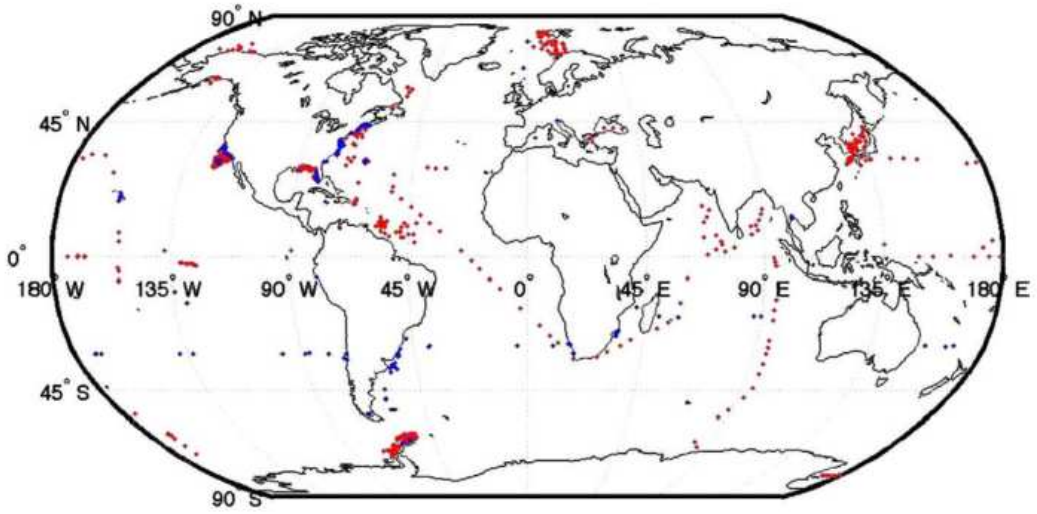

Figure 3.1 - NOMADv2 after quality control in red (total, N=2,372) and in blue are MODIS-Aqua validation satellite match-up points.

Source: Moore et al. (2009).

Semi-analytical (SA) models that relay on radiative transfer inversion schemes to derive IOPs and Chl*a* from AOPs, have a lower dependence on *in situ* parameterizations. Some specific parameters, however, still need to be parameterized or empirically derived, such as the a_{phy}* and the b_{bp} and a_{cdm} spectral slopes. Hence, even for the SA models there is need for *in situ* data sets, which are even scarcer with a great lack of *in situ* IOP measurements due to the complexity of such measurements, especially regarding a_s and

b_{bp} (N=80, for the NOMAD). The specific b_{bp} properties (spectral slope and efficiency factors) are generally obtained using synthetic data sets with radiative transfer (RT) modeling. Nonetheless, there are limitations inherent to the RT models and current knowledge of the IOP relations, and *in situ* measurements are still required for further improvements of bio-optical models (MARITORENA et al., 2002; IOCCG, 2006).

Besides the need for accurate radiometric and bio-optical quantities, recent works have revealed the needs for further understanding of the deviations regarding the global parameterizations and their relations with natural bio-optical variability. Moore et al. (2009) analyzed the OC4 deviations and proposed an Optical Water Type classification, scheme based on R_{rs} spectra, to map the OC4 uncertainties related to each class. Szeto et al. (2011) further analyzed some systematic over and underestimations of the OC4 associated with specific oceanic basins. The Atlantic Ocean, for instance, had a trend to be overestimated, whereas the Pacific and especially Southern Ocean tended to be underestimated. According to the authors, the overestimations were related to higher a_{phy}/Chl*a* (a_{phy}*), a_{cdm}/Chl*a* (a_{cdm}*) and b_{bp}/Chl*a* (b_{bp}*), and vice-versa, which was in accordance with a previous work of Loisel et al. (2010). These sources of bio-optical variability are cited as coming from regional biogeochemical processes, photochemical degradation, distribution of the phytoplankton community structure and the bulk particle assemblage (MOREL; GENTILI, 2009; LOISEL et al., 2010; SZETO et al., 2011). Although these relations are known to be linked, there is not yet a clear understanding on how specifically they occur and interact, and what are the dominant processes involved. Furthermore, it is still unknown if the bio-optical variabilities are in fact directly associated with dominant processes within the oceanic basins or to more specific biogeographical provinces. And if it is actually possible to define geographical boundaries with a new concept of bio-optical provinces linked to biogeochemical and ecological functioning, or if these variabilities are so dynamic that one would preferably work with other classification schemes not tided to geographical concepts. Szeto et al. (2011), for instance, proposed specific OC4 fits for each basin, whereas Moore et al. (2009) proposed a dynamic classification scheme which maybe spatio-temporal variable and not tied to a respective location. These analyses, however, require more extensive data sets widely spread in the global ocean. Szeto et al. (2011) even call attention for the fragility of their analysis due to the geographical restriction of the NOMAD set, and

highlight the importance of further works across different oceanic regions. Such analyses may provide means to obtain more accurate bio-optical modeling and serve as basis for further specialized products, such as the definition of bio-optical provinces with specific ecological and biogeochemical roles, and even the distribution of phytoplankton types, which is the state of art in OCR research.

These are some of the main challenges currently faced by the OCR scientific community and directions of further research efforts. The following subsections exhibit the general concepts of AOPs and IOPs (and OACs), as well as their relations with the forward and inversion models used in the present work.

3.2. Remote sensing reflectance

The above-water remote sensing reflectance (R_{rs}) (units, sr^{-1}) is defined as the ratio between the water leaving radiance (L_w) (units, $W.m^{-2}.sr^{-1}$) and the solar downwelling irradiance at the surface (E_d) (units, $W.m^{-2}$):

$$R_{rs}(\theta_v,\varphi_v,\theta_S,\varphi_S,\lambda)=\left[\frac{L_w(_v,\varphi_v,\theta_S,\varphi_S,\lambda)}{E_d(\theta_S,\varphi_S,\lambda)}\right] \tag{3.1}$$

where θ_v and φ_v are the zenith and azimuthal sensor-viewing angles; θ_S and φ_S are the solar zenith and azimuthal angles; λ is the spectral wavelength. Approximately 90% of the L_w signal corresponds to the light backscattered by the OACs within the first optical depth (δ) of the water column (GORDON; MCCLUNEY, 1975). This depth is correspondent to the diffuse attenuation coefficient K_d^{-1}, i.e., an optical parameter that defines the E_d exponential decrease with depth (z):

$$E_d(\lambda,z)=E_{d0}(\lambda,0^-)exp(-K_d(\lambda,z)z) \tag{3.2}$$

where 0^- corresponds to the depth just below the surface. The depth just above the surface is identified herein as 0^+.

3.3. Optically Active Constituents (OACs)

The main optically active constituents (OACs) present in marine environments may be cited as: the water molecules, the phytoplankton community, coloured dissolved organic matter (CDOM), detritus (particulate organic matter and adsorbed minerals) and suspended sediments (e.g. transported from river flows and bottom resuspension, in coastal regions) (IOCCG, 2002).There is a high range of other OACs that may also have significant roles in the bulk oceanic inherent optical properties, such as, hydrosols (micro air bubbles and inorganic particles), calcium carbonate coccolith plates (detached from coccolithophores), heterotrophic bacteria and virus (STRAMSKI et al., 2001). These, however, are usually treated in more specific occasions, such as in the presence of coccolith blooms, or when more detailed analysis are possible, e.g. with radiative transfer modeling.

The chemical composition of the OACs mainly determine their absorption properties, whereas the physical-chemical properties of shape, size and index of refraction determine their scattering properties. The total absorption (a) and backscattering (b_b) coefficients (units, m^{-1}) are given by the sum of the partial coefficients of each OAC:

$$a(\lambda) = a_w(\lambda) + a_p(\lambda) + a_s(\lambda) \tag{3.3}$$

$$b_b(\lambda) = b_{bw}(\lambda) + b_{bp}(\lambda) \tag{3.4}$$

The subscripts *w*, *p* and *s* stand for water, particle and CDOM, respectively. The a_p can be subdivided in the phytoplankton component (a_{phy}) and detritus (a_d). The detritus is actually commonly added to the a_s component namely, a_{cdm} or a_{dg} (g from gelbstoff), because of the similarity of their spectral behaviors, and the difficulty to separate their

contribution using remote sensing data (IOCCG, 2006). The a_{phy} can be partitioned in different phytoplankton groups in PFT models (HIRATA et al., 2008), and the b_{bp} can be partitioned in mineral particles, detritus, bubbles, bacteria, virus, phytoplankton, coccolith plates, depending on the needs and possible detailed level one may accomplish (STRAMSKI et al., 2001).

3.3.1. Water molecules

The water molecules have a high absorption coefficient in the shorter wavelengths of the ultraviolet (UV), low in the visible (VIS) and high again towards the longer wavelengths of the NIR spectral region (POPE; FRY, 1997). The molecular scattering is a Rayleigh-type, with an exponential increase towards the shorter bands of the blue and a quasi-isotropic distribution with a 50% backscattering efficiency (half of the incident light is backscattered). The seawater b_{bw} is somewhat different from the pure fresh water b_{bw}, which may be corrected with an adjusted factor for the salinity (TWARDOWSKI et al., 2007). The a_w and b_{bw} are used as constants in the bio-optical models and are parameterized using laboratory measurements and radiative transfer modeling (MOREL, 1974; BUITEVELD et al., 1994; POPE; FRY, 1997; TWARDOWSKI et al., 2007).

3.3.2. Coloured dissolved organic matter and detritus

The coloured dissolved organic matter (CDOM) also known as chromophoric DOM, yellow substance, gelbstoff and gilvin, is the fraction of the dissolved organic matter (DOM) (<0.2 μm) that absorbs light in the blue and UV. The CDOM spectral absorption (a_s or a_g) can be described by an exponential law function of wavelength, for which there is an amplitude parameter that is associated with the concentration of the substance, given by the absorption measured at a reference wavelength (λ_0), and a slope parameter (S) (units, nm^{-1}) that defines the shape of the exponential decrease with wavelength (BRICAUD et al., 1981):

$$a_s(\lambda) = a_s(\lambda_0)\exp(-S(\lambda_0 - \lambda)) \tag{3.5}$$

As previously mentioned, the detritus, which is the coloured particulate organic matter (a_d), has a similar spectral behavior and is thus, commonly treated in addition to the a_s contribution, due to practicity for remote sensing applications. The equation is exactly the same as in Equation 3.5, changing the a_s term for a_{cdm} (CDOM + detritus). These two components, albeit having spectral similarities and being part of degradation products in the carbon cycle, they are regulated by different biogeochemical processes and may vary independently in the ocean layers. In open ocean waters, the a_s contribution is usually much greater than a_d, and has a higher variability in relation to the phytoplankton biomass (Chl*a*) (SIEGEL et al., 2002).

The sources and sinks of CDOM are still not well understood, especially in remote open ocean waters due to the lack of *in situ* measurements, and with high precision (BRICAUD et al., 2010). For coastal regions subjected to river discharges, continental drainage and bottom resuspension, the highest contributions are from continental fulvic and humic acids (MATSUOKA et al., 2012), whereas in remote oceanic regions the local (autochthonous) marine sources are from degradation and respiration processes involving the phyto, zoo and bacterioplankton community, e.g. exudation, excretion, phytoplankton decay, virus cell lysis, grazing and sloppy feeding (STEINBERG et al., 2004). It was initially thought that the marine CDOM was mostly related to long term degradation processes involving past phytoplankton communities (BRICAUD et al., 1981). Recent works, however, have revealed important direct contributions of zooplankton (through excretion, sloppy feeding, fecal dissolution and mucus production) (STEINBERG et al., 2004) and phytoplankton exudation (ROMERA-CASTILLO et al., 2010), with varying quantities and qualities for each group of species. The CDOM content in oceanic waters has important ecological roles regulating the zoo, phyto and bacterioplankton communities. One is the attenuation of the UV light in the surface layers, serving as a photoprotector for harmful UV. On the other hand, the CDOM light harvesting in the blue region also competes with phytoplankton photosynthesis, regulating its growth. The sinking sources of CDOM are mostly bacterial degradation, current transport, and photochemical degradation in stratified systems. The photodegradation (or photobleaching), has an important role on biogeochemical cycling and radiative flux, as the derived products are: carbon-based gases, e.g. dioxide carbon (CO_2) and monoxide carbon (CO); low molecular-weighed

organic compounds (facilitating bacterial decomposition); and inorganic nutrients of nitrogen and phosphorous, available for primary production (MORAN; ZEPP, 1997).

The detritus is a lower end-product of the degradation processes of phytoplankton decay and usually has a stronger co-variation with the phytoplankton biomass (BRICAUD et al., 1998), although there may be some also some significant horizontal and vertical variations in the oceans (BRICAUD et al., 2010). An important role of the detritus for biogeochemical cycling, is the carbon storage in the ocean bottom, with larger particles that have sinking rates higher than the degradation and remineralization processes within the water column (DUCKLOW et al., 2001).

With all the complexity of the processes involved in the detritus and CDOM cycles, in both coastal and open ocean waters, significant variations in the global mean relation between a_{cdm} and Chl*a* have been reported, and called attention for observations of ecosystem functioning, global and regional biogeochemical cycling and possible climate changes (SIEGEL et al., 2002; MOREL; GENTILI, 2009; BRICAUD et al., 2010; MATSUOKA et al., 2012). Besides the amplitude variations in a_{cdm}, the spectral *S* parameter may also have some significant variations associated with its chemical structure, origin, matrix type (e.g. phytoplankton and zooplankton species), microbial activity and photodegradation processes (MARITORENA et al., 2002; BRICAUD et al., 2010). Hence, this parameter may also reveal or indicate some important processes related to the local community and biogeochemical cycling.

3.3.3. Particulate material

Absorption properties

For ocean colour purposes the particulate material is technically defined as the material retained in a 0.7 μm (nominal) pore-sized filter, whereas the dissolved material is what passes through a 0.2 μm pore (MUELLER et al., 2003). The particulate absorption coefficient is divided into the detritus (a_d) fraction, also referred to as non-algal particles (NAP), and the phytoplankton fraction (a_{phy}). The NAP term defines a higher range of living and non-living particles, besides the organic detritus such as, heterotrophic bacteria and minerals. However, these are usually non or weakly absorbing components,

and the most common term used for this fraction is still detritus. For remote sensing applications the a_d is summed to the a_s component, as previously described.

The a_{phy} function can be described by an amplitude parameter related to the biomass, indexed by Chl*a*, and a spectral parameter that defines the spectral shape, which is the specific absorption coefficient (a_{phy}*) (MOREL, 1980; BRICAUD et al., 1995; MARITORENA et al., 2002):

$$a_{phy}(\lambda) = \text{Chl}a * a_{phy*}(\lambda) \tag{3.6}$$

The a_{phy}* is the a_{phy} normalized by Chl*a* and corresponds to the phytoplankton absorption capacity in units of m^2.mgChla^{-1}. This parameter describes the effective area per milligram of chlorophyll *a* that absorbs light. Several ocean colour models use parameterized global means of the a_{phy}* to obtain either a_{phy} or Chl*a* in inversion schemes. Bricaud and Morel (1981) were the first to propose a global a_{phy}* spectra. Up-dates with further *in-situ* data and optimization fitting schemes have been applied since then (SIEGEL et al., 2002; BRICAUD et al., 2004). Nonetheless, there are significant variations in the a_{phy}* associated with phytoplankton groups and photoadaptation strategies, which are pointed as one of the main sources of deviations of ocean colour models (LOISEL et al., 2010; SZETO et al., 2011).

The a_{phy}* variability is caused by variations in the composition and concentration of the photosynthetic and photoprotective pigments, which will depend on the phytoplankton group/species and physiological state (age, nutrient, temperature and light regime) (MOREL; BRICAUD, 1981). The primary pigment present in all groups is the chlorophyll *a*. The accessory pigments (e.g. chlorophyll *b* and *c*, carotenoids and phycobiliproteins) are present in different compositions and concentrations, and some are used as biomarkers to identify specific groups in HPLC analysis (e.g. Divinyl chlorophyll-*b* for prochlorophytes and Peridinin for dinoflagellates Type1) (WRIGHT, 2005). There are some overlapping absorption bands, but each pigment has specific absorption peaks and their composition will determine the spectral shape of the a_{phy}*

(WOŹNIAK et al. 1998). The main source of variability of the a_{phy}* (> 80%) is, however, related to the intracellular concentration of the pigments, which causes a pigment shading effect namely "packaging effect" (SATHYENDRANATH et al., 1987; CIOTTI et al., 2002). The packaging effect has a direct relation with the phytoplankton size structure and co-varying physiological state, determined by the general ecological distribution of the dominant size associated with the trophic state. For instance, small *Prochlorococcus* prokaryotic cells (0.5-0.6 μm) are usually related to stratified low/nutrient/high light penetration waters, and tend to have low intracellular Chl*a* with low shading effects, and exhibiting high a_{phy}*. On the other hand, larger diatom groups (>20 μm) with complex cell structures organized in chloroplasts, occur generally associated with high nutrient/low-light penetration, well-mixed environments, and therefore need to have higher intracellular pigments, which in turns, has high shading effects and low a_{phy}* (CIOTTI et al., 2002). It seems contradictory that the cells under lower light levels have lower absorption capacity, but the need to produce higher Chl*a* to enhance the light harvesting for the entire cell, compromises, on the other hand, the absorption capacity of each individual molecule due to the consequent shading effects. Hence the bulk absorption is higher, but with a lower cross section. This co-variation of the a_{phy}* with the dominant cell size structure has been used in bio-optical models to enhance Chl*a* estimations and to retrieve the distribution of sized PFT groups (CIOTTI; BRICAUD, 2006; DEVRED et al., 2006; BREWIN et al., 2010).

Particle backscattering properties

In respect to the backscattering properties of the particulate material, the ocean colour models usually treat the particle component as the bulk living and non-living assemblage, denoted as particle backscattering coefficient (b_{bp}). Nonetheless, more specialized models may divide the b_{bp} in other components e.g. phytoplankton groups, heterotrophic bacteria, virus, minerals, coccolith plates, microbubbles, as previously described (STRAMSKI; KIEFER, 1991; STRAMSKI; et al., 2001; WESTBERRY, 2005; GORDON et al., 2009). However, even when analyzing the b_{bp} of the bulk particle assemblage, some general analysis may still be made associated with the composition and some specific characteristics based on variations of the specific parameters, e.g. backscattering efficiency factors and spectral dependency.

The b_{bp} is described by a power law function with an amplitude parameter determined in a reference wavelength ($b_{bp}(\lambda_0)$) and a spectral dependency defined by the slope (η):

$$b_{bp}(\lambda) = b_{bp}(\lambda_0)[\lambda_0 / \lambda]^{-\eta} \quad (3.7)$$

Both amplitude and spectral parameters of b_{bp} will vary with physical-chemical properties of the particle assemblage of: concentration, size, shape and refractive index. Another form to write the above equation is partitioning the amplitude parameter in a concentration number (N = number of particles per unit volume, units m^{-3}) and a cross section coefficient denoted as σ_{bp} (units, m^2), which provides the effective area of an element that scatters in the backward direction (given by: $\sigma_{bp} = b_{bp}/N$). Another term commonly used is the backscattering efficiency (Q_{bb}) which is an adimensional ratio between the light backscattered and the incident flux on the geometrical cross section of the particle. A similar term also applied in bio-optical models is the b_{bp} probability ratio which is also a unitless term ($\tilde{b}_{bp}(\lambda) = b_{bp}(\lambda)/b_p(\lambda)$) that defines the proportion of the flux that is backscattered in respect to the light scattered in all directions. This ratio is used, for instance, to derive the b_{bp} from b_p measurements (GORDON; BROWN, 1988; MOREL; MARITORENA, 2001). The b_{bp} normalized by the Chl*a*, known as the specific Chl*a* coefficient (b_{bp}*, analog to a_{phy}*) (units, m^2.mgChla^{-1}), is also used as an index of the b_{bp} cross section in respect to the phytoplankton pigment and co-varying particles (AHN et al., 1992). All these specific b_{bp} properties are dependent on the size, shape and index of refraction of the particle assemblage, as will be herein described.

The refractive index is a complex number composed of a real part, which is the ratio of the speed of light in seawater relative to that in the particle, and an imaginary part, which is proportional to the particle absorption. The b_{bp} of a phytoplankton culture, for instance, roughly mimics the inverse pigment absorption spectra (AHN et al., 1992). Hence, the refractive index will depend on how the physical-chemical properties of the particle medium propagate light (differently from the seawater medium) and its absorption properties. Particles with high index of refraction tend to have higher Q_{bb}

(e.g. minerals), whereas particles with low index have low Q_{bb}, and thus, lower contribution in the bulk b_{bp} (e.g. phytoplankton) (STRAMSKI; KIEFER, 1991; AHN et al., 1992;)

The particle shape introduces complex relations especially regarding nano-micro plankton cells and organic compounds with complex morphological structures. The visible spectral range, however, is more sensitive to small particles (<10 μm), which in nature tend to have more spherical shapes. Hence, ocean colour modelers have extensively adopted the Mie theory to determine b_{bp} relations with oceanic particles, assuming its simplifications. Mie theory describes the scattering processes of homogenous, non-absorbing, spherical particles using Maxwell's equations. Although there are limitations in its application, Mie solutions have proved very useful and reliable for oceanic particles (STRAMSKI; KIEFER, 1991).

Mie theory can explain the dependency of the scattering processes in terms of the particle size distribution (PSD). There are three types of scattering processes related to different particle size ranges that define the angular distribution of the scattered light (proportion of light that is forward, side and backscattered) and the quality of the scattered light (spectral dependency). Using a dimensionless term $q=2\pi r/\lambda$, where r is the particle radius, the scattering types of are: a) Rayleigh-type: $q<<1$, for particles much smaller than λ that have a quasi-isotropic volume scattering function (β_v) (units, $m^{-1}.sr^{-1}$) (which describes the distribution of the rays in each scattered solid angle) and a 4 slope (η) (with an exponential increase towards the shorter bands) (e.g. water and air molecules); b) Mie-Type: $0.1<q<50$, for particles with a radius approximately equivalent to λ, the forward scattering is much higher than the backscattering portion, with an anisotropic distribution, and η is between 3 to 1, with a greater contribution of longer λ (green-red) (e.g. particles in the size range of 0.12 to 11 μm, of ultrapico to nanoplankton, submicron bubbles and detritus); c) Non-selective-type: $q>50$, for particles much larger than λ, the scattering is highly anisotropic (high forward scattering) and the spectral dependency is neutral, $\eta = 0$ (equal for all wavelengths) (e.g. nano and microplankton, microbubbles, detritus and minerals). Following the size criteria, for the same particle $\tilde{b}_{bp}$ decreases as the size increases. One should keep in mind though, that when analyzing mixed particle assemblages, the index of refraction

and complex shapes of the different particles will also determine the bulk $\widetilde{b}_{bp}$ and b_{bp}, adding more complexity to these relations (STRAMSKI; KIEFER, 1991).

The scattering types occur simultaneously, although one process is likely to be dominant depending on the particle size distribution. The PSD, defined by the size and abundance of particles, can be represented by mathematical functions that describe the co-variation between these two variables. For oceanic marine particles the PSD is commonly described by a power law Junge-type function with a mean exponent (ξ) of 4. The function describes the increase of the particle concentration per unit volume (m^{-3}) with the decrease in size: for instance, small colloids and virus generally occur in a much higher concentration than microplankton cells in the same unit volume. The b_{bp} and PSD functions can be joined using Mie theory and radiative transfer functions using the following expression (KOSTADINOV et al., 2009):

$$b_{b,p}(\lambda) = \int_{D_{min}}^{D_{max}} \frac{\pi}{4} D^2 Q_{b_b}(D, \lambda, m) N_0 \left(\frac{D}{D_0} \right)^{-\xi} dD \tag{3.8}$$

Where, D is the particle diameter integrated in the interval of D_{max} and D_{min}, $\pi/4D^2$ is the particle geometrical cross section, Q_{bb} is the backscattering efficiency factor and m is the refraction index. The second term of the equation refers to the particle concentration of a diameter range, defined by the PSD function, where, N_0 is the concentration number (number/m^3) in a reference diameter D_0 and ξ is the slope of the power law function.

Applying such radiative transfer simulations, KOSTADINOV et al. (2009) found that there may be a direct linear relationship between the b_{bp} and PSD slope parameters (η and ξ) for η>1 (490-550 nm), which are inverse to the bulk b_{bp} amplitude variations. For instance, oligotrophic waters with low Chl*a* that are dominated by small particles have high η and ξ, and low b_{bp}, whereas highly productive waters likely dominated by larger particles have lower η and ξ, and higher b_{bp}. These relations have been used to associate

remote sensing derived η to the PSD, and ultimately to map the distribution of PFTs (LOISEL et al., 2006; KOSTADINOV et al., 2009). The results are promising, however model simulations always have many simplifications and limitations, and the extrapolation for particles beyond 10 μm may be unrealistic as the η should be spectrally neutral beyond this range. Another point is that the authors analyzed the retrieved PSD in terms of the phytoplankton size groups, supposing a tight co-variation between the bulk PSD of the particle assemblage with the PFTs. These interpretations should be thus made with care, as there are still ongoing investigations in this regard.

The main challenges for the ocean colour community regarding b_{bp} are due to the lack of *in situ* measurements of b_p, b_{bp} and PSD. Hence, most relations and parameterizations have relied on radiative transfer modeling with Mie solutions and synthetic data sets. The factors that determine the b_{bp} ratio and η slope are well known, however the nature of the particles that effectively contribute to the bulk oceanic b_{bp}, their PSD, size range and co-variations with the abundance and size structure of the phytoplankton groups, still remain unclear. There is however, a rather robust relation between b_p and Chl*a* for Case 1 waters (MOREL; PRIEUR, 1977). Morel (1980) was the first to publish a power law fit between these two variables using *in situ* data, which was further updated by Loisel and Morel (1998) (with 850 match-ups):

$$b_p(550) = 0.416[\text{Chl}a]^{0.766} \tag{3.9}$$

The positive relation between b_p and Chl*a* is reasonably explained by the higher scattering medium with a higher concentration of phytoplankton and co-varying living and non-living particles (HUOT et al., 2008). The spectral b_{bp} may then be derived from b_{p550} applying the $\tilde{b}_{bp}$ ratio and the power law function (Equation 3.7). In attempt to this, Gordon et al. (1988) proposed the use of a 1 η slope, following Mie solutions with a mean PSD for oceanic particles (with a 4 ξ slope and 1.05 refractive index), and a $\tilde{b}_{bp}$ of 0.5-2%, diminishing with the increase of Chl*a*. The dependency of the η slope with Chl*a* was made to account for the increasing absorption of the phytoplankton and co-

varying detritus material, in the shorter spectral bands. The $\tilde{b}_{bp}$ variation was based on previous observations that the bulk b_{bp} ratio for ocean particles would be 1-2% (GORDON; MOREL, 1983), whereas the phytoplankton cells have on average 0.5% (MOREL; BRICAUD, 1981). Hence, one would expect that with the increase in Chl*a*, phytoplankton cells would have a higher contribution on the scattering processes and thus, diminish the bulk $\tilde{b}_{bp}$. Morel and Maritorena (2001) further improved the model using the Loisel and Morel (1998) b_p vs. Chl*a* fit, and adjusting the $\tilde{b}_{bp}$ and η variations with Chl*a*, according to:

$$b_{bp}(\lambda) = \{[0.002 + 0.01(0.5 - 0.25\log_{10}[\text{Chl}a]](\lambda/\lambda_0)^{\eta}\}b_p(\lambda_0, \text{Chl}a) \quad (3.10)$$

where: $\eta = (1/2)(\log_{10}[\text{Chl}a] - 0.3)$ for $0.02<[\text{Chl}a]<2$ mg.m^{-3}, and η=0 for [Chl*a*]<2 mg.m^{-3}.

The first term in the brackets corresponds to the $\tilde{b}_{bp}(\lambda)$ which is modeled with a 0.002 (0.2%) minimal background for 100 mg.m^{-3} of Chl*a*, increasing with the decrease of the log transformed Chl*a*, up to 0.012 (1.2%) for 0.01 mg.m^{-3} of Chl*a*. The spectral power law function is applied to $\tilde{b}_{bp}(\lambda)$, and the η slope also varies from 1 to 0 for a Chl*a* range of 0.02 to 2 mg.m^{-3}. The second term in the equation is the b_p empirically determined by Loisel and Morel (1998) (Equation 3.9).

This b_{bp} model has been widely used in forward bio-optical modeling (retrieving AOPs from IOPs) however, there are some limitations to be considered. Morel and Maritorena (2001) point out some of the open issues for the $\tilde{b}_{bp}(\lambda)$ and η variations with Chl*a*, knowing that the phytoplankton has a very low $\tilde{b}_{bp}(\lambda)$ (~10^3-10^4) (AHN et al., 1992) and should thus, have a minimal influence in the bulk b_{bp} even at high Chl*a*. Huot et al. (2008) further analyzed a data set from the eastern South Pacific and found a robust relation between b_{bp} and Chl*a*, similar to that obtained for b_p vs. Chl*a* by Loisel and

Morel (1998). With some other analysis of the $\tilde{b}_{bp}(\lambda)$, they also found that within a Chl*a* range of 0.02 to >2 mg.m^{-3}, the $\tilde{b}_{bp}(\lambda)$ is insignificantly variable with the Chl*a* and spectrally neutral, likely because of the very low phytoplankton contribution to the bulk b_{bp}. Nevertheless, the Chl*a* still showed a robust relation with b_{bp} likely because there may be a tight relation between the phytoplankton community and the particles that effectively contribute to b_{bp} (e.g. heterotrophic bacteria, virus and submicron detritus). Hence, they propose that b_{bp} could be robustly derived from Chl*a*. This relation however, was found to be spectrally dependent and new η values were obtained for the fit, varying from 1.935 for 0.02 mg.m^{-3} to 0.833 for 2 mg.m^{-3} (almost twice as higher as in the Morel and Maritorena (2001) model). Huot and collaborators' (2008) major contributions were to provide b_p and b_{bp} measurements and novel analysis, across different biogeochemical provinces. Their considerations, however are still limited to the eastern South Pacific (with low aerosol deposition compared to other oceanic regions), and further analysis regarding the identification of the effective b_{bp} components, their relations with the phytoplankton community, and measurements of their optical properties and PSD, are still desired.

Further works, have also revealed a variability of the b_{bp}* (b_{bp}/Chl*a*), which was pointed as one of the main sources of the OC4 deviations (along with the a_{cdm}* and a_{phy}* variability) (LOISEL et al., 2010). The b_{bp}* is an index of the b_{bp} efficiency and even though its variability is known to be driven by the PSD, refractive index and shape of the bulk particle assemblage, the respective influence of each of these factors, is still poorly known (LOISEL et al., 2010). Thus, there are still important issues to be investigated regarding these variabilities, their impacts on ocean colour models and their importance for the interpretations on the composition of the particle assemblage and their roles on biogeochemical processes.

3.3.4. Phytoplankton Functional Types (PFT)

The main concept of Phytoplankton Functional Types (PFTs) is defined as groups of species that have similar biogeochemical and ecological roles (REYNOLDS, 2002). Due to the tight relations between important roles on carbon cycling and trophic flux with the size structure of the phytoplankton community, a common approach has been

to define PFTs according to their size classes: pico (0.2–2 μm); nano (2–20 μm); and microplankton (>20 μm) (SIEBURTH et al. 1978). This approach has been used to improve biogeochemical models (LE QUERE, 2006; FINKEL et al., 2009; LE QUÉRÉ et al., 2010), and has been explored by the OCR community, since some optical properties can be associated with the size classes, such as the a_{phy}*, b_{bp} spectral slope and efficiency factors, and the co-variations of the dominant size structure with Chl*a* (NAIR et al., 2008; RUDORFF; KAMPEL, 2012).

The phytoplankton size structure encompasses important information regarding both functional and ecophysiological properties of the groups. A general description of the main phyto-sized groups is given below:

Picoplankton (0.2-2 μm): composed mainly by picoeukaryotic cells, prochlorophytes and cyanobacteria, non-nitrogen (N_2)-fixers (e.g. *Synechococcus*) and N_2 -fixers, e.g. *Richelia*. These groups are widely spread in tropical and sub-tropical regions and because of their high surface:volume ratio they are well adapted to oligotrophic stratified waters with low-nutrient-high light penetration waters, such as the central oceanic gyres (FINKEL et al., 2009). *Richelia* is a diazotrophic endosymbiont commonly found in within the intercellular structure of diatoms. The picoplankton's main role on carbon cycling is within the microbial loop and nutrient regeneration. Because of their extensive geographic distribution *Synechococcus* and *Prochlorococcus* are cited as being responsible for approximately 35-50% of the total oceanic primary production (OPP). Diazotrophic cyanobacteria also have an important role on regulating new OPP, especially in nutrient limited oceanic environments. Besides *Richelia*, there are many other free-living and symbiont unicellular marine diazotrophic cyanobacteria that are less studied, but known to be abundant, and with important roles in oceanic N_2 fixation (ZEHR et al., 2001). *Trichodesmium* is also an important colony type diazotrophic cyanobacteria, however with larger sizes (SUBRAMANIAM et al., 1999).

Nanoplankton (2-20 μm): composed mainly by flagellate species widely spread in mid-latitude sub-tropical regions. Two important types of nanoplankters are the Dimethyl Sulphide (DMS) producers and the calcifiers (FINKEL et al., 2009). The DMS producers are composed by the classes: Dinophyceae, Haptophyceae, Chrysophyceae, Pelagophyceae and Prasinophyceae. They have an important role in the sulfur cycle and

global radiation balance, due to the release of sulfate aerosols that are condensation nuclei for cloud formation (KWINT; KRAMER, 1995). Some species are known to form extensive blooms in coastal and oceanic areas, such as *Phaeocystis sp*. (SCHOEMANN et al., 2005). The coccolithophore calcifiers (*Prymnesiophyceae*), on the other hand, produce calcium carbonate ($CaCO_2$) coccolith plates that cover their cells. Hence, besides being a source of $CaCO_2$ in the ocean upper layers, they have an important role on carbon export due to the high sinking rate of the detached coccolith plates. More than half of the carbon in the ocean bottom sediments is in the form of inorganic $CaCO_2$ produced by these and other microorganisms (e.g. foraminifers) (RAVEN et al., 2005). There are some concerns regarding possible effects of ocean acidification processes, due to higher concentrations of atmospheric carbon dioxide (CO_2), which may be diminishing coccolithophoride populations in the ocean (RAVEN et al., 2005, HOEGH-GULDBERG; BRUNO, 2010). Hence, this group has received considerable attention for environmental monitoring, especially with satellite imagery due to the high reflectivity of the plates forming extensive turquoise coloured blooms easily identified in the images (GORDON et al., 2009).

Microplankton (>20 µm): composed mainly by diatoms and dinoflagellates, with a distribution mostly associated with mid and high latitudes, and coastal well-mixed enriched environments (e.g. upwelling zones) (LE QUERE, 2006; FINKEL et al., 2009). The silicifiers that use silicate to form their cell walls are composed by the following classes: chrysophyta, silicoflagellates, xanthophyta and bacillariophyta. The last one are the diatoms, which have a major role on new OPP and carbon export, since their large and heavy cells make them sink rapidly to the deep ocean (SARTHOU et al., 2005). Dinoflagellates have a minor but also important role on carbon export. Some species may exhibit altering heterotrophic behaviors and some are also toxic for zooplankton, fish and human. These last ones can produce harmful algal bloom events (e.g. *Karenia Brevis*, *Gymnodinium*) (KAHRU; MITCHELL, 1998).

Regarding the optical properties of the PFTs there are two main branches of ocean colour models: (i) based on first order Chl*a* variations and the co-varying dominant size structure; and (ii) based on specific optical properties, which cause second order spectral variations in the R_{rs}. The first approach is based on mean global relations

between the trophic state (indexed by Chl*a* or $a_{phy}443$) and the dominant phyto-sized structure, with pico groups dominating low Chl*a* waters and micro groups high Chl*a* (UITZ et al., 2006; HIRATA et al., 2009). The main gaps of this approach is regarding phytoplankton blooms that may occur also associated with pico and nano classes, deviating from the global mean relation. The second approach explores the differences in the composition of the accessory pigments (BRICAUD et al., 2007; ASTORECA et al., 2009), a_{phy}* (CIOTTI; BRICAUD, 2006), η (KOSTADINOV et al., 2009) and b_{bp} efficiency factors (e.g. coccolithophores (GORDON et al., 2009) and *Trichodesmium* (WESTBERRY; SIEGEL, 2005)), or even the bulk specific optical variabilities (ALVAIN et al., 2006). Other approaches may also combine the trophic relations and specific optical properties (BREWIN et al., 2010; DEVRED et al., 2006; SATHYENDRANATH et al., 2004), or even use auxiliary ecological data to identify specific groups (e.g., temperature, geographic location, etc. (RAITSOS et al., 2008)).

In few years of research great advances have been achieved with the PFT bio-optical models, especially providing global mean maps of the PFT distribution from space. Nonetheless, most models are still restricted to the input data sets, constraining the applications for unsampled and more optically complex regions. Hence, when applying these models to specific regions, high deviations are still observed. A model that was chosen to be applied in routine ocean colour satellite processing schemes is the Ciotti and Bricaud (2006) size index approach (CB06), due to its relative simplicity and reasonable achievements in global applications. The size index model proposed by Ciotti and Bricaud (2006) follows previous analysis of Ciotti et al. (2002) of the variations of the a_{phy}* with the dominant phyto-size structure. The model retrieves a size index (S_f) that corresponds to the proportion of the picoplankton fraction, based on the variation of the specific absorption coefficient with the packaging effects. The index is derived from a linear spectral mixture fitting model, on which the end-members are the normalized absorption coefficient of the extreme sizes of pico ($a_{*<pico>}$) and microplankton ($a_{*<micro>}$):

$$a_{phy}(\lambda) = a_{phy}(505)[S_f a_{*<pico>}(\lambda)] + [(1 - S_f) a_{*<micro>}(\lambda)] \qquad (3.11)$$

Where a_φ is the phytoplankton absorption spectra and $a_{phy}(505)$ is the absorption at 505 nm which was used to normalize the end-members. The $a_{phy}(\lambda)$ and $a_{phy}(505)$ may be obtained using semi-analytical inversion schemes or empirical models (e.g. $a_\varphi(505) = 0.0185\ [Chla]^{0.68}$ (BRICAUD et al., 1998)). The S_f index is the spectral fitting factor retrieved, and varies from 1 (with picoplankton dominance) to 0 (for microplankton dominance). This model was tested with SeaWiFS data, in the southeast Brazilian coast, using a semi-analytical IOP model (ROESLER; PERRY, 1995). The size index was retrieved with a 17% error, which was considered satisfactory even when applied to optically complex coastal waters (CIOTTI; BRICAUD, 2006).

There are however, some gaps and constraints in the phyto-size classification scheme that need careful attention. For instance, some unicellular cyanobacteria may achieve sizes up to 20 μm (ZEHR et al., 2001), whereas some dinoflagellates and diatoms may also have smaller sizes sharing the nano and pico-sized groups. These deviations may cause mis-leading interpretations of the composition and biogeochemical and ecological roles of the classified groups. Another issue is that some groups may be within the same size class, but have also other important biogeochemical and ecological roles, that should be differentiated, such as the diazotrophic cyanobacteria, coccolithophorides, and toxic dinoflagellates. Hence, further investigation of bio-optical properties that may be used for complementary distinction of PFTs are desirable (NAIR et al., 2008; RUDORFF; KAMPEL, 2012).

3.4. Ocean Colour Models

Ocean colour models may be classified in empirical, semi-analytical or analytical approaches. Empirical models are developed whereof statistical relations established between remote sensing data and bio-physical-chemical parameters, which require large data sets with simultaneous *in situ* measurements. These models can describe complex relations, but are dependent on the availability of the data, and have limitations on the extrapolation of the predicted estimate from the set used for its formulation (IOCCG, 2006). Semi-analytical (SA) algorithms relate the AOPs with IOPs and OACs using radiative transfer equations (GORDON et al., 1988). The SA models allow to derive multiple parameters and are less dependent on *in situ* parameterizations, although not

completely since some properties still rely on parameterizations, such as the specific coefficients (e.g., a_{phy}*, η, S). Analytical algorithms are strictly based on theoretical radiative transfer solutions and spectral decomposition techniques to derive the AOPs or IOPs. Hence, they are independent of *in situ* parameterizations, but generally require accessible high signal-to-noise (S:N) hyper-spectral data, which is still not very much accessible for current satellite ocean colour monitoring (MCCLAIN, 2009).

For the SA and analytical models there are two paths used in ocean colour modeling: the forward and inverse schemes. The forward approach corresponds to the estimation of AOPs (e.g. L_w, K_d, R_{rs}) using IOPs (e.g. absorption, backscattering coefficients) or Chl*a* as inputs. The inverse approach, as one may sense, is the estimation of IOPs and OACs from AOPs. The former may be used to obtain missing parameters in an AOP data-set with simulated data, obtain parameterizations, or improve analysis on the radiative transfer processes and for closure experiments (modeled vs. measured). The inverse approach, on the other hand, is applied to obtain the biogeophysical properties (from IOPs and OACs) using radiometric *in situ* and satellite data.

3.4.1. Forward Semi-analytical Models

The above-water remote sensing reflectance (R_{rs}) can be modeled using the following approximation with radiative transfer equations (RTE) (MOREL et al., 2002):

$$R_{rs}(\lambda) \approx \frac{f'(\lambda)}{Q'(\lambda)} \frac{t_{(w,a)} t_{(a,w)}}{n_w^2} \frac{b_b(\lambda)}{a(\lambda) + b_b(\lambda)} \tag{3.12}$$

Where the ratio f'/Q' (units, sr^{-1}), which depends on environmental and bidirectional effects, relates the AOP R_{rs} to IOPs b_b and a (MOREL; GENTILI, 1996; MOREL et al., 2002), t(w,a) and t(a,w) are the water-air and air-water transmittance factors, which are equivalent and close to ≈ 0.98, regardless of the sea state, and n_w is the refraction index of the sea water (≈1.34) (AUSTIN, 1974). b_b is the total backscattering coefficient and a is the total absorption. For simplicity, Case 1 waters may use an approximation of b_b/a

instead of the complete term of $b_b/(a+b_b)$, considering that $a>>b_b$ and thus, the probability of a photon to scatter more than once is very low (when single scattering dominates) (MOBLEY, 2004). In such case, the "loss" due to multiple scattering may be considered negligible. For the b_b/a term the f'/Q' ratio is somewhat different and referred as f/Q (MOREL et al., 2002). The RTE approximation also assumes that the water column is homogenous, with a co-varying b_b/a with depths (MOBLEY, 2004).

The Q (units, sr) is a bidirectional factor of the R_{rs}, accounting for the anisotropy of both the incident light field and diffuse backscattered light. The factor is equivalent to the remote sensing reflectance (R_{rs}) divided by the diffuse reflectance (R), which is integrated in the entire backward hemisphere ($R=E_u/E_d$) (hence, $Q= R/R_{rs}$). For an isotropic volume scattering function (VSF) (β_v equal for all angles), Q is approximate to π, and for anisotropic scattering Q is either higher or lower at any angle. Since the factor is dependent on the scattering processes, it will vary with wavelength, the IOPs (water OAC's concentration), sky illumination conditions (solar angles and atmospheric optical thickness-τ_a), and the sensor-viewing geometry. It is generally higher for viewing angles departing from nadir, higher OAC concentration, and solar zenith angle (SZA), with its maximum usually at 550 nm (MOREL et al., 2002; LEWIS et al., 2011).

The f is an environmental factor that relates AOPs to IOPs, as $R=f(b_b/a)$. It is what mainly regulates the amplitude variation of R depending on the IOPs and illumination conditions (τ_a and SZA) (MOREL; GENTILI, 1993). The f factor is more spectrally neutral, although there are some variations especially for low and high Chl*a* waters (MOREL et al., 2002).

There are some other forward modeling approximations with empirical and semi-analytical approaches that have been proposed in the past few years. A well-known and commonly used semi-analytical model is the Morel and Maritorena (2001) (referred herein as MM01). The MM01 is based on the same b_b/a approximation as in equation 3.11, for Case 1 waters. The difference is that the model estimates K_d and b_b using Chl*a* inputs (with empirical and SA relations), and then in a step-by-step iterative processes, sequentially models a, R and R_{rs}, with RTE approximations. The main advantage of this approach is that it links the RTE concepts of forward modeling, with empirical relations that allow one to determine the IOPs and AOPs, solely with the Chl*a* as input. Hence,

one does not need a and b_{bp} measurements for the forward modeling, which are only recently becoming more available for OCR research.

The MM01 is applied in the following way: first $K_d(\lambda)$ is derived using the empirical power law fit: $K_d(\lambda)=K_w(\lambda)+\chi(\lambda)[\text{Chl}a]^{e(\lambda)}$ (where, K_w is the water diffuse attenuation coefficient); and $b_b(\lambda)$ is derived using $b_{bp}(\lambda)$ obtained as in equations 3.9 and 3.10, and summed to b_{bw}. Then a first set of the total absorption $a(\lambda)$ is derived using a simplified term of $a(\lambda)=0.75K_d(\lambda)$ and the below water diffuse reflectance ($R(\lambda)$) is derived using: $R=f(b_b/a)$. A second $a(\lambda)$ is then derived using a more complete approximation, according to Gershun's equations:

$$a = K_d \mu_d [1 + R(\mu_d / \mu_u)]^{-1} [1 - R + (K_d)^{-1} dR / dZ] \quad (3.13)$$

where μ_d is the mean cosine of the downwelling irradiance (E_d) and μ_u of the upwelling irradiance (E_u). The equation is applied with some simplifications, setting μ_u to a mean 0.40 value, neglecting dR/dZ and using μ_d from a look-up-table (LUT) obtained from RT simulations varying with SZA and Chl$a$ (μ_d ~0.90). Then begins an iterative process to readjust the a and R to more precise values, estimating a second $R(\lambda)$ with the second $a(\lambda)$; then a third $a(\lambda)$, and so on until the 4^{rth} $R(\lambda)$. The above water remote sensing reflectance is finally determined as: $R_{rs} = (Rt^2)/(Qn_w^2)$.

3.4.2. Empirical and inverse SA models

The first bio-optical model used for the retrieval of satellite ocean colour products was the empirical band ratio algorithm for Chl$a$, that evolved to the MBR OC4 (O'REILLY et al., 2000). Despite of the simplicity of the empirical approach, the OC4 is still widely applied for global Case 1 waters retrieving the most accurate Chl$a$ satellite product for Case 1 waters (SZETO et al., 2011). On the other hand, this approach is limited to solely one biogeochemical product, limiting the information that can be retrieved from OCR, and is constrained to solely Case 1 waters, where Chl$a$ should be the dominant constituent governing the bulk bio-optical properties.

With the advances on the knowledge of the bio-optical relations and computational capacity, a high range of semi-analytical (SA) models have been proposed in the past few years, with inversion schemes to obtain multiple parameters, i.e. Chl*a*, a_{phy}, a_{cdm} and b_{bp}, simultaneously from R_{rs} spectra (IOCCG, 2006). Some examples are the MERIS Neural Network Algorithm (DOERFFER et al., 2002); the MODIS semi-analytical algorithm (CARDER et al., 1999), the Quasi-Analytical Algorithm (QAA) (LEE et al., 2002) and the Garver-Siegel-Maritorena (GSM) (MARITORENA et al., 2002). There are many others, as there has been a race to develop the most accurate model adapted for different satellite sensors. Nonetheless, the current efforts of the OCR community have been to concentrate on improving existent models rather than developing novel ones (WERDELL et al., 2013). Of all these, the most commonly applied for satellite monitoring, that are implemented in routinely distribution offices, are the GSM and QAA. These two models have shown reasonable performances for global ocean-colour retrieval (IOCCG, 2006) and will be further detailed as they were chosen for the analysis in the present work. The main constrains of the SA approaches are: the dependence on parameterizations of some specific IOPs and AOPs, such as the *a*phy*, η, S and f/Q (or g factor); as well as, the retrieval of ambiguous results due to non-linear relations with multiple combinations of IOPs that may be retrieved from same R_{rs} spectra; and computational capacity to processes large data sets using more resolved models (IOCCG, 2006). These are some reasons that explain why the empirical approach is still extensively used retrieving more accurate Chl*a* values for Case 1 waters. Nonetheless, the SA approach provides more venues for further enhancement of bio-optical retrievals, as the comprehension of optical relations and variability within the ocean are better understood. SA models may obtain a much greater range of biogeophysical properties and be applied for different water types with independent variations between the OACs (IOCCG, 2006).

3.4.2.1. Empirical MBR OC4 (O'REILLY et al., 2000)

The empirical OC4 maximum band ratio (MBR) Chl*a* model (O'REILLY et al., 2000) is based on a 4th order polynomial fit of the three R_{rs} band ratios (443; 490; 510/555) with log transformed Chl*a*. The principal of the MBR is an optimized selection of the ratio with best S:N for each Chl*a* level. For oligotrophic waters the 443/555 retrieves

the MBR with a high S:N ratio, whereas high Chl*a* waters have a low $R_{rs}(443)$ signal due to the high absorption, and the S:N is much lower, hence the 510/555 retrieves a more accurate MBR. Beside the S:N ratio, the atmospheric correction is usually also more accurate for the longer bands in high Chl*a* waters, due to the near infrared (NIR) extrapolation techniques applied (O'REILLY et al., 2000). The OC4 is constantly updated with global *in situ* R_{rs} and Chl*a* data sets and its last version is the 6th with the NOMAD v2 data set (~3,467 match-ups). The OC4v6 is:

$$\log_{10}(\text{Chl}a) = 0.3272 - 2.9940X + 2.721X^2 - 1.2259X^3 - 0.5683X^4 \quad (3.14a)$$

$$X = \log_{10}\left(\frac{\max[R_{rs}(443), R_{rs}(490), R_{rs}(510)]}{R_{rs}(555)}\right) \quad (3.14b)$$

Despite of being empirically derived and thus restricted to the input global data set, which has serious geographical limitations as discussed in previous sections, the data set covers a high Chl*a* dynamic range (0.02-72 mg.m^{-3}) and is widely applied, usually retrieving the most accurate satellite Chl*a* values for Case 1 waters (WERDELL; BAILEY, 2005; MOORE et al., 2009; SZETO et al., 2011).

3.4.2.2. Inverse models: GSM01 (MARITORENA et al., 2002)

The Garver-Siegel-Maritorena version 1 (GSM01) is a semi-analytical approach developed by Garver and Siegel (1997) and modified by Maritorena et al. (2002) with an optimized global tuning of the specific parameters: $a_{phy}^*(\lambda)$, b_{bp} spectral slope (η) and a_{cdm} slope (S). The model is based on the quadratic function of Gordon et al. (1988):

$$R_{rs}(\lambda) = \frac{t^2}{{n_w}^2} \sum_{i=1}^{2} g_i \left(\frac{b_{bw}(\lambda) + b_{bp}(\lambda_0)(\lambda/\lambda_0)^{-n}}{a_w(\lambda) + a_{cdm}(\lambda_0)\exp(-S(\lambda-\lambda_0)) + [\mathrm{Chl}]a_{phy^*}(\lambda) + b_{bw}(\lambda) + b_{bp}(\lambda_0)(\lambda/\lambda_0)^{-n}} \right)^i \quad (3.15)$$

The g parameters (g_1 = 0,0949 e g_2 = 0,0794) are equivalent to the *f'/Q'* ratio of Morel et al. (2002). The known parameters which characterize the spectral shape are: the water coefficients and the specific coefficients (a_{phy}*(λ), η and S). The unknown correspond to the amplitude variations of the R_{rs} at λ_0 and are the b_{bp}(443), a_{cdm}(443) and Chl*a*. The R_{rs} inputs are the six SeaWiFS spectral bands (412, 443, 490, 510, 555 and 670 nm) and the fitting procedure is done with a non-linear Levenberg Marquardt minimum square regression fit. The a_{phy}*(λ) was derived using *in situ* data, whereas the η and S were tuned using synthetic IOP data, for a global set of Case 1 waters. The main advantage of the approach is the derivation of the IOPs and Chl*a* independently and simultaneously in a relatively simple scheme. The constrains are the natural deviations of the specific IOPs from the global fits, and possibilities of ambiguous results due to similarities of R_{rs} spectra (IOCCG, 2006).

3.4.2.3. Inverse models: QAA (LEE et al., 2002)

The Quasi-Analytical Algorithm (QAA) was proposed by Lee et al. (2002) and updated by Lee et al. (2007) in its 4th version. The last is the 5th version adjusted with NOMAD v2. The model is adapted for MODIS, SeaWiFS and MERIS bands (using the same coefficients for adjacent bands without significant impacts). The QAA is applied in a step-by-step process: 1) first deriving the total absorption and backscattering coefficients; and then 2) the phytoplankton and CDM absorption, which are obtained by an analytical decomposition of the total a(λ).

1st Step: The first step is divided in the following sub-steps:

1) first the total a(λ_0= 555 nm) is derived using an empirical model adjusted with synthetic simulated data (IOCCG, 2006):

$$a(555) = a_{\mathrm{w}}(555) + 10^{-1.146-1.366x-0.469x^2} \tag{3.16a}$$

$$X = \log\left(\frac{R_{\mathrm{rs}}(443) + R_{\mathrm{rs}}(490)}{R_{\mathrm{rs}}(555) + 2\dfrac{R_{\mathrm{rs}}(670)}{R_{\mathrm{rs}}(490)}R_{\mathrm{rs}}(670)}\right) \tag{3.16b}$$

The 443, 555 and 670 nm bands were chosen for the fit to optimize the performance of the model for both low and high Chl*a* waters.

2) The below water remote sensing reflectance (r_{rs}) is derived with the following approximation (LEE et al., 1999):

$$r_{\mathrm{rs}}(\lambda) = R_{\mathrm{rs}}(\lambda)/(0.52 + 1.7R_{\mathrm{rs}}(\lambda)) \tag{3.17}$$

3) The $b_{\mathrm{b}}(\lambda_0)$ is determined using the Gordon et al. (1988) quadratic RTE approximation (and with the previously derived $a(\lambda_0)$ and $r_{\mathrm{rs}}(\lambda_0)$):

$$\frac{b_{\mathrm{b}}(\lambda)}{a(\lambda) + b_{\mathrm{b}}(\lambda)} = \frac{-g_0 + \sqrt{(g_0)^2 + 4g_1 * r_{rs}(\lambda)}}{2g_1} \tag{3.18}$$

Where g_0=0.089 and g_1=0.125, adjusted from Case 1 and 2 waters.

4) $b_{\mathrm{bp}}(\lambda)$ is determined from $b_{\mathrm{b}}(\lambda_0)$ subtracting the $b_{\mathrm{bw}}(\lambda_0)$ term, and using the η slope determined from an empirical model (adjusted with NOMADv2):

$$\eta = 2.0\left(1 - 1.2\exp\left(-0.9\frac{r_{rs}(443)}{r_{rs}(\lambda_0)}\right)\right) \tag{3.19}$$

5) The spectral $a(\lambda)$ is then determined using the spectral $b_{bp}(\lambda)$ and the RTE quadratic function of Equation 3.18.

2nd Step: To obtain a_{phy} and a_{cdm} a spectral decomposition technique is then used with a system of equations containing two ratios (ζ and ξ') of adjacent bands, determined with semi-analytical functions:

$$\begin{cases} a_{cdm}(440) = \dfrac{(a(410) - \zeta a(440))}{\xi - \zeta} - \dfrac{(a_w(410) - \zeta a_w(440))}{\xi - \zeta} \\ a_{phy}(440) = a(440) - a_{cdm}(440) - a_w(440) \end{cases} \tag{3.20a}$$

$$\zeta = a_{phy}(410) / a_{phy}(440) = 0.74 + \frac{0.2}{0.8 + r_{rs}(440) / r_{rs}(\lambda_0)} \tag{3.20b}$$

$$\xi = a_{cdm}(410) / a_{cdm}(440) = \exp(S(440 - 410)) \tag{3.20c}$$

$$S = 0.015 + \frac{0.002}{0.6 + r_{rs}(443) / r_{rs}(\lambda_0)} \tag{3.20d}$$

The main advantages of the QAA are that it is applicable for both Case 1 and Case 2 waters due to the different set of bands used in the blue, green and red, and the independence of all relations with Chl*a*. It is also more flexible to variations in the specific coefficients, since η and S are not fixed, but empirically derived using r_{rs} ratios.

3.5. Water Type Classification

Given the complexity of the different OACs and their interactions with the submersed light field, classification schemes of optical water types have been proposed and are commonly used for general interpretations of ocean colour variability and for bio-optical modeling applications. The first classification scheme proposed in literature was according to Jerlov (1968), in which he defined 5 typical classes of oceanic waters and 9 classes of coastal waters using a global data base of surface downward irradiance transmittance spectra (~1 m). This classification was very useful for the beginning of ocean colour research however, there was not yet a comprehensive knowledge of the IOPs that affected and determined the ocean colour variability. Ten years later Morel and Prieur (1977) proposed a more generic scheme, based on current findings, which is up to date the most used classification due to its practical application for bio-optical modeling purposes: the Case 1 and Case 2 water types. According to them, Case 1 waters is a class for which the phytoplankton concentration is higher that of the other particles, and their pigment (plus degradation products) has thus, the major role in the biogenic absorption. Gordon and Morel (1983) added further analysis and stated that all the other biogenic compounds (e.g. CDOM and detritus) should co-vary with the phytoplankton biomass, as they are products of the algae decay and exudation, and zooplankton grazing. Case 2 waters are related to sediment and CDOM dominated waters that vary independently due to external sources of river discharge, sediment resuspension and aerosol dusts. The Case 1 classification has been widely used as a restriction of application for global ocean colour models, which are parameterized for such conditions of co-varying substances with the phytoplankton biomass. Whereas, Case 2 waters have been referred to optically complex environments mainly of coastal and in-land waters, for which more complex and mostly site-specific parameterizations are needed (IOCCG, 2000).

This classification scheme has provided basis for great advances in ocean colour modeling over the global ocean. Nevertheless, there are several issues regarding the applicability of this scheme. The discussion of the validity of such a classification in the way it has been applied, for “global” Case 1 models, has been brought up by the ocean colour community (MOBLEY et al., 2004) and is still not well resolved. New findings

of the complexity and variability of the processes that govern the CDOM and detritus (e.g. exudation, algae decay, sloppy feeding, bacterial decomposition, photo-bleaching and current transport), across different biogeochemical provinces and seasons, have opened new avenues for researches regarding the bio-optical variability of these compounds and their relevance for interpretations biogeochemical cycles (MOREL; GENTILI, 2009). The comprehension of other important OACs that may have even more independent variations, e.g. hydrosols, coccolith, bacteria, virus, have also highlighted the importance of the particle backscattering (b_{bp}) variability (STRAMSKI et al., 2001; HUOT et al., 2008), which is much less understood than the biogenic absorption, and may have a significant role on ocean colour variability and associated biogeochemical processes (BROWN et al., 2008). Moreover, even within the phytoplankton community structure, second order variabilities due to the composition and concentration of accessory pigments and the size structure of the different dominant groups, have brought up new insights on the sources of second order variations between the R_{rs} and Chl*a* (or a_{phy}). Hence, even for "strictly" Case 1 waters, there is a variability intrinsic to the former relation that has received considerable attention, especially with the recent demand of biogeochemical modelers for the identification of phytoplankton function types (PFT) from space (NAIR et al., 2008).

The simplified Case 1 and Case 2 classification was thus important for the early years of the OCR development, allowing to address the problem in a feasible manner with the the state of art knowledge and tools (instrumental and computational). This was important for the evolution of a series of ocean colour products and the generation of global maps that allowed a synoptic view of biogeochemical parameters, with the first order variation linked to the phytoplankton biomass. With the new insights and needs for more accurate and specialized products (e.g. CDOM deviation index and PFT), new conceptual frameworks of ocean colour modeling with further classification schemes are needed. Some new classifications have been proposed for applications of the OC4 empirical model. Moore et al. (2009) proposed a class-based approach namely Optical Water Type (OWT), which defined eight classes based on R_{rs} spectra. The model was applied to produce uncertainty maps of the OC4 weighed by the classes, but it can also be applied to defined class-specific parameterizations for the OC4 and other bio-optical models. The main constrain is that there are only a limited number of match-up points

for each class (5-549 points), but this may be overcome with new up-dates of the NOMAD. The OWT was further improved by Moore et al. (2012) to add a class associated to coccolithophore blooms, as there are frequent extensive bloom formations in the mid and high latitudes.

The Ocean Basin approach (named herein as OB) proposed by Szeto et al. (2011) is still in a preliminary phase as the authors recognize that due to the limited geographic coverage of the NOMAD, one may not yet state that the ocean basins are significantly optically different. This is why they entitled their article as a question rather than a statemente: "Are the oceans optically different?". The authors did however encounter evidences of systematic over and underestimations of the OC4 for each of the oceans: Atlantic, Pacific, Indian and Southern Ocean. These systematic deviations were statistically associated with the specific optical properties i.e., a_{phy}* and CDOM deviations. Hence, they hypothyse that each basin may have dominant specific optical properties related to the PFT distribution and biogechemical processes. Each of the oceans could thus, have a regional specific parameterezation for the OC4, as they preminarily propose in the end of the article. Nonetheless, they do not yet intend to propose the immediate application of the approach, but rather highlight the importance of consolidating regional data sets with further *in situ* surveis, across different biogeochemical provinces and at different seasons. This would allow a more comprehensive analysis to confirm the validaty and significance of the approach.

These class-based approaches have been applied for the OC4 model, however SA models could also make use of such classifications schemes to account for the variability of the specific IOPs and perhaps reduce ambiguous results. In attempt to this a generic Generalized IOP model (GIOP) recently implemented on SeaDAS software (NASA ocean colour group) (since 2010), aims to allow more flexibility for the users to run the SA models (WERDELL et al., 2013). The user can choose the inversion/optimization method (e.g. Levenberg-Marquardt, matrix inversion) and different ways to determine the specific IOPs, either with a user-defined (of global, regional or class-specific parameterizations) or using different models: e.g. Ciotti and Bricaud (2006) for a_{phy}*, Lee et al. (2007) for S and η; or Loisel et al. (2006) for η.

Further improvements concern also the implementation of a_s and a_d separate eigenvectors (with specific parameterizations).

There is an overall agreement in the OCR community that the Case 1 and 2 classification scheme needs to be reviewed for further ocean colour applications, as there are important bio-optical variabilities that need to be accounted for to obtain more accurate products and further information on biogeochemical processes. Whether this may be done by proposing new classification schemes that synthetize the dominate variabilities into optical classes, or by developing more analytical spectral decomposition approaches that are less dependent on parameterizations, is still under investigation. The present work focuses on the first alternative with an application of a classed-based approach for the study region to define optical water types associated with the specific optical properties. Nonetheless, it also makes use of the second alternative combining semi or quasi-analytical models to derive the IOPs, as will be detailed in the Materials and Methods section. The follow sub-topics briefly describe the OWT and OB approaches that were also tested in the present work.

3.5.1. Optical Water Type - OWT (MOORE et al., 2009)

The Optical Water Type (OWT) approach (MOORE et al., 2009) was implemented to define dynamic optical water types based on R_{rs} spectra (adapted for SeaWiFS, MODIS or MERIS bands) and produce uncertainty Chl*a* maps for the OC4. The rational was that the OC4 uncertainty is dependent on the bio-optical variability, being higher for more complex optical waters with non-linear optical relations. Hence, instead of using a mean Chl*a* uncertainty level for the OC4 product, the objective was to provide uncertainty values on a pixel-by-pixel basis (for satellite maps), with weighted functions of the uncertainties assigned for each class. The approach was implemented first defining the OWT classes using *in situ* $R_{rs}(0^-)$ from the NOMAD v2 (n=2,372) and a Fuzzy-c-Means cluster Algorithm (FCM) (Figure 3.2). The FCM was chosen because it allows one to define the optimal number of clusters using *validity functions.* These functions measure the performance of a clustering result, with parameters of the distance (separation) and distribution of the points around a cluster (compactness). The optimal number was of 8 OWT classes for the global ocean, being 1-4 of Case 1, with

progressive increase of Chl*a* mean values, and 5-8 of Case 2, with a progressive contribution of sediment dominated waters (Figure 3.2).

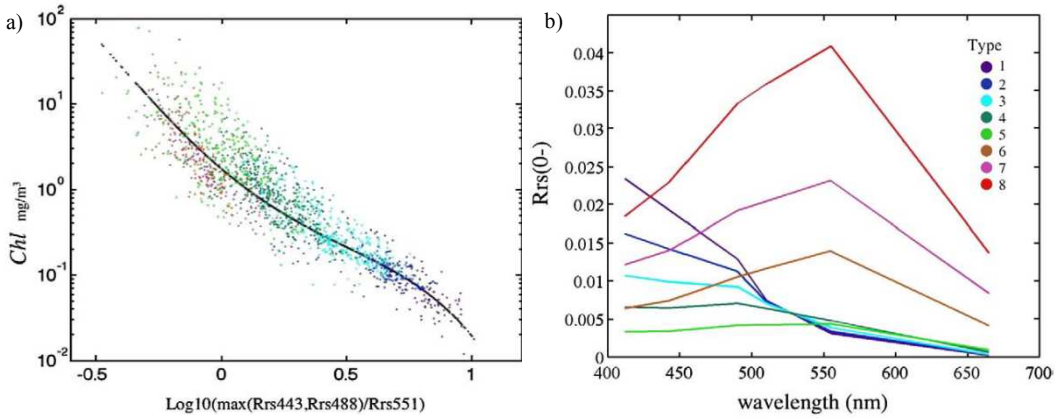

Figure 3.2 – a) The OC3M global fit and the NOMAD v2 set with the match-ups colored according to the OWT classification; (the x and y axes are in log scale) and b) the mean R_{rs} (0^{-}) spectra representative of each OWT class defined in the Fuzzy-c-Means cluster analysis.

Source: Moore et al. (2009)

The means and covariance of the R_{rs} of each class were used to define fuzzy membership functions as: 1- F(Z^2), where Z^2 is a squared Mahalanobis distance and F is a cumulative chi-square distribution. The Mahalanobis distance is equivalent to the standardized random variable (X): Z=(X−M)/SD, where M is the mean and SD the standard deviation. This distance takes into account not only the geometrical distance (Euclidean) but also the shape of the dispersion of points around the cluster. The fuzzy membership functions defined for each class, can then be applied to assign a membership value for any R_{rs} spectra, which defines the degree that the spectra "belongs" to each of the classes (varying from 1-0). To apply this classification scheme for a satellite image for instance, each pixel will have a membership value for each class and the maximum value will define which class it belongs to. This is called a soft clustering technique.

The second and third steps of their approach were more related to the generation of the uncertainty maps. 2) In the second step they estimated the error statistics for each OWT class using satellite and *in situ* Chl*a* match-ups from a MODIS-Aqua validation data set (N=541) (Figure 3.1) (BAILLEY; WERDELL, 2006). 3) In the third step they applied the classification scheme of step one to a MODIS image and the fuzzy memberships for each pixel, normalized by their sum were used as weighing factors to estimate the uncertainty level for each pixel. As the OWT varies in space and time, this approach allows obtaining dynamic uncertainty OC4 maps as a new ocean colour product.

The OWT classes are defined in first order by the mean Chl*a* levels and dominance of other OACs, such as CDOM and sediments. There are, however, some overlapping Chl*a* minimum and maximum values within the classes that raise evidences of second order specific optical variabilities that are also encompassed in the definition of each class. These optical variabilities however, were only supposed as being related to CDOM and phytoplankton distributions, and were not yet deeply investigated due to the lack of *in situ* IOPs. Further works should thus concentrate on investigating theses relations and verifying to what extent the OWT classes may be associated with the PFT distribution and biogeochemical processes. As well as, if this classification is valid for a generalized global approach, as the NOMAD is geographically limited.

3.5.2. Ocean basin approach (SZETO et al., 2011)

The ocean basin (abreviated here as OB) approach proposed by Szeto et al. (2011) is a regional "classification scheme" of the dominant optical differences of the global ocean. The provide ocean basin specific parameterizations for the OC4 in their appendix (Figure 3.3). Nonetheless, the authors emphasize that they do not intend at this stage to conclude this classification scheme due to the limited geographic coverage of the NOMADv2, and they encorage further works and *in situ* surveys.

According to their analyses the Atlantic tends to be overestimated by the global OC4v6 due to a tendency of the basin to have higher a_{cdm}/Chl*a* and a_{phy}*. Whereas the Pacific has a slight tendency to be underestimated due to the lower specific IOPs, and the Southern Ocean even more. A preminilary analysis of these relations would be to associate the Atlantic basin to smaller PFT groups and high biodegradation processes

and CDM sources. The Pacific and Southern oceans would have a tendency of dominance of larger PFTs and lower CDM production, with high POM sinking and likely also have higher photodegradation processes (during the austral summer).

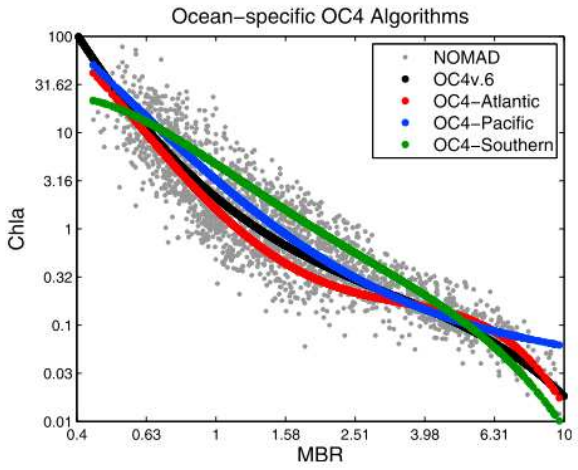

Figure 3.3 – Ocean-specific OC4 fits for the Ocean Basin approach, using the NOMAD v2 set. (the x and y axes are in log scale).

Source: Szeto et al. (2011).

4 MATERIALS AND METHODS

This Chapter provides a general description of the study area, the main activities developed and methodologies applied for data processing and analysis. The methods more specific of the uncertainty analysis and bio-optical variability, will be exposed in more detail in the Chapters regarding each topic.

4.1. Study Area

The study area comprehends a high range of biogeochemical provinces defined by prevailing physical forcing characteristics (i.e. wind stress, solar irradiance and sea surface temperature) that determine the nutrient flux into the euphotic zone (i.e. mixed layer depth) and the resultant distribution and productivity of the pelagic biological community (PLATT; SATHYENDRANATH, 1999). The provinces are defined according to Longhurst (2007), and have been extensively used to link the distribution of bio-geophysical parameters and understanding their ecological and biogeochemical roles in oceanographic researches (WATSON et al., 2003). The MV1102 crossed the southern Atlantic (33^{o}-53^{o} S and 15^{o}-70^{o} W), passing through the south limit of the Benguela Current Coastal Province (BENG) (close to the Eastern Africa Coastal Province (EAFR)), the South Atlantic Gyral Province (SATL), the South Subtropical Convergence Province (SSTC), the Subantarctic Water Ring Province (SANT) and Southwest Atlantic Shelves Province (FKLD). Then it crossed the Magellan Strait, passing through the Chilean Fjords, out to the Southeast Pacific, countering the Chile-Peru (Humboldt) Current Coastal Province (HUMB), along the central-south Chilean coast (47-35^{o} S and 74-76^{o} W) (LONGHURST, 2007) (Figure 4.2).

All these regions are subjected to predominantly adverse environmental conditions with strong winds, currents and waves, due to the persistent westerlies that circle the southern hemisphere between the parallels of 40-70^{o}S, without much physical obstacle. The frontal retroflection zone of the Agulhas current and Benguela Upwelling System and the Brazil-Malvinas Confluence Zone (BMCZ) are also highly dynamic and energetic regions with strong currents, vortices, and eddies (STRAMMA; ENGLAND, 1999). Mid-latitude atmospheric cyclones and fronts are other phenomena that influence surface wind and waves and contribute to persistently high cloudiness over the southern

oceans (HAYNES et al., 2011). These are great constraints and challenges for satellite and *in situ* ocean colour remote sensing in the study region.

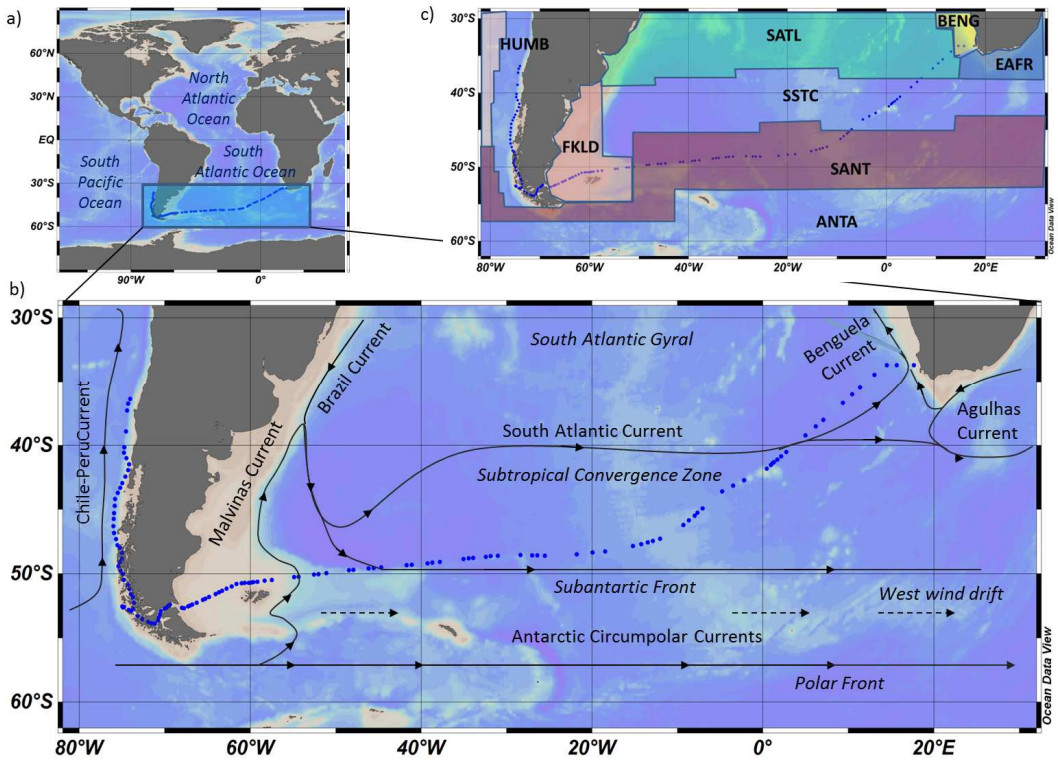

Figure 4.1 – Map of the study region showing the MV1102 ship track, currents, frontal zones, and bottom ocean topography (provided by the 2009 World Ocean Atlas in ODV v4.5) (a and b). Map showing the biogeochemical provinces of Longhurst (2007), with boundaries defined by climatological means (c). The blue dots correspond to the complete set of 134 stations collected during the cruise (CTD and FL).

In terms of water masses and bio-optical properties, the sampled region is characterized by diverse and complex systems throughout the biogeochemical provinces. The BENG is influenced by a persistent Eastern Boundary Upwelling System, in which the northward Benguela Current in conjunction with the Earth rotation, results in a perpendicular transport of the coastal surface waters towards the open ocean (i.e. Ekman transport). This transport pumps up cold nutrient enriched waters from the deep South Atlantic Central Water (SACW) to the surface layers, promoting high phytoplankton

growth and productivity in the southwest African coast (LONGHURST, 2007; AIKEN et al., 2009). There are however, some spatio-temporal variations in the intensity of the upwelling due to seasonal mesoscale wind regimes, local sea bottom topography and orientation of the coastline. The Cape Peninsula Upwelling Cell (CP) located off Cape Town (34^{o} S), from where the R/V Melville departed, is one of the strongest cells of the BENG, due to the narrow shelf and predominance of intensive southern winds, especially during the austral summer. Extensive phytoplankton blooms are commonly observed spread out from the CP cell core up to the shoreline during strong upwelling events (AIKEN et al., 2007). The Agulhas Retroflexion Zone, where the westward warm Agulhas Current meets the cold Benguela Current, is also a highly dynamic region with mesoscale eddies and vortices that form upwelling cells, which also enhance phytoplankton growth in the southwest African Coast (SHILLINGTON; REASON, 2006). This high productivity provides high fishery standing stocks for the local industry (SHILLINGTON; REASON, 2006).

The South Atlantic Gyral (SATL) comprises the anticyclone circulation of the South Atlantic and is characterized by a very stable system with low seasonal variations of physical forcing of wind stress and solar irradiance. Hence, the water column is highly stratified with deep pycno and nitraclines (LONGHURST, 2007). The upper layer of the South Atlantic Central Water (SACW) is thus characterized by high saline and temperature and low nutrient waters, with high light penetration. These oligotrophic waters of the SATL are thus, mostly dominated by picoplankton organisms mainly related to regenerated primary production (MARANÓN et al., 2000; FINKEL et al., 2009). The South Atlantic Subtropical Convergence (SSTC) is a much higher dynamic region characterized by the frontal boundary between the SATL and SANT, which is marked by a strong temperature-salinity gradient. The intrusion of colder, less saline and high nutrient low chlorophyll (HNLC) Subantarctic Surface Waters (SASW) of the Southern Ocean, passing below the warmer, more saline and oligotrophic waters of the SACW, promotes the enhancement of phytoplankton biomass in the SSTC. Thus, there is also a strong Chl*a* gradient in this frontal zone that follows the patterns of mesoscale meanders (LONGHURST, 2007).

The Subantarctic Water Ring Province (SANT) is a higher latitudinal frontal zone, between the SSTC and Antarctic Polar Province (ANTA), with dominance of SASW within the upper layer. As a high latitude frontal zone it is also characterized by high spatio-temporal dynamics, marked by a strong seasonality driven by the wind stress and the solar irradiance. During winter the strong westerlies and low solar intensity and photoperiod promote high vertical mixtures with a deep mixed layer depth (MLD). As spring comes, the winds are less intense and the increase of solar intensity and photoperiod promotes a more stable stratified water column with a shallower MLD, which enables phytoplankton growth within the nutrient enriched euphotic layer. Current transports of continental runoffs and ice-melting from the surrounding continents and islands (i.e., Patagonian Shelf, South Georgia Islands and Antarctic Peninsula), may also contribute to micronutrient fertilizations along the SANT, especially during the austral spring and summer (GAIERO et al., 2003; KORB; WHITEHOUSE, 2004; PARK et al., 2010). The fast flowing Antarctic Circumpolar Current (ACC), with a jet-like eastward flow, also demarks the high spatial variability of the SANT, with active meandering and eddy shedding (LONGHURST, 2007).

The Southwest Atlantic Shelves Province (FKLD) is a coastal province that comprises the Argentinean continental shelf (PAT) and the Malvinas plateau. It encompasses one of the world's most extensive and plain shelves with up to 800 km of extension into the ocean (at 50^{o} S), and is also one of the highest productive systems of the global ocean. The biological productivity of this region is due to the intrusion of nutrient enriched Subantarctic waters carried by the Malvinas Current onto the continental shelf, and to strong mixing with eddies and vortices (LONGHURST, 2007; LUTZ et al., 2010). In the northern part of the FKLD a large size river, the La Plata River, contributes to the complex mixture of these coastal waters. Crossing the Patagonian shelf, the R/V Melville passed through the Magellan Strait, a narrow and steep channel located between the southern end of the South American continent and the Tierra del Fuego island (Argentina and Chile). The channel connects the South Atlantic and South Pacific oceans, and the water circulation is predominantly regulated by strong tides, with a mixture of (mainly) eastward flowing Subantarctic Pacific waters, continental runoff and glacial-fluvial waters (ANTEZANA, 1999). These mixtures characterize waters within the strait with generally high POM and fine sediments in suspension, especially

in the shallow sectors with resuspension of bottom sediments, promoted by strong bottom currents (CAPELLO et al., 2011).

On the other side of the strait, the R/V Melville passed through the Chilean south and central coast across the Humboldt (Chile-Peru) Current Coastal Province (HUMB). The central-northern sector the HUMB is a productive system due to the Eastern Boundary Upwelling System, sustaining high phytoplankton growth and fishery standing stocks. In the southern sector the strong westerlies suppress the upwelling, but there are evidences of high phytoplankton growth promoted by the intrusions of HNLC waters of the ACC up to the iron enriched surface layers of the continental shelf (ROMERO et al., 2001; ROMERO; HEBBELN, 2003).

Figure 4.3 shows an 8 day MODIS composite map of Chl*a* (OCM3) averaged over the sampling period of the MV1102. The Chl*a* OCM3 range is compatible with the measured fluorimetric Chl*a* at the stations, varying from 0.08 to 11.1 mg.m^{-3}. The OCM3 map shows clearly the high Chl*a* gradient of the different BGCP sampled in the MV1102, as well as their dynamic boundaries.

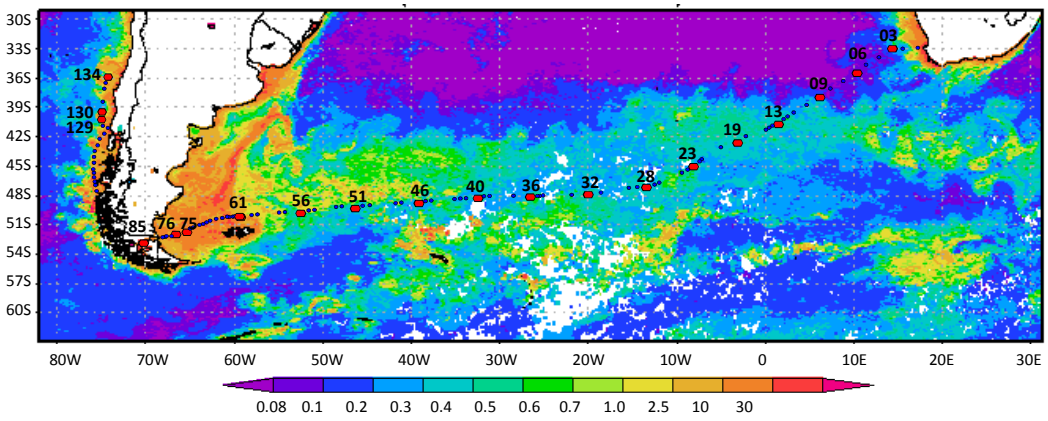

Figure 4.2 - A MODIS OC3M Chl*a* (mg.m^{-3}) map averaged over the MV1102 sampling period (16/02/11-06/03/11) (4 km). The red dots correspond to the CTD stations and blue dots to the flowthrough stations.

4.2. General overview

The present work was divided in two main steps - (i) data collection, laboratory analysis and processing, and (ii) data integration and analysis, as shown in the flowchart of Figure 4.1. The R/V Melville (Scripps Institution of Oceanography, SIO) departed from Cape Town (South Africa) on February 20th and arrived at Valparaiso (Chile) on March 14th, near the end of the austral summer of 2011. A total of 20 complete stations were made with surface and vertical profiles including radiometric and bio-optical sampling (referred as radiometric or CTD stations). The radiometric measurements comprehended above-water and in-water profiles with different radiometers. The bio-optical measurements were obtained at 4 discrete depths: surface (1 m), sub-surface, chlorophyll *a* fluorescence maximum (Fl_{max}) and upper layer (up to ~120 m). 40 non-stop flow-through (FL) stations were also sampled for bio-optical measurements at sub-surface waters (4 m). For the uncertainty analyses only the 20 radiometric stations were used and for the bio-optical variability the 40 FL were also added (with exception for a radiometric station realized in the middle of the Magellan) (Table 3.1).

Since one of the objectives was to analyze the uncertainties regarding the different instruments and methods provided by the ocean colour groups, the samples and radiometric data sets were sent to the different laboratories for pre-processing analysis. The radiometric data was processed by the groups that provided each instrument (identified by their institutions): ASD Fieldspec Hand-Held (ASD Inc.) (*Instituto Nacional de Pesquisas Espaciais,* INPE, Brazil); HOCR PRO II (Satlantic Inc.) (INPE); TriOS (Optical Sensors Inc.) (*Laboratoire d'Océanologie et de Géosciences, Université du Littoral-Côte d'Opale,* LOG, France) and PRR (Biospherical Inc.) (SIO, USA). The particle backscattering coefficient (b_{bp}) was measured with a HydroScat (HOBILabs Inc.) provided by SIO. The CDOM samples were analyzed on board immediately after collection. All the other samples were preserved in liquid nitrogen and sent to different laboratories for posterior analysis. Duplicates for the particle absorption coefficient (a_p) were sent to the *Instituto Oceanografico da Universidade de São Paulo* (IOUSP, Brazil) and the *Instituto Nacional de Investigación y Desarrollo Pesquero* (INIDEP, Argentina). The fluorimetric Chl*a* samples were sent to: INIDEP and SIO. The HPLC duplicates were sent to the Horn Point laboratory, University of Maryland (HPL, USA)

and the *Institut de Recherche pour le Développement* (IRD, France). The flow cytometry samples were sent to the *Universidade Federal do Rio de Janeiro* (UFRJ) and the microscopy samples to INIDEP.

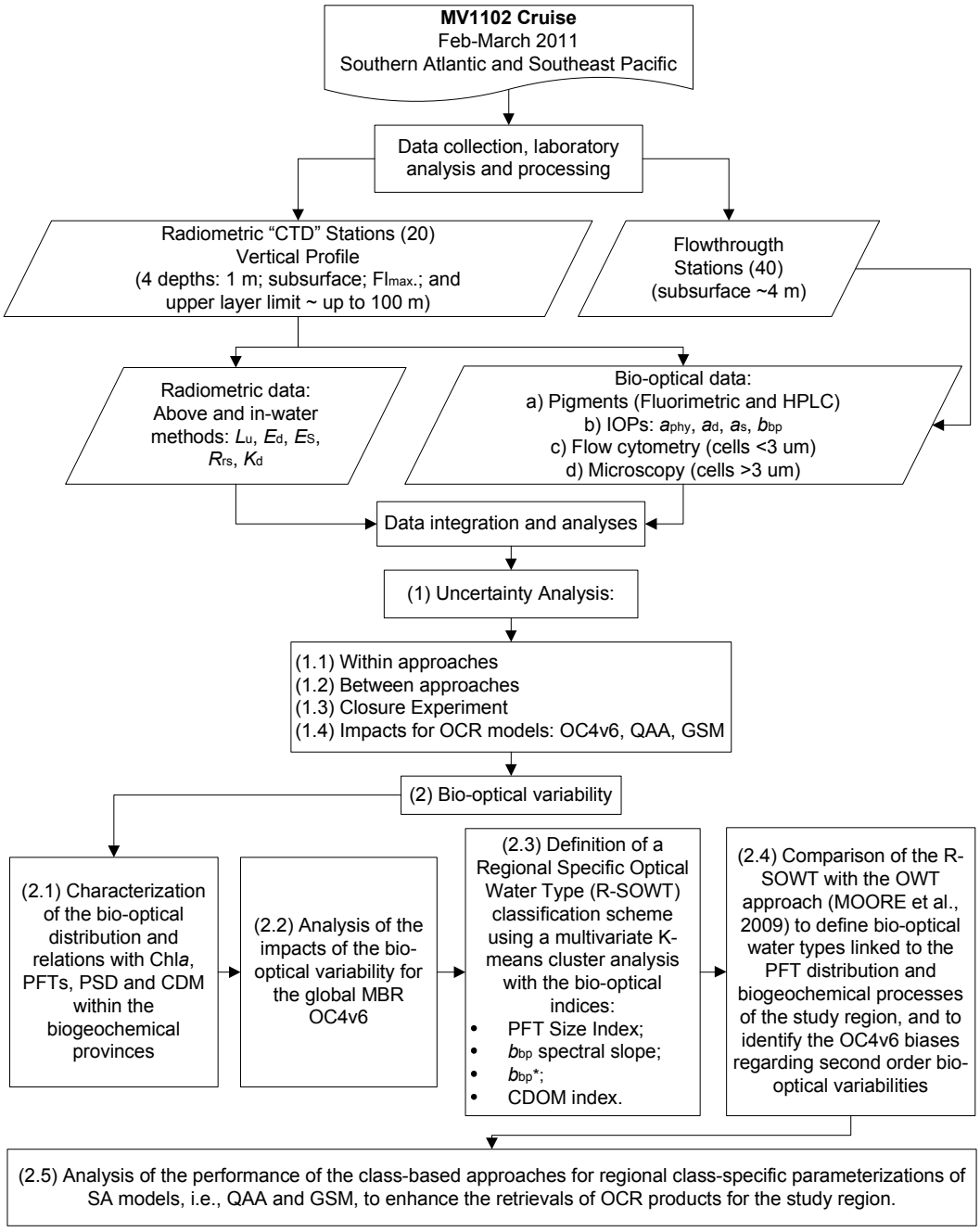

Figure 4.3- Flowchart of the main activities of data collection, processing and analysis.

The analysis and integration of the data were divided according to the two main objectives of the present study: first with the Uncertainty analysis (1), which comprehended the comparison within the different approaches used to obtain R_{rs} measurements (1.1); between the different approaches (1.2); in a closure experiment, comparing modeled and measured R_{rs} (1.3) and analysis of the impacts of the uncertainties for OCR models i.e., OC4v6, QAAv5 and GSM01 (1.4). The second part comprehended the analysis of the bio-optical variability (2), with a characterization of the distribution of the IOPs and analysis of their relations with the Chl*a* levels, PFT distribution, microbial and bulk particle assemblage and CDM variability (2.1); analysis of the sources and impacts of the second order variabilities for the OC4v6 model (2.2); and a proposal of a regional specific Optical Water Types (R-SOWT) classification scheme to synthesize the variability using a K-mean Multivariate Cluster analysis, and the bio-optical indices: PFT Size index, bbp*, η and CDOM index (2.3); a comparison of the R-SOWT and OWT (MOORE et al. 2009) approaches to define bio-optical classes with relevant biogeochemical information for the study region (2.4); and finally evaluate the application of the class-based approaches (R-SOWT and OWT) for regional class-specific parameterizations of SA models, i.e., QAA and GSM, to improve the retrieval of OCR products for the study region (2.5) (Figure 4.1).

Table 4.1 – Description of the stations, data and analysis realized for each set.

Stations	N	Depths	Type	Measurements/Data	Analysis
Radiometric (CTD)	20	surface & profile (4 depths)	Radiometric	Above-water R_{rs}	Uncertainty Analysis, Bio-optical Variability
			Bio-optical	Chl*a*, a_p, a_s, b_{bp}, Flow cytometry, microscopy (*)	
Fl	40	surface	Bio-optical	Chl*a*, a_p, a_s, b_{bp}, Flow cytometry, microscopy (*)	Bio-optical Variability

Microscopy analysis (*) were realized for only 7 stations including both the radiometric and Fl stations.

4.3. Cruise description

The radiometric stations were conducted once a day, around 11 to 13h local time. The local time around noon was preferred to avoided high solar zenith angles (SZA), especially at the higher latitudes. For precaution of the instrument each deployment was made separately, in subsequent times. Thus, the radiometric measurements of the different instruments and the water collection were not exactly simultaneous, but as close as possible (15-60 min between deployments). The instruments used for marine reflectance were: the above-water ASD (Figure 4.4a) and the in-water HyperOCR PRO II (HOCR) (Figure 4.4d), PRR (Figure 4.4c), and TriOS (Figure 4.4e). The deck sensors of the in-water instruments were installed in the highest mast of the ship (Figure 4.4b). The instruments were independently calibrated, and the data sets processed by the laboratories that provided each instrument. The independent calibration and data processing schemes were maintained, contrary to other inter-comparison works (HOOKER; MARITORENA, 2000), with the aim to analyze the bulk uncertainties regarding *in situ* ocean colour radiometry in a realistic framework of global ocean colour data sets (BAILEY; WERDELL, 2006).

Water sample collection for bio-optical measurements was made with a rosette bottle system coupled with a Conductivity-Temperature-Depth (CTD) sensor (Figure 4.4f) at four depths distributed in the upper ocean layer, i.e., at 1 m for sub-surface measurements; between 7-40 m within the first and second optical depths; at the fluorescence maximum depth (Fl_{max}) (measured by a fluorescence probe attached to the CTD sensor) and below the Fl_{max} up to 100 m deep. Sub-samples were separated for CDOM, particle absorption, and pigment analysis (fluorimetric Chl*a* and HPLC), immediately filtered onboard. CDOM absorption analyses were analyzed onboard, while particle absorption and pigment samples were stored in liquid nitrogen for post-cruise laboratory analysis. Sub-samples were also separated for flow cytometry analysis. A HydroScat (Hobilabs Inc.) scatterometer was deployed on the rosette system to measure the backscattering coefficient of marine particles in 6 spectral bands (420-700 nm) (HS6) (Figure 4.4f).

The FL stations were on going non-stop stations using the flow-through system to collect water samples at a sub-surface depth (4 m). These stations did not contemplate

radiometric measurements, but had a complete set of bio-optical measurements, including: a_s, a_p, pigment concentration (fluorimetric and HPLC), b_{bp} and flow cytometry analyses. The b_{bp} measurements were performed in a black bucket, trying to avoid the influence of wall reflection and bubble effects. This complete set allowed the application of RTE forward modeling to retrieve R_{rs} from the IOPs (i.e. a and b_b).

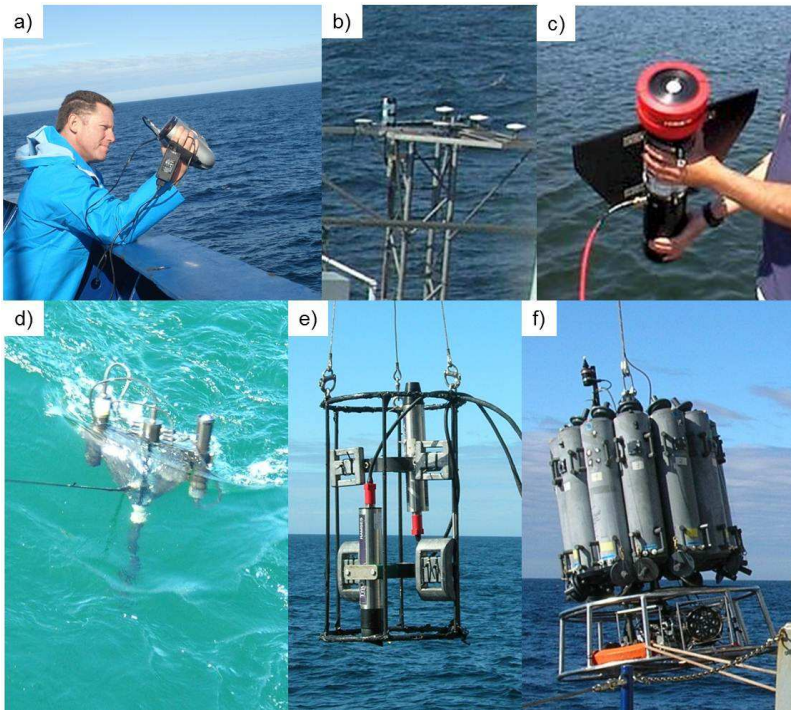

Figure 4.4 - Instruments used in the MV1102: a) above-water ASD Fieldspec HandHeld; b) HOCR, PRR and TriOS deck sensors; c) PRR free-falling profiler; d) HOCR free-falling profiler; e) TriOS winched profiler; f) rosette bottle system coupled with a CTD and HS6.

4.4. Radiometric measurements

All radiometric acquisition and data processing routines followed the NASA 2003 protocol recommendations (MUELLER et al., 2003). The differences in the processing methods applied for each data were in respect to the specifications of the measurements obtained by each instrument. Some differences also exist in higher level processing, such as the quality control and choice of the extrapolation depths (for in-water

methods). To compare the same quantity for all data sets, i.e., to minimize the effects of short-scale light field variations, we used the remote sensing reflectance just above the sea surface (R_{rs}), defined as the ratio between the water-leaving radiance (L_w) and the downwelling solar irradiance (E_d), above the sea surface (0^+). Since the scope of this work is for OCR applications, R_{rs} was compared for ocean colour bands centered on 412, 443, 490, 510, and 555 nm (10 nm bandwidth), within the spectral interval recommended for OCR inter-comparison exercises (< 600 nm) (MUELLER et al., 2003). Satellite sensors such as MERIS and MODIS measure in similar spectral bands.

4.4.1. Above-water approach

ASD Fieldspec HandHeld

The ASD Fieldspec HandHeld (Analytical Spectral Devices, Inc.) is a hyper-spectral radiometer (350-1100 nm, 1 nm bandwidth) with 25^o field-of-view (FOV). The measurements were performed with a sensor-viewing geometry of 45^o zenith angle and approximately 137^o azimuth angle, with respect to the Sun direction. This geometry was selected to avoid instrument and platform shading, and to minimize sky, sun glint, and platform reflection on the ocean surface (MOBLEY, 1999; FOUGNIE et al., 1999; HOOKER; MOREL, 2003). The upwelling radiance measured by the ASD corresponds to the total radiance emerged from the ocean surface (L_T), which needs to be corrected for the sea surface reflection to obtain L_w. The main source of sea surface reflection is skylight, and the correction was made by subtracting the sky radiance (L_{sky}), measured when pointing the sensor to the sky (in the same plane as L_T and same zenith angle), multiplied by a sea surface reflectance factor (ρ_{sky}) (MUELLER et al., 2003). The ρ_{sky} factor was adjusted for each condition according to the sea surface roughness indexed by the wind speed, the SZA, and sensor-viewing geometry, according to Mobley (1999). The E_d was determined by measuring the radiance reflected from a white Lambertian Spectralon plaque (L_{pl}) (with 99% of reflectance - ρ_{pl}). At each station an average of ten casts was taken with sequential measurements of L_T, L_{sky} and L_{pl}. The $R_{rs}(0^+)$ was estimated using Equation 1 for each cast:

$$R_{rs}(\lambda,0^+) = \frac{L_w(\lambda,0^+)}{E_d(\lambda,0^+)} \approx \frac{L_T(\lambda,0^+) - \rho_{sky} L_{sky}(\lambda,0^+)}{[L_{pl}(\lambda,0^+)\pi]/\rho_{pl}} \quad (4.1)$$

Residual Correction

The correction of the sky glint on the sea surface is the most critical step of the above-water approach (for instruments with no polarization measurement capability). The wavy facets cause a complex geometrical light design between the target and the sensor, and it is difficult to determine the exact ρ_{sky} for each condition (MOBLEY, 1999; TOOLE et al., 2000). Another issue is that Mobley's (1999) factor was modeled for a 10^o FOV, not for the 25^o ASD FOV. Besides this, even though the effects of other contaminants, such as cloud and sun glint, and platform reflection, are minimized with the acquisition geometry, they are not totally avoided. Thus, an offset in the near infrared (NIR) is still commonly observed even after the L_{sky} correction (TOOLE et al., 2000; HOOKER; MOREL, 2003; DOXARAN et al., 2004). To correct for the residual reflection of the sea surface different approaches were tested according to Toole et al. (2000) and Hooker and Morel (2003). The white offset correction is the most simple to apply since it uses a zero baseline in the NIR region for the entire reflectance spectrum. The procedure assumes that the contaminating sources are spectrally white and that L_w is zero at longer wavelengths (≥NIR) due to high water absorption (TOOLE et al., 2000). The former is not totally realistic, as the perturbing effects likely have spectral dependencies, although much less than the sky radiance in cloudless conditions, for instance. However, if one wants to model correctly the spectral behavior of each residual source, the correction scheme turns out to be much more complicated and not always successful, as these spectral dependencies may vary under different conditions, e.g., cloud type, thickness and distribution (MOBLEY, 1999) and platform paint (HOOKER; MOREL, 2003). Thus, while the white-offset method may cause under-corrections for the shorter wavelengths, spectral dependent schemes may cause over-corrections, as was observed for a couple of cases when testing other approaches. The second assumption of the zero L_w in the NIR is valid for waters with low concentrations of suspended sediments and low to moderate Chl*a*. This was valid for the MV1102

stations, with exception only for the Magellan Strait station, which was treated separately. The reference band used to set the baseline was centered at 800 nm (20 nm bandwidth), since measurements at longer wavelengths had low signal-to-noise ratios (SNR), and L_w is expected to be significant at shorter wavelengths for productive waters. The correction applied was:

$$R_{rs}'(\lambda,0^+) = R_{rs}(\lambda,0^+) - R_{rs}(800,0^+) \tag{4.2}$$

The zero baseline at 800 nm was applied for all stations except at the Magellan Strait station, in which the spectrum with the minimum value of L_w at 800 nm was used as a baseline to correct the spectra for the other casts.

Whitecaps and bubble clouds generated by breaking waves that may be present in the ocean surface and first few meters, will also be somewhat corrected with the residual correction (RC) scheme. Both sources produce significantly higher R_{rs} signals in the NIR spectral region, increasing at the shorter wavelengths (blue-green) (FROUIN et al., 1996; STRAMSKI; TEGOWSKI, 2001; PISKOZUB et al., 2009). Hence, in the presence of such effects, subtracting the NIR offset will still leave some unwanted signal in the shorter spectral bands.

Quality Control

To minimize the effects of under-corrections at the shorter spectral bands and eliminate highly contaminated spectra (outliers), a quality control filtration scheme was proposed based on the mean R_{rs}'(400) value and a threshold on the coefficient of variation (standard deviation divided by the mean, CV) between the casts (~10). Casts with CV higher than 10 % were considered spectrally contaminated and discarded. The 10 % threshold was chosen based on observations at each station and an overall best agreement. The mean R_{rs}'(400) value was chosen as a reference as opposed to the minimum value (that could be less contaminated by residual sources), because some observations exhibited artifacts that also caused unexpected lower values, for example

due to different illumination conditions on either one of the sequential measurements to retrieve R_{rs} (the consequence of broken clouds). This is shown and further discussed in the results.

Bidirectional effects

The R_{rs} has a bidirectional angular distribution that varies with the optical properties of the water, which may be indexed by the Chl*a*, the illumination conditions (SZA and cloud cover) and sensor viewing angle (MOREL; GENTILI, 1996; MOREL et al., 2002; LEE et al., 2004). The first two factors should not impact much the measurements during a same station, however the viewing angle for upwelling radiance in the above- and in-water techniques is different, i.e., 45^{o} and 0^{o}, respectively. Thus, for inter-comparison purposes correcting bidirectional effects is necessary, i.e., transforming R_{rs}' into R_{rs}^{o}, the remote sensing reflectance for a nadir-viewing sensor and zero SZA (Sun at zenith). The correction is performed using the following equation:

$$R_{rs}^{o}(\lambda,0^{+}) = R_{rs}'(\lambda,0^{+})\left[\frac{\Re_{o}}{\Re(\theta_{o},\theta_{v},U)}\frac{f_{o}(\lambda,\tau_{a},Chl)}{Q_{o}(\lambda,\tau_{a},Chl)}\left(\frac{f(\lambda,\theta_{o},\tau_{a},Chl)}{Q(\lambda,\theta_{v},\varphi,\theta_{o},\tau_{a},Chl)}\right)^{-1}\right] \quad (4.3)$$

where R_{rs}^{o} is the corrected reflectance and $\Re$ is a factor accounting for reflection and refraction at the air-water interface that varies mainly with sensor-viewing geometry (θ_v) and sea state (wind speed, U). The subscript "o" stands for the factors correspondent to a nadir-viewing sensor and nadir SZA. For clear and partly cloudy skies, f, Q and $\Re$ were determined as a function of Chl*a*, SZA, sensor-viewing geometry, and wind speed (taking into account Raman scattering), according to Morel et al. (2002) and Mueller et al. (2003). For overcast skies, since the SZA dependency is small, the calculations were made for a SZA of 30^{o} and a uniform sky radiance distribution. No other adjustment was made to account for actual cloudiness and aerosol optical thickness.

4.4.2. In-water approach

The instruments used for the in-water approach were profiling systems consisted of three inter-calibrated radiometers that respectively measured downwelling irradiance (E_d) and upwelling radiance (L_u) as a function of depth and the above-water downwelling irradiance (E_S). The E_d and L_u profilers are equipped with tilt and pressure sensors, a temperature-conductivity probe and fluorimeter (to get information about the vertical distribution of the chlorophyll concentration). The E_S deck sensors were mounted on the highest mast on the topmost level of the ship, to avoid any platform shading (Figure 4.4b). The free-falling profilers (HOCR and PRR) were deployed at the leeward side of the stern, letting the instruments drift more than 50 m away before profiling, and releasing the cable in a velocity sufficient to avoid both loosening (*belly effect*) and stretching. The winched profiler (TriOS) was deployed in an open cage (Figure 4.4e) at the starboard side, always oriented to the side viewing the Sun to minimize effects of platform shading. After applying the calibration files and pre-processing routines (i.e., immersion factor correction and profile editing), some procedures were common to all in-water systems and are summarized in the following.

Normalization of the illumination variation during casts

To account for the illumination variation during casts, the E_d and L_u profiles were normalized using the ratio between E_S measured at the time $t(0^-)$ of the surface depth and E_S measured at the time $t(z)$ of each subsequent depth z (MUELLER et al., 2003):

$$R^*_n(z,\lambda) = \frac{R^*(z,\lambda)E_S[t(0^-),\lambda]}{E_S[t(z),\lambda]} \tag{4.4}$$

where R^*_n is the normalized quantity (radiance and irradiance), R^* is the measurement at each depth, and E_S values at $t(0^-)$ and $t(z)$ are averaged over a period of at least 15-20 seconds to account for short-scale illumination variations (MUELLER et al., 2003).

K_d Analysis

Profiles of the diffuse attenuation coefficient for E_d (K_d) and L_u (K_u) were determined according to Smith and Baker (1986) as the local slope of ln[(E_d'(z)] (and ln[(L_u'(z)]) using 5-15 integration points (measured depths) with a linear regression fit. The approach assumes that K_d is constant within the interval $(z_m-\Delta z) \leq z < (z_m+\Delta z)$ (where z_m is the center depth), following the relation below:

$$\ln[E_d''(z,\lambda)] \cong \ln[E_d'(z_m,\lambda)] - (z - z_m)K_d(z_m,\lambda) \quad (4.5)$$

Using this relation $K_d(z_m)$ is determined as the slope of a least square linear regression fit of measured ln[(E_d'(z)] versus ($z-z_m$).

Extrapolation to surface values

a) Downwelling solar irradiance

The above-water downwelling irradiance was estimated in two ways: a) using the extrapolated $E_d(z)$ value from the profiler, i.e., $E_d(0^+)$, and b) using $E_S(t(z=0))$ from the deck sensor. For the extrapolated $E_d(0^+)$, first the value just below surface, $E_d(0^-)$, is determined using the $K_d(z)$ profile and selecting a depth interval for which $E_d(z)$ may be extrapolated to $E_d(0^-)$, as the intercept of the least square regression fit at z=0 m, using Equation 5. This assumes a constant K_d within the extrapolated interval from z_m to z=0 m. The choice of the extrapolated interval is a critical step for the in-water approach. Ideally values closer to surface (or at least within the first optical depth) are better. However, E_d profiles are highly influenced by focus and defocusing effects of the downwelling rays due to the wavy facets of the ocean surface, and by the presence of intermittent bubble clouds that may be present at depths up to 7 m for wind speeds ≥10 $m.s^{-1}$ (STRAMSKI; TEGOWSKI, 2001). Deeper measurements, on the other hand, are more affected by vertical bio-optical variability, inelastic water molecule Raman scattering (AIKEN et al., 2000; HOOKER; MARITORENA, 2000), and $K_d(z)$

variations due to the decreasing downwelling average cosine (μ_d) (MOBLEY, 2004). The choice of the extrapolated interval will thus depend on the influence of all these effects, at each station. The irradiance just above the surface, $E_d(0^+)$, is then derived from $E_d(0^-)$ accounting for the loss due to the upward air-water interface reflection and gain of the downward reflected flux:

$$E_d(0^+,\lambda) = E_d(0^-,\lambda)\frac{1-<r>R(0^-,\lambda)}{1-<\rho>} \tag{4.6}$$

where $<r>$ is the mean water-air Fresnel reflectance factor for the diffuse upward flux, E_u, ($r \approx 0.48$); R is the irradiance reflectance, $E_u(0^-)/E_d(0^-)$, $<\rho>$ is the bulk air-water Fresnel reflectance factor for the downward irradiance of Sun and sky reflected on the surface (MOREL; ANTOINE, 1993) ($<\rho>$ varied from 0.032 to 0.065). The upward irradiance, $E_u(0^-)$, is estimated using the following relation:

$$E_u(0^-,\lambda) = L_u(0^-,\lambda)Q_n(\theta_o, \mathrm{Chl}, \lambda) \tag{4.7}$$

where Q_n is the bidirectional factor for a nadir-viewing sensor (MOREL et al., 2002).

b) *Water-leaving radiance* (L_w)

The water leaving radiance L_w is determined in a similar way as $E_d(0^+)$, by first retrieving $L_u(0^-)$ using the $K_u(z)$ profile and $L_u(z)$ extrapolation with the intercept of the least square regression fit at z=0m (Equation 5). Then, accounting for the loss of the upward $L_u(0^-)$ through the air-water interface as follows:

$$L_W(\lambda) = L_u(0^-, \lambda)\frac{(1-\rho)}{n_w{}^2} \tag{4.8}$$

where ρ is the Fresnel reflectance factor of the seawater for the upward radiance and n_w is the refractive index. The term $(1\text{-}\rho)/n_w{}^2$ is fairly constant regardless of the sea state and can be set to ~0.543 (Austin, 1974).

Self-shading effects

As the in-water instruments measure L_u at a nadir-viewing angle, L_u is somewhat affected by the instrument shading, referred as *self-shading* effects. Such effects were corrected for the extrapolated L_u values according to Gordon and Ding (1992):

$$\widetilde{L}_u(\lambda,0^-) \approx \frac{\hat{L}_u(\lambda,0^-)}{1-\varepsilon(\lambda)},\ \varepsilon(\lambda) \approx 1-e^{-\kappa' a(\lambda) r} \tag{4.9}$$

where $\widetilde{L}_u(\lambda,0^-)$ is the true value and $\hat{L}_u(\lambda,0^-)$ is the measured value, ε is the error between the measured and estimated values, $\kappa' \approx \frac{y}{\tan\theta'_o}$, θ'_o is the refracted solar zenith angle for direct and diffuse irradiance, y is an empirical factor, r is the instrument physical radius and a is the total absorption. The HOCR r is 5.7 cm, the PRR r is 10.2 cm and the TriOS r is 4.83 cm. The total absorption was determined using the Morel and Maritorena (2001) model (MM01) from the measured K_d and R_{rs}, to maintain the radiometric measurements independent from the bio-optical measurements (Equation 3.11). The backscattering coefficient (b_b) was determined using Equations 3.9 and 3.10; and the Chl*a* was estimated using the MM01 empirical fit of the maximum R band ratio of $R(E_u/E_d)$ (443; 490; 510/555) versus Chl*a*.

Above water remote sensing reflectance ($R_{rs}(0^+)$)

For each system, the above-water remote sensing reflectance ($R_{rs}=L_w/E_d$) was determined in two ways: using the profiler E_d or the deck sensor E_S. The correction for bidirectional effects (Equation 4.3) was also applied to correct for SZA variations and compute R_{rs}^o. Detailed specifications of each in-water instrument are present in the following sub-sections, as well as differences in the data processing schemes, which were mostly in respect to the method used to select the depth intervals of the extrapolation of E_d and L_u to the surface.

HyperOCR PRO II (Satlantic Inc.)

The HyperOCR PRO II (HOCR) is a free-falling profiler system with hyper-spectral radiometers (349-802 nm) (3 nm bandwidth) that measure continuously with depth. The main advantage of this system is that it drifts away from the platform avoiding any type of effects from the ship or cage structure (e.g. shading, reflection and in-water perturbations) (HOOKER; MARITORENA, 2000). Two deployments were made at each station to analyze the environmental variability between casts. The radiometric data was pre-processed using Prosoft 7.7.16 (Satlantic Inc.) for radiometric calibration and some correction procedures, i.e., immersion factor correction, data filtering (tilt $<5^o$and velocity >0.5 m.s^{-1} thresholds) and binning and interpolation (every 1 m) to remove spicks and smooth the profile. For the K_d profile an interval of 5-7 integration points (5-7 m) was used in Equation 4.5, and the choice of the depths to extrapolation E_d and L_u to surface was done in two ways: a) D1: with a fixed interval using the first sub-surface depths: 2-8 m; and b) D2: with an optimized selection of the interval, analyzing the profile from 5-20 m, and selecting the depths with the best R^2 fit for the K_d determination in Equation 4.5. The 5 m upper limit was chosen to avoid (or at least minimize) the effects of bubble clouds and the lower of 20 m lower limit to minimize effects of bio-optical stratification, Raman scattering and noise due to lower signals. A quality control scheme was also applied to avoid using casts with highly noisy $L_u(z)$ and $E_d(z)$ profiles, and the cast was discarded whenever there was an R^2 lower than 0.85 for the linear regression fit of $\ln E_d$ and $\ln L_u$ (within 1-20 m).

PRR (Biospherical Inc.)

The Profiling Reflectance Radiometer (PRR) is a free-falling system similar to HOCR that measures 19 spectral bands in the range of 313-875 nm. Only one cast for each station was recorded for the PRR. A detailed description of the data processing used for the PRR can be found in Mitchell and Kahru (1998). Radiometric corrections and calibrations were applied in established routines, as well as, profile editing with filtering thresholds for low radiance and irradiance values, and profile smoothing, with binning and interpolation (every 1 m, as for the HOCR). The K_d profile was determined as in Equation 4.5 using 5 integration points (5 m) and the depth interval for the extrapolation procedure was chosen according to a visual analysis of each profile, selecting the interval closest to surface, and with least noise.

TriOS (TriOS Optical Sensors Inc.)

The TriOS is a winched profiling system with hyper-spectral radiometers (320-950 nm, 1 nm bandwidth). Measurements were taken at discrete depths along the water column for one cast per station. The data pre-processing consisted of radiometric calibration and corrections for the immersion factor following Ohde and Siegel (2003). Since the E_d and L_u measurements were recorded solely every 2 or 4 m, the K_d was estimated using the entire depths interval of 5-40 m (with 9-15 integration points in Equation 4.5). The extrapolation procedure and R_{rs} determination was also somewhat different from the HOCR and PRR. Below surface $E_d(0^-)$ and $L_u(0^-)$ values were determined n times using each $E_d(z)$ and $L_u(z)$ within 5-20 m and the constant K_d, according to the following expression of the exponential decrease of light with depth:

$$R^*(0^-, \lambda) = R^*(z, \lambda)\exp(K_d(\lambda)z) \tag{4.11}$$

where R^* is the radiometric quantity (E_d or L_u). The above-water (0^+) quantities were then determined using Equations 4.6 to 8. The R_{rs} was calculated for each extrapolated E_d or L_w values and then finally averaged.

A final R_{rs} was determined for each approach (ASD, HOCR, PRR and TriOS) either by averaging or selecting a best retrieval based on the uncertainty analysis and quality controls.

4.5. Bio-optical measurements

Replicates were collected for each parameter and the mean value and standard deviation were calculated for each station.

4.5.1. Biogenic Absorption

The CDOM and particle absorption were determined following Mitchell et al. (2002). Duplicate samples were collected for each parameter and the mean absorption was calculated for each station. The CDOM samples were immediately filtered onboard after collection using a 0.2 μm pore-sized Nucleopore Membrane filter. The CDOM was measured with a Cary-50 UV-VIS-NIR spectrometer in a 10 cm cuvette. Real blanks (MiliQ water filtered through the 0.2 μm membrane filter pore) and pure MiliQ blanks (not filtered) were both measured at each station to evaluate possible blank degradation and contamination of the filtration system during the cruise. The MiliQ optical density (OD) spectra were within ±0.005, showing a good consistency throughout the cruise. A fitted exponential spectrum of the mean real blank was used as a global baseline to correct each sample for the water absorption, as recommended by Mitchell et al. (2002). The CDOM absorption (a_s) spectra were smoothed averaging the wavelengths with a 9 nm bandwidth running filter. For values lower than the instrument uncertainty level (<0.005 m^{-1}), an exponential fit was used (fitted from 380-500 nm).

For the particle absorption (a_p) the replicates were analyzed in different laboratories, using the same protocol (MITCHELL et al., 2002) and instrument, a Shimadzu UV-2450 spectrometer. The samples were filtered onboard with a 0.7 μm nominal pore-sized GFF (glass fiber filter) and had volumes varying from 500-4260 ml depending on the sample concentration. The conversion coefficients used to retrieve a_p from the measured filter optical density were taken from Mitchell (1990). The detritus absorption (a_d) was measured after extracting pigments with 100 % methanol (during 2-4h) and phytoplankton absorption (a_{phy}) was obtained after subtracting a_d from a_p. Since some

a_d spectra remained with some residual pigment contamination, an exponential fit was applied for this data set following recommendations of Bricaud et al. (2010). First the contaminated intervals were removed: 320-365 nm (for microsporine amino acids, MAAs); and 380-520 nm and 640-700 nm (for phytoplankton pigments); to determine the exponential slope (S_d) with a non-linear least square fit. Then a reference band (with a 9 nm interval) at 525 nm was chosen to apply the extrapolated fit using Equation 3.5.

4.5.2. Particle backscattering

The particle backscattering coefficient was measured with the HydroScat-6 (HS6) in 6 spectral bands (420, 442, 470, 510, 590 and 700 nm). The HS6 was deployed by a winch in a cage setup (Figure 4.4f) to measure at continuous depths within the upper layer (~0-100 m). The b_{bp} was also measured in the water samples that were collected with the rosette system (at the 4 depths), using the black bucket (43 cm height and 31 cm Ø). These measurements were used to compare with the *in situ* profile and to analyze the contribution of the submicron fraction <0.7 µm, repeating the measurements in the same sample after filtering through a 0.7 µm GFF. The fractional experiments were applied only for the Fl_{max} depth collected in the CTD stations and for some surface FL stations. To analyze the consistency of the HS6 measurements and possible effects of the reflection of the bucket walls, some measurements of pure MiliQ water b_b were also taken in the bucket.

The HS6 actually measures the volume scattering function (β_v) at 140^o which is then processed into b_b by integrating β_v over the entire backward hemisphere (90-180^o), weighing by the scattering phase function that describes the angular dependency of β_v. The data was processed using Hydrosoft 2.9 (Hobilabs Inc.) with correction of the loss due to particle absorption through the path-length (between the instrument and detected volume) using the Chl*a*, a_d and a_s measurements of each station. To obtain more accurate b_b values the molecular scattering function (β_w) is subtracted from the total (β_v) to derive the particle backscattering coefficient (b_{bp}). Then the water backscattering coefficient (b_{bw}) is added to retrieve the total b_b. The scattering phase function is substituted by a sensor-response function (χ) provided by the manufacturer with the calibration files. b_b is determined according to Maffione and Dana (1997):

$$b_b(\lambda) = 2\pi\chi(\lambda)[\beta(\lambda,140^o) - \beta_w(\lambda)] + b_{bw}(\lambda) \quad (4.12)$$

In this equation, b_{bw} and β_w were obtained according to Twardowski et al. (2007) adjusted from Buiteveld et al. (1994) for pure seawater (using the mean salinity measured at the MV1102). The function χ provided by the manufacturer was determined experimentally over a wide range of Chl*a*, using a HydroBeta that measures β_v at multiple angles. The average value is close to the theoretical value of 1.08 reported in Maffione and Dana (1997). The b_b values were averaged over the depth interval corresponding to the most homogeneous profile closest to surface, avoiding noise and bubble cloud influence (between 4-12 m). To obtain b_b for the ocean colour bands the values were interpolated using a power law fit for b_{bp} (after subtraction of b_{bw}) (MOREL et al., 2007) (Equation 3.7). The fit was optimized with a non-linear regression fit (Levenberg-Marquardt) using two or three band intervals (420-470; 470-590 and 590-700 nm) to adjust the curve as closest as possible to the measured values.

4.5.3. Pigments (HPLC and fluorimetric methods)

The phytoplankton pigment samples were filtered in a 0.7 µm pore-sized GFF immediately after collection and stored in liquid nitrogen until laboratory analysis. The Chl*a* replicates were analyzed with three different methods: a) Chl*a*1: with the High Performance Liquid Chromatography (HPLC) technique, following Van Heukelem and Thomas (2001); b) Chl*a*2: with the standard fluorimetric method, with acidification (to subtract pheophytin *a*) (HOLM-HANSEN et al., 1965); and c) Chl*a*3: with a spectrofluorimeter following Lutz et al. (2010), similar to the narrow band fluorimetric method proposed by Welschmeyer (1994).

The HPLC measurements are considered to be the most accurate since they separate each pigment type through a polarized high pressure column prior to the optical analysis. Hence, there are no interferences of mixed pigments on the spectral responses, and a more accurate concentration of each pigment may be retrieved. The drawback is that it is a complex analysis, with an expensive instrumentation and the need of well-trained chemists to run the analysis. The HPLC samples also require a greater volume to

have an amount of pigment sufficient for an accurate signal, which is most critical for trace pigments and in clear waters. The volumes filtered for the MV1102 HPLC samples were between 500 ml to 4260 ml. The filtration time was attentively controlled to not exceed the recommended 40 min, but there had to be compromise between the filtration time and volume filtered, and some samples that required a greater volume had filtering times up to 1h15 (at the stations with clearest waters). In the present work only the replicate analyzed at HPL (Horn Point NASA laboratory) was used. A comparison with the set analyzed at IRD (France) showed a high agreement (r^2 = 1; root mean square error = 0.09 $mg.m^{-3}$) denoting a very good consistency for the HPLC data set.

The HPLC followed the Van Heukelem and Thomas (2001) fast repetition method. The pigments were extracted with 90% acetone, after macerating the filter samples with an ultra-sonic probe (sonicator) and left for ~4-7 hours in a -25^{o} C freezer (with the solvent and using dim light). The extracted solution is filtered to obtain only the extract with the pigments and vortexed to homogenize and separate a 500 µm volume to run through the HPLC column. The pigment extract is added to a mix of solvents (e.g. 83% methanol and 17% aqueous tetrabutyl ammonium acetate, final concentrations) before passing in the column. The column is composed of an active sorbent with solid granular materials (~3-5 µm pore-sized) (i.e. silica) namely, stationary phase. The high pressure pumped through the column is used to fasten the sample running time and enhance the separation of the pigments, with a higher interaction of the extract with the stationary phase. When the extract (+ solvents) passes through the column, the pigments have different degrees of interaction with the stationary phase (i.e. hydrophobic, dipole-dipole and ionic), which is regulated by the pressure, temperature and polarization of the molecules. Hence, each pigment takes a certain time to pass through the column denoted as retention time (RT). At the end of the column there is a detector that emits light and measures the absorption peak of the passing pigment "packages". The RT and absorption peaks are used to identify and quantify the pigments (WRIGHT, 2005).

The pigments analyzed were: the chlorophylls: chlorophyll *a* (chl*a*) and its degradation products - chlorophilide *a* (chlide), pheophoride *a* (phide) and pheophytin *a* (phytin); the divinyl-chl*a* (d-chl*a*); chlorophyll *b* (chl*b*); divinyl-chl*b* (d-chl*b*); chlorophyll *c* (chl*c*) (*c*1, *c*2 and *c*3); and the carotenoids (carotenes and xanthophylls): 19'-

-butanoyloxyfucoxanthin (19'BF), 19'-hexanoyloxyfucoxanthin (19'HF), alloxanthin (allo), diadinoxanthin (diadino), diatoxanthin (diato), fucoxanthin (fuco), peridinin (perid), zeaxanthin (zea); lutein (lut), neoxanthin (neo), violaxanthin (viola), prasinoxanthin (prasin), gyroxanthin diester (gyr-diester). The total Chl*a* (TChl*a*) used for the HPLC analysis corresponded to: chlorophyll *a* + chlorophyllide *a* + divinyl chlorophyll *a*.

The fluorimetric methods also used for the determination of the Chl*a* are much more simple and less expensive and have been extensively applying in world-wide oceanographic expeditions. Hence, most of the global data bases are composed of fluorimetric Chl*a*. Nonetheless, as this method is based essentially on the excitation of a chl*a* absorption band and the measurement of a fluorescence emission band, there may be some contamination of other pigments mixed in the sample, that have overlapping fluorescence bands. This is the main source of uncertainty of the fluorimetric method and lots of efforts have been applied to compare HPLC and fluorimetric Chl*a* measurements to evaluate these biases and seek the compatibility between the data sets. Another advantage of the fluorimetric methods is that it is very sensitive and requires only small filtered volumes which can be obtained in a short filtering time, minimizing pigment degradation during the filtration. The filtered volumes for the MV1102 varied from 300-1040 ml and the filtering time did not exceed 30 min.

The Chl*a*2 standard fluorimetric method (HOLM-HANSEN et al., 1965) was processed in the follow way. After storage in liquid nitrogen the filter was extracted in 90% acetone for ~24 hours in a freezer (-20^{o}C). The samples were homogenized and vortexed (~10s) before and after the extraction period. The fluorescence was measured in a Turner Design fluorimeter with the excitation band centered at the chl*a* absorption peak (~430 nm) and the emission band filter centered at the chl*a* fluorescence peak (~685 nm). After the first measurement 2 drops of 10% of acid chloride (HCl) is added to shift the chl*a* fluorescence peak and measure the pheo fluorescence contribution to subtract from the first measurement and obtain solely the chl*a* concentration. The measurements are corrected with an acetone blank. This method is known as the broad band fluorimetric acidification method.

The Chl*a*3 was measured with a spectrofluorimeter (LUTZ et al., 2010). The method is similar to the narrow band (NB) fluorimetric method of Welschmeyer (1994). The pigments were extracted with 100% methanol for 12-24h in freezer (-20^{o}C), after sonicating (~30s) before and after the extraction period. The Chl*a*3 method does not need to acidify the sample to subtract the pheo, because it uses two monochromators able to choose the wavelength of fluorescence avoiding any contamination of other overlapping signals. The emission wavelength is centered at 430 nm and the excitation at 666 nm. The samples are thus measured once by the spectrofluorimeter and corrected for the methanol absorption with a solvent blank.

4.5.4. Flow cytometry

The flow cytometry is a technique used to identify and count the concentration mainly of pico-sized plankton of heterotrophic bacteria (HB), picoautotrophic eukaryotes (EUK) and cyanobacteria (*Synechococcus* - SYN and *Prochlorococcus*- PROC). Smaller and larger cells can also be analyzed, e.g. virus, nano and micro plankton, but only the former were analyzed for the MV1102. The analysis was run on the flux cytometer in which the sample passes through a narrow column (≈ 20 µm Ø) containing a fluid sheet, in which each cell can be separated and optically measured. At one side of the column lays a laser light source that emits at 488 nm, and at the other side are two detectors: one at 180^{o} to measure the forward scattering - FSC and the other at 90^{o} to measure the side scattering – SSC. The filters of the detectors separate the scattered and fluorescence emitted light (FL1(green) = 530 nm; FL2 (orange) = 585 nm e FL3 (red)= 750 nm). The FSC indicates the cell size and the SSC the complexity of the internal and external cell morphology. The fluorescence bands are used to identify the groups (HB, EUK, SYN and PROCH) (MARIE et al., 2005).

The samples were collected in a 2 ml vial and preserved in a solution of 2% paraformaldehyde (final concentration) and in liquid nitrogen. Before the analysis fluorescent beads (2-3 µm) (microspheres) with a known concentration were added to the samples, to use as reference for the identification, sizing and cell counting of each group. The velocity of the flux and voltage are adjusted for the size range of particles in interest for the analysis. One needs also to set a minimum size range to separate noise, debris and virus. A fluorescent marker for nucleic acids (SYBR Green) is added to the

samples to mark the HB for their identification. The HB are sub-divided in two groups: the High Nucleic Acid (HNA) and Low Nucleic Acid (LNA), which are mainly separated by their size (HNA are larger). The picoautotrophic groups are identified by the red fluorescence peak (FL3). The EUK are separate by their larger size range (0.1 - 3 μm). The SYN are separated from PROCH due to the presence of the phycoerythrin pigment, that has an orange fluorescence (FL2) and they are usually also somewhat larger (≈ 0.8-1.5 μm) than PROC (≈ 0.5-0.6 μm).

The groups are identified by "gates" that the analyst will defined based on all the parameters (FSC, SSC, FL1, FL2 e FL3) and according to literature references. For each sample the gate needs to be readjusted due to environmental variations of the population (e.g. surface depths may have smaller HB groups while deep waters may have larger groups). The raw data is exported to text files with the information of the number of scattering events within each gate. With the auxiliary data of running time, flux and concentration of the beads, the concentration of each group contained in the gates were calculated in units of cells.ml^{-1}.

4.5.5. Microscopy Analysis

Microscopy samples were collected at selected stations and analyzed at INIPED (Argentina). Seven stations were available to complement the analysis of the present work (St 01, 23, 32, 46, 61 and 76). The samples were collected in plastic bottles of 150 ml, and preserved with 3 ml of neutralized paraformaldehyde (0.4%, final concentration). The identification and quantification of the phytoplankton cells (~3 to 100 μm), were made using an inverted microscope and a sedimentation chamber (50 ml) (UTERMÖHL, 1958). The cells were identified and grouped according to their genera i.e., diatoms, dinoflagellates, calcareous and non-calcareous haptophytes, prasinophytes, and separated into size classes of pico, nano and micro cells.

5 UNCERTAINTY ANALYSIS

5.1. Introduction

The present Chapter aimed to assess the sources of uncertainties regarding *in situ* radiometry and bio-optical measurements of the MV1102. According to the SeaWiFS NASA protocol the R_{rs} should have a maximum 5% level of uncertainty for ocean colour applications of bio-optical modeling, satellite validation and vicarious calibration. This strict limit is a challenge for highly controlled *in situ* measurements, and much more critical for global data bases that are composed of radiometric and bio-optical match-ups provided by ocean colour groups that use different instruments and data processing routines (e.g., NOMAD) (WERDELL &BAILEY, 2005). Despite of the extensive efforts of NASA SeaWiFS-MODIS projects to define the best *in situ* approaches and unify a standard protocol for the collection and data processing scheme, there are still differences inherent to the instrument packages and random effects of environmental noises that are difficult to overcome. Hence, a significant source of variability within the global ocean-colour models is caused by the uncertainties of the *in situ* data (WERDELL et al., 2009).

The radiometric measurements are the most problematic as they are highly sensitive of variations in the illumination (cloud coverage, atmospheric turbidity, SZA) and sea state conditions (e.g. wavy facets, whitecaps, bubbles, waves, etc.). The above-water approach consists of measurements made by an onboard radiometer to derive the water leaving radiance (L_w) and downwelling solar irradiance (E_d). The major advantage of this approach is that the measurements can be obtained with the platform in movement and take advantage of opportunity cruises (DESCHAMPS et al. 2004). It is also considered better for turbid coastal waters where the in-water approach is usually more biased due to the high light attenuation and water column stratification (MUELLER et al., 2003). The above-water also retrieves the quantities in a more similar way as the satellite measurements, being more straightforwardly comparable, and it has a more compact and simple instrumentation in terms of size, weight, and operating logistics. The main constraints and difficulties are the requirement of clear skies for instruments that need aerosol optical thickness e.g., SIMBAD (DESCHAMPS et al. 2004), and the contamination of reflected skylight on the ocean surface (MOBLEY, 1999), e.g., ASD.

There are well defined correction schemes to remove the skylight glint, however other sources that have simultaneous effects, such as the sun and cloud glint (MOBLEY, 1999) and the platform reflection (HOOKER; MOREL 2003), are more difficult to correct. Whitecaps and underwater bubble clouds also contribute to the above-water signal (FROUIN et al. 1996; PISKOZUB et al. 2009). These contributions can be avoided during the measurements or removed in the processing. Above-water measurements are also always obtained with off-nadir-viewing angles to avoid self-shading and platform interference, thus bidirectional effects are important especially for waters with high particle concentration and high solar zenith angles (SZA) (MOREL; GENTILI, 1996; MOREL et al., 2002; HOOKER et al., 2004).

The in-water approach is based on submersed radiometers that measure the upwelling radiance (L_u) and downwelling irradiance (E_d) and a deck sensor that measures above-water downwelling irradiance (E_S). There are different instrument designs, such as the ones that are attached to moored buoys and sample at stationary depths, the profilers that are winched and attached to deploying cages, and the free-falling instruments that drift away from the platform attached solely to a telemetry cable. The in-water approach has been extensively used in satellite calibration and validation programs (HOOKER et al., 2002; MUELLER et al., 2003; BAILEY; WERDELL, 2006). It is considered to provide the most accurate radiometric measurements, since not perturbed by reflected skylight on the ocean surface, a major source of error in the above-water approach. However, there are some important issues related mostly to the extrapolation procedures and variability of the submersed light field (STRAMSKA; DICKEY, 1998).

The choice of the best depths interval to use for the extrapolation to above-water quantities is not simple, and varies depending on the environmental conditions. Besides the vertical variability of the bio-optical properties in the water column, the underwater light field can be affected by diverse sources of noise and variations. They include: the focus and defocusing effects of the downwelling solar rays due to the wavy facets of the sea surface (MUELLER et al., 2003; ZIBORDI et al., 2009; GERNEZ; ANTOINE, 2009), the variation of the attenuation depths due to wave motion (STRAMSKA; DICKEY, 1998), the intermittent presence of bubble clouds from breaking waves (FLATAU et al., 1999), illumination variation during casts (MUELLER et al., 2003),

sensor tilt, instrument self-shading (ZIBORDI; FERRARI, 1995; LEATHERS et al., 2004), and platform shading (HOOKER; MARITORENA, 2000). All these may cause significant levels of uncertainties in the underwater and extrapolated quantities. Some correction procedures have been incorporated in standard protocols, such as for the illumination variation during casts (normalized by the deck sensor), sensor tilt thresholds, and instrument self-shading correction. However, other effects, such as the vertical stratification, wavy facets, and bubble clouds are more difficult to correct and the selection of the best depth interval to minimize these noises turns out to be subjective and not trivial (HOOKER et al., 2002; MUELLER et al., 2003). These effects may be more significant for the E_d profile and many authors, including NASA, have recommended the use of the deck sensor E_S to retrieve more accurate R_{rs} (MUELLER et al., 2003). Most inter-comparison studies have used this quantity as a reference to compare other approaches. Some authors, however, have argued that despite the higher biases related to E_d, some in-water perturbations affect both E_d and L_u in similar ways, and therefore the use of both quantities to retrieve R_{rs}, may normalize these noises and actually retrieve R_{rs} more accurately (MITCHELL; KAHRU, 1998). Therefore, not even the choice of a reference with supposedly the best accuracy is a trivial task for inter-comparison studies.

Some works (GREEN; SOSIK, 2004; CHANG et al., 2007) have attempted to compare measured and modeled R_{rs} using measured IOPs, i.e., absorption and backscattering coefficients and Chl*a*. Such a closure experiment presents challenges, as there may be significant uncertainties associated with the modeled R_{rs} due to biases in the IOPs and constants used, as well as, the limitations inherent to the assumptions of the models. For example, there are many unknowns in respect to the particle backscattering coefficient (b_{bp}) for both theoretical models and *in situ* measurements (ANTOINE et al., 2011). The Chl*a* measurements using HPLC and fluorimetric methods are also subject of extensive inter-comparison works and differences of 30% or more can be encountered with the different methods (DAEMEN, 1986; LUTZ et al., 2010). Nevertheless, comparing modeled and measured R_{rs} is an interesting approach, since the quantities are obtained in a totally independent and distinctive way, and the modeled R_{rs} is not affected at all by environmental variability and instrumental effects on the light field. Thus, the closure experiment could perhaps highlight some of these effects on the different approaches,

and indicate least biased retrievals, as well as elucidate uncertainties also regarding the bio-optical measurements and the relations between AOPs and IOPs.

Other investigations of *in situ* radiometry errors utilize radiative transfer modeling in an idealized 2-dimensional computational environment (e.g., Hydrolight). These experiments allow one to isolate each factor separately and use arbitrary intervals of bio-optical properties to test different conditions. They have provided great insights on the relations of apparent and inherent optical properties (MOREL et al., 2002), as well as the environmental influences on the light field distribution, such as the sky radiance distribution under different illumination conditions, geometrical effects of the sensor-viewing and solar angles, and implications of the sea surface roughness due to wind speed (MOBLEY, 1999; TOOLE et al., 2000) and of the presence of bubble clouds (FLATAU et al., 1999; PISKOZUB et al., 2009). As a result, some of these works have provided look-up-tables (LUTs) with parameterized coefficients that can be used to correct for specific conditions, such as: the sea surface reflectance factor for skylight glint provided by Mobley (1999), and the environmental and bidirectional factors fQ^{-1} ratio provided by Morel et al. (2002).

All these works, including *in situ* experiments organized to evaluate the models or to focus on specific effects, have been important to identify and quantify *in situ* radiometry errors. Ideally it would be wise to avoid the influence of the major sources of errors during a collection. In a monitoring program or an oceanographic expedition the ship may be oriented to optimize sensor viewing. The environmental conditions, however, are unlikely to be controlled, and one may not be able to wait for favorable conditions. In this framework, there are so many different interferences, such as platform tilt, displacement of the different sensors, sea surface roughness, swells, intermittent presence of bubble clouds, foams and whitecaps, and illumination variations due to broken clouds. With all these complexities it is not trivial to identify the main sources of errors and the best ways to correct for each one. Moreover, for each correction procedure one needs to use factors that are usually modeled or empirically derived, which introduces additional uncertainty.

With the aim to assess the uncertainty of *in situ* ocean-colour radiometry and bio-optical measurements acquired during the MV1102 cruise, an inter-comparison framework was

applied for the different approaches with distinct instrumental and processing methods. The radiometric instruments used were the above-water Fieldspec HandHeld ASD, the in-water free falling profilers HOCR and PRR, and the winched TriOS. The data sets of each instrument were processed separately using routine protocols applied by the ocean-colour laboratories that provided each instrument. The measured quantities were all processed into above-water remote sensing reflectance (R_{rs}). The uncertainty analysis included an intra-comparison scheme to analyze environmental and data processing uncertainties within each approach, an inter-comparison scheme between the approaches, and a comparison with modeled R_{rs}, using measured IOP and Chl*a* (closure experiment). The uncertainties related to the IOPs and Chl*a* were also evaluated and discussed, as well as the implications on the retrieval of ocean-colour products generated by selected operational bio-optical models and inversion schemes. The rationale was to investigate all possible uncertainties affecting *in situ* ocean-color radiometry and related bio-optical measurements, in the complex framework of an oceanographic expedition sampling a wide range of ecosystems and bio-geographic provinces under generally adverse conditions, using different instruments and data processing routines. The goal was also to provide the best R_{rs} and its uncertainty for further ocean-colour variability studies along the MV1102 ship track, and to recommend *in situ* ocean-colour radiometry procedures for purposes of bio-optical modeling.

5.2. Material and Methods

The data set used for the present analysis comprehended the radiometric and bio-optical measurements of the 20 CTD stations (Figure 4.3). The measurements were all processed as described in Chapter 4 (sections 4.4 and 4.5). To analyze the uncertainties related to the R_{rs} for the above-water approach, after each processing steps, the retrieved R_{rs} was defined as: a) ASD1: with sky glint correction; b) ASD2: with the residual correction (RC); c) ASD3: with the quality control (QC); and d) ASD4: with bidirectional correction (BD). To analyze the uncertainties within the in-water approaches comparisons were made for the R_{rs}: a) between casts (A and B) and b) the different extrapolation depths (D1 and D2) using the HOCR data set; and c) using the different downwelling solar irradiances (E_d and E_S) for the three profiling systems

(HOCR, PRR and TriOS). Uncertainties regarding self-shading (SS) and bidirectional effects were also addressed.

For the closure experiment, the bio-optical measurements were first analyzed in terms of their uncertainties and then averaged within the first optical depth ($\delta \sim 1/K_d$) to apply in the RTE models. The a_s, a_p and Chl*a* replicates were compared and either averaged or selected in a quality control scheme for a final retrieval. The measurements were integrated within δ using a weighted average of the first two sub-surface samples, to approximate the values for the closure, as δ corresponds to 90% of the remote sensing signal measured above the ocean surface (GORDON; MCCLUNEY, 1975). This averaging procedure assumes the homogeneity of the IOPs within the first optical depth, for which a and b_p should co-vary, and thus, b_p/a vertically constant. The assumption may be valid for typical Case 1 waters, where both a and b_b are primarily regulated by the phytoplankton assemblage (directly or indirectly). However, there may be independent variations of a and b_{bp} caused by phytoplankton photoacclimation mechanisms or bio-optical vertical stratification (ZANEVELD et al., 2005). To verify the validity and implications of such assumptions on the closure experiment, an homogeneity index (H)=$<b_{bp}/a>/[<b_{bp}>/<a>]$ was calculated for each station according to Zaneveld et al. (2005).

The closure was applied using two forward models: a) the RTE approach of Morel et al. (2002) namely, RTE M_*f*/*Q*, with the *f*/*Q* ratios calculated as a function of Chl*a* (for nadir viewing angle and SZA) (Equation 3.12 - using the simplified b_b/a approximation), and b) the MM01 (MOREL; MARITORENA, 2001) (Equations 3.12 and 3.13). The b_b/a approximation may be applied for Case 1 waters assuming vertical homogeneity and single a scattering dominance (MOBLEY, 2004). For station 85 in the Magellan Strait, the more accurate term $b_b/(a+b_b)$ was used due to multiple scattering caused by sediment-dominated waters. The approximation of Lee et al. (2004) with $b_b/(a+b_b)$ and a quadratic function using a g factor instead of the *f*/*Q* ratio, was also tested and compared. The g factor takes into account all the IOPs and not just Chl*a* as an index of the volume scattering function. The advantage of using the *f*/*Q* ratio is the easier application for bidirectional corrections (Equation 4.3).

The Morel and Maritorena (2001) model (denoted as MM01) was also compared to the measured R_{rs} measurements, because it is a well-known model and uses only the measured Chl*a* as input, which allows an estimation of K_d, a, b_b and ultimately R_{rs} (the b_{bp} model is adapted from Loisel and Morel (1998)). The model also assumes a vertically homogeneous medium and considers that Chl*a* is the dominant property determining K_d (the other optically active constituents – detritus and CDOM should co-vary with Chl*a*). This assumption fails for the Magellan Strait station, which was therefore left out of the MM01 computations.

Implications of the uncertainties in terms of ocean colour remote sensing and bio-optical modeling are discussed using the R_{rs} measurements to estimate Chl*a* with the maximum band ratio (MBR) OC4v6 empirical relation (O'REILLY, 1998; O'REILLY et al., 2000) and with inversion models for IOP retrievals, namely the Quasi-Analytical Algorithm (QAA) (LEE et al., 2002) and the Garver-Siegel-Maritorena (GSM01) scheme (MARITORENA, et al., 2002).

5.2.1. Statistical indices

Various statistical indices provide information on the possible sources of uncertainties associated with a quantity. The most commonly used for inter-comparison studies of radiometric quantities are the unbiased percent difference (UPD) (Equation 5.1), the relative percent difference (RPD) and the modular RPD for absolute differences (RPD*) (Equation 5.2), as well as the root mean square error (RMSE) (Equation 5.3), standard deviation (SD) (Equation 5.4), the determination coefficient (r^2) and the slope (s) of linear regression analysis (TOOLE et al., 2000; ANOINTE et al., 2008). These indices are all used in the present study. The UPD considers that all measurements are biased and indicated whether the biases are positive or negative (with over or underestimation). The RPD* quantifies the total bias and indicates the occurrence of systematic errors, such as radiometric calibration and instrument and/or platform shading, with a consistent bias. The RMSE, SD and r^2 provide dispersion measurements between the quantities with more information on random errors that may be related to environmental effects, such as sky glint effects for the above-water measurements and wave focusing and defocusing for the in-water approaches (TOOLE et al., 2000). Specifically, the indices read:

$$\mathrm{UPD}\ (\%) = \sum\{(x_1 - x_2)/[(x_1 + x_2)/2]\}/N * 100 \quad (5.1)$$

$$\left|\mathrm{RPD}\right|(\%) = \sum[\left|x_1 - x_2\right|/x_2]/N * 100 \quad (5.2)$$

$$\mathrm{RMSE} = \sqrt{1/N\sum(x_1 - x_2)^2} \quad (5.3)$$

$$\mathrm{SD} = \sqrt{1/(N-1)\sum(x_1 - \bar{x})^2} \quad (5.4)$$

In the above equations, x_1 and x_2 are the values obtained by the different methods, x_2 being the "reference" considered least biased, N is the number of match-ups and $\bar{x}$ is the mean. The coefficient of variation (CV = SD/mean*100) was also used in some analysis as a measure of dispersion.

The R_{rs} comparisons were made for the ocean colour bands (412, 443, 490, 510 and 555 nm) and band ratios (412-510/555) relevant for bio-optical modeling.

5.3. Results

5.3.1. Environmental conditions

The radiometric stations along the MV1102 had a fairly high Chl*a* gradient from 0.13-4.89 mg.m^{-3} (Clh*a*3). The Southern Atlantic (stations St 03 to 56) (Figure 4.3) was characterized by oligo-mesotrophic waters (0.13 to 0.74 mg.m^{-3}) (Figure 5.1). The first stations had the lowest Chl*a* values and were within the SATL (St 03 and 06), with typical clear blue oceanic waters. The highest Chl*a* stations of the southern Atlantic were related to the presence of seamounts in the middle of the South Atlantic basin (St 19), the Argentinean shelf-break (St 51 ot 56) and across the Patagonian Shelf (PAT)

(St 61to 76) (in the FKLD province) (Table 5.1), with typical greenish waters (MOREL; PRIEUR, 1977).

Table 5.1 - Environmental conditions of the radiometric stations (St), with latitude (LAT), longitude (LON), instrument type (INS), Chl*a*, maximum fluorescence depth (Fl_{max}), first optical depth ($1/K_d490$), solar zenith angle (SZA), wave significant height (WSH) and direction (DIR), wind speed (*U*) and direction (DIR), cloud cover (CC), and observations of sky and sea state conditions.

St	LAT (°)	LON (°)	INS Type	Chl*a* ($mg.m^{-3}$)	Fl_{max} (m)	$1/K_d$ 490 (m)	SZA (°)	WSH (m) (DIR^o)	*U* ($m.s^{-1}$) (DIR^o)	CC 1/8	sky and sea state
03	-33.6	14.4	1,2	0.21±0.004	55	16	33	2.1 (210)	7.7 (129)	3/8	CS
06	-36.0	10.4	1,2,3	0.13±0.006	85	33	41	1.6 (214)	3.8 (46)	2/8	CS
09	-38.5	6.2	1,2,3	0.68±0.004	1	13	35	2.3 (239)	6.9 (141)	7/8	OC
13	-41.1	1.7	1,2,3	0.49±0.008	1	16	38	1.8 (236)	4.2 (12)	8/8	OC
19	-43.1	-3.5	2,3,4	0.60±0.007	35	16	45	2.6 (332)	13.5 (159)	8/8	OC, R
23	-45.4	-8.0	1,2,3,4	0.56±0.004	45	17	43	2.4 (235)	6.2 (149)	8/8	OC
28	-47.5	-13.5	1,2,3,4	0.55±0.016	50	15	48	2.2 (219)	6.1 (115)	8/8	OC
32	-48.3	-19.9	1,2,3,4	0.54±0.044	30	16	52	2.2 (122)	6.8 (46)	8/8	OC/FOG
36	-48.5	-27.0	2,3,4	0.53±0.029	30	13	48	2.4 (338)	9.9 (207)	8/8	OC/FOG
40	-48.6	-32.5	1,2,3,4	0.50±0.010	30	14	51	1.6 (140)	0.8 (153)	7/8	HILV
46	-49.1	-39.3	1,2,3,4	1.05±0.050	20	11	55	1.5 (226)	7.3 (311)	7/8	HILV
51	-49.5	-46.2	1,2,3,4	0.60±0.007	20	16	52	2.4 (300)	7.8 (212)	6/8	HILV/R
56	-50.0	-52.6	2,3,4	0.80±0.002	35	16	55	2 (216)	6.4 (273)	8/8	OC/FOG
61	-50.6	-59.2	1,2,3,4	1.70±0.033	1	8	52	2.3 (353)	11.5 (330)	5/8	BC/R
75	-52.0	-65.6	1,2,3,4	2.35±0.036	13	6	56	1.6 (26)	5.6 (4)	1/8	CS
76	-52.2	-66.3	1,2,3,4	4.89±0.216	10	4	53	1.3 (179)	3.7 (329)	4/8	BC
85	-52.7	-70.0	1,2,3	3.40±0.047	10	4	59		4.7 (47)	8/8	OC
129	-40.5	-74.8	1,2,3	0.43±0.000	42	15	56		5.1 (171)	4/8	BC
130	-40.1	-74.7	1,2,3	0.75±0.128	25	11	39		4.7 (166)	6/8	BC
134	-36.4	-74.1	1,2,3	2.33±0.024	1	6	54		11.5(181)	4/8	BC/R

*The instrument types correspond to: 1 ASD, 2 HOCR, 3 PRR and 4 TriOS. BC: broken clouds; CS: clear sky; OC: overcast; HILV: high illumination variation; R: rough sea- strong winds and high waves. Chl*a* corresponds to Chl*a*3 (mean and SD integrated in $1/K_d$). The SZA is correspondent to the beginning of the station and varied ±2-7^o within the station (with 1.5 hours of measurements).

The station in the middle of the Magellan Strait (St 85) had relatively high Chl*a* (3.4 $mg.m^{-3}$) and waters typically dominated by suspended sediments with a yellow-whitish colour (MOREL; PRIEUR, 1977). The strait is narrow and predominantly governed by strong tide currents that resuspend bottom sediments in shallow areas, which may have contributed for the high sediment load observed at St 85 (40 m deep), as well as the

coastal erosion, run-off and river inputs within the channel (ANTEZANA, 1999). The stations along the Chilean coast (St 129 to 134) (in the HUMB province) had intermittent values of higher and lower Chl*a* (0.43-2.33 $mg.m^{-3}$), with the highest values at St 134, with typically dark greenish waters. This station was located just off Conceptión, Chile, where there is an upwelling cell, namely *Punta Lavapies*. The Chilean continental shelf is narrow and despite of the proximity to the coast, the stations were off the shelf break (>2,000 m deep). The southern Chilean coast is not much influenced by coastal upwelling because the strong westerlies act on its suppression, nevertheless, there are evidences that intrusions of High Nutrient Low Chlorophyll (HNLC) waters of the Southern Ocean onto the iron enriched continental shelf, promote enhancement of phytoplankton growth along the southern Chilean Coast (ROMERO et al., 2001), which may explain the relatively higher Chl*a* at St 130.

The environmental conditions of each station are summarized in Table 5.1 regarding illumination, sea state conditions and bio-optical indexes: of Chl*a*, the maximum fluorescence depth (Fl_{max}) and the first optical depth ($1/K_d$). Other auxiliary data, such as bottom depths, sea level barotropic pressure, air and sea surface temperatures, cloud type and distribution, swell significant height and direction, and photographs of the sky and sea surface, were also obtained. Regarding the illumination and sea state there was a high range of conditions, from favorable clear skies with low winds (<5 $m.s^{-1}$) (e.g. St 06), to harsh conditions of broken clouds and rough seas (U>7 $m.s^{-1}$ and WSH>2 m) (e.g. St 51). Most of the stations, were held under rather adverse conditions, either with moderate to stronger winds (5 to 13.5 $m.s^{-1}$) and higher waves (>2.2 m), or with broken clouds that caused high illumination variations with a fast changing sky.

In respect to the bio-optical vertical distribution, most stations had a fairly homogenous profile within the first optical depth, based on the Chl*a* profile The Chl*a* SD was on average ±0.034 $mg.m^{-3}$, and only two stations had more stratified profiles: one in the PAT with ±0.216 $mg.m^{-3}$ SD (St 76) and one in the Chilean coast with ±0.128 $mg.m^{-3}$ SD (St 130) (Table 5.1). The Fl_{max} was below the first optical depth for most stations and ranged from 1-85 m, whereas the first optical depth ranged from 4-33 m, with the minimum value at the PAT and Magellan Strait stations (St 76 and 85) and maximum at the SATL station (St 06).

5.3.2. Above-water approach

For the above-water approach only 17 stations were sampled because some stations had rain or technical problems with the battery. Since there were only three almost completely clear sky days (<3/8 CC) and most of the other days had over than 50% of cloud coverage (>4/8 CC), sun glint was not a major issue for the above-water ASD measurements. The station that had some noticeable effects of sun glint was St 61, which had relatively high wind speeds (U >11 m.s^{-1}) and SZA (52^{o}) (Table 5.1). For St 06 with an almost clear sky and low winds (U >5 m.s^{-1}), sun glint was effectively avoided with the sensor-viewing geometry, as the casts were perfectly matched and had low R_{rs} values in the NIR.

Skylight surface reflection was effectively corrected using the adjusted sea surface reflectance factor for the solar-sensor-viewing geometry and sea surface roughness (indexed by wind speed), according to Mobley (1999). The ρ_{sky} factor varied from 0.028-0.0375, with the maximum at the stations with highest wind speeds and SZA. The use of the adjusted ρ_{sky} accounting for wind was important to correct for the skylight reflection, as wind speeds were mostly above 5 m.s^{-1}, and enhanced the factor up to 25% for the maximum wind speed. The effects of wind on the contribution of sky glint to the L_T are discussed by Mobley (1999) and Toole et al. (2000). The wind generated wavy facets change the geometry of the upwelling rays and increase the area sampled by the sensor, with rays coming from remote spots out of the projected FOV. The higher the wind speed, the greater the sampled area and higher sky glint contribution to the L_T. Thus, a greater ρ_{sky} may account for such effect, as simulated in Hydrolight by Mobley (1999). This correction however was not sufficient for more complex conditions, such as in the presence of clouds, and other contaminating sources such as sun glint, whitecaps and bubbles, causing high R_{rs} in the NIR and high SD for the entire spectra (Figure 5.1a).

The main challenge for the ASD approach was regarding cloud glint and illumination variation due to broken clouds. Cloud glint is the light reflected from the clouds back to the ocean surface, and can be highly variable in magnitude and spectral shape depending on the type, thickness and distribution of the clouds in the sky. Thus, its effect is extremely difficult to model for the correction of the sea surface reflection to

retrieve L_w (MOBLEY, 1999). The residual correction (RC) was therefore, necessary to retrieve more reliable R_{rs} even after applying the sea surface reflectance factor, for most cases of the MV1102 (Figure 5.1a and b).

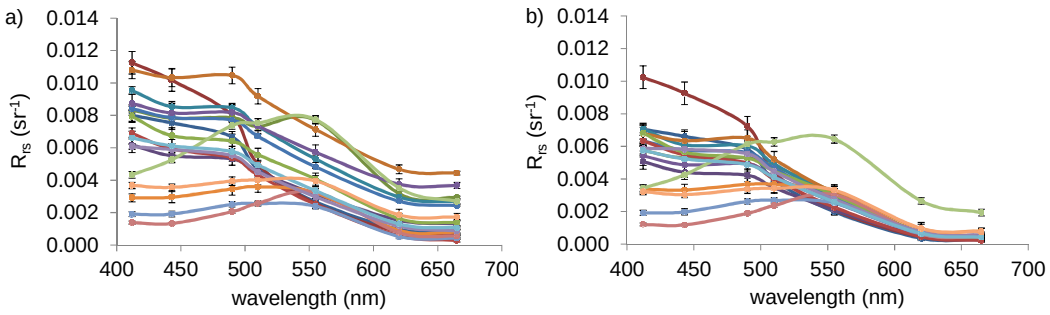

Figure 5.1 - Mean R_{rs} and standard deviation of the ocean colour bands (412-665 nm) retrieved with the above-water ASD: before (a) and after the residual correction and quality control (b) (N=17).

Besides cloud glint, the high illumination variation during measurements with broken clouds, especially with a rapid changing sky and intermittent sun shining and cloud shading, was a major source of uncertainty for the ASD measurements. Figure 5.2 shows an extreme example of this effect for a cast at St 130. The L_{sky} and L_w were in agreement with the other casts, while the L_{pl} of the same set of measurements (highlighted in black) was much lower due to cloud shading. This mismatch of illumination conditions between the measurements caused a highly biased R_{rs} spectrum, especially for the shorter wavelengths. This case was an extreme example of the effect of illumination variation, however much slighter, but notable effects were observed in other stations. In some cases the contrary also happened, with higher illumination conditions for the L_{pl} measurement, causing a biased R_{rs} with lower values in the blue spectral region. The filtering technique applied for the quality control (QC) scheme, based on the mean $R_{rs}(400)$, was effective to eliminate these highly biased spectra, both with higher or lower unreliable R_{rs} values. The QC also eliminated spectra with higher residual contaminations of skylight reflection, cloud and sun glint, as well as whitecaps and bubble clouds that were under-corrected in the shorter wavelengths, diminishing the

SD in the blue-green spectral region (Figure 5.1b), as all these residual sources tend to provide higher L_w for the shorter blue and green bands (TOOLE et al., 2000; PISKOZUB et al., 2009).

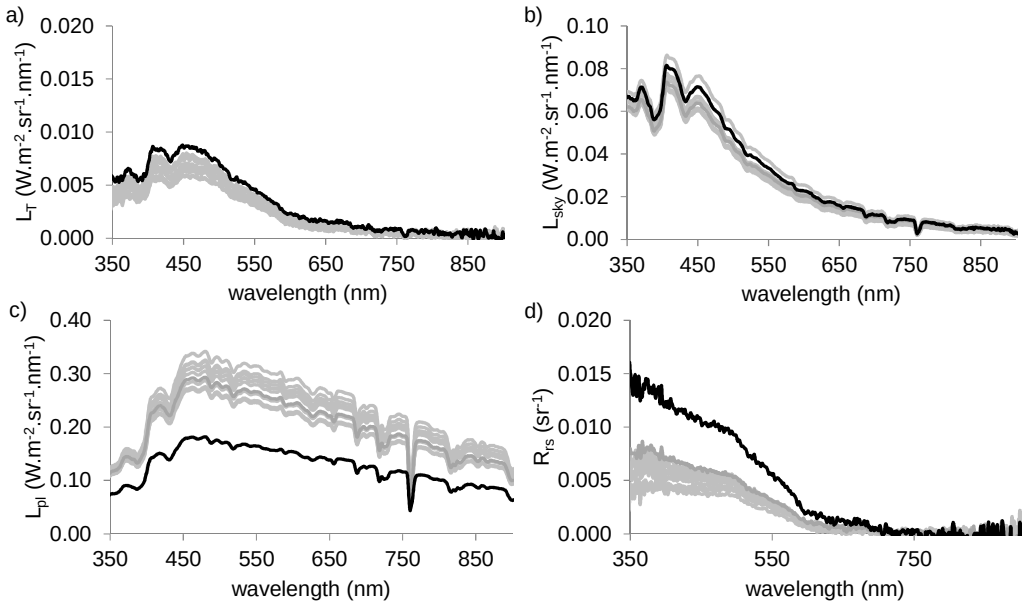

Figure.5.2 - L_T (a), L_{sky} (b), L_{pl} (c) ($W.m^{-2}.sr^{-1}.nm^{-1}$) and R_{rs} (d) (sr^{-1}) measurements for St 130 (N= 10 casts).

Table 5.2 shows the statistical differences between each processing step of the ASD. The R_{rs} without RC overestimated 18-21 % (UPD) the ocean colour bands (412-555 nm), with 0.0017 sr^{-1} RMSE. This indicates the high effects of residual sources (mostly due to cloud glint) and the importance of applying the RC to the above-water measurements. The band ratios, on the other hand, were 8-11% lower without the RC, which could indicate a slight distortion caused by the uncorrected residuals at the shorter spectral bands, as the residual sources (e.g. sun, cloud glint, whitecaps and bubble clouds) have an increasing contribution towards the shorter wavelengths (FROUIN et al., 1996; MUELLER et al., 2003; PISKOZUB et al., 2009). Hence, after the white offset RC, the shorter wavelengths still remained somewhat under-corrected.

Table 5.2 - Statistical differences between the ASD processing steps (N=17).

		λ412	λ443	λ490	λ510	λ555	412/555	443/555	490/555	510/555
ASD1	UPD (%)	17.6	18.7	18.3	21.0	21.0	-11.3	-10.2	-10.6	-7.9
vs. 2	RPD* (%)	21.24	22.8	22.2	26.1	38.8	11.61	10.4	9.7	7.6
	RMSE (sr^{-1})	0.0017	0.0017	0.0016	0.0016	0.0016	0.37	0.31	0.29	0.18
	SD (sr^{-1})	0.0008	0.0008	0.0008	0.0008	0.0008	0.18	0.16	0.15	0.09
	r^2	0.85	0.81	0.76	0.67	0.58	0.96	0.96	0.93	0.90
ASD2	UPD (%)	0.3	0.2	0.5	0.7	1.0	-0.07	-0.8	-0.5	-0.3
vs. 3	RPD* (%)	3.83	3.0	2.5	2.6	2.9	2.48	1.7	0.9	0.6
	RMSE (sr^{-1})	0.0003	0.0002	0.0002	0.0001	0.0001	0.05	0.03	0.02	0.01
	SD (sr^{-1})	0.0001	0.0001	0.0001	0.0001	0.0001	0.02	0.02	0.01	0.01
	r^2	0.99	0.99	0.99	0.98	0.99	1.00	1.00	1.00	0.99
ASD3	UPD (%)	-0.1	0.0	0.1	0.2	2.9	-3.0	-2.9	-2.8	-2.7
vs. 4	RPD* (%)	4.54	4.7	4.7	4.6	8.3	2.5	2.5	2.3	2.3
	RMSE (sr^{-1})	0.0003	0.0003	0.0003	0.0002	0.0005	0.16	0.15	0.15	0.14
	SD (sr^{-1})	0.0001	0.0001	0.0002	0.0001	0.0002	0.08	0.08	0.08	0.07
	r^2	0.99	0.98	0.97	0.96	0.83	0.98	0.98	0.96	0.88

ASD1 vs. 2: before and after the residual correction (RC); ASD2 vs. 3: before and after the quality control (QC); ASD3 vs. 4: before and after the bidirectional correction. UPD is the unbiased percent difference; RPD* the absolute relative percent difference; RMSE the root mean square error, SD the standard deviation and r^2 the determination coefficient of the regression analysis.

The QC scheme aimed to diminish the distortion in the blue-green spectral region caused by residual contaminating sources, as well as, the effects of illumination mismatches. The overall differences after applying the QC, however, were not very high with 3-4% RPD* for the bands and 0.6-2.5% for the ratios (Table 5.2). In a case by case analysis, however, for some stations the QC was very effective in eliminating contaminated spectra, due especially to the illumination variation artifacts (as shown in Figure 5.2). The use of the mean $R_{rs}(400)$ as the reference for the QC was a conservative choice, as the minimum value could encompass less spectrally contaminated spectra due to the residual sources. Nonetheless, as some artifacts caused by illumination variation also caused unrealistic lower R_{rs} values, the use of the minimum value could lead also to underestimations of the true R_{rs}. Another important point to highlight is that filtrations schemes based solely on the NIR bands (as in Hooker et al. (2003)) would not work under such conditions of high illumination variation, as the highest biases caused by this artifact occurred at the shorter bands (Figure 5.2).

The correction for bidirectional effects was somewhat higher for the 555 band, especially for the stations with higher Chl*a* (>1 $mg.m^{-3}$) with an overall 8% RPD*. The *f*/*Q* ratio is in fact highest at 560 nm for increasing Chl*a* (>0.3 $mg.m^{-3}$) (MOREL et al., 2002). The BD correction made a difference of 2.5% for the band ratios, indicating some importance of this correction not only for straightforward comparisons of R_{rs}, but also for bio-optical modeling and vicarious calibration. The bidirectional correction was mostly important for the stations with high SZA and Chl*a* which were in the PAT (St 61-76). Morel and Gentili (1996) and Morel et al. (2002) made extensive discussions on the effects of the R_{rs} bidirectionality and variations of the *f*/*Q* ratio with Chl*a*, SZA, wavelength and sensor-viewing angles. Lee et al. (2004) and Park and Ruddick (2005) discuss these effects not only on terms of Chl*a* but directly in relation to the IOPs (*a* and b_b). The higher the concentration and particle size, the higher the anisotropy of the volume scattering function (VSF). The illumination conditions with higher SZA and sensor-viewing angles also usually correspond to higher *f*/*Q* values. This is why this correction is especially important for non-nadir-viewing instruments and measurements at high SZA (high latitudes, early morning or late afternoon).

5.3.3. In-water approach

For the in-water HOCR approach the uncertainties involving solely the differences between casts (with subsequent measurements) were in order of 10.3-12.1% RPD* (0.0003-0.0007 sr^{-1} RMSE), with 0.35-0.91 r^2 for the OCR bands, characterizing significant environmental disturbance. These differences are more characteristic of random noises that mostly depend on short time scale variations, such as illumination variations due to broken clouds (and the local displacement of the profiler and deck sensors), intermittent bubble clouds generated by breaking waves, wave focus and defocusing effects on the downwelling rays and the number of sampled points at each depths due to tilt variation and the descending rate. The second cast (B) had usually a smoother profile, denoting less noise effects. The first cast may usually be more "chaotic", while the second may have a better distance from the platform, avoiding disturbances from the platform, and starting with a more stable position on the surface to profile (with less tilt effects). The positive and negative biases were equally distributed among the stations, although with a slight tendency of the first cast to

provide lower values than the second, with a 0 to -3.8% UPD (Figure 5.3). The random effects may actually influence both casts in different ways, and the use of two or more casts to obtain a final averaged R_{rs} is thus, recommended to normalize as much as possible the environmental effects. These effects were lower for the band ratios (4-8% RPD*) showing that some environmental noises may be spectrally correlated and the use of ratios may also normalize some of these effects.

Table 5.3 shows the comparisons of the different casts using solely $R_{rs}(E_d)$ for simplicity. When using E_S from the deck sensor the differences in the R_{rs} between casts were slightly higher (in order of 2%). This may indicate that some environmental variabilities within the casts could have similar effects on both L_u and E_d, and the ratio of these two quantities could normalize some of the noises (e.g., in-water perturbations), as discussed by Mitchell and Kahru (1998). Under high illumination variation conditions the local displacement of the profiler and deck sensors would also be a source of uncertainty enhancing the biases and differences between casts when using E_S.

Table 5.3 - Statistical differences between the HOCR R_{rs} processing steps.

		λ412	λ443	λ490	λ510	λ555	412/555	443/555	490/555	510/555
$R_{rs}(E_d)$	RPD*(%)	11.7	12.0	12.1	11.3	10.3	7.9	6.7	5.3	4.0
A vs.	RMSE(sr^{-1})	0.0007	0.0006	0.0006	0.0005	0.0003	0.27	0.22	0.16	0.09
B	SD(sr^{-1})	0.0004	0.0004	0.0003	0.0003	0.0002	0.15	0.12	0.08	0.05
N=18	r^2	0.91	0.90	0.82	0.56	0.35	0.95	0.96	0.96	0.95
$R_{rs}(E_d)$	RPD*(%)	11.68	11.7	11.5	11.3	11.4	5.1	4.2	2.8	1.9
D1 vs.	RMSE(sr^{-1})	0.0007	0.0007	0.0007	0.0006	0.0004	0.25	0.20	0.13	0.06
D2	SD(sr^{-1})	0.0004	0.0004	0.0004	0.0003	0.0002	0.14	0.11	0.08	0.04
N=20	r^2	0.90	0.89	0.79	0.59	0.77	0.97	0.97	0.97	0.98
$R_{rs}(E_d)$	RPD*(%)	6.5	6.5	6.3	6.1	6.0	3.3	3.0	2.3	1.6
vs.	RMSE(sr^{-1})	0.0005	0.0005	0.0004	0.0004	0.0002	0.09	0.08	0.06	0.03
$R_{rs}(E_S)$	SD(sr^{-1})	0.0003	0.0003	0.0002	0.0002	0.0001	0.05	0.05	0.04	0.02
N=20	r^2	0.96	0.95	0.90	0.83	0.95	1.00	1.00	1.00	1.00

A and B stands for the first and second casts; D1 and D2 for the extrapolation depths and $R_{rs}(E_d)$ when using E_d from the profiler and $R_{rs}(E_S)$ when using the deck sensor. The second variable was always used as the reference (as in Figure 5.3).

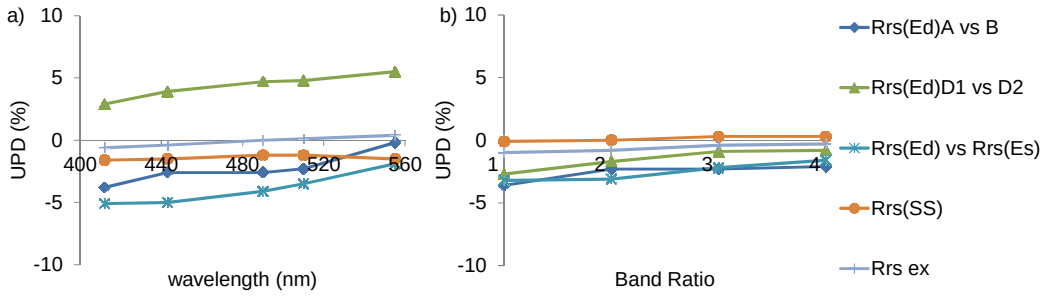

Figure.5.3 - Unbiased percent difference (UPD) of the ocean colour bands (a) and ratios (b) (1= 412/555; 2= 443/555; 3= 490/555; 4=510/555) for the HOCR R_{rs} processing. A and B are the different casts; D1 and D2 the depth intervals; E_d and E_S, the downwelling irradiance of the deck and profiler sensors; *SS* the self-shading correction and *ex* the bidirectional correction.

The different depths interval used for the extrapolation of L_u and E_d to surface also accounted for significant differences on the R_{rs}, with 11.2-11.6 % RPD* (0.0003-0.0007 sr^{-1} RMSE) (Table 5.3). The r^2 was relatively high for all bands (0.59-0.92) denoting a more "systematic" bias, with a tendency of overestimation of R_{rs} using shallower depths (2.6-5.6% UPD) (Table 5.3 and Figure 5.3a). In this case, using $R_{rs}(E_S)$ the differences were practically the same compared to $R_{rs}(E_d)$. Shallower depths are preferred for the extrapolation procedure when the environmental conditions are favorable with low winds and waves. However, most of the stations were held under rather adverse environmental conditions (U>5 $m.s^{-1}$ and WSH>2 m), and shallower depths were usually much noisier under such conditions. Bubble clouds can occur up to 7 m deep for winds ~ 10 $m.s^{-1}$ and can increase the R_{rs} by a factor of 2, especially for the shorter spectral bands (green and yellowish) (STRAMSKI; TEGOWSKI, 2001). The focus and defocusing effects on the downwelling rays caused by the wavy facets of the sea surface, is also a high source of uncertainty especially for E_d at shallower depths, and with rough seas (HOOKER et al., 2002; MUELLER et al., 2003). The wavy facets deflect the downwelling rays, and rays coming from a greater area of the sea surface may reach the sensor and enhance the measured E_d, ultimately overestimating E_d (0^+). This may explain the lower r^2 for the 555 nm band in the A vs. B and D1 vs. D2 comparisons. The longer bands are more affected by random effects, due to the

proportion of direct light, as the increasing water absorption diminishes the proportion of diffuse light (STRAMSKA; DICKEY, 1998).

The problems of using greater depths, on the other hand, regard the assumptions of the homogeneity of the water column and a constant K_d within the extrapolated interval, as well as the increasing effects of Raman scattering. The two last are more drastic for longer wavelengths due to the exponential increase of water absorption (beyond 500 nm), and consequent decrease of the light penetration in the water column. The loss of photons due to absorption decreases the downwelling irradiance average cosine (μ_d) along the optical path, which in turns increases K_d ($\approx a/\mu_d$) (MOBLEY, 1994). The lower signal also favors an increasing contribution of Raman scattering, which becomes significant for wavelengths longer than 500 nm at depths greater than 10 m (LOISEL; STRAMSKI, 2000). Since the comparisons were only for bands up to 555 nm, and most of the D2 intervals were still not very deep (between 5-12 m), Raman scattering was not expected to have significant effects, and no specific correction was applied. Only for a few stations with noisier profiles due to stronger winds (>10 $m.s^{-1}$), the D2 encompassed greater depths (but still never exceeding 20 m). The K_d variation with depths was also not expected to be much significant due to the same reasons, although slight effects could promote greater bias for the 510 and 555 nm bands, using depths greater than 10 m. This was actually noticed in the extrapolated $E_d(0^+)$ when there was either a higher or lower shift of the spectra beyond 500 nm (data not shown).

The effects of using different depth intervals (D1 and D2) on the band ratios were rather low with a RPD* of 2-5% (Table 5.3 and Figure 5.5). The spectrally correlated biases were normalized with the band ratios, however some spectrally dependent sources were still present. The differences that remained could be due to the spectral biases associated with each of the intervals used. The shallower depths may have spectrally dependent effects of bubble clouds, with higher R_{rs} especially for the yellowish-green bands (490-555 nm) (PISKOZUB et al., 2009), which diminish the ratios. This would explain the slightly negative biases for the D1 ratios (as shown in Figure 5.3b). The deeper interval (D2), on the other hand, could retrieve some lower R_{rs} values for the longer spectral bands due to the increasing K_d, overestimating the ratios. The Raman scattering, if significant, would cause the contrary enhancing the R_{rs} values at longer wavelengths,

which was not the case. The biases for the ratios were only 1% lower using $R_{rs}(E_S)$. All these effects cause variabilities in both E_d and L_u, but in somewhat greater proportions for E_d, what may explain the slightly higher differences for the R_{rs} ratios when using E_d, rather than E_S. In resume, the shallower depths retrieved higher R_{rs} which were most likely due to noisier profiles and to greater effects of bubble clouds. Hence, D2 was considered the best procedure, although some spectral biases may also be associated with this approach (i.e., Raman scattering and K_d variation).

The differences in using E_d or E_S to obtain R_{rs} accounted for 6 % RPD* (0.0002-0.0005 sr^{-1} RMSE) for the bands and 1.6-3.3% for the ratios (Table 5.3). The $R_{rs}(E_d)$ tended to retrieve lower R_{rs} values with -2 to -5% UPD (Figure 5.3), which could indicate less biased values, as the main sources of noise tend to increase R_{rs}. The E_d is certainty more affected by greater sources of uncertainty of in-water perturbations than E_S. However, as the L_u may also be affected in similar ways to these contamination sources, the use of E_d to normalize L_u would smooth out some of these noises (MITCHELL; KAHRU, 1998). The E_S, on the other hand, did not have any of these in-water perturbations and extrapolation problems, but some uncertainties were likely associated with the platform tilt (pitch and roll), illumination variations due to broken clouds and local displacement of the sensors. Both retrievals are therefore biased in different ways, and the choice of one or the other (or the average) will depend on the environmental conditions and variability of the data set.

In respect to the self-shading effects the differences on the R_{rs} were only 1 to 1.5% RPD* (0.0001 sr^{-1} RMSE), with slightly higher values after applying the correction (Figure 5.3). This effect was slightly higher for the 555 nm band due to the greater attenuation caused by water absorption. The band ratios had insignificant differences (<1%). The low effects of this correction scheme for the present analyses is mainly because of the small geometrical radius of the HOCR and due to the mostly clear waters sampled in the MV1102. Because of such low effects observed for similar instruments, some ocean colour research groups have chosen to not apply the SS correction, on the bases that while applying such a correction scheme one may introduce other uncertainties, which is not worthwhile when the benefit is low (MITCHELL; KAHRU, 1998). In highly absorbing mediums with high phytoplankton biomass and CDOM,

however, this correction will be more significant, especially for the blue spectral bands, with higher shading effect of the instrument on the upwelling radiance (GORDON; DING, 1992). Instruments with larger radius will also have greater effects and thus, one needs to analyze carefully the importance of this correction for particular applications, when deciding to apply it or not. In the present work the three in-water instruments had small physical diameters and sampled under mostly low to intermediate Chl*a* waters, so the SS correction was not so important. Only for the stations with higher Chla (>3 $mg.m^{-3}$) at the Patagonian Shelf and the turbid waters of the Magellan Strait, the SS made a greater difference (~ 4%, RPD* at $R_{rs}(412)$). A limitation of the correction applied in the present work was that a constant correction factor was applied and the variations of the shelf-shading effects with depths were not accounted. Nonetheless, as solely depths up to 20 m were used for the extrapolations of all in-water approaches, and the longest band evaluated was 555 nm, such effects were likely minor.

The BD effects were the lowest with less than 1% RPD* for both bands and ratios. For nadir viewing instruments this effect only depends on the Chl*a* and SZA. The SZA was considerably high for most cases (~50^{o}) (Table 5.1), nevertheless, most of these stations were also held under overcast conditions, which characterize a more uniform sky radiance distribution, minimizing the SZA effects. The BD effect was highest (5% RPD*) for station 76 with the highest Chl*a* (4.8 $mg.m^{-3}$) and SZA (59^{o}).

Regarding the PRR and TriOS approaches only the differences between $R_{rs}(E_d)$ and $R_{rs}(E_S)$ were analyzed since there was only one cast per station for these instruments, and the SS and BD effects were similar for the three in-water approaches. For the PRR the differences were of 9 to 10% RPD* (0.0004-0.0006 sr^{-1} RMSE) for the bands, with an overall tendency of overestimation (5% UPD) using $R_{rs}(E_d)$ (Table 5.4). This could indicate slightly higher uncertainties related to the $R_{rs}(E_d)$, caused by $E_d(0^+)$ underestimations, in the PRR data set. This is contrary to the differences observed for the HOCR, in which $R_{rs}(E_d)$ was usually lower than $R_{rs}(E_S)$. Such comparisons highlight the sensitivity of these measurements and the challenge to predict the bulk effects of the environmental variability for the in-water and deck sensors during a cast, as well as to define the most accurate procedure. As the HOCR used more than one cast and had a more "controlled" scheme for the choice of the extrapolation depths, one could suppose

that it may have provided more accurate R_{rs} measurements compared to the PRR. Anyhow, as it may be difficult to predict these environmental effects, the use of both quantities ($R_{rs}(E_d)$ and $R_{rs}(E_S)$) may more be desirable rather on relying on just one.

The TriOS approach had a low number of stations (N=13) due to some logistics problems with its deployment in the beginning and end of the cruise (e.g. ship orientation) (Table 5.1). The differences between $R_{rs}(E_d)$ and $R_{rs}(E_S)$ were the highest with 25-30% RPD* (0.0005-0.0010 sr^{-1} RMSE), with a systematic overestimation of $R_{rs}(E_d)$ (17-23% UPD) (Table 5.4), denoting some high uncertainties on either one of the quantities for the TriOS approach.

Table 5.4 - Statistical differences between the TriOS and PRR $R_{rs}(E_d)$ and $R_{rs}(E_S)$.

		λ 412	λ 443	λ 490	λ 510	λ555	412/555	443/555	490/555	510/555
PRR	UPD(%)	5.4	5.5	4.3	4.6	5.1	0.3	0.4	-0.8	-0.5
$R_{rs}(E_d)$	RPD*(%)	8.9	9.0	9.0	9.5	10.5	3.6	2.7	1.9	1.2
vs.	RMSE(sr^{-1})	0.0005	0.0006	0.0006	0.0006	0.0004	0.05	0.04	0.04	0.02
$R_{rs}(E_S)$	SD(sr^{-1})	0.0003	0.0003	0.0003	0.0003	0.0002	0.03	0.02	0.02	0.01
N=18	r^2	0.96	0.94	0.90	0.87	0. 91	0.96	0.94	0.90	0.87
TriOS	UPD (%)	23.6	21.2	20.0	19.3	17.3	6.3	3.8	2.7	2.0
$R_{rs}(E_d)$	RPD*(%)	29.73	28.0	26.2	25.7	24.9	11.79	12.0	7.0	3.7
vs.	RMSE(sr^{-1})	0.0010	0.0008	0.0008	0.0007	0.0005	0.14	0.13	0.09	0.05
$R_{rs}(E_S)$	SD(sr^{-1})	0.0005	0.0004	0.0004	0.0004	0.0003	0.07	0.06	0.05	0.03
N=13	r^2	0.83	0.79	0.72	0.89	0.65	0.98	0.98	0.99	0.99

When comparing the R_{rs} of the different approaches, the TriOS $R_{rs}(E_d)$ was closer to the HOCR, PRR and ASD, while the TriOS $R_{rs}(E_S)$ was much lower (>50%). At some stations simultaneous measurements of E_S with the TriOS, HOCR and PRR deck sensors were taken and the RPD* was 4 to 6% (from 400-700 nm), showing a good match for the deck sensors, within calibration uncertainties (HOOKER; MARITORENA, 2000). One reason that could explain the lower TriOS $R_{rs}(E_S)$ is related to the deployment method. The winched profiler is deployed right beside the ship superstructure and the sensor is much more subjected to platform shading and in-water perturbations, which may cause lower R_{rs} values for this approach (HOOKER; MARITORENA, 2000). Stations 129, 130 and 134 were even discharged from the

analysis as they had clearly high platform shading effects, due to ship disorientation in respect to the solar plane. Another reason could be due to the extrapolation procedure. Since the TriOS measurements were taken at discrete depths (every 2-4 m) and the entire profile from 5-40 m was used for the K_d estimation, and 5-20 m for the extrapolation of E_d and L_u, this method was likely more affected by noises of lower signal and biases of using a constant K_d. As E_d and L_u are affected in similar manners for all these effects, using both quantities would normalize some of them, whereas, normalizing L_u with E_S would amplify the biases related to L_u. Hence, in this case, we considered $R_{rs}(E_d)$ much less biased.

Based on the uncertainty analyses, the final R_{rs} for each approach was obtained in the following manner: for the HOCR only the second extrapolation depths was used (D2), while the casts (A and B) and the $R_{rs}(E_d)$ and $R_{rs}(E_S)$ were averaged, since the differences were reasonably low, and as each set is influenced by different environmental effects, the average was considered a reasonable approach to smooth some of these variations. The same procedure was applied for the PRR (averaging $R_{rs}(E_d)$ and $R_{rs}(E_S)$). For the TriOS, as the differences were so high and there were evidences of higher biases associated with the $R_{rs}(E_S)$, only the $R_{rs}(E_d)$ was used for the final R_{rs}. All quantities used the same BD and SS corrections.

5.3.4. Instrument Inter-comparisons

To analyze the overall differences between the instruments, the HOCR was used as a reference to compare all the others: ASD, PRR and TriOS, using the final R_{rs} obtained for each approach (Table 5.5 and Figure 5.4). The HOCR was chosen as reference because the free-falling profiler is considered one of the least biased approaches for *in situ* radiometry (HOOKER; MARITORENA, 2000) and it was measured with more than one cast, diminishing the environmental noises.

The PRR had an RDP* of 12 to 14% (0.0004-0.0007 sr^{-1} RMSE) with a slight tendency of overestimation, especially for the 510 and 555 nm bands (9 and 6% UPD). The r^2 was high (0.72-0.99) denoting a good consistency between the two instruments. The ratios had 4-6.5% RPD*, with underestimations for the 412-490/555 ratios and a slight overestimation of the 510/555 ratio (Table 5.5). The PRR overestimations were

associated with the stations with most adverse environmental conditions. St 19 had the highest difference with 31% UPD at 510 nm, and was the station with strongest winds (13 $m.s^{-1}$) and highest waves (2.6 m) (Table 5.1). Stations 32 and 56 had 23 and 29% UPD and were stations with heavy fog conditions, in which the low E_d levels could have caused higher biases in the R_{rs} measurements. St 130 had a 22% UPD and was a station with high illumination variation, with broken clouds, and a more stratified vertical profile (Table 5.1). Since there was a more rigorous quality control for the HOCR data set, with a criterion selection of the extrapolation depths interval (with the highest r^2 in the interval of 5-20 m, as explained in section 4.4.2), the PRR approach may have overestimated the R_{rs} values due to the higher effects of environmental biases. An evidence of this was that the differences between $R_{rs}(E_d)$ and $R_{rs}(E_S)$ was much lower for the HOCR than the PRR, especially at the stations this most adverse conditions e.g., St 19 had 1 and 9% RPD*, for HOCR and PRR, respectively. The higher positive bias for the PRR 510 nm band could be caused by a higher influence of bubble clouds at some stations, as a shallower depth interval was generally used for the extrapolation procedure in the PRR approach.

Table 5.5 - Statistical differences between the approaches using the HOCR as reference for each comparison (PRR, TriOS and ASD).

		λ 412	λ 443	λ 490	λ 510	λ555	412/555	443/555	490/555	510/555
	UPD(%)	-0.1	1.7	4.3	8.7	6.2	-6.3	-4.4	-1.9	2.6
	RPD*(%)	12.0	12.7	12.4	14.2	12.2	6.5	5.3	3.3	3.9
PRR	RMSE(sr^{-1})	0.0007	0.0007	0.0007	0.0007	0.0004	0.20	0.11	0.07	0.07
	SD(sr^{-1})	0.0003	0.0003	0.0003	0.0004	0.0004	0.10	0.06	0.04	0.04
N=19	r^2	0.91	0.90	0.84	0.72	0.99	0.99	0.99	0.99	0.99
	UPD(%)	-27.2	-29.2	-25.8	-26.7	-18.9	-8.5	-10.7	-7.2	-6.0
	RPD*(%)	26.5	27.2	24.3	25.2	19.4	9.3	10.2	8.7	7.6
TriOS	RMSE(sr^{-1})	0.0013	0.0011	0.0010	0.0009	0.0005	0.19	0.18	0.15	0.13
	SD(sr^{-1})	0.007	0.006	0.0005	0.0005	0.0003	0.09	0.07	0.08	0.07
N =12	r^2	0.77	0.80	0.77	0.65	0.53	0.96	0.96	0.95	0.95
	UPD(%)	8.4	9.3	10.7	9.1	12.8	-4.4	-3.5	-2.2	-3.8
	RPD*(%)	21.25	19.0	15.2	12.0	15.1	12.66	10.2	6.1	4.5
ASD	RMSE(sr^{-1})	0.0009	0.0008	0.0007	0.0005	0.0004	0.31	0.23	0.16	0.10
	SD(sr^{-1})	0.0005	0.0004	0.0004	0.0003	0.0003	0.15	0.11	0.08	0.05
N =17	r^2	0.86	0.87	0.86	0.80	0.94	0.97	0.97	0.97	0.97

Both PRR and HOCR are free-falling profilers and have the advantage to drift away from the platform avoiding perturbations from the superstructure (HOOKER; MARITORENA, 2000). Thus, it is expected for these two approaches to have a very close agreement. The differences should desirably be lower than 5%, as encountered in other works (HOOKER; MARITORENA, 2000). The present work had some higher differences, however, considering that just the variability between casts for the HOCR accounted for 10-12% RPD* (Table 5.2), the differences between the PRR and HOCR were very close to this range (13-14%). Most of the uncertainty between these approaches was therefore associated with environmental variabilities that affect both instruments. An important point to highlight, though, is the choice of the extrapolation depths that is a critical step for the in-water approach and could account for differences up to 12% or more, as shown herein. This effect is actually difficult to evaluate between the approaches, since they are different profiles and the choice of the depths is still performed in a subjective manner, analyzing each profile to selecting the best interval. A criterion used for the HOCR selection, based on the best r^2 fit of the $\ln E_d$ and $\ln L_u$ profiles could be a better approach than solely a visual analysis, which may have contributed for the lower R_{rs} values for the HOCR. There was also an attentive care to use depths higher than 5-7 m to avoid bubble clouds, which may have caused the higher R_{rs} related to the 510 nm band for the PRR. The selection of the extrapolation depths may take use of a criterion that could lead to the best choice, nonetheless, in any manner, a well-trained technician with knowledge of the physical processes and environmental issues will always be crucial for this step.

The TriOS had the highest differences with 19-27% RPD* (0.0005-0.0013 sr^{-1} RMSE), obtaining lower R_{rs} values (Table 5.5). The TriOS underestimation in relation to the HOCR (and the other approaches, PRR and ASD) could be explained by the platform shading and the use of greater depths for the extrapolation procedure. Only at St 56 the TriOS slightly overestimated the R_{rs} in respect the HOCR (but still underestimated in relation to the PRR and ASD) (Figure 5.4). The higher contribution of diffuse light due to heavy fog, could have contributed to less platform shading effects for the TriOS, obtaining higher R_{rs} values at this station. There could also have been some effects of bubble clouds at the surface depths, since the sea state was rather rough and as the

TriOS used 5-20 m depth interval for the extrapolation procedure, whereas the HOCR used greater depths (~18 m) at this station.

The impact of the vertical bio-optical stratification in the differences between the TriOS and HOCR was tested by determining the below-water R_{rs} using the RTE approach at each sampled depth (from 0 to 20 m), and comparing the averaged depths used in the HOCR and TriOS extrapolation procedures for each station (e.g., R_{rs}(7-12m) vs. R_{rs}(5-20m)). The overall difference averaged for all stations (and bands) was 5% RPD*, indicating a rather low impact of the bio-optical variability for the different depth interval chosen in each approach. The highest difference was for St 76 that had the most stratified condition with 22% RPD* (at 443 nm). Since the TriOS approach used a greater interval (5-20 m), it usually encompassed depths within, or closer to, the Fl_{max} (Table 5.1) (with higher a_p and a_s), which may have contributed for the lower extrapolated R_{rs} values. The HOCR, on the other hand, used depths closer to the first optical depth (usually ~5-12 m) which was more homogeneous and representative of the depth relevant for above-water OCR. Of course this test was only a rough approximation since the bio-optical measurements were obtained only at 4 depths within the upper layer (1-100 m). Anyway, it was a mean to analyze the possible impacts of the bio-optical variability on the R_{rs} at different depths, independent of other noises and biases affecting the instrument measurements.

Another source of uncertainty for the TriOS approach could be on the K_d determination for the extrapolation procedure as a higher depth interval was used (5-40 m). Analyzing the continuous K_d data set from the HOCR, the potential differences in the K_d where actually difficult to verify as the depths higher than 20 m had noisier profiles for most stations. Nevertheless, it was possible to observe a co-varying change in the K_d following the fluorescence profile, with its maximum coincident to the Fl_{max}. Averaging the entire profile from 5-40 m, it usually still provided close K_d values to the HOCR approach. The K_d increase with depth likely due to the decreasing μ_d, was only observed for bands longer than 600 nm (for depths up to 40 m). Hence, the K_d variation did not seem significant for the present analysis. The most important source of differences between the HOCR and TriOS data sets were thus, likely caused by the shading effects of the ship superstructure, causing the lower TriOS R_{rs} values. One point to mention

however, is that although the HOCR used depths greater than 5 m to avoid the effects of bubble clouds, some residual effects may have persisted, especially for stations under high winds and waves and lower Chl*a*, for which the bubble scattering contribution is highest (STRAMSKI; TEGOWSKI, 2001; PISKOZUB et al., 2009). This may have also caused some overestimations of the R_{rs} HOCR (as well as, for the PRR and especially ASD). Using greater depths, the TriOS may have avoided more effectively the bubble clouds. Nevertheless, despite the higher differences between the bands, the ratios had much lower biases with an RPD* only up to 10%, indicating that the main biases between the HOCR and TriOS approaches were spectrally correlated, and effectively minimized for the ratios.

Regarding the above-water approach, the ASD RPD* ranged from 12-21% (0.0004-0.0009 sr^{-1} RMSE) with a tendency of overestimation in respect to the in-water HOCR (Table 5.5). The band ratios had lower differences with 4.5-12.6%, increasing for the ratios with the shortest bands (412/555). This increase was observed for all approaches, denoting the effects of some spectrally dependent biases. For the above-water approach these spectral effects with higher R_{rs} for the shorter bands are likely caused by under-corrections of sky, cloud and/or sun glint (MOBLEY, 1999), platform reflection (HOOKER; MOREL, 2003), presence of whitecaps (FROUIN et al., 1996) and in-water bubble clouds (PISKOZUB et al., 2009; STRAMSKI; TEGOWSKI, 2001). While most sources usually cause an increase in the R_{rs} towards the shorter spectral bands, some sources such as the platform reflection on the sea surface may have a higher impact on the 510 and 555 bands (depending on the paint colour) (HOOKER; MOREL, 2003). Bubble clouds also cause a peak of higher R_{rs} at the green and yellowish bands (490-555 nm), which may have contributed to a higher positive UPD for the 555 band (as for the PRR, Table 5.5). The contribution of the bubble clouds to the R_{rs} will vary with the concentration and size distribution of the bubbles, distance to the cloud core, presence of adsorbing organic compounds (interacting with the bubbles), and the IOP concentration (with higher effects for lower Chl*a* waters) (STRAMSKI; TEGOWSKI, 2001; PISKOZUB et al., 2009). With such complex interactions it is difficult to effectively identify these effects in *in situ* measurements, but some evidences may be pointed out in the present analyses. This effect should be highest for the above-water

approach, as the in-water approaches used depths usually greater than 5 m, contributing for the ASD R_{rs} overestimations.

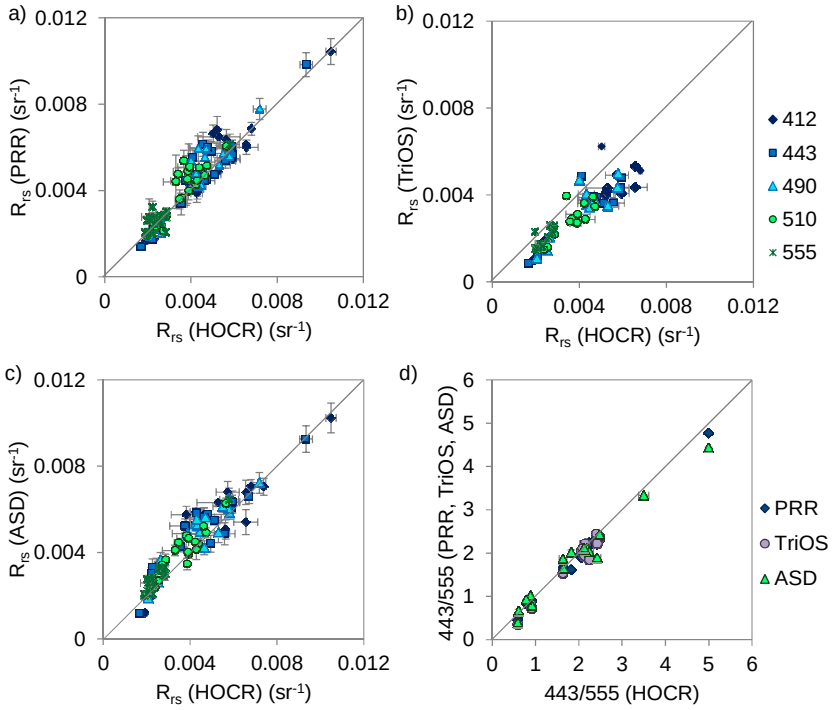

Figure 5.4 - Comparison of the HOCR R_{rs} with the PRR (a), TriOS (b), ASD (c), and the 443/555 ratio of all instruments (mean and standard deviation).

Despite of all sources of uncertainties listed above, and the mostly adverse environmental conditions faced during the MV1102, the above and in-water approaches had reasonable matches, within expected differences encountered in previous works that compared similar approaches (HOOKER; MARITORENA, 2000; TOOLE et al., 2000). Even with some relatively high differences (>20%), all the instruments had high r^2 values for both the spectral bands and ratios (Table 5.5 and Figure 5.4), showing a strong covariation of the biases. Most of the differences were also within the standard deviations of each approach, which was usually high due to the environmental effects (between casts, and E_d and E_S) (Figure 5.4).

To summarize the relations between the uncertainties of the measured R_{rs} with the environmental conditions, a non-parametric Spearman correlation analysis was made with the RPD* of the different approaches. The above-water ASD had some correlation with the wind speed (r_s=0.21), illumination variation (r_s =0.21) and Chl*a* (r_s =0.58). No specific condition seemed to govern the biases, however the combination of adverse conditions lead to the highest uncertainties. Such as for St 61 with high illumination variation (70% CC), wind speeds (~11.5 $m.s^{-1}$), Chl*a* (1.5 $mg.m^{-3}$) and vertical bio-optical stratification (Table 5.1). The other stations with high uncertainties had either higher Chl*a* and bio-optical stratification (St 76), heavy fog (St 56), illumination variation (St 51, 129-134) or the combination of such conditions. Wind speed effects seemed to be more drastic when higher than 10 $m.s^{-1}$ with partially clouded skies (St 61 and 134). The PRR and TriOS RPD* did not correlate with any environmental condition, showing a lower dependency of the in-water approaches with the environmental variability. With only a few data points, especially for the TriOS (N=12), it was actually difficult to analyze significant correlations between the biases and environmental conditions. Nonetheless, looking at a case by case analysis, the highest biases for the TriOS (>40% RPD*) were at the stations with strongest bio-optical stratification (St 75 and 76) in the PAT, and with the combination of intensive winds (7.8 $m.s^{-1}$), wave height (2.4 m) and illumination variation (St 51). Wind generated bubble clouds and wavy facets had minor effects on this approach due to the higher depths used in the extrapolation procedure, whereas waters with higher Chl*a* caused higher uncertainties due to the light attenuation and vertical stratification.

The differences between the instruments and approaches were higher than the 5 % recommended by the SeaWiFS protocol for accurate *in situ* R_{rs}. Nonetheless, most of the inter-comparison studies that achieved this goal used highly controlled schemes with instrument inter-calibration, the exact same data processing code, held under mostly favorable environmental conditions (clear skies and low winds) and for predominantly Case 1 waters or moderately complex waters (HOOKER; MARITORENA, 2000; ZIBORDI et al., 2009). Under more diverse conditions and embracing also more eutrophic and turbid coastal waters, Toole et al. (2000) found similar and even higher differences between the above and in-water approaches (up to 44%). A recent work of Lee et al. (2013) comparing in-water free falling profilers and a new above-water

approach with a blocking cone from reflected skylight, also showed 8-20% UPD in the 400-555 nm range, being the highest for the shortest bands, with measurements in optically complex inland waters, but with mild environmental conditions (Lake Michigan, USA).

For the present work, since the main object was to evaluate the bulk uncertainties related to *in situ* radiometry obtained in a realistic framework of an oceanographic cruise, each set of instruments was independently calibrated and processed by different ocean colour laboratories. Considering the small number of stations encompassing highly differing environments from oceanic to coastal eutrophic and turbid waters, and mostly adverse environmental conditions, with moderate to strong winds and high illumination variation, the overall differences were actually reasonable. The uncertainties associated to environmental variabilities within the approaches were almost as high as between each other. The highest uncertainties were related to the winched profiler (TriOS), most likely due to higher effects of platform shading and uncertainties in the extrapolation procedure with greater depths. Whereas, for the above-water approach the biases were mostly related to cloud glint, illumination variation and bubble clouds. Since all approaches had some degree of biases affected by different environmental sources, a final merged R_{rs} averaging all instruments was used to smooth the main variations and obtain a least biased R_{rs}, namely INS. Since some stations had a high SD due to more adverse environmental conditions, a quality control scheme was applied withdrawing the measurements that had a CV ≥15% for all bands in the merging process to obtain final R_{rs}. The final INS, thus, comprehended 2-4 different measurements (from the approaches) and the mean SD was 0.0004-0.0005 sr^{-1}, with a mean CV of 11.0 to 12.7% (Table 5.6). Since the band errors were mostly correlated the band ratios had lower CV with 3.6-5%.

Table 5.6 - Mean standard deviation and coefficient of variation (%) of the INS for the ocean colour bands and ratios.

		λ 412	λ 443	λ 490	λ 510	λ555	412/555	443/555	490/555	510/555
INS	SD	0.0005	0.0005	0.0005	0.0004	0.0004	0.10	0.08	0.07	0.06
	CV (%)	12.5	12.7	12.4	12.1	11.0	4.9	4.3	3.6	3.7

5.3.5. Measured versus modeled R_{rs}

The final merged INS R_{rs} was compared to the modeled R_{rs} with the RTE and MM01 approaches, as a closure experiment. Before applying the RTE and MM01, however, one needs to access the uncertainties regarding the IOP and Chl*a* used as input for these models. Some uncertainty analyses were thus also conducted for these data sets.

5.3.5.1. IOP uncertainties

The RPD* for the particle absorption coefficient (a_p443) duplicates was 4%, characterizing a close match and good consistency. The phytoplankton (a_{phy}) and, especially, detritus absorption coefficients (a_d) duplicates had some higher differences with 6% for $a_{phy}443$ and 31% for a_d443. The higher differences for a_d443 were likely due to inefficiencies of the pigment extraction procedure and the generally low signals especial for low Chl*a* waters. The solvent used for the extraction procedure was 100% methanol which is known to be a very efficient pigment extractor (WASMUND et al., 2006). However, some phytoplankton groups have hard cell walls that make this procedure more difficult and time consuming (requiring a much longer extraction time), such as, cyanobacteria and green algae. Some pigment features were thus, still observed in the a_d spectra even after 3 hours of extraction. An exponential fit was thus applied for the a_d spectra to remove these features. The spectral slope (S_d) was determined using a non-linear regression fit within the interval of 300-700 nm, but taking out the intervals with pigment residual contaminations (i.e. 320-365; 380-520; 640-700 nm) (Figure 5.5), as recommended by Bricaud, et al. (2010). The reference band used to derive the fitted spectra was centered at 525 nm (λ_0). The exponential fit for the a_d spectra followed the expression:

$$a_d(\lambda) = a_d(\lambda_0)\exp(-S_d(\lambda - \lambda_0)) \quad (5.5)$$

The a_{phy} was then recalculated subtracting the adjusted a_d from the measured a_p.

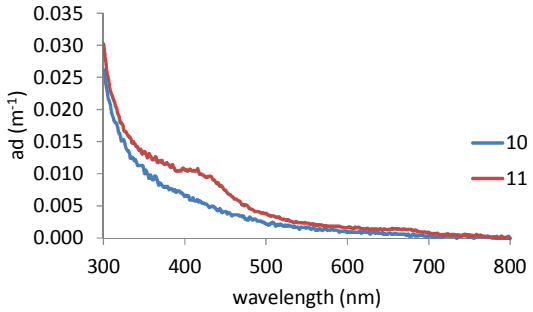

Figure 5.5 – a_d spectra of a station with (11) and without (10) residual pigment contamination.

The CDOM absorption (a_s) is also a highly sensitive measurement due to the low values encountered in oceanic waters, and had a mean percent difference of 18% for the 443 band. The highest RPD* values were for the stations with clearest waters (St 03 to 06). An exponential fit was applied only for values below 0.005 m^{-1}, which is in the limit of instrument accuracy (Cary-50, with a 10 cm cuvette). The a_s slope was determined within the interval of 380-550 nm and the fit followed the same expression as in Equation 18, changing the reference band to 443 nm. Whenever the differences between replicates exceeded 10% a perceptive analysis of possible outliers was performed, comparing depths and stations with similar bio-optical characteristics.

There is a limitation intrinsic to the a_p and a_s standard methods that does not consider the contribution of particles between 0.7 and 0.2 µm that are "lost" in the filtration process, as the a_p uses a 0.7 µm filter pore, and the a_s 0.2 µm. Nevertheless, the contribution of this submicron detritus fraction is considered negligible for the total biogenic absorption, and thus, it is a common sense to ignore its contribution (MITCHELL et al., 2003). The absence of this fraction should cause an overestimation of the RTE R_{rs}, which was not the case, as will be further shown.

The pure seawater absorption coefficient also has some uncertainties associated with the measurements published in literature, especially for wavelengths shorter than 420 nm, due to difficulties in obtaining highly purified samples and accurate measurements with low detection limits (MOREL et al., 2007). Further improvements on these analyses are recommended as measurements in ultraoligotrophic waters revealed twice as lower

values than pure water coefficients as reported by Morel et al. (2007). Nonetheless, for the interval used in the present work (412-555 nm), the values proposed by Pope and Fry (1997) are still considered the most reliable. The uncertainties in a_w should only have significant impacts for the clearest waters, where its contribution to the total absorption is highest, and only St 06 had such oligotrophic waters with (0.13 $mg.m^{-3}$), which was still far from being ultraoligotrophic (<0.02 $mg.m^{-3}$).

To evaluate the consistency of the absorption measurements comparisons were made with data sets from previous works with equivalent Chl*a* ranges (0.13-4.8 $mg.m^{-3}$) (without considering the Magellan Strait station). The $a_{phy}443$ (0.011-0.260 m^{-1}), a_s443(0.003-0.066 m^{-1}) and $a_{cdm}443$ (CDOM + detritus) (0.005-0.082 m^{-1}) were very close to the respective ranges with a close match to the regression fits of IOP vs. Chl*a* obtained in these works (and within their dispersions) (BRICAUD et al., 2004; MOREL; GENTILI, 2009; LOISEL et al., 2010) (as shown in the following Chapter). This denotes a good consistency of the MV1102 absorption data sets. For the present work the $a_{phy}443$ vs. Chl*a* had an r^2 of 0.97, the a_s vs. Chl*a* of 0.66 and $a_{cdm}443$ vs. Chl*a* of 0.72 (with a minimum square power law fit for the regression analysis) (N=19).

Regarding the backscattering coefficient (b_b) the main sources of uncertainties are in respect to: a) calibration problems; b) the sensor response function (χ), used to weigh the volume scattering function; c) mismatches of sampled volumes due to the physical arrangement of the detectors; d) and the water backscattering coefficient b_{bw}, that may vary with temperature, salinity and the depolarization ratio (MOREL, 1974; BUITEVELD et al., 1994; TWARDOWSKI et al., 2007).

To test the consistency of the measurements in terms of some possible calibration issues, comparisons were made with measurements of pure MiliQ water in a black bucket (43 cm height and 31 cm Ø), and the theoretical b_{bw} spectra proposed by Buiteveld et al. (1994) (BT94). The effect of the reflection of the bucket walls was evaluated comparing the *in situ* profiles with bucket measurements of samples collected at corresponding depths. The matches were very close with an overall 5% CV for all bands, with exception for the 443 and 510 nm bands, which had high SDs for both bucket and *in situ* measurements (Figure 5.6a). As some stations had a perfect match between the bucket and *in situ* profile, even for the clearest waters (St 3 and 6), and

considering that there are likely other sources of uncertainties which may be even higher, such as the mis-match of sampled volumes, the contribution of the bucket wall backscattering (b_{bwall}) was considered negligible. Moreover, to perform the correction of the b_{bwall}, one would need highly purified water to use as a background for estimating its contribution, which in practice is not trivial to obtain. Hence, we chose not to apply this correction to avoid adding more uncertainties either than adequately correcting for it. Comparing the b_{bw} of MiliQ measured in the bucket with the BT94 theoretical pure fresh water spectra (for 20°C), the MiliQ had an offset of 0.00014-0.0002 m^{-1} for the 420, 470, 590 and 700 nm bands, which is within the instrument accuracy limits. The 443 and 510 nm bands however, showed unrealistic high values, just as was observed for the profiles and bucket measurements obtained along the MV1102 transect (Figure 5.6b). Despite that the HS6 used in the MV1102 is frequently calibrated by the manufacture and carefully maintained in laboratory, for some reason these two bands may have had some serious calibration problems throughout the cruise and thus had to be left out for the further analysis within the present work. The other bands however, showed a very good consistency and were used to obtain the b_{bp} extrapolated to the OCR bands using a power law exponential fit.

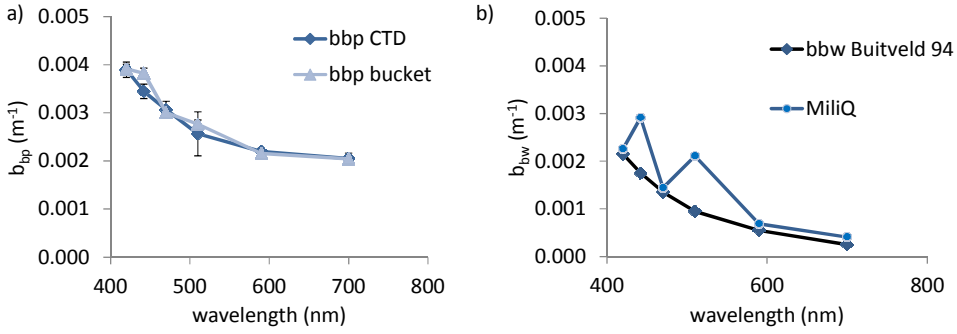

Figure 5.6 - b_{bp} measurements showing an example of a comparison of the *in situ* vertical profile of the HS6 and bucket measurement of the surface depths (below 7 m) at St 09 (a), and b_{bw} measurements of MiliQ water in the bucket compared to the Buiteveld et al. (1994) theoretical pure fresh water spectra (b).

Regarding the sensor response function, this factor is dependent on the VSF of the particles and will vary with the particle size distribution (PSD), types (refractive index) and shapes. The manufacture provides the χ with a 10% uncertainty level, averaged over a high range of coastal and oceanic Chl*a* waters. To analyze the impact of the variability of this factor for the MV1102 stations, we tested different χ values measured for different correspondent Chl*a* levels, provided by Hobilabs Inc. (1.08-1.28). The CV for the b_{bp} obtained using the different χ factors, was lower than 4%, being the highest at the station with clearest waters (St 06).

The impact of the use of different pure seawater coefficients, was evaluated comparing the standard Morel (1974) (M74) and the more recent proposed by Twardowski et al., (2007), adapted from Buiteveld et al. (1994), to adjust for salty waters (referred as BT07). The temperature range of the MV1102 stations was 7 to 20^{o}C and if accounted for the b_{bw} retrieval, it would have an impact of only 0.36% CV, using the BT07 approach. The salinity had a lower dynamic range (33-36.7), but a slightly higher impact on the b_{bw}, with a 2.3% CV. Anyhow, since these variations were low, the mean values of temperature (20^{o}C) and salinity (34.5) were considered adequate to obtain a mean b_{bw} for the MV1102 stations. The b_{bw} BT07 was determined according to the following expression:

$$b_{bw} = b_{bw0}(1 + 0.3S/37) \tag{5.6}$$

where b_{bw0} is the pure fresh b_{bw} parameterized by Buiteveld et al. (1994).

The M74 pure seawater coefficient is adjusted for 20^{o}C and 37-39 of salinity. The main differences of the M74 and BT07 are, besides the salinity adjustment, the different parameterizations of the depolarization ratios of the water molecules. The M74 uses a ratio of 0.09 while BT07 uses 0.051. The differences between the b_{bp} retrieved using either one of the b_{bw} was highest for the shortest band (420 nm) and the clearest water (St 06, 0.13 mg.m^{-3}) with 11% RPD*. For the highest Chl*a* station (4.8 mg.m^{-3}) the RPD* was 7% at 420 nm. The M74 retrieves higher b_b values and lower b_{bp}. The impact

on the RTE R_{rs} was of 2% RPD* for the 412 nm band at St 06. The M74 is extensively used for b_{bp} retrievals and is the standard default used in Hydrosoft for the HS6 data processing. The BT07 approach has been used in more recent works as it allows one to adjust the salinity factor and is based on more recent depolarization ratio measurements (TWARDOWSKI et al., 2007; STRAMSKI et al., 2008). Hence, for the present work the BT07 approach was chosen for the b_{bw} parameterization.

The sigma correction, had higher effects for the stations with highly attenuating waters with a maximum of 9% RPD* for St 76 (with 4.8 $mg.m^{-3}$ Chl*a*), whereas St 06 had a 3% RPD* at the shortest band (420 nm). Without applying the sigma correction, the b_{bp} is underestimated due to the loss of signal caused by the absorption in the pathlength between the sampled volume and the detector. A limitation for this correction is that one needs to know the Chl*a*, a_d, a_s (and their spectral slopes) to apply the correction adequately. Thus, its success will depend on the availability of such measurements, as well as their accuracy.

As a final attempt to verify the consistency of the HS6 b_{bp} data set, since these measurements are highly sensitive due to the low signals and the challenges listed above, a comparison was made with simultaneous measurements obtained from an ECO BB3 (Wetlabs Inc.) sensor attached to the HOCR profiler at each station. The differences between the $b_{bp}700$ of the two instruments were on average 4.4% (RPD*), with a slight tendency of the HS6 to retrieve higher values. The r^2 was 0.91 denoting a high covariation, which is in agreement with other works that compared the two sensors (HUOT et al., 2008; STRAMSKI et al., 2008). The differences regarding the instruments' optical configuration, measured scattering angles, calibration and data processing of the HS6 and ECO BB3 are detailed in Twardowski et al. (2007) and Stramski et al. (2008). Comparing the b_{bp} HS6 measurements with other values from literature with correspondent Chl*a* across oceanic and coastal waters (GREEN; SOSIK, 2004), the b_{bp} range was approximate, between 0.002-0.004 m^{-1} for $b_{bp}555$ (without considering St 85, which had a $b_{bp}555$ of 0.016 m^{-1} due to the presence of sediments in suspension). The $b_{bp}555$ vs. Chl*a* power law fit had a r^2 of 0.71 and was very close to the Morel and Maritorena (2001) (MM01) and Huot et al. (2008) fits (and within their dispersions as shown in Rudorff et al., (2012)). Therefore, the b_{bp} values obtained in the

present work were considered reliable and consistent with previous works. The bulk b_{bp} variability measured within the first optical depth (below 5 m to avoid bubble influence), was 1-8% RPD*, which characterize the uncertainty levels in respect to the natural variability of the sampled volumes

5.3.5.2. Chl*a* uncertainty

The uncertainties regarding the Chl*a* measurements using different methods is an issue that has received considerable attention in the past years. Nonetheless, some questions are still not well consolidated and meaningful differences have been reported within different Chl*a* measurements (WASMUND et al., 2006; LUTZ et al., 2010). The HPLC method (Chl*a*1) is known to retrieve the most accurate Chl*a* since it separates each pigment (through a high pressure column) before measuring their absorption peak, avoiding the contamination of other pigments and degradation products. The standard fluorimetric method (Chl*a*2) (HOLM-HANSEN et al., 1965), on the other hand, is known to retrieve the most biased Chl*a* due to the contamination of Chl*b* and Chl*c* in the measured fluorescence signal. The measured broad fluorescence band encompasses not only the Chl*a* signal, but also Chl*a* degradation products, such as Pheophytin *a* (Pheo). To account for the Pheo overlapping signal, after the first reading, the sample is subjected to acidification, which shifts the Chl*a* fluorescence peak and supposedly only Pheo fluorescence is measured in the second reading. However, in the presence of phytoplankton groups with Chl*b* (e.g. Chlorophyceae), this pigment also overlaps the Pheo fluorescence signal after the acidification, causing an overestimation of the Pheo concentration and consequent underestimation of Chl*a* (after Pheo subtraction). Phytoplankton groups with Chl*c* (e.g. diatoms, haptophytes), on the other hand, have an inverse effect of overestimating the Chl*a* with overlapping signals on the Chl*a* fluorescence peak (TREES et al., 1985; VERNET; LORENZEN, 1987). The spectrofluorimeter approach (Chl*a*3) (LUTZ et a., 2010) has the advantage of measuring the Chl*a* at the wavelength centered solely at the Chl*a* fluorescence peak, avoiding the contamination of other pigments and degradation products. This is a more recent fluorescence method and has been pointed out as a highly accurate method in some comparison studies (WASMUND et al., 2006; HENRIQUES et al., 2007; LUTZ et al.,

2010). This method, however, also requires a very fine adjustment of the instrument to precisely measure the Chl*a* fluorescence peak, and avoid signal contaminations.

For the comparisons in the present work the HPLC TChl*a* was used as a reference to compare the other two methods (N=20). The three data sets had high r^2 values (0.96 for Chl*a*2 and 0.98 for Chl*a*3) (Figure 5.7a), showing a strong co-variation and low dispersion between the measurements. Nevertheless, the biases were high, especially for the Chl*a*3 with 55% RPD* and 0.125 $mg.m^{-3}$ RMSE. The Chl*a*2 had a slightly higher dispersion but with lower differences with 20% RPD* and 0.033 $mg.m^{-3}$ RMSE. The high systematic overestimation of the spectrofluorimeter method in relation to the HPLC could be explained by two main reasons: a) the different filtration times used for the HPLC and fluorimetric samples, and b) the different solvents used for the pigment extraction. Since the HPLC requires a much larger volume of filtered sample to accurately retrieve all the pigments that may be present, a longer filtration time was needed for the HPLC samples, which could have implied in a higher loss of chlorophyll *a* due to degradation (WASMUND et al., 2006). The fluorimetric samples, on the other hand, require much smaller volumes to obtain significant detection signals, and the filtration time was much lower. For instance, some stations had only 500 mL filtered for fluorimetric samples, whereas 3-4 L for the HPLC. In fact, there was a slight positive covariation between the concentration of degradation pigments (e.g. Pheophytins, Pheophorides, and Chlorides) and the filtration time for the HPLC samples (but not statistically significant). There was always a compromise in not letting the filtration time exceed too much the recommended 40 min, but also having a reasonable volume required for the HPLC analysis, so some samples took up to 1h20 to filter. This effect however, may not have been so much significant, as the Chl*a*2 also used much smaller sample volumes, taking only up to 30 min to filter, and still had a close match with Chl*a*1. What could thus, explain the major differences between the Chl*a*3 and both Chl*a*1 and Chl*a*2 methods, was probably the solvent used for the pigment extraction. Previous works have shown that the differences between 100% methanol and 90% acetone for the pigment extraction (using the same method), may account for over than 30% CV differences on the Chl*a* retrieval, being methanol the most efficient extractor (WASMUND et al., 2006; HENRIQUES et al., 2007; LUTZ et al., 2010). Both Chl*a*1 and 2 used acetone as the extractor, while Chl*a*3 used 100% methanol.

To better evaluate which Chl*a* retrieval could be the most biased, since the HPLC is a standard method that should retrieve the most reliable measurements, and the spectrofluorimeter could also have some residual contaminations of overlapping fluorescence signals (Pheo), a comparison was made between the Chl*a* and $K_d(490)$ obtained from the HOCR (in the surface layer) (Figure 5.7b). The Chl*a*3 vs. $K_d(490)$ was very close to the power law fit obtained by Morel and Maritorena (2001). The modeled $K_d(490)$ with the MM01 using Chl*a*3 as input had a 0.92 r^2 and 12% RPD*, compared to the measured HOCR $K_d(490)$. Whereas, the HPLC Chl*a*1 had a higher dispersion compared to the HOCR $K_d(490)$, and a lower match with the MM01, with a 0.89 r^2 and 27% RPD* (measured vs. modeled K_d490) (Figure 5.7b).

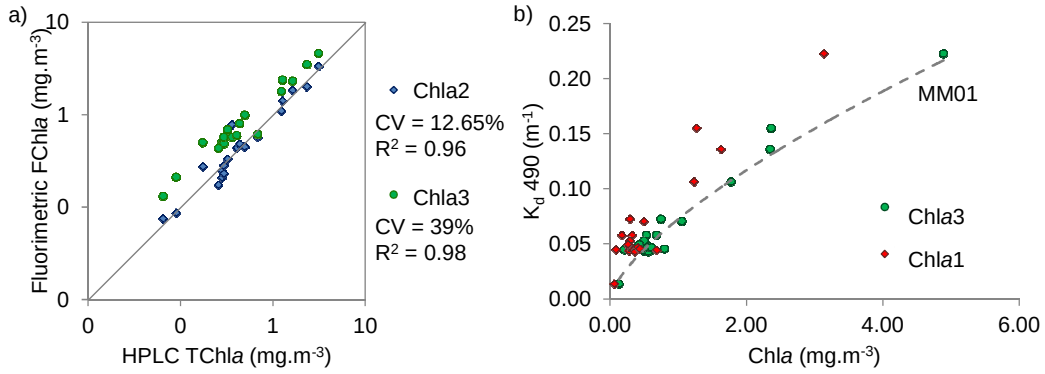

Figure 5.7 - Comparison of the Chl*a* measurements of the standard fluorimetric (Chl*a*2) and narrow band (Chl*a*3) methods with the HPLC (Chl*a*1) (a) (in log10 scale). Chl*a* vs. $K_d(490)$ using Chl*a*3 and Chl*a*1, and the MM01 fit (dashed curve) (b).

The closer match between the Chl*a*2 and Chl*a*1, may be explained by the use of the same extraction solvent (90% acetone) and the presence of both Chl*b* and Chl*c* in the samples (determined with HPLC), which could have compensated over and underestimations of Chl*a* using the standard fluorimetric method. Based on these analyses the method that retrieved the most accurate Chl*a* was considered the spectrofluorimeter method (Chl*a*3), due to the efficiency of the extraction method (with 100% methanol) compared to the HPLC which used 90% acetone, and the precision of

the method. Since the differences were high, the Chl*a*3 was selected to be used for the further analysis in the present work (e.g. as input in the MM01 R_{rs} model), instead of averaging all methods.

Since the use of 90% acetone is widely applied in both fluorimetric and HPLC methods, a correction fit using the Chl*a*1 and Chl*a*3 of the entire MV1102 data set with 177 match-ups, and Chl*a*3 ranging from 0.077 to 5.80 mg.m^{-3} (0.97 r^2), is proposed:

$$\text{Chl}a^* = \text{Chl}a'1.4072 + 0.1412 \tag{5.7}$$

where Chl*a** is the corrected quantity and Chl*a*' measured with acetone (by HPLC). The above relation does not attempt to be blindly used for such corrections in other studies, as there are likely other biases included in this relation, such as pigment degradation and the relatively low Chl*a* range. Notwithstanding, it should call the attention for the needs to consider this possible source of bias.

5.3.5.3. R_{rs} comparisons: INS vs. RTE

The bulk uncertainties of the RTE R_{rs} regarding the IOP measurements integrated within first optical depth ($1/K_d$), are expressed in the SD and CV of Table 5.7. The RTE SD was determined calculating n times the RTE (using Equation 3.12) with different combinations of the IOPs (a_s, a_p and b_{bp}) within their SD range:

$$X''(\lambda) = X'(\lambda) + \text{RN}*\text{SD}(\lambda) \tag{5.8}$$

where X" is any possible value of the IOPs ±SD, X' is the mean quantity (with no noise) and RN is a random number between -1 to 1, that can vary equally for all bands (λ) (for correlated errors) and independently for non-correlated errors.

The RTE SD was determined averaging both correlated and non-correlated errors, and was 0.0001 sr^{-1} for the bands (2.3-3.4% CV) and 0.02-0.04 for the ratios (1.7-2.1% CV) (Table 5.7). The uncertainties were rather low, due to the low levels of uncertainty associated with the IOPs. As the shorter blue bands of the R_{rs} are more affected by the absorption variability, whereas the longer green bands are more dominated by the b_{bp} signal, the uncertainties for the shorter bands (<490 nm) were associated mainly to a_s, and secondarily to a_p, whereas the longer bands (510 and 555 nm) where more related to b_{bp} uncertainties. There are also other potential sources of uncertainties in the RTE that were not quantified in the SD computations, but are important to be mentioned, such as the vertical stratification of the IOPs and the f/Q factor, obtained from Morel et al. (2002) (according to the Chl*a*, SZA and sensor-viewing geometry for clear skies). Albeit not quantified, these factors were somewhat analyzed, as further discussed.

Table 5.7 - Mean standard deviation and coefficient of variation (%) of the RTE for the ocean colour bands and ratios.

		λ 412	λ 443	λ 490	λ 510	λ555	412/555	443/555	490/555	510/555
RTE	SD	0.0001	0.0001	0.0001	0.0001	0.0001	0.04	0.03	0.03	0.02
	CV (%)	2.3	2.6	3.4	3.4	3.2	2.1	2.0	2.0	1.7

Comparing the INS with the RTE, the INS overestimated the R_{rs} with a 15-28% UPD for the bands, and 11-12% for the ratios (Table 5.8). Despite of these relatively high differences, they were rather systematic biases with a low dispersion and high r^2 values for both bands and ratios (r^2=0.85-0.94) (Table 5.8 and Figure 5.8). The RPD* ranged from 18 to 34% for the bands and 13 to 17% for the ratios. The RMSE was highest for the shortest band with 0.0012 sr^{-1} (0.0006 sr^{-1} SD). The higher r^2 for the 555 nm band was "forced" by the Magellan Strait station that had a high R_{rs}(555) due to the presence of sediments and a good match with the modeled R_{rs}, despite of being more optically complex waters. As both measured and modeled R_{rs} have uncertainties intrinsic to each approach, the possible sources of biases will be discussed in the following.

Table 5.8 - Statistical differences between the R_{rs} (INS), modeled RTE and MM01.

		λ412	λ443	λ490	λ510	λ555	412 /555	443 /555	490 /555	510 /555
INS	UPD (%)	25.5	27.3	27.9	26.1	15.0	10.6	12.4	12.4	11.2
vs.	RPD* (%)	31.5	33.8	33.0	31.4	18.2	16.1	17.1	15.4	13.4
RTE	RMSE(sr^{-1})	0.0012	0.0011	0.0011	0.0009	0.0004	0.39	0.35	0.30	0.21
M(f/Q)	SD(sr^{-1})	0.0006	0.0006	0.0005	0.0004	0.0002	0.20	0.17	0.15	0.10
N=20	r^2	0.87	0.88	0.86	0.85	0.93	0.93	0.94	0.93	0.92
INS	UPD (%)	10.3	10.4	7.6	15.4	2.7	7.6	7.5	5.3	12.8
vs.	RPD* (%)	26.4	25.0	21.3	24.6	12.0	18.4	16.8	13.2	16.1
MM01	RMSE(sr^{-1})	0.0014	0.0011	0.0009	0.0008	0.0003	0.40	0.33	0.26	0.25
N=19	SD(sr^{-1})	0.0006	0.0005	0.0005	0.0004	0.0002	0.20	0.16	0.13	0.12
	r^2	0.84	0.91	0.88	0.75	0.25	0.90	0.95	0.95	0.92

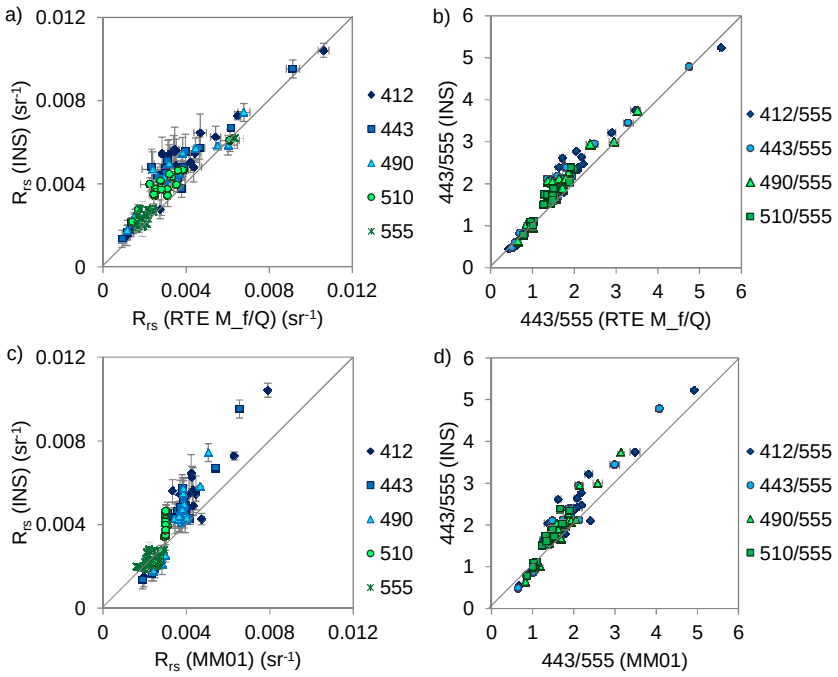

Figure 5.8 - Comparison of the measured INS R_{rs} with the modeled RTE bands (a) and ratios (b), and the same for the MM01 ((c) bands and (d) ratios).

Regarding the RTE approach, some biases may be due to the bio-optical vertical stratification. The IOPs were integrated within the first optical depth, however they could only be linearly averaged if the IOPs co-varied with depths, with a vertically constant b_{bp}/a (MOBELY, 2004) The validity of this assumption was tested using an

homogeneity index (H) for the IOPs following Zaneveld et al. (2005), where (H)=<b_{bp}/a>/[<b_{bp}>/<a>]. The H index was approximate to one for all stations, denoting fairly homogenous profiles within $1/K_d$. There were some slight deviations, but still very low, for stations 76 (1.04) and 130 (1.02), which had the most stratified conditions. Hence, the bio-optical stratification was a minor issue for the RTE approach, with likely low impacts on the modeled R_{rs}.

Another source of bias between the RTE and INS could be due to inelastic scattering, which was not entirely accounted in the RTE approach. Raman scattering was somewhat accounted in the f/Q ratio (MOREL et al., 2002), as their tabulated values were simulated with Raman contribution in different Chl*a* ranges. The CDOM fluorescence however, was not considered at all in the RTE approach. However, as most of the MV1102 stations had rather low CDOM content, this effect was expected to be minor. Some stations of the Patagonian Shelf, Magellan Strait and at the Chilean coast, however, had higher CDOM content, which could have contributed with fluorescence signals in the measured R_{rs}. In high CDOM waters (a_s400> 0.2 m^{-1}), its fluorescence could enhance the L_u up to 10-20 % at its maximum peak band (~490 nm), and somewhat less in a broad band from 400-530 nm (HUOT et al., 2007). The coastal MV1102 stations did not have such high CDOM values, except for the Magellan that had an a_s400 of 0.23 m^{-1}, whereas the others ranged from 0.07 to 0.14 m^{-1}. Hence, this effect may have been mostly minor, but some of the differences between the INS and RTE in the 400-510 nm range, could have been partly, due to the CDOM fluorescence. In fact, there was a slightly higher UPD for the 490 nm band (as observed in Table 5.8), which may indicate some of this effect.

Regarding the f/Q ratio, the errors may be associated mainly with the uncertainties in the relations between Chl*a* (and the bulk IOPs) and the VSF used to derive the bidirectional factors in radiative transfer simulations, as well as the differences in the illumination conditions of the modeled clear sky conditions against the true partially clouded and overcast conditions. In respect to the first issue, there are still many unknowns in these relations (MOBLEY et al., 2002) as there are few *in situ* measurements of the VSF over a wide range ocean waters. More complex formulations that use the IOPs instead of Chl*a* in the model simulations, may account better for

variations in the VSF, as well as the contribution of multiple scattering (of both molecules and particles) (LEE et al., 2004; PARK; RUDDICK, 2005). Instead of the f/Q ratio one may also use a g factor with a quadratic function that relates R_{rs} to the IOPs in a similar manner (as explained in section 3.4.1). The differences in the retrieval of the RTE using either the f/Q ratio (and simplifications in Morel et al. (2002)) or the quadratic factor of Lee et al. (2004) and Park and Ruddick (2005), were in order of 6-10% RPD*, with an overall tendency of overestimation of the RTE using the Morel et al. (2002) factor. This overestimation may be caused by the simplification of the term $b_b/(a+b_b)$ to b_b/a, not accounting for multiple scattering, although the f/Q factor used is adjusted for this simplification (MOREL et al., 2002). These differences, however, do not explain the main differences encountered between the RTE and INS, as the modeled R_{rs} using the Morel et al. (2002) approach (RTE M_f/Q) was still lower than the INS.

As one may observe in Figure 5.8a and b, the highest differences between INS and RTE, were for the stations with intermediate R_{rs} values, which were mostly at the STCZ, under cloudy and heavy fog conditions (<10 km of visibility). Hence, an important source of the INS bias could be due to cloud and fog effects. To analyze the possible impacts of the illumination conditions on the differences between the RTE and INS, comparisons were made dividing the stations according to the percentage of cloud coverage (CC) (following Table 5.1), as: 1) completely overcast (including the foggy stations) (8/8 CC) (N=9); 2) mostly clear sky (0-3/8 CC) (N=3) and 3) partially cloudy (4-7/8 CC) (N=8) (Figure 5.9). The number of stations representative of each condition was low, nevertheless, some plausible observations may be made due to the high differences encountered for each condition and the consistency of the biases between all the approaches of the measured R_{rs} (for both above and in-water methods).

The highest differences were for the stations with partially cloudy skies with a UPD of 25-35% for the bands and 9-10% for the ratios (Figure 5.9). The biases were somewhat higher for the shorter bands (412-510 nm), but the ratios significantly diminished the biases and were rather white, indicating the dominance of spectrally correlated errors. The high biases associated with cloudy conditions are likely caused by short time scale illumination variations caused by intermittent sun shining and cloud shading, especially with a rapid changing sky, and the non-uniform sky radiance distribution (TOOLE et

al., 2000). Some of the stations had very high variations during the measurements, from almost overcast to direct sun light incidence within a few seconds. These biases were thus, mainly caused by mismatches of the illumination conditions for the measurements obtained by the sensors for the in-water approach (due to the local displacement of the deck sensor and profiler) and for the different sampled areas (of the ocean, sky and plaque) for the above-water approach (as shown in in the example of St 130, Figure 5.2). Although some variations were normalized in the data processing scheme of the in-water approach (using Equation 4.4), high frequency variations due to rapid changes still remained due to the displacement of the sensors. These high illumination variations during the casts caused a noisier profile for the in-water approach, which also implied in higher biases for the extrapolation procedure. For the above-water approach, cloud glint effects under partially cloudy conditions was also a major source of bias which enhanced the measured R_{rs}, as previously discussed.

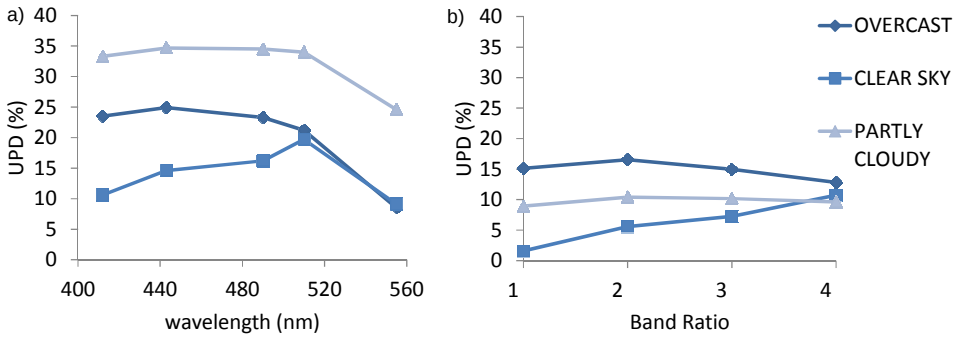

Figure 5.9 - UPD (%) between INS and RTE R_{rs} for the different illumination conditions according to cloud coverage (completely overcast, clear sky and partly cloudy) for the bands (a) and ratios (b) (1=412/555; 2=443/555; 3=490/555; 4=510/555).

Mostly clear skies had the lowest biases with an UPD ranging from 9-20% for the bands, and 2-10% for the ratios. The highest biases were for the 443-510 bands, likely associated with the stronger influence of bubble clouds for this group of stations (St 03, 06 and 75). Stations 03 and 06 showed indeed a bias peak especially at the 510 nm band (and the 510/555 ratio) for both the above and in-water approaches. Despite of having low-moderate winds (4-8 $m.s^{-1}$), these stations had the clearest waters (<0.2 $mg.m^{-3}$) for

which the bubble effects are highest due to the lower contribution of the biogenic material in light absorption and scattering (STRAMSKI; TEGOWSKI, 2001; PISKOZUB et al., 2009). Although efforts were made to avoid the bubble clouds for the in-water approaches (using depths > 5m), there could have been residual effects that were highest for the clearest waters. The above-water approach also should have had minor effects of bubble clouds after the residual correction, but still with some under-corrected residuals for the shorter bands.

The overcast stations had an overall UPD of 8.5-25%, increasing towards the shorter bands, and 13-16% for the ratios. The biases were on average 10% higher than the clear sky condition for the blue bands (412-490 nm). The highest biases were related to the heavy fog conditions, likely due to the low E_d levels. The increase in the measured R_{rs} for overcast conditions, was also observed by Doxaran et al. (2003), that compared *in situ* above-water measurements for waters with equivalent OAC concentrations, under clear sky and overcast conditions. The authors attributed the higher R_{rs} for overcast conditions, especially for the shorter bands, to a probable increase on the f/Q ratio due to the higher proportions of diffuse light. One could argue that the above-water measurements could also have under-corrections of cloud glint effects on the ocean surface that may also cause higher R_{rs} (MOBLEY, 1999). Analyzing each approach separately, the above-water R_{rs} had 18% higher $R_{rs}(412)$ for overcast conditions (compared to clear sky), while the in-water approaches had on average 12% higher UPD. Thus, some proportion of the contaminated R_{rs} for the above-water approach may actually be due to cloud glint effects, however a higher f/Q ratio due to higher contributions of diffuse light, may also be significant for both above and in-water approaches. Doxaran et al. (2003) recommended the use of band ratio algorithms for bio-optical modeling to minimize such effects. In the present work, the band ratios actually did compensate most biases, however spectrally dependent residual sources were still present with an UPD up to 15% for the ratios under overcast conditions (Figure 5.9b). Moreover, bio-optical models with inversion schemes (e.g., semi-analytical models) generally do not relay on band ratios (or at least not solely) and thus, an adequate correction for these effects would be more desirable, whenever possible.

The higher biases of the shorter bands for the overcast and cloudy conditions may be explained by the different effects of that the illumination conditions have on the E_d and L_u. While the E_d is composed by both direct and diffuse light, the L_u is essentially composed of the diffuse upwelling light, as it is the scattered fraction of E_d in the upward direction. Since the shorter wavelengths are more efficiently scattered by water molecules, variations in the diffuse light contribution will have higher effects on the L_u for the shorter bands (STRAMSKA; DICKEY, 1998). Higher proportions of diffuse light due to cloud coverage (or fog) could thus, have an effect of decreasing E_d (with less direct light) and "increasing" the L_u fraction, which would explain the higher R_{rs}, especially for the shorter bands. Morel and Gentili (1993) showed with radiative transfer modeling that the Q factor (at nadir) is somewhat higher for overcast days (~5-10%) with a more isotropic backscattered light-field caused by a higher contribution of diffuse light. This was also is in accordance with *in situ* measurements obtained by Lewis et al. (2011) using with a "fish eye" radiometer. Morel and Gentili (1991) also showed with radiative transfer modeling, that the f factor, which is mainly what regulates the R_{rs} magnitude, is rather constant and spectrally white for clear sky days (for intermediate Chl*a*), but may vary significantly for cloudy (or foggy) conditions. The f factor is raised by the increase of the diffuse component and is spectrally variable, increasing from the red to blue, as the proportion of diffuse light increases. They tested this for a couple of cases of water types (with high and low Chl*a*), cloud coverage and visibility, and found that the f factor may be enhanced up to 12% for completely diffuse skies. Testing an adjusted f/Q ratio for the stations with overcast conditions (~10% higher, according to Morel and Gentili (1991), Morel and Gentili (1993); and Lewis et al., (2011)), the overall differences between the RTE and INS (including all the stations) were reduced in ~10% for the bands and 2% for the ratios. The UPD now ranged from 12 to 20% for the bands and 7 to 8% for the ratios. The differences were still moderately high, due to the biases associated to the high illumination variations, but much closer to the uncertainties within the INS measurements and RTE approximations.

To verify the possible impacts of the sea state conditions on the INS biases, a comparison was also made for the stations with rough sea conditions with intensive winds (>6 m^{-1}) and higher waves (>2 m), against the calmer conditions. The differences were in order of 6% higher for the bands and 1-2% for the ratios under rough

conditions. This denotes a much lower impact of this source of variability in comparison to the illumination conditions, but still somewhat important. The higher differences for rough seas may be related to a higher variability in the sea surface reflection for the above-water approach (MOBLEY, 1999), presence of whitecaps and bubble clouds (PISKOZUB et al., 2009), variations in the light attenuation (for the in-water L_u due to swell motion) and higher focus and defocusing effects of the downwelling rays for the in-water E_d (STRAMSKA; DICKEY, 1998). These effects may be much higher when analyzing each approach separately as discussed in the previous sub-sections. The above-water approach had higher overestimations compared with the in-water HOCR, as it was likely more affected by cloud glint and bubble clouds, contributing to higher R_{rs} values for the merged INS. Bubble clouds also showed evidences of residual contributions in the in-water approaches which may also have contributed for high R_{rs}. The effects of illumination variation conditions also generally overestimated the R_{rs} (although with a higher dispersion) and affected both the above and in-water approaches. All these effects were smoothed averaging the casts and approaches to obtain the final INS, nonetheless, some biases still remained in the measured R_{rs}, as shown in the present analysis.

One needs to keep in mind though, that some important sources of uncertainty may also be related to the RTE approach, with limitations in the IOP measurements, the constants used (e.g. b_{bw}, a_w and f/Q), contribution of inelastic scattering (Raman and fluorescence) and the approximations assumed (e.g., single scattering, homogeneity of the water column). As analyzed herein, these sources were however, not as high as the variabilities associated with the *in situ* measurements caused by the environmental effects. Anyhow, there are still needs for further improvements in the RTE modeling, with better parameterizations of the VSF and R_{rs} bidirectional factors varying under different illumination conditions and within a high range of IOPs. Recent works have shown some new *in situ* measurements of the L_u within the entire upward hemisphere and showing the L_u anisotropy for different IOP and illumination conditions, using a "fish-eye" radiometer (VOSS et al., 2003; LEWIS et al., 2011; ANTOINE et al., 2012). These works have brought up new insights regarding the bidirectional aspects of the R_{rs} and measured values of the Q factor (E_u / L_u), which may help reveal further questions of the in-water light-field variations and the relations between the apparent and inherent

optical properties. Further studies with *in situ* experiments and radiative transfer modeling may improve RTE parameterizations, as well as *in situ* R_{rs} correction schemes, which are essential for such closure analysis.

5.3.5.4. R_{rs} comparisons: INS vs. MM01

For the MM01 approach the Chl*a*3 (integrated in the first optical depth) was used to estimate K_d, b_{bp}, a and ultimately R_{rs}. The differences between the INS and MM01 R_{rs} ranged from 11.8 to 28.2% RPD* (0.0003-0.0013 sr^{-1} RMSE), increasing towards the shorter bands (Table 5.8 and Figure 5.9c). The r^2 for the 555 band was low (0.25) because the Magellan Strait station was not included in this comparison. The higher dispersion associated with this band for mostly clear waters may be due to the lower R_{rs} values and higher effects of random sources of uncertainty, such as, the focus and defocusing of downwelling rays. The band ratios differences ranged from 14.1 to 19.7% RPD*, being highest for the ratio with the shortest band (412/555), but with a high r^2 for all ratios (0.90-0.95).

As in the comparison of the RTE approach, for the MM01 there was also a higher bias associated with intermediate R_{rs} values that were correspondent to the stations with highest environmental uncertainties with illumination variability and diffuse skies, causing INS overestimations. The main differences for the MM01 closure were in respect to a higher dispersion likely related to uncertainties in the MM01 approach, with some overestimations for the lowest R_{rs} values and underestimations of the highest R_{rs} (Figure 5.9c and d). The causes of these over and underestimations of the MM01 model could be due to natural dispersions in the global mean relations of the model fit, regarding the Chl*a* versus $K_d(\lambda)$ relation and Chl*a* versus $b_{bp}(\lambda)$. To investigate the dispersion in these relations for the MV1102 stations, comparisons were made between the modeled and measured non-water absorption (a_{nw}) and b_{bp} (Table 5.10 and Figure 5.10). The MM01 had an overall tendency of underestimation of the a_{nw} at shorter bands (412-490 nm) (-13.9 to -22.9% UPD) and overestimation at the 510 and 555 bands (3.1 to 19.2 % UPD). In a similar manner, the b_{bp} model tended to underestimate the shorter bands (-8.6 to -22.8 % UPD for 443 and 412 nm) and overestimate the longer bands (9.7 to 25.2% UPD, for 490-555 nm) (Table 5.9 and Figure 5.10). This similar tendency of both a_{nw} and b_{bp} compensated some of the R_{rs} amplitude variations, which explains why

the MM01 had some lower overall differences with the INS (Table 5.8 and Figure 5.10). Nonetheless, despite of these compensation effects for the bands, the a_{nw} and b_b biases were not spectrally correlated, and thus, the band ratios had higher differences in the INS vs. MM01 comparison (Table 5.8).

Table 5.9 - Statistical differences between the R_{rs} (INS), modeled RTE and MM01.

		λ412	λ443	λ490	λ510	λ555
a_{nw}	UPD (%)	-22.9	-22.3	-13.9	3.1	19.2
vs.	RPD* (%)	20.26	18.9	16.4	15.6	32.3
MM01	RMSE (m^{-1})	0.035	0.033	0.016	0.005	0.005
N=19	SD (m^{-1})	0.017	0.017	0.008	0.003	0.003
	r^2	0.95	0.97	0.97	0.97	0.97
b_{bp}	UPD (%)	-22.8	-8.6	9.7	15.0	25.2
vs.	RPD* (%)	30.3	26.2	28.5	31.3	40.3
MM01	RMSE (m^{-1})	0.0012	0.0011	0.0011	0.0012	0.0013
N=19	SD (m^{-1})	0.0006	0.0005	0.0006	0.0006	0.0006
	r^2	0.45	0.59	0.70	0.72	0.72

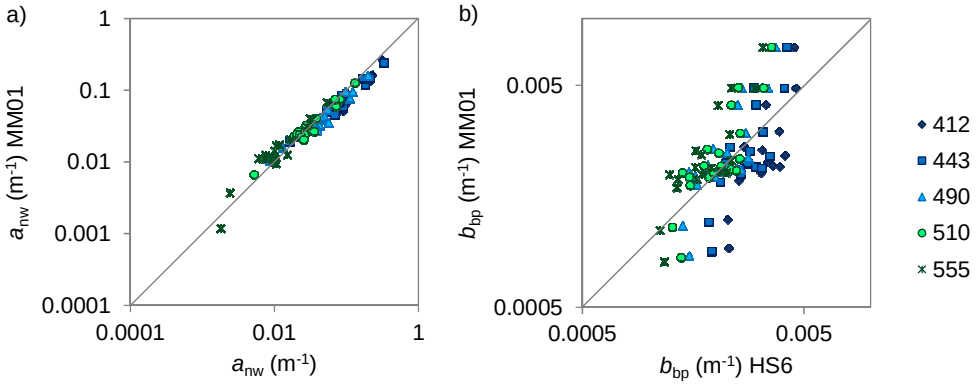

Figure 5.10 - MM01 retrievals versus measured a_{nw} (a) and b_{bp} (b) (in log10 scale).

In a case by case analysis, the MM01 a_{nw} had generally a close match, increasingly underestimating the shorter bands for higher Chl*a* waters. Only at St 06 (with the lowest Chl*a*) the a_{nw} was slightly overestimated at all bands (Figure 5.10). The biases associated with the blue bands (412 and 443 nm) may be explained by the variations of

CDOM and detritus (CDM) content in respect to the Chl*a*. The MM01 fit is adjusted for a global mean relation between K_d and Chl*a*, and assumes that the CDM co-varies with Chl*a*. This is expected for Case 1 waters (MOREL; PRIEUR, 1977) for which the bulk biogenic material (living and non-living) should be regulated by the phytoplankton community. Notwithstanding, recent works have shown that there is a significant spatio-temporal variation of CDM (especially CDOM) in respect to the phytoplankton biomass, even for typical Case 1 waters in remote areas of open ocean waters (SIEGEL et al., 2002; MOREL; GENTILI, 2009). Such CDM variability may be major sources of uncertainties for the shorter bands of the MM01 a_{nw} model. The slight overestimation of the a_{nw} at St 06 may indicate lower CDM at this station and the underestimations at all the other stations may indicate an overall tendency of higher CDM. The SATL is in fact mostly characterized by a lower CDM index (i.e., CDM in relation to Chl*a*), due to more photodegradation processes associated with the deeply stratified waters, whereas the STCZ has stronger gradients, with vertical mixing cells (MOREL; GENTILI, 2009). The PAT and Chilean coastal regions also generally higher CDM index likely related to greater coastal influences (MOREL; GENTILI, 2009).

Another issue that may be minor but also important, are the variations in the Chl*a* and K_d relation caused by the specific phytoplankton absorption coefficient (a_{phy}*=a_{phy}/Chl*a* m^2.mgChla^{-1}). The variations in the a_{phy}* predominantly due to differences in the intercellular pigment concentration and resultant pigment self-shading effects (SATHYENDRANATH et al., 1987; CIOTTI et al., 2002). The intercellular pigment concentration varies mainly with the cell structure, size and physiological state (BRICAUD et al., 2004). In natural marine environments larger cells usually have higher packaging effects with lower a_{phy}* and are dominant in higher Chl*a* waters, whereas smaller picoplankton cells have higher a_{phy}* and are more dominant in lower Chl*a* waters (BRICAUD et al., 2004). A mean relation between Chl*a* and a_{phy} could thus capture this variability. However, variabilities in the phytoplankton size structure, intracellular Chl*a* and concentration of accessory pigments due to photoacclimatation processes, may result in deviations in the mean Chl*a* to a_{phy} relation (BRICAUD et al., 2004). In the present study, despite of the relatively high Chl*a* range from oligo to eutrophic waters (0.10-4.8 mg.m^{-3}) the a_{phy}* was rather high for all stations (mean 0.06±0.01 m^2.mgChla^{-1}). Hence, the MM01 may have underestimated the a_{nw} at the

blue bands (Figure 5.10), due to the generally higher a_{phy}* obtained throughout the study region.

The b_{bp} model was even more problematic with some higher biases and dispersion between the measured and modeled quantities (Figure 5.10). The MM01 underestimated the b_{bp} at all bands for stations 03, 06, 09, 23 and 28. For all the other stations with intermediate Chl*a* (0.3-1.0 mg.m^{-3}) the MM01 underestimated the blue bands (412 and 443 nm) and was closer or slightly overestimated the longer bands (510 and 555 nm). For higher Chl*a* waters (>1.5 mg.m^{-3}) the b_{bp} MM01 overestimated at all bands (Figure 5.10). The MM01 assumes a b_{bp} efficiency of 1% and a -1 b_{bp} spectral slope for a lower Chl*a* limit of 0.2 mg.m^{-3}, that progressively increases up to 0 to an upper limit of 2 mg.m^{-3}. For Chl*a* above this limit, the b_{bp} is assumed to be spectrally invariable to account for the overall tendency of the bulk biogenic matter to be more absorbing and less scattering with increasing Chl*a* (for typical Case 1 waters, with particles with low index of refraction) (MOREL; MARITORENA, 2001). These values of the b_{bp} efficiency and spectral slope are determined with theoretical calculations using Mie theory (for non-absorbing spherical particles) and a Junge-type particle size distribution (PSD) with a -4 slope (*j*). Variations in these parameters are the main causes of the dispersion in the MM01 b_{bp} model. The stations for which the b_{bp} model underestimated at all bands, had the highest b_{bp} normalized by Chl*a* (b_{bp}*, 0.005±0.002 m^{-2}.mgChl*a*), which may be an indicator of the bulk b_{bp} efficiency of the particle assemblage. Whereas, the stations for which the b_{bp} model overestimated at all bands, had in fact the lowest b_{bp}* (0.001±0.0003 m^{-2}.mgChl*a*). High b_{bp}* may be related to smaller particles and/or with higher index of refraction (LOISEL et al., 2010).

For the stations with intermediate Chl*a*, for which the b_{bp} had a closer match at 510 and 555 nm, the underestimation of the blue bands was mostly due to differences in the b_{bp} slope. The measured slope was higher than the model parameter for all stations, ranging from -2.3 (for St 03, with 0.2 mg.m^{-3}) to -1.1 (for St 75 with 2.35 mg.m^{-3}) (determined by the power law fit between 433-555 nm). These values are significantly higher than the -1 to 0 interval used in the MM01 model for the same Chl*a* range, and are consistent with recent works that also analyzed *in situ* b_{bp} measurements (HUOT et al., 2008). The b_{bp} slope has a close relation with the PSD, which has been generally treated as a Junge-

type distribution with a -4 slope for marine particles in radiative transfer computations. Recent models have related the b_{bp} spectral slope with the PSD slope and found direct relations between higher b_{bp} slopes and the dominance of smaller particles which generally tend to be related to oligotrophic waters, and vice versa (LOISEL et al., 2006; KOSTADINOV et al., 2009). This seems to be in accordance with the general trend of the MV1102 stations with higher (negative) b_{bp} slopes at the oligotrophic stations of the SATL and STCZ and lower at the meso-eutrophic stations of the PAT and Chilean coast, although there was not a significant relation between the slope and Chl*a*. Anyway, these are only limited considerations as more analyses with PSD *in situ* measurements and b_{bp} at more wavelengths and scattering angles are desirable for consistent conclusions. Further analysis and discussions in this respect are shown in the following Chapter. Anyhow, there was clearly a dispersion in the MM01 b_{bp} model likely due to the natural variations in the b_{bp} efficiency and spectral slope.

For a final overall look of the differences between the INS, RTE and MM01 approaches in the closure analyses, the R_{rs} spectra of each station are shown in Figure 5.11. One may observe that there were closer matches between the INS and RTE for the stations with mostly clear skies or completely overcast, for all Chl*a* ranges (oligotrophic: St 03 and 06; meso: 9, 13 and 19; and eutrophic: St 75, 76, 85 and 134). The stations with highest differences and INS SDs were the ones with heavy fog (St 32, 36 and 56) and highest illumination variation conditions (St 40, 46 and 51). St 51 was the station with the most adverse conditions of high illumination variation, moderate to strong winds (~7.8 $m.s^{-1}$) and high waves (~2.4 m). As previously discussed, adjusted f/Q ratios for the different illuminations accounting for the different proportions in the direct and diffuse light, may enhance the measured and modeled R_{rs} match-ups and be applied for *in situ* R_{rs} correction schemes. Nevertheless, high biases were still associated with environmental variabilities, regarding high illumination variations and sea state conditions. Due to the random characteristic of these sources, specific corrections for *in situ* approaches are rather difficult to define. Considering each approach separately the differences should be even higher as each one was affected in different ways by the environmental sources. Thus, averaging the measured R_{rs} obtained by the different approaches was a reasonable alternative to normalize and diminish some of the environmental effects.

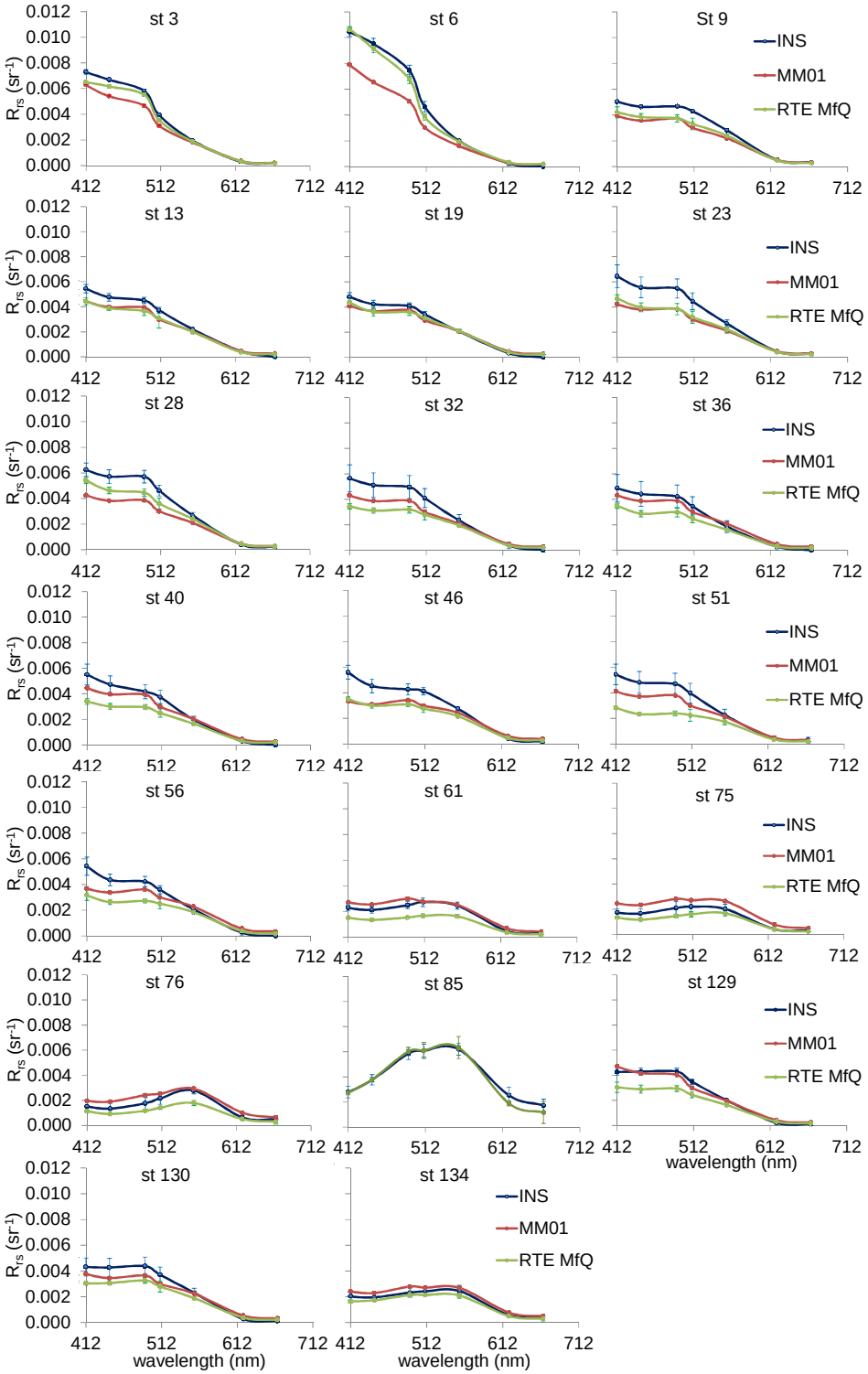

Figure 5.11 - Mean R_{rs} INS, RTE and MM01 spectra for each station.

For the MM01 one may note that the stations with lowest Chl*a* were underestimated by the modeled R_{rs} (St 03 and 06), which was mainly due to b_{bp} underestimations and partly to a_{nw} overestimations. Whereas, the stations with highest Chl*a* were mostly overestimated (St 61, 75, 76 and 134) due to b_{bp} overestimation and a_{nw} underestimation of the MM01. The stations with intermediate Chl*a* oscillated with over and underestimations due to the higher uncertainties in the INS (caused by the environmental variability) and compensation effects of the MM01 a_{nw} and b_{bp} under and overestimations. Although one may argue if the study region embraces strictly Case 1 waters, even across the SATL and STCZ there were significant biases in the MM01 retrievals for a_{nw} and b_{bp}. Further studies with *in situ* measurements of a_{phy}*, b_{bp}*, b_{bp} slope and the PSD, over a wide variety of biogeochemical provinces, should provide greater insights on the variability and distribution of these properties, and enhance bio-optical forward models. At the state of art, however, the application of such models with current global parameterizations still need higher attention on the dispersion of the global fits, even for typical Case 1 waters.

5.3.6. Implications for ocean colour remote sensing

5.3.6.1. OC4v6 empirical model

Despite of the moderate to high differences of the R_{rs} bands between the different approaches, the band ratios had much lower biases with an overall RPD* of 10% for the measured R_{rs}, and 15% between INS and RTE. This denotes less implications of the biases for ocean colour bio-optical models that rely on band ratios. For the OC4v6 empirical model (O'REILLY et al., 2000) the RPD* between the modeled and measured Chl*a*3 was 13.2% (0.16 mg.m^{-3} RMSE and 0.08 SD mg.m^{-3}) using RTE, and 25.2% (0.25 mg.m^{-3} RMSE and 0.13 SD mg.m^{-3}) using INS (both with a high covariation, r^2 of 0.98). The biases where twice as higher for the INS ratios, but still within the 35% error limit for the Chl*a* retrieval recommended in the SeaWiFS protocol (O'REILLY et al., 2000). Moreover, applying an analysis of variance (ANOVA) the INS and RTE OC4v6 retrievals were not significantly different (p>0.05), denoting a reasonable performance of the INS with low impacts of the biases. One should have in mind however, that using one particular *in situ* R_{rs} approach would likely imply in higher biases for the OC4v6, as part of the environmental noises were smoothed by the averaged INS.

The biases of the modeled Chl*a* using the RTE maximum band ratio (MBR) are partly due to the uncertainties in the IOP measurements and RTE approximations, but also (and probably mostly) due to the uncertainties inherent to the OC4v6 model. These uncertainties are related to biases in the data set used as input to adjust the model and the dispersions in the Chl*a* versus MBR global fit due to natural bio-optical variability (BRICAUD et al., 2004; MOORE et al., 2009; MOREL; GENTILI, 2009; LOISEL et al., 2010; SZETO et al., 2011; RUDORFF et al., 2012). Thus, approximately 50% (or more) of the observed biases for the OC4v6 model, in the present work, could be due to bio-optical variability and intrinsic uncertainties of the model fit.

The modeled versus measured Chl*a* with the INS the RTE are shown in Figure 5.12. The error bars were determined using Equation 5.8, averaging correlated and non-correlated errors. The RTE MBR had a dispersion more centered on the OC4v6 global fit (Figure 5.12a), whereas the INS MBR had a shift of some stations, that turned to be underestimated by the OC4v6 (Figure 5.12b). This shift was mainly caused by the INS R_{rs} positive biases due to spectrally dependent environmental noises. As most of the noises caused higher R_{rs}, increasing towards the shorter bands, such as the illumination variations artifacts, residual cloud glint contamination and higher proportions of the diffuse light due to cloud coverage (and fog), these biases increased the MBR, consequently underestimating the Chl*a* by the OC4v6. Other residual sources could also have caused inverse effects diminishing the MBR, with higher R_{rs} for the green bands (510 and 555 nm), such as the bubble clouds (STRAMSKI; TEGOWSKI, 2001) and platform sea surface refection (HOOKER; MOREL, 2003). However, these seemed to have minor impacts compared to the other sources analyzed in the present work. Anyhow, despite of the observed impacts of the INS biases on the MBR model, most of the stations were still close to the OC4v6 fit (within their SD) and approximate to the RTE dispersion range (Figure 5.12a and b).

Figure 5.12c shows the modeled versus measured Chl*a* using the RTE MBR and HPLC Chl*a*1. Since the HPLC systematically underestimated the Chl*a* (in respect to Chl*a*3), mainly due to the inefficient pigment extraction procedure (with 90% acetone), when using this measurement as “reference”, the stations turn out to be overestimation by the OC4v6. Using the HPLC Chl*a*1 and INS MBR however, the HPLC underestimations

and the INS overestimations were somewhat compensated and the dispersion appeared more alike Figure 5.12a with the RTE MBR versus Chl*a*3. This compensation effect could thus, minimize the biases of both sets used to parameterize such models.

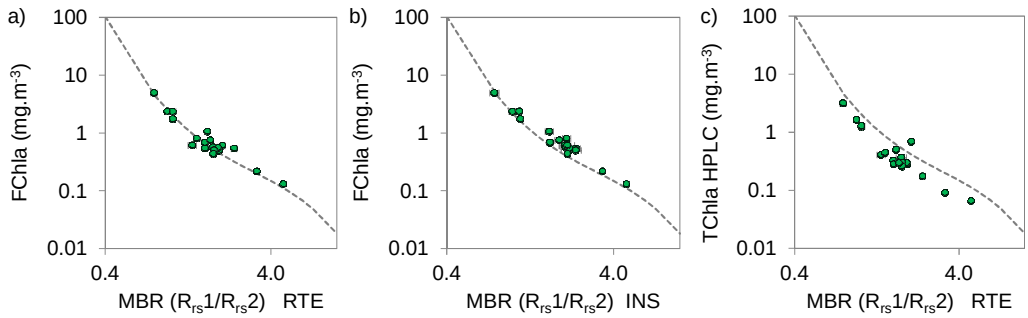

Figure 5.12 - Maximum band ration (MBR) OC4v6 using RTE (a) and INS (b) (mean ±SD) compared to the measured Chl*a*3 (FChl*a*) and Chl*a*1 (HPLC) (c) (plotted in log10 scale). Dashed lines correspond to the global OC4v6 fit (N=19, without St 85).

The above analyses showed some implications of the uncertainties of both R_{rs} and Chl*a* measurements on the bio-optical MBR model, and how the use of different approaches could change some trends, biases and even interpretations of possible sources of bio-optical variability. The global OC4v6 fit is composed of *in situ* match-ups of measured R_{rs} and Chl*a* mixing all the approaches analyzed in the present work (among others), with a higher proportion of above-water R_{rs} and the standard Chl*a* fluorimetric method (Chl*a*2), which are in fact the most biased approaches. Even though there is an increasing contribution of R_{rs} from in-water approaches and HPLC Chl*a* for new updates of the global database (O'REILLY et al., 2000), these measurements may also have some considerable biases as discussed herein. The use of different approaches is thus, a good alternative to determine the uncertainties of the data sets and obtain more reliable *in situ* data, either by merging the retrievals or selecting the least biased. The biases of the R_{rs} and Chl*a* may be somewhat compensated in the OC4v6 model and still be within the intrinsic uncertainties of the global fit. Nevertheless, further efforts on understanding the main sources of noises and means to achieve more accurate *in situ*

radiometric and bio-optical measurements are vital for the correct performance of such empirical models, as well as the investigations of natural bio-optical variability.

5.3.6.2. Semi-analytical models (GSM01 and QAA)

The semi-analytical models GSM01 (MARITORENA et al., 2002) and QAAv5 (LEE et al., 2002) use the R_{rs} spectra from 410-680 nm to simultaneously derive the IOPs using inversion schemes, either in a step by step process (QAA) or with an optimized non-linear least square fit (GSM). As they do not relay on band ratios (or at least not solely for the QAA), the INS biases should have higher impacts on these products. Thus, comparisons of the modeled and measured IOPs were also evaluated for these models. Table 5.10 summarizes the SD and CV of the QAA and GSM01 products using RTE and INS, simulating the errors with Equation 5.8. The SD of the "true" measured quantities are in respect to the measurement variations between replicates.

Table 5.10 - Standard deviation (SD) and coefficient of variation (CV) of the modeled (QAA and GSM01) and measured IOPs and Chl*a*.

		RTE			INS		
QAA		b_{bp} 440	a_{phy} 440	a_{cdm} 440	b_{bp} 440	a_{phy} 440	a_{cdm} 440
COR	SD	0.0002	0.0032	0.0016	0.0004	0.0019	0.0010
	CV (%)	6.8	5.0	6.4	11.2	3.4	3.8
UNCOR	SD	0.0002	0.0037	0.0027	0.0004	0.0048	0.0053
	CV (%)	7.3	5.7	9.3	11.8	8.2	16.3
GSM01		b_{bp} 443	Chl*a*	a_{cdm} 443	b_{bp} 443	Chl*a*	a_{cdm} 443
COR	SD	0.0003	0.053	0.0010	0.0003	0.035	0.0008
	CV (%)	14.3	5.52	3.15	11.1	4.4	3.7
UNCOR	SD	0.0003	0.106	0.0033	0.0004	0.128	0.0047
	CV (%)	14.5	11.2	9.4	15.3	15.2	15.0
Measured		b_{bp} 440	a_{phy} 440	a_{cdm} 440			
	SD	0.0001	0.0012	0.0012			
	CV (%)	1.7	2.3	4.1			

The SD is in m^{-1} for b_{bp}, a_{phy} and a_{cdm} (between replicates). COR stands for spectrally correlated errors and UNCOR for un-correlated.

The $b_{bp}440$ was the most sensitive to the R_{rs} amplitude variations, as there were higher deviations for the INS (±0.0005 sr^{-1}) than the RTE (±0.0001 sr^{-1}), for both correlated and non-correlated errors, especially using the QAA model (e.g. 0.0004 m^{-1} SD and 11.2% CV for INS, against 0.0002 m^{-1} SD 6.8% CV for RTE). The biogenic absorption coefficients ($a_{phy}440$ and $a_{cdm}440$ for the QAA, and Chl*a* and $a_{cdm}443$ for the GSM), on the other hand, were more sensitive to spectral variations of the R_{rs}, as the highest deviations were for non-correlated errors (e.g. 16.3% CV for $a_{cdm}440$ INS non-correlated errors and 3.8% for correlated errors, with QAA). These variations are consistent as the b_{bp} is what mainly regulates the R_{rs} magnitude, while the absorption determines more its spectral shape. Hence, amplitude variations of the R_{rs} are likely to affect more the b_{bp} retrievals, whereas spectral variations affect more the a_{nw}. An important thing to note was that the SD of the modeled IOPs using RTE was much higher than the measurement's SDs. This indicates a high sensitivity of the inversion schemes to slight spectral variations of the R_{rs}, propagating the errors to much higher levels. The products retrieved with the INS, however, did not have so much higher deviations compared to the RTE, denoting only moderate impacts of the INS biases.

The comparisons between the modeled and measured quantities are shown in Table 5.11 and Figure 5.13. The QAA retrievals using RTE had an RPD* of 8.7% for $b_{bp}440$, 14.6% for $a_{phy}440$ and 31.1% for $a_{cdm}440$. Using the INS the dispersions and deviations were somewhat higher for all products (Figure 5.13a-c). The RPD* was 18.1% for $b_{bp}440$, 23.1% for $a_{phy}440$ and 37.3% for $a_{cdm}440$. The dominant spectral biases of the INS provided a R_{rs} spectra typical of waters with lower concentration of biogenic material (with lower absorption in the blue bands), as a consequence of the positive biases, increasing towards the shorter bands. This effect caused underestimations for the $a_{phy}440$ (-25.1% UPD) and $a_{cdm}440$ (-32.7% UPD) (similarly to the OC4v6 model), and some overestimations for the $b_{bp}440$ (15.3% UPD). Comparing the RTE and INS performances, one may note that the biases for the RTE were also considerably high, especially for the a_{cdm}, which was also mostly underestimated (-24.6% UPD). Thus, similarly to the OC4v6 model, for the QAA, 50% or more of the biases of the INS retrievals were likely due to natural sources of bio-optical variability and intrinsic uncertainties of the QAA model. Although mostly based on analytical inversion schemes, some IOPs (and specific properties) are empirically derived and/or

parameterized in the step by step process. Thus, the uncertainties in the R_{rs} and IOP data sets used to tune the model, as well as, their natural variability, are main sources of uncertainties for the QAA model. For instance, the b_{bp} spectral slope, which is retrieved using a band ratio (440/555) empirical fit, varied from -1.96 to -0.53 (mean, -1.35), whereas the measured values ranged from -2.3 to -1.1 (mean, -1.7). The a_{cdm} spectral slope (S), retrieved in a similar manner with an empirical band ratio fit, also showed some deviations varying from 0.0153 to 0.0167 nm^{-1} (mean, 0.0159 nm^{-1}), whereas the measured values ranged from 0.011 to 0.019 nm^{-1} (mean, 0.0154 nm^{-1}).

The GSM01 had some different results, with actually a higher $b_{bp}443$ bias using the RTE (32.8% RPD*) than INS (18.4% RPD*), and both with a higher SD (Table 5.11 and Figure 5.13d). In compensation, the Chl*a* and $a_{cdm}443$ had a better match using the RTE with an RPD* of 24.8% and 21.9%, respectively, against 36.3% and 35.4% using INS (Table 5.11). The high $b_{bp}443$ SD for both RTE and INS, indicates a high sensitivity of this product for even slight R_{rs} amplitude variations. The GSM underestimated all the RTE $b_{bp}443$ retrievals (-38.9% UPD), whereas the Chl*a* and $a_{cdm}443$ were closer to the 1:1 line (Figure 5.13e-f).

Table 5.11 - Statistical differences between the modeled and measured ocean colour products of the QAA and GSM01 using RTE and INS Rrs.

		RTE			INS		
		b_{bp} 440	a_{phy} 440	a_{cdm} 440	b_{bp} 440	a_{phy} 440	a_{cdm} 440
	UPD (%)	3.62	4.9	-24.6	15.3	-25.1	-32.7
QAA	RPD* (%)	8.69	14.6	31.1	18.1	23.1	37.3
	RMSE (m^{-1})	0.0003	0.009	0.015	0.0006	0.014	0.016
N=18	SD (m^{-1})	0.0001	0.005	0.008	0.0003	0.007	0.008
	r^2	0.82	0.97	0.77	0.85	0.89	0.79
		b_{bp} 443	Chl*a*	a_{cdm} 443	b_{bp} 443	Chl*a*	a_{cdm} 443
	UPD (%)	-39.8	-11.4	-17.9	-15.0	-44.1	-39.2
GSM01	RPD* (%)	32.8	24.8	21.9	18.4	36.3	35.4
	RMSE	0.0010	0.37	0.009	0.0006	0.27	0.014
N=18	SD	0.0005	0.19	0.005	0.0003	0.13	0.007
	r^2	0.56	0.84	0.89	0.61	0.94	0.85

GSM01 the RMSE and SD is in m^{-1} for $b_{bp}443$ and $a_{cdm}443$ and $mg.m^{-3}$ for Chl*a*. The number of match-ups is 18 because the Magellan Strait was left out of the analysis and St75 failed in the QAA inversion.

The systematic underestimation of the GSM $b_{bp}443$ could be due mostly to the lower b_{bp} spectral slope that the GSM uses (-1.0337), compared to the mean measured slopes (mean, -1.66, varying from 2.18 to -0.97). In the same manner as for the QAA, the INS biases caused higher $b_{bp}443$ retrievals and lower Chl*a* and $a_{cdm}443$ (-44% and -39% UPD, respectively) for the GSM (Table 5.11 and Figure 5.13d-f). The lower biases for the $b_{bp}443$ INS was actually obtained because of the higher $b_{bp}443$ retrievals, causing less underestimations, whereas the Chl*a* and $a_{cdm}443$ had higher underestimations. The moderately high biases obtained using the RTE revealed also for the GSM, the intrinsic uncertainties of the inversion scheme and parameterizations used for the specific IOPs. Besides of the variability of the b_{bp} slope, the $a_{phy}^*(\lambda)$ also diverged from the GSM optimized global fit (0.05582 $m^2.mg^{-1}$), ranging from 0.037-0.086 $m^2.mg^{-1}$ (mean, 0.062 $m^2.mg^{-1}$), as well as the a_{cdm} slope (*S*) that had a lower a mean of 0.0154 nm^{-1} against 0.0206 nm^{-1} for the GSM fit.

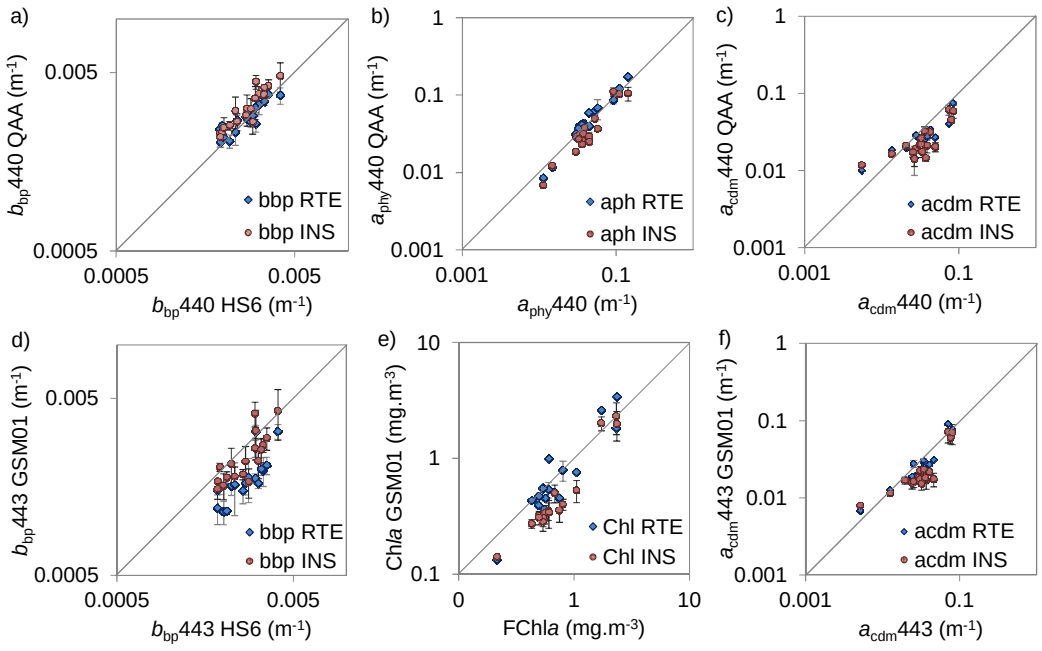

Figure 5.13 - Modeled versus measured ocean colour products of the QAA (a-c) ($b_{bp}443$, $a_{phy}443$ and $a_{cdm}443$) and GSM01 (d-f) ($b_{bp}440$, Chl*a* and $a_{cdm}443$) using RTE and INS. The error bars correspond to the averaged correlated and non-correlated errors and the plots are in log scale.

The parameterizations of the specific IOPs is a challenge for the semi-analytical models as there are few *in situ* data sets, especially for a_{cdm} and b_{bp}, across diverse biogeochemical provinces, to adequately tune the models (MARITORENA et al., 2002; IOCCG, 2006). Moreover, second order bio-optical variability that diverge from the global fits will still remain, unless other approaches are used, such as class-based models or analytical inversion schemes for these parameters. Thus, as discussed for the OC4v6 and QAAv5 models, the uncertainties inherent to the GSM01 may have accounted for 50% or more of the biases obtained for the INS products. Applying the ANOVA test the INS retrievals for both QAAv5 and GSM01 where not significantly different from the RTE retrievals (p>0.05), supporting an overall reasonable performance of the INS, with relatively low impacts of the R_{rs} biases.

In summary, for the semi-analytical models analyzed herein, the biases of the INS data set caused mainly overestimations of the b_{bp} and underestimations of the biogenic absorption coefficients (a_{phy} and a_{cdm}), which were consequent of the positive R_{rs} biases increasing towards the shorter bands, due to the predominant environmental noises that affected the *in situ* R_{rs} for both above and in-water methods (i.e., high illumination variations with a rapid changing sky; higher proportions of diffuse light and cloud glint effects). A considerable portion of the biases obtained for the INS ocean colour products were however, due to inherent uncertainties of the bio-optical models, as there were also moderately high biases when applying the RTE. Comparing the OC4v6 retrievals with the GSM Chl*a*, the RPD was somewhat lower (13% against 25%), denoting higher biases associated with the products obtained by the inversion schemes, likely due to the higher level of complexity of these approaches. Hence, the higher biases obtained for the INS semi-analytical retrievals were not only related to the higher impacts of the INS biases when using R_{rs} spectra (and not ratios), but also to the higher uncertainties intrinsic to the SA models. For all of the bio-optical retrievals using OC4v6, GSM01 and QAAv5, the INS generally raised the biases in approximately 10% (compared to the RTE), which was still within the requirements of ocean colour bio-optical accuracy (>35% for Chl*a* retrievals). One should attempt though, that these differences could be much higher when using solely one approach for the *in situ* R_{rs}, as these models showed a high sensitivity to slight R_{rs} spectral variations. The merged INS approach provided R_{rs} measurement less affected by the bulk environmental noises, which caused different

spectral biases in each for the *in situ* approaches, enabling a more robust performance for the ocean colour retrievals.

5.3.7. Final considerations

The uncertainties regarding *in situ* radiometry for both above- and in-water approaches can be considerably high without careful data acquisition protocols and adequate data processing schemes, as shown in the inter-comparison analyses of the present work. The R_{rs} measurements are obtained indirectly, after correction for contaminating surface reflection sources (above-water) or extrapolation through depth and transmission across the water-air interface (in-water approaches), using models and factors that introduce uncertainties in the retrievals. Besides this, the radiometric measurements are highly sensitive to changes in the illumination conditions, sea state, and IOPs of the water column, and during cruises in regions subjected to tough environmental conditions the challenges to obtain accurate processed *in situ* R_{rs} data are extremely difficult.

Regarding the above-water ASD the main sources of uncertainty were from illumination variation artifacts due to broken clouds and residual contaminations of cloud, Sun and sky glint, and bubble clouds generated by breaking waves. The sky glint contribution was reasonably corrected using the sky reflectance factor adjusted for the wind speed and SZA (MOBLEY, 1999). Significant residual contaminations however, were still present and were reduced by applying the RC and QC schemes. Such schemes were effective to reduce higher uncertainties on the R_{rs} retrievals caused by environmental variability, although some spectrally dependent biases still remained under-corrected for the shorter bands (blue-green). This correction scheme may be still recommended for above-water *in situ* radiometry since it is simple and reasonably effective, despite the complexity of the different contamination sources. A spectrally dependent RC model would be a better alternative to improve the L_w determination, however, it is not trivial to model the magnitude and spectral dependency of some sources that are highly variable, such as the cloud glint that varies with the type, thickness, coverage, and distribution of clouds. For more eutrophic and turbid waters, the white offset RC may be applied in a more conservative manner using the minimum R_{rs} NIR value, instead of a null baseline. For the QC filtering scheme, using the 400 nm band instead of a NIR band, proposed in other works (ZIBORDI et al., 2002; HOOKER et al., 2003), was also

effective to eliminate contaminated spectra that were highly biased at the shorter bands. Bidirectional effects were relatively minor yet important, especially for the stations with meso-eutrophic waters and high SZA, highlighting the importance of this correction especially for above-water techniques that measure at slanted viewing angles.

Regarding the free-falling profilers, i.e., HOCR and PRR, the measured R_{rs} was less affected by the environmental variability. Nevertheless, to obtain accurate R_{rs} measurements, even for these approaches, one needs to apply a series of correction schemes, and most importantly have a good criterion for the choice of the depth interval used in the extrapolation of the radiometric quantities. Using shallow depths is more desirable, but this procedure is much more subjected to environmental noises with high fluctuations of the light field distribution due to the wavy facets and intermittent presence of bubble clouds. At greater depths, on the other hand, signals are lower, and the K_d variation, bio-optical stratification, and Raman scattering effects are larger. As these effects increase with wavelength due to the higher water absorption, one may even consider using different depths intervals to retrieve more accurate extrapolated quantities, i.e., using shallower depths for longer bands (>550 nm). Even being very careful in this critical step, biases in the order of 10-20% may still be encountered between different casts and using either the deck or profiler sensors to normalize L_w. Since the deck sensor provides a direct measurement of the above-water downwelling solar irradiance, several authors argue that it should provide more accurate R_{rs} (MUELLER et al., 2003). Nevertheless, some authors also recommend using E_d from the profiler as a mean to reduce the in-water perturbations that affect both E_d and L_u in similar ways (MITCHELL; KAHRU, 1998). Their ratio could therefore normalize some of the environmental variability, and provide more accurate R_{rs}, even with a more biased E_d (compared to E_S). However, some differences exist in the noises affecting in-water E_d and L_u, both in magnitude and spectral quality, which also needs careful attention (e.g., focusing and defocusing effects on E_d and wave motion on L_u). On the other hand, there are also uncertainties associated to the deck sensor, due to the platform tilt and spatial distance with the profiler. Thus, none of the quantities are unbiased, and the averaging of the casts and the R_{rs} determined using both the profiler and deck sensors was considered the best alternative to smooth the main environmental noises and retrieve a more accurate R_{rs}.

Regarding the TriOS approach evidence was provided of higher effects associated to platform shading and biases of the extrapolation procedure that used wider depth intervals. These effects were prominent for higher Chl*a* waters, i.e., with more light attenuation and bio-optical stratification. The in-water effects were so large that the R_{rs} obtained using the deck sensor amplified the L_u biases in such a way that the differences were greater than 50%. Using the E_d from the profiler normalized most of these effects, yielding much closer R_{rs} compared with the other approaches. Hence, for the winched TriOS approach, the R_{rs} obtained using E_d from the profiler was much more reliable.

The free-falling profilers are commonly considered as providing the most accurate radiometric measurements, due to the lower impact of ship perturbations (i.e., shadowing and in-water disturbance) and no effects of sea surface reflection (HOOKER et al., 2002; HOOKER; MARITORENA, 2000; MUELLER et al., 2003). Nevertheless, the uncertainties solely between casts of the HOCR were on average 10-12%, denoting that under slightly different environmental conditions, even the most accurate approach may suffer from significant environmental noises. Since each approach had biases caused by different environmental perturbations, the averaging of all approaches aimed to normalize most of these variations and obtain a more accurate R_{rs}, less dependent on such effects. A recent approach proposed by Lee et al. (2013), the skylight-blocked approach (SBA), aims at retrieving more robust L_w, sort of merging the above and in-water approaches. The SBA uses an adapted HOCR system attached to a floating buoy that drifts away from the platform, and has a L_u sensor pointed down just above the water surface covered by a black cone that protects from skylight rays that reflect into the sensor FOV. The rationale is to obtain direct measurements of water leaving radiance without having to extrapolate subsurface L_u, and exempt from sea surface reflection. The approach was tested in Lake Michigan (USA) for mild sea state conditions and showed promising results with a good consistency and precision of the measurements. The challenge however, is to apply it under rough environmental conditions with agitated seas, where the sensor may be constantly submerging and emerging by small waves or the cone can deflect due to swells, allowing skylight reflected rays into the sensor FOV. Hence, it still needs to be tested at sea under adverse conditions to evaluate its general capability. An important advantage of this system is also that it allows one to obtain a high number of simultaneous L_w and E_d acquisitions,

enabling the application of a robust quality control scheme and obtaining averaged data, likely with less environmental noises (with > 60 measurements in a few minutes). Anyhow, whatever the approach that is applied, there will certainly be high environmental noises under tough environmental conditions, as reported in the present work. Hence, the overall recommendation is to use different approaches, with diverse instrumentation, and as many repetitive measurements as possible, i.e., at least 10 casts for the above-water and 3 for the in-water, to: a) identify outliers in filtering quality control schemes; b) check for the precision of a particular approach; c) check the consistency between the measurements of different approaches; and d) finally obtain an averaged R_{rs} using all approaches or selecting the "least biased", that reduces the spectral biases and noises inherent to each approach.

In the closure analysis the final merged INS had differences of 18-34% (RPD*) with the modeled RTE, indicating moderate to large uncertainties associated mostly to the measured R_{rs}, but also partly to uncertainties in the modeled R_{rs}. The largest uncertainties in the INS were observed at the stations with high illumination variation. Rough sea state conditions played a minor, but somewhat important role in the environmental biases for both the above and in-water approaches, due to the wavy facets and bubble cloud effects. The worst case was for St 51 with the combination of high illumination variation, strong winds (>7 $m.s^{-1}$) and high waves (>2 m), showing differences >40% with the RTE.

The band ratios reduced the biases to much lower proportions (i.e., by ~50%), but did not eliminate them completely, since some contaminations were spectrally dependent, increasing towards the shorter bands (i.e., illumination variation artifacts, higher proportion of diffuse light and cloud glint). When it is not possible to avoid cloudy skies, applying higher-level correction schemes with filtering quality control schemes is desirable, as well as using f/Q factors that consider not only the IOP variability, but also the illumination conditions, taking into account the different proportions of diffuse and direct light. More diffuse skies, for instance, may enhance the *in situ* R_{rs} of both above and in-water approaches by up to 10%. Although a considerable amount of *in situ* radiometric measurements are realized under cloudy conditions, these sources of uncertainty are generally ignored in R_{rs} correction schemes (DOXARAN et al., 2003).

The impact on R_{rs} may not be so large, but may result in a systematic bias that amplifies in bio-optical modeling for ocean colour retrievals. Further radiative transfer simulations providing comprehensive look-up-tables of f/Q ratios for different proportions of diffuse skies, with varying IOPs and sensor-solar geometries, are thus desirable to improve such corrections.

The MM01 approach revealed some biases related to assumptions of Case 1 water conditions and the global parameterizations. The differences between the MM01 R_{rs} and INS were slightly smaller than those between the RTE and INS, due mainly to compensation effects of under and overestimations of the MM01 b_{bp} and a_{nw}, rather than better performance of the MM01 and INS match. The application of such forward models need careful attention and analysis of the bio-optical variability, since some relations (or assumptions), such as the relations of CDOM and Chl*a*, even for typical Case 1 waters, may vary (or not hold) depending on region and season (SIEGEL et al., 2002; MOREL; GENTILI, 2009). The b_{bp} model should also be further improved, with investigations on the variability of the b_{bp} efficiency and spectral dependency across different biogeochemical regions. In the same manner, the a_{phy}*, although measured more comprehensively, still requires further investigations of its variability with the community size structure and physiological state, and of ways to capture this variability in forward models and inversion schemes.

In respect to uncertainties in the IOP measurements, the largest biases were obtained for a_s and a_d due to the low signals with measurements more sensitive to instrument noise and small sample variations. Thus, adequate procedures and instrumentation should be used to make these measurements more accurate. For instance, longer cuvettes for the a_s may be required to increase the optical pathlength in clearer waters. Longer pigment extraction procedures with efficient solvents may also be required for the a_d measurements in clearer waters. The b_{bp} is also a highly sensitive measurement, and even the choice of the b_{bw} can make a difference (~10%) on the b_{bp} retrieval, especially for the blue bands and in clear waters. Spectral variations should always be checked if they are in natural order, or from instrument issues, as was observed in the present work for two bands that had to be left out of the analysis, probably due to calibration distortions that occurred during the cruise. The handling and transport of these

instruments can cause such artifacts, and even with regular calibration, the consistency of the measurements should be always checked.

Regarding the Chl*a* determinations, the differences between the various methods were considerably large (>30%), with significant impact on bio-optical modeling. The HPLC is unarguably the most accurate technique for pigment determination, as it separates each pigment before measuring the absorption peak. Nevertheless, there may be significant biases in the sample preparation procedure, which could compromise the analysis. The 90% acetone is shown in several works to have a much lower extraction efficiency compared to 100% methanol, and the use of these different solvents may result in differences over than 30% in the measured Chl*a*. These differences can be especially large in the presence of phytoplankton groups with hard cell walls, which are more difficult to extract. Solvents with higher extraction efficiencies are highly recommended, and when not possible, some correction for the underestimation is desirable, as proposed herein. The standard fluorimetric method and the HPLC provided reasonable agreement, since both used 90% acetone and since compensations effects likely occurred due to the presence of both Chl*b* and Chl*c*. The spectrofluorimeter method was considered the most accurate due to the precision of the method and efficient extraction procedure (with 100% methanol). Further inter-comparison analysis of different solvents and techniques to measure Chl*a* are still required and highly recommended to understand better the differences and obtain the most accurate values, which are essential for ocean-colour and biogeochemical studies.

The INS uncertainties resulted in 10% higher biases for the retrieval of ocean colour products with both empirical (OC4v6) and semi-analytical algorithms (QAAv5 and GSM01). As the dominant environmental noises tended to overestimate the R_{rs} with a spectrally dependent positive bias increasing towards the shorter bands, this effect caused underestimation of Chl*a* and the biogenic absorption coefficients, and overestimation of b_{bp}. These rather systematic biases could cause some distortions when tuning a model with *in situ* measurements, or lead to misinterpretation of the bio-optical variability. Nevertheless, in view of the comparisons with the RTE retrievals, the INS biases had still a relatively small impact on the derived ocean colour products, and

within required uncertainty limits. Hence, the INS errors may be still acceptable for such applications.

The present work contributes, with important comparison exercises, to *in situ* radiometry and closure analysis, in a realistic framework of an oceanographic expedition across optically complex waters and under mostly adverse environmental conditions across the Southern Atlantic and Southeast Pacific. The main sources of uncertainties were identified and discussed for each approach and environmental condition, and better processing schemes were proposed to obtain more accurate *in situ* R_{rs}. Above all, our main recommendation is to use varied approaches and as much measurements as possible to derive an averaged R_{rs}, smoothing out the major sources of environmental variability. The radiometric quantities are highly sensitive to slight variations in the illumination and sea state conditions and further improvements in the correction schemes for both above and in-water approaches are desirable, some following recommendations of standard protocols (MUELLER et al., 2003) and others mentioned throughout the work (e.g., improvements in the *f/Q* LUTs). Recommendations are also given for the bio-optical measurements of the IOPs and Chl*a*, which require high quality care, as large uncertainties could also be associated to these data sets. The accuracy of all these quantities is vital for ocean colour modeling, studies of bio-optical variability, and ultimately satellite monitoring, as their biases may propagate to larger errors in the retrieved ocean colour products. Regional and global data sets that integrate these data types from diverse laboratories, with different instrumentation and data processing schemes, should provide the uncertainty levels associated to each quantity. In the present work, the INS uncertainties were over than 10%, but still within acceptable levels for bio-optical modeling. Even though higher accuracy is desirable for the *in situ* radiometric measurements, the state of the art parameterizations of both empirical bio-optical models and inversion schemes also need further improvements to properly describe and enable further understanding of the bio-optical variability in the world oceans.

6 BIO-OPTICAL VARIABILITY

6.1. Introduction

The present Chapter presents analysis of the bio-optical variability across the Southern Atlantic and Southeast Pacific, for the end of the austral summer of 2011. The empirical OC4 maximum band ratio (MBR) model has generally a good accuracy for Case 1 waters in which the biogenic components mainly co-vary with the phytoplankton assemblage (O'REILLY et al., 2000). The global *in situ* NOMAD base used for the development and tuning of such model, is constantly updated with new surveys across the oceans. Nevertheless, there are still large unsampled regions, which may compromise the performance of this and other OCR models when applied to satellite data, and limit the interpretations of ocean colour variability for these regions (SZETO et al., 2011).

The first order variation of the MBR is linked to the bulk phytoplankton biomass, indexed by the Chl*a*, and the co-varying biogenic material. The deviations of the MBR versus Chl*a* relation, in respect to the global fit, are due partly to the uncertainties regarding the R_{rs} and Chl*a* measurements (as shown in the previous Chapter), and partly to second order variations of the bio-optical properties of the living and non-living particle assemblage and dissolved substances (MOORE et al., 2009; LOISEL et al., 2010; SZETO et al., 2011). Such second order variations may be associated with the phytoplankton community structure, varying in terms of size, accessory pigment composition, intracellular pigment concentration, cell wall composition and shape; variations in the bulk particle assemblage in terms of composition and size distribution (PSD) (including detritus, hydrosols, minerals, bacteria and virus) and varying proportions of the coloured dissolved and particulate organic matter (CDM) (SZETO et al., 2011). All of these constituents determine the bulk optical properties of a specific sampling site, and any variation from the mean relation that links each of these with the Chl*a* and MBR will result in a second order variation, and dispersion of the OC4 model.

Recent studies have shown that three specific optical properties may potentially trace the second order variations that cause the deviations in the MBR model: i.e., the particle backscattering coefficient and phytoplankton absorption coefficient normalized by

Chl*a*, (b_{bp}* and a_{phy}*, respectively) and the CDM absorption coefficient (a_{cdm}) normalized by the non-water absorption (a_{nw}) (a_{cdm}/a_{nw}) (LOISEL et al., 2010; SZETO et al., 2011). The first two may be related to the efficiency of a particle to backscatter and absorb light, in respect to each milligram of Chl*a*, and the third is related to the variations in the proportions of the CDM in respect to the bulk biogenic material. The identification of these sources of second order variability may provide means to enhance bio-optical modeling for OCR products, as well as to obtain further information associated with the biogeochemical parameters that determine these optical variabilities.

The b_{bp}* may vary with the size, shape, concentration and refractive index of the bulk living and non-living particle assemblage. Higher b_{bp}* values for instance, may be related to greater proportions of smaller particles and/or with high index of refraction, whereas lower values may be associated with greater proportions of low index larger particles (LOISEL et al., 2010). Nonetheless, even though there are strong evidences that the b_{bp} is an important source of ocean colour variability across the ocean (BROWN et al., 2008) and that there are strong relations between the b_{bp} efficiency and the particle size distribution (PSD) and refractive index, there are still many unknowns regarding the actual sources of oceanic b_{bp}. Whereas, some works have discussed that non-living submicron hydrosols and detritus may be the strongest oceanic b_{bp} sources (STRAMSKI et al., 2001), others have discussed that larger phytoplankton sized particles may be in fact significant b_{bp} contributors (DALL'OLMO et al., 2009; WHITMIRE et al., 2010). As b_{bp} *in situ* measurements have only been available more recently with the emergence of new instrumentations, there are only a few measurements across the oceans (only 80 for the NOMADv2). Hence, there are still many issues to resolve in respect to the sources and variability of this optical property.

The specific phytoplankton absorption coefficient (a_{phy}*) will vary with the exposure of each chl*a* molecule to light, which depends on the intercellular pigment organization, composition (accessory pigments) and concentration (SATHYENDRANATH; PLATT, 2007). The higher exposure to light, the higher absorbing capacity of each chl*a* molecule and higher a_{phy}*. Cells that have pigments organized in chloroplasts (eukaryotes) and produce a higher concentration of pigments, on the other hand, will suffer pigment self-shading effects that diminishes the a_{phy}*, known as the "packaging

effect" (SATHYENDRANATH et al., 1987). In natural environments the variability in the a_{phy}* may be associated with the dominant size structure of the phytoplankton community (SATHYENDRANATH et al., 1987; CIOTTI et al., 2002). Small picoplankton cells usually have low intracellular pigment concentration and high a_{phy}*, while large microplankton have higher pigment concentration and lower a_{phy}*. Other factors that may have also significant effects on the a_{phy}* are the composition of accessory pigments and the photoacclimatation processes associated with the light availability and cell physiological state (due to age, nutrient availability and temperature) (BRICAUD et al., 2004).

The a_{cdm}/a_{nw} ratio is related to the variations in the proportions of CDOM and detritus in respect to the bulk biogenic absorption, and more specifically to the phytoplankton absorption. The variability of the CDM in respect to the phytoplankton biomass has received more attention in the past few years, especially after the proposed CDOM index of Morel and Gentili (2009). It was previously thought that the CDM had a relatively stable co-variation with Chl*a* for Case 1 waters, as it should be essentially regulated by the past and present phytoplankton living stock (BRICAUD et al., 1998). Nonetheless, recent studies have shown that there may be in fact significant variations in the CDM proportions even for remote open ocean waters, linked to different loss and source processes: of plankton exudation, zooplankton grazing, bacterial decomposition, photodegradation, physical fragmentation, current transport, upwelling and downwelling processes, among others (SIEGEL et al., 2002). Hence, the variability of the CDM proportions is much more complex than previously thought and may actually provide important information regarding regional and local biogeochemical processes (SIEGEL et al., 2002; MOREL; GENTILI, 2009).

In this context, the present work is aimed to analyze the bio-optical variability across the Southern Atlantic and Southeast Pacific, which comprehends a high range of biogeochemical provinces (BGCP) with relevant roles on global and regional carbon cycles, and which are extensive unsampled regions not contemplated in the NOMAD base. The purposes of the analysis were to characterize the surface distribution of the bio-optical properties across the different BGCPs, identifying the sources of first and second order variability related to PFT distribution, particle assemblage and processes

regulating the CDM sources and losses. A second goal was to identify the impacts of the bio-optical variability on the OC4 MBR model for the study region, and compare with previous analysis across different oceanic regions, such as proposed by Szeto et al. (2011). The ultimate goal was to synthetize the variability applying multivariate statistical techniques and a clustering analysis to propose a Regional Specific Optical Water Types (R-SOWT) classification scheme. The R-SOWT was compared to the OWT approach proposed by Moore et al. (2009) and evaluated in terms of the definition of dynamic optical water types with relevant biogeochemical information and to enhance OCR products for the study region, applying class-specific parameterizations schemes for semi-analytical models, i.e., the QAA and GSM.

6.2. Material and Methods

The present work was divided in four main steps: a) Analysis of the distribution of the bio-optical properties across the study region; b) Impacts of the variability for the OC4v6; c) Synthesis of the variability and proposal of the Regional Specific Optical Water Types (R-SOWT) classification scheme; and d) Application of the R-SOWT for class-specific parameterizations using the QAA and GSM models.

For the identification of the BGCPs across the study region and the distribution of the bio-optical properties, 59 stations (CTD + FL) were used. The focus of the present work was on the horizontal surface distribution of the IOPs, however the vertical profiles of the CTD stations were also used in some analysis to complement discussions of the processes governing the bio-optical variability.

To characterize the bio-optical distribution and its relations with the biogeochemical properties, the following parameters and indices were used: a) the Chl*a*3, as an index of the phytoplankton biomass; b) for the IOPs: the absorption coefficients of the phytoplankton ($a_{phy}443$), CDOM (a_s443), detritus (a_d443) and CDM ($a_{cdm}443$) and the particle backscattering coefficient ($b_{bp}443$, 555); d) for the specific IOPs: the specific phytoplankton absorption coefficient (a_{phy}*443, $a_{phy}443$/Chl*a*), the specific particle backscattering coefficient (b_{bp}*555, $b_{bp}555$/Chl*a*), the b_{bp} spectral slope (η) (443-555 nm), the a_{cdm}/a_{nw} ratio and CDOM index (MOREL and GENTILI, 2009) and the a_{cdm} spectral slope (S_{cdm}) (380-500 nm); e) for the phytoplankton community structure: the

HPLC pigment ratios and sized fractions of micro, nano and pico, determined according to Vidussi et al. (2001) and Uitz et al. (2006); identification and cell counts of the microscopy analysis (available for 7 stations); and the size indices of Bricaud et al. (2004) (B04 SI) and Ciotti and Bricaud (2006) (CB06 SI); and d) for the microbial assemblage: the total heterotrophic bacteria concentration (HB), and normalized by Chl*a* (HB*); the percentages of the groups of: High Nucleic Acid (HNA) bacteria, Low Nucleic Acid (LNA) bacteria, picoeukaryotes (EUK), *Synechoccocus* cyanobacteria (SYN) and *Prochlorococcus* (PROCH); and the particle size distribution (PSD) slope (ξ) for the microbial assemblage, determined with the power law fit of cell concentration normalized by the mean diameter vs. the mean diameter of each group.

The Morel and Gentili (2009) CDOM index (MG09 CI) is a unitless quantity that specifies the deviation of the CDOM content in relation to the global CDOM vs. Chl*a* relation, and was obtained using the following equation:

$$\phi_{\mathrm{CDOM}} = a_{\mathrm{s}}412/\{0.0524[\mathrm{Chl}a]^{0.63}\} \tag{6.1}$$

Values higher than 1 mean that the CDOM is higher in respect to the global relation with the phytoplankton biomass, whereas values lower than 1 are for lower CDOM. Morel and Gentili (2009) developed a look-up-table (LUT) of the index based on the global relation of Equation 6.1, and the CDOM deviations using simulated MM01 R_{rs} ratios $R_{\mathrm{rs}}(412/555)$ and $R_{\mathrm{rs}}(490/555)$. The first ratio is highly influenced by CDOM, whereas the second is more affected by phytoplankton pigments, hence higher CDOM would cause a lower $R_{\mathrm{rs}}(412/555)$ and vice-verse. This LUT is routinely applied to retrieve the index from satellite. For the present analysis of the *in situ* data set the index was retrieved using Equation 6.1 with measured $a_{\mathrm{s}}412$. Some satellite imagery was also used to analyze the spatial variability of the index using the standard OCR product with MODIS 8-day composites provided by the NASA Giovanni Ocean Colour Data Product Visualization portal.

The PFT size fractions determined using the HPLC pigment composition and concentration, used a multivariate regression model of the biomarker pigment ratios following Uitz et al. (2006) adapted from Vidussi et al. (2001):

$$\text{pico}(\%) = 100 * (0.86[\text{Zea}] + 1.01[\text{Chl}b + \text{D\_Chl}b]) / \text{DP} \quad (6.1a)$$

$$\text{nano}(\%) = 100 * (0.60[\text{Allo}] + 0.35[19'\text{BF}] + 1.27[19'\text{HF}])/\text{DP} \quad (6.1b)$$

$$\text{micro}(\%) = 100 * (1.41[\text{Fuco}] + 1.41[\text{Perid}])/\text{DP} \quad (6.1c)$$

Where DP is the sum of the weighted fractions of the diagnostic pigments:

$$\text{DP} = (0.86[\text{Zea}] + 1.01[\text{Chl}b + \text{DV\_Chl}b] + 0.60[\text{Allo}] + 0.35[19'\text{BF}] + 1.27[19'\text{HF}] + 1.41[\text{Fuco}] + 1.41[\text{Perid}] \quad (6.1d)$$

The Bricaud et al. (2004) size index (B04 SI) provides the combination of the three fractions to define a unique number that is proportional to the dominant size fraction:

$$\text{SI(B04)} = (1 * [\text{pico}\%] + 5 * [\text{nano}\%] + 50 * [\text{micro}\%])/100 \quad (6.2)$$

The pigments ratios used for auxiliary analyses of the phytoplankton composition (divided by TChl*a*) were, among others: Zea* as an indicator of *Synechococcus* and *Prochlorococcus*; Pras* indicator of Prasinophyceae; 19'HF+19'BF* for Haptophytes

(including Coccolithophorids) and some dinoflagellates; Chl$c_{1,2}$* for diatoms; and Perid* for dinoflagellates. The Ciotti and Bricaud (2006) size index (CB06 SI) is the same as exposed in Equation 3.11 (Chapter 3) and was estimated using the measured a_{phy}. The pico and micro endmembers (normalized by $a_{phy}505$) were obtained from Ciotti et al. (2002) and Ciotti et al. (2006).

The identification of the water masses and BGCPs along the MV1102 transect was made using temperature-salinity-oxygen diagrams (T-S) and surface maps of the Chl*a*, using the Ocean Data View (ODVv4) Software (SCHLITZER, 2002). The surface distribution of the IOPs and bio-optical indices were also analyzed using surface maps generated in ODVv4. Analyses of larger scale Chl*a* distributions across the study region were also complemented with OC3M MODIS maps provided by the NASA Giovanni Ocean Colour Data Product Visualization portal.

The deviations of the OC4v6 MBR empirical model (Equation 3.14) caused by the second order variations of the bio-optical properties were analyzed comparing modeled and measured Chl*a* and using statistical uncertainty indices of the relative and absolute differences (RPD* and RPD) and regression analysis (r^2 and RMSE) (as in Equations 5.1-3, shown in Chapter 5). The sources of under and overestimations were analyzed partitioning the data set into quartiles of the 25% lowest (D1) and highest (D2) specific IOPs (a_{phy}*, b_{bp}*, a_{cdm}/a_{nw} and CDOM index) and determining the mean RPD of each quartile, following Loisel et al. (2010). In order to avoid any influence of the environmental and instrumental biases on the R_{rs}, as well as to enhance the match-ups with the FL stations, the R_{rs} used for all stations (CTD + FL) was determined using the RTE M_*f*/*Q* approach, as in Chapter 5.

To synthetize the bio-optical variability across the study region multivariate statistical analyses were applied using Spearman Rank non-parametric correlation (r_s) and Principal Component Analysis (PCA). A K-means cluster analysis was applied to group the stations into bio-optical water types, using the specific IOPs and bio-optical indices, i.e., CB06 SI, MG09 CI, b_{bp}*555 and η, all of which may be obtained by OCR bio-optical models for further satellite applications. The regional classification scheme, named after Regional Specific Optical Water Types (R-SOWT), was compared with the Optical Water Type (OWT) approach of Moore et al. (2009), in terms of the efficiency

to map classes associated with first and second order bio-optical variations, with relevant information regarding the PFT distribution, particle assemblage and the CDM variability. The class-based approaches were finally applied for class-specific parameterizations of SA models i.e., QAA and GSM, and compared with the performance of the global fits used in each model, to analyze their potential application for the enhancement of OCR products in the study region.

6.3. Results and discussions

6.3.1. Characterization of the bio-optical distribution

6.3.1.1. Identification of the biogeochemical provinces

The MV1102 stations were grouped within the biogeochemical provinces (BGCP) defined according to Longhurst (2007) by their geographical location and physico-chemical properties of the water masses, as shown in the T-S diagram and surface maps of Figure 6.1. Since the province boundaries are spatio-temporally dynamic, with a marked seasonal latitudinal variation for the study region (LONGHURST, 2007), the identification of the waters masses with their biophysical properties enabled a finer definition of the boundaries for the study period (Feb-Mar 2011, end of the austral summer). A total of 6 provinces with very distinct properties were identified within the sampled transect: the Benguela Current Coastal Province (BENG); the South Atlantic Gyral Province (SATL); the South Subtropical Convergence Province (SSTC); the Subantarctic Water Ring Province (SANT); the Southwest Atlantic Shelves Province (FKLD) and the Chile-Peru Current Coastal Province (HUMB).

The first station (St 01) off the coast of South Africa had a much lower temperature and salinity (13.4^{o}C and 34.9) and higher oxygen concentration (5.7 ml.l^{-1}) than the adjacent stations, indicating the influence of the Cape Peninsula Upwelling Cell (CP) (34^{o} S), within the Benguela Current Coastal Province (BENG) (LONGHURST, 2007). The upwelling in the southern sector of the BENG is more occurrent during the austral summer due to the predominance of favorable intensive southwestern winds, and is characterized by pulses of strong wind-driven upwelling events and intermediate relaxation phases (HARDMAN-MOUNTFORD et al., 2003; SHILLINGTON;

REASON, 2006). The Chl*a* of St 01 confirmed the presence of nutrient enriched upwelled waters, being much higher than the adjacent stations (3.78 $mg.m^{-3}$) (Figure 6.1d). Continental inputs of river discharge, runoffs, coastal erosion, rain fall and aerosol dusts from the South African desert, with micronutrient depositioning (KRUEGER et al., 2008), also contribute for the high productivity of this region, sustaining high fishery stocks (SHILLINGTON; REASON, 2006). Colonial micro-sized diatoms usually dominate the coastal phytoplankton blooms during the strong upwelling events. After silica depletion, dinoflagellates succeed the bloom in the relaxation phase, some of which may be even of toxic species, causing red tides with massive fish mortality (i.e. the dinoflagellate *Karenia Brevis sp.*). These events are usually related to oxygen-deficient waters (< 2 $mg.l^{-1}$) (PITCHER et al., 2008), which was not the case of St 01, more characteristic of recent upwelled waters, likely dominated by diatoms.

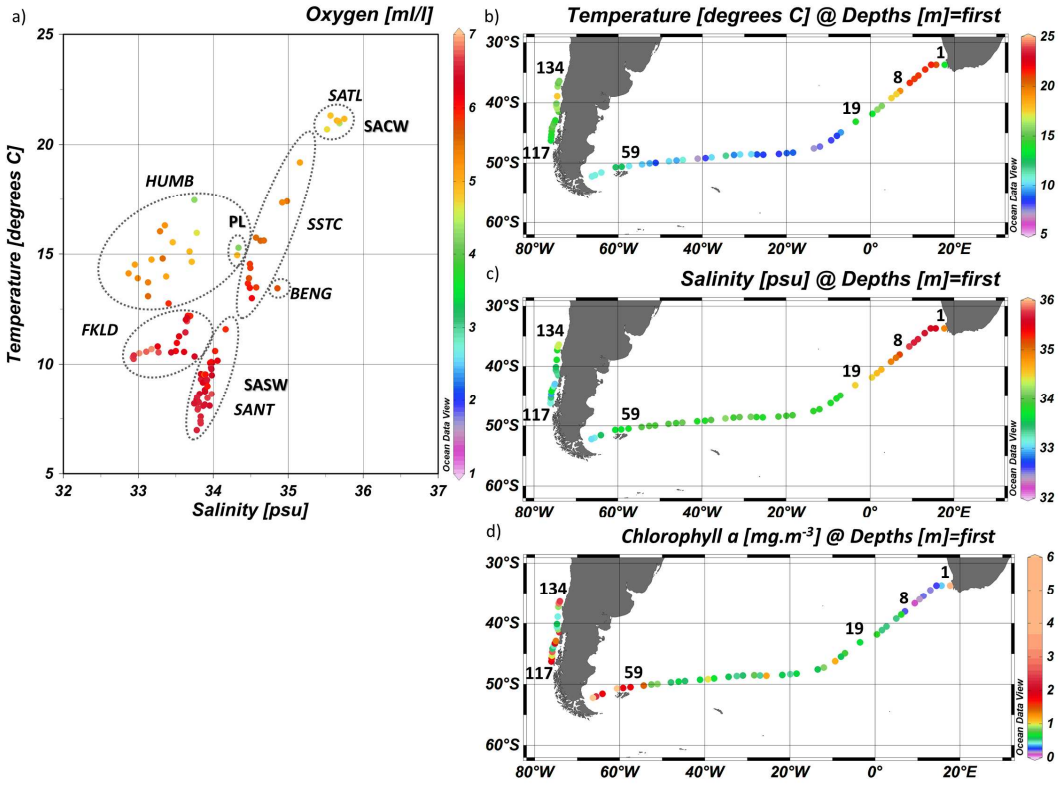

Figure 6.1– Temperature-Salinity diagram, and oxygen concentration determined from a CTD package (a); and surface maps of the: temperature (b), salinity (c) and Chl*a* (n=59).

The following stations in the southeastward direction (St 02-08) had the highest temperature and salinity (20.8 ±0.7^{o}C and 35.6 ±0.1) and the lowest oxygen concentration (4.8 ±0.2 ml.l^{-1}), indicating the presence of the surface layer of the South Atlantic Central Water (SACW), within the South Atlantic Gyral Province (SATL) (STRAMMA; ENGLAND, 1999; STRAMMA, 2001; MERCIER et al., 2003) (Figure 6.1). The lowest Chl*a* for this group of stations (mean, 0.19 ±0.09 mg.m^{-3}) was characteristic of the deeply stratified oligotrophic waters of the SATL (AIKEN et al., 2000). The subtropical gyre is a stable environment with low wind stress and seasonal variations of the solar irradiance (in both intensity and daylength). Hence, the nutricline is maintained very deep throughout all seasons, especially towards the center of the gyre (> 100 m). During the austral summer, there is an expansion of the gyre reaching its southern most limit up to ≈ 35^{o} S (LONGHURST, 2007), which was approximate to St 08 (38^{o} S). The most stratified and oligotrophic waters of the gyre towards its center, are generally dominated by small prochlorophytes (BOUMAN et al., 2011). Stations 06 and 07 with the lowest Chl*a* (0.13 and 0.08 mg.m^{-3}), were more characteristic of such conditions. At the borders of the gyre, the bowl-shaped isodepths for nutrients slope upwards towards the edges, shallowing the nitracline and enhancing phytoplankton growth. Hence, the SATL borders are marked by an increase in the Chl*a*, with greater contributions of *Synechococcus* and small flagellates (LONGHURST, 2007). This was the case of stations 02-05 and 08, with an increasing Chl*a* gradient (0.22±0.08 mg.m^{-3}). Station 02 may have had also some influence of the BENG coastal province due to its proximity and higher Chl*a* (0.367 mg.m^{-3}). Nonetheless, since the temperature and salinity demarked a greater influence of the SACW, which was very distinct from St 01 of the BENG, St 02 was considered to belong to the SATL province.

For complementary analysis showing a more broad spatial coverage of the distribution of the Chl*a* field among the BGCPs, a monthly composite of the OC3M averaged over the sampling period (18/02-14/03/11) is shown in Figure 6.2. The currents and frontal zones were mapped according to Stramma and England (1999) using averaged climatologies and representing approximate locations. In the OC3M map one can clearly observe the highly productive waters of the BENG encompassing St 01 and the southward expansion of the SATL up to 35-40^{o}S encompassing stations 02-08, with the

most oligotrophic waters towards its center (St 06 and 07) and increasing Chl*a* at its borders (St 02-05 and 08).

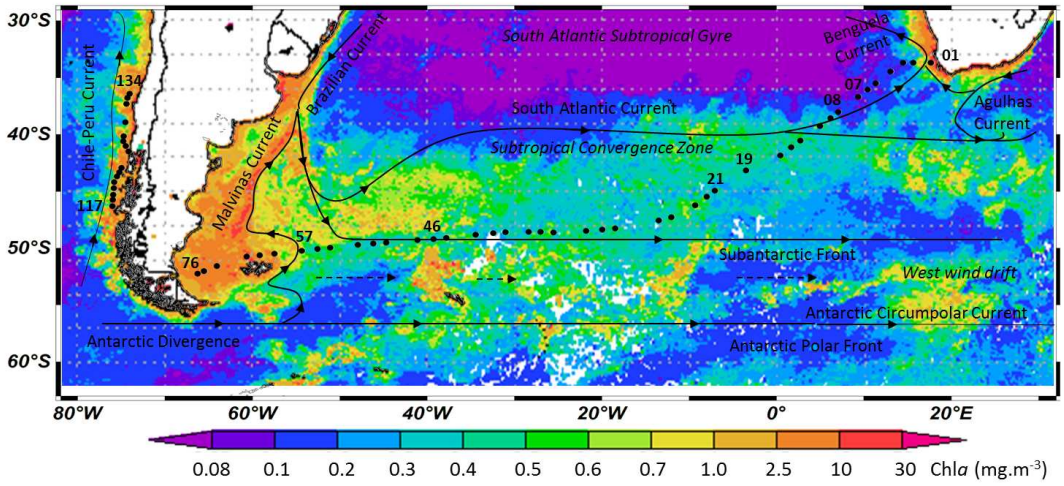

Figure 6.2 – MODIS OC3M map averaged for the sampling period (02/18-03/14/2011) (4 km), with the currents and frontal systems indicated, according to Stramma and England (1999) The black dots correspond to the CTD and FL stations.

Stations 09-19 showed a sharp temperature-salinity gradient diminishing towards the south (up to 43°S) (14.1-17.4°C and 34.5-35.0), concomitant with an increase in the oxygen concentration (5.8 ±0.1 ml.l^{-1}), characteristic of the frontal zone of the South Subtropical Convergence Province (SSTC) (STRAMMA; ENGLAND, 1999; STRAMMA, 2001; MERCIER et al., 2003) (Figure 6.1). The Chl*a* levels were somewhat higher than the SATL (0.52 ±0.17 mg.m^{-3}) (Figure 6.1 and 6.2), indicating the enhancement of phytoplankton biomass typical of the Subtropical Front (STF) (AIKEN et al., 2000). The SSTC is characterized by a persistent higher Chl*a* zone (≈0.3 mg.m^{-3}), due to the constant convergence of the northern SACW and southern Subantarctic Surface Water (SASW), promoting biomass accumulation and mixing of nutrients that are limiting in either one of the water masses i.e., iron in the High Nutrient Low Chlorophyll (HNLC) waters of the SASW and nitrate in the SACW. The intrusions of the warmer and more saline SACW over the colder and less saline SASW with meanderings, also promote a near-surface thermal stability which favors the

development and maintenance of phytoplankton blooms (LONGHURST, 2007). The SSTC is hence, characterized by permanent moderate to higher Chl*a* waters, generally dominated by diatoms during spring and summer blooms, and *Synechococcus* and small flagellates throughout the other seasons (AIKEN et al., 2000; LONGHURST, 2007).

The following stations in the southeast direction (St 21-57) had the lowest temperatures, with a lower salinity (9.0 ±1.1^{o}C and 33.9 ±0.1) and high oxygen concentration (6.3 ±0.2 ml.l^{-1}), indicating the presence of SASW of the Subantarctic Water Ring Province (SANT) (Figure 6.1) (STRAMMA; ENGLAND, 1999; STRAMMA, 2001; MERCIER et al., 2003). The SANT lies between the SSTC and Antarctic Polar Province (ANTA), being limited in its northern portion by the STF and in the south by the Subantarctic Front (SAF) (Figure 6.2). The intensive and persistent westerlies and the fast flowing Antarctic Circumpolar Current (ACC) with active meandering and eddy shedding, especially in the frontal zones of the STF and SAF, characterize the SANT as a highly dynamic province of the Southern Ocean. The Chl*a* gradient was somewhat higher compared to the SSTC (mean, 0.71 ±0.25 mg.m^{-3}) and showed a high spatial variability with a pattern of intermittent higher and lower Chl*a* patches (Figure 6.1d and 6.2). The higher Chl*a* levels encountered during the MV0211 was likely associated with the seasonal summer phytoplankton bloom across the SANT (LONGHURST, 2007). The spatial heterogeneity of the Chl*a*, denoted also the higher complexity of this province with different processes simultaneously interacting in the controls of the phytoplankton growth and decay.

The most extensive phytoplankton bloom of the SANT occurs during the austral spring (November), coincident with the shoaling of the mixed layer depth (MLD), induced by the increasing solar heat flux, diminishing wind stress and sea ice retreat from the higher latitudes (LONGHURST, 2007). In this nutrient enriched and more stable upper layer environment, phytoplankton grow and accumulate over extensive areas across the SANT, as observed in the MODIS OC3M monthly composite image of November 2010 in Figure 6.3. The bloom starts in the western region, where there are more continental sources providing iron enriched inputs (i.e. the Patagonian and Malvinas Shelves, Antarctic Peninsula, South Georgia and South Sandwich Islands), and is advected eastward by the ACC (LONGHURST, 2007). The spring bloom decays throughout the

season, likely associated with nutrient depletion (i.e. silica and iron) and zooplankton grazing, and a second bloom peaks during the mid-summer (January-February), although in a smaller and more restricted spatial scale (BOYD, 2002), as shown in Figure 6.2. This second peak may be triggered by the renewal of the nutrients in the upper layer, through remineralization processes, and new inputs, which may be from ice melting and runoffs from adjacent continental systems and upwelling cells formed by eddies, induced by topographic effects that cause changes in the ACC flow (e.g. in the surroundings of the Scotia Ridge, South Sandwich and South Georgia islands) (MOORE; ABBOTT, 2000; BOYD, 2002; LONGHURST, 2007). When such mesoscale eddies occur near coastal regions or frontal zones, they are even more likely to sustain higher phytoplankton growth, providing more sources of nutrients mixing into the upper layer (LONGHURST, 2007; BORRIONE; SCHITZER, 2012). A typical case of these eddy-induced phytoplankton blooms, is the bloom that occurs up stream of the South Georgia Island, which can be noticed in both the spring and summer OC3M maps (Figure 6.2 and 6.3b). This bloom is related to an anti-cyclone mesoscale eddy formed by a northward deflection of the ACC flow as it hits the submerged elevations just before the islands. This phenomenon injects iron enriched waters to the upper layer sustaining the bloom with bimodal peaks throughout spring and summer (KORB; WHITEHOUSE, 2004; PARK et al., 2010; BORRIONE; SCHLITZER, 2012).

The SASW is known to have high concentrations of nitrate and phosphate, but low concentrations of iron and also silica in some regions, which limits phytoplankton growth in the so called High Nutrient Low Chlorophyll (HNLC) waters (BOYD, 2002). Other factors, such as the light availability (which also influences on the nutrient up take rates), water column stability (which is generally low in the well mixed waters of the Southern Ocean) and zooplankton grazing (which is also generally intensive) are also important factors regulating the spatio-temporal variations of the phytoplankton distribution across the Southern Ocean. Hence, there are simultaneous interactions between different factors (BOYD, 2002). Iron experiments carried out across the Southern Ocean have revealed that this micronutrient is in fact a strong limiting factor and the main sources may be obtained in the surroundings of coastal regions, upwelling cells and frontal zones, sustaining higher phytoplankton growth during the spring and summer blooms (BOYD, 2002; LONGHURST, 2007). Aeolian dusts from the adjacent

Patagonian Andes have also been thought to contribute to the iron enrichment in open ocean waters of the Southern Ocean, either by direct depositioning in the water or afterwards from ice melting. Nonetheless, the bioavailability and stability of the iron in sea-water are highly variable and recent studies have revealed a rather minor role of this source for phytoplankton growth in the Southern Ocean (KLUNDER et al., 2011). At least it is not likely to act in a short time scale, as some chemical reactions are needed to provide natural pathways for the acid mobilization of mineral dusts to make soluble bioavailable iron, such as through Dimethyl Sulphide (DMS) production (e.g. by *Pheocystis Antarctica*). Moreover, the wind bursts transporting Patagonian aeolian dusts to the open waters of the Southern Ocean occur generally in February, which is much after the major spring bloom (LONGHURST, 2007).

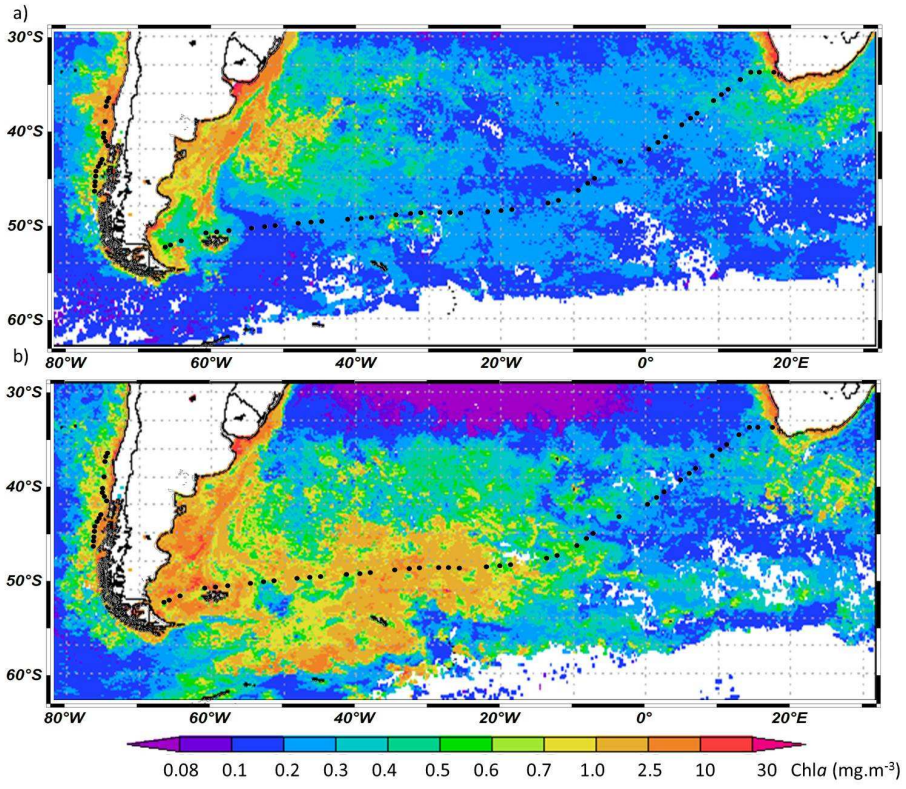

Figure 6.3 – OC3M MODIS monthly composites (4 km) of September (a) and November (b), 2010. The black dots correspond to the MV1102 stations for comparison.

The spring-summer blooms of the SANT are generally dominated by large colonial diatoms (LONGHURST, 2007; BORRIONE; SCHLITZER, 2012), nonetheless, some smaller nano diatoms and haptophytes may also prevail, especially during the second summer bloom, where some nutrients may be limiting the development of larger diatoms (BOYD, 2002, KORB; WHITEHOUSE, 2004). The HNLC waters of the SANT, away from the blooming areas, are dominated by smaller pico and nano flagellates (i.e. S*ynechococcus*, picoeukaryotes, prasinophytes and haptophytes), which are more adapted to low nutrient concentrations and light availability, as their high surface:volume ratio enables a higher nutrient uptake efficiency and a greater light absorption capacity (BOYD, 2002).

The factors that control the phytoplankton biomass distribution and community structure are still not so well understood for the Southern Ocean, as there are different interdependencies and relations between the nutrient balances and phytoplankton up-takes. Nonetheless, there are strong evidences that the shallowing of the MLD plays an important role on the first spring bloom, and that continental sources and eddy upwelling cells induced by submerged topographic effects, also have an important, but more localized role on the blooms throughout spring and summer (BOYD, 2000; LONGHURST, 2007). These mesoscale and local effects, which are more evident in the minor summer bloom, can explain the high spatial heterogeneity of the Chl*a* marked by a patchy pattern across the SANT, observed during the MV1102. The OC3M Chl*a* map obtained during the sampling period puts out in more evidence this spatial heterogeneity, likely associated with upwelling cells induced by topographic effects (Figure 6.2). Figure 6.4 shows the MV1102 stations overplayed on a sea bottom topography map (obtained from the Ocean Data View- ODV library (SCHLITZER, 2002)) with the higher Chl*a* stations (>0.7 $mg.m^{-3}$) highlighted in red. All of these stations were located near or across seafloor elevations with abrupt changes in the submerged topography. St 17 (in the SSTC) was just above a seamount southwest of the Cape Basin. Stations 21, 25 and 26 were across the Mid-Atlantic Ridge and stations 34 and 37 were above the Isla Orcadas Ridge. St 46 was located just at the beginning of the Malvinas Plateau and seemed to be influenced also by adjacent productive waters, with a higher Chl*a* plume advected from the Patagonian Shelves in the northern side, and the South Georgia bloom advected from the south (Figure 6.2). St 54-56 were located

across the continental slope of the Patagonian-Malvinas Shelves, and were likely influenced by the shelfbreak upwelling advected eastward from these coastal enriched waters (Figure 6.2).

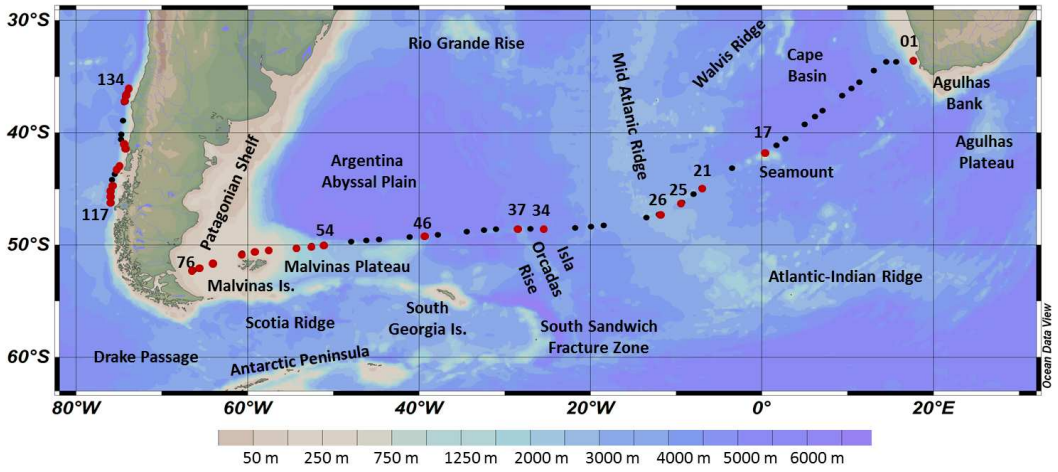

Figure 6.4 - Map of the sea bottom topography from the ODV library. The stations highlighted in red are the for Chl*a*> 0.7 mg.m^{-3}.

Analyzing stations 02-57 solely encompassing open ocean waters, the correlation between the bottom depth recorded by the ship multi-beam ecossound and the measured Chl*a* was -0.45 (p<0.05), indicating the influence of topographic effects on mesoscale upwelling eddies and phytoplankton growth across the Southern Atlantic. Such effects have been discussed by a number of researchers, which have first noticed these relations after the incoming of satellite-available products of Chl*a* maps and sea surface altimetry tracing eddies and vortices, combined with topographic sea bottom maps (BOYD, 2002; FALKOWSKI et al., 1998; LONGHURST, 2007; MOORE et al., 1999; PARK et al., 2010). The abrupt local changes in the ACC flow due to changes on the height, direction and slope of the seafloor combined with the wind stress and local hydrographic patterns, can cause such phenomenon that generate mesoscale upwelling cells. These cells may sustain high phytoplankton blooms throughout spring and summer, especially when associated with near-coastal or frontal zones, providing inputs of new nutrients into the euphotic layer, such as the typical bloom area upstream of

South Georgia (BORRIONE; SCHLITZER, 2012). The effects of storms and winds mixing the water column are also likely important sources of nutrients in the upper layers, enhancing phytoplankton growth and productivity after the passage of strong systems (BABIN et al., 2005).

Stations 59-76 had low temperatures characteristic of Subantarctic waters (11.0 ±0.8^{o}C), but with a transitional decrease of salinity (33.4 ±0.3) indicating the presence of coastal waters from the Southwest Atlantic Shelves Province (FKLD) (Figure 6.1) (PIOLA; MATANO, 2001; LONGHURST, 2007; RIVAS, 2010). Station 59 was located just across the shelfbreak of the Malvinas Islands (< 300 m). St 65 was located in the mid Patagonian shelf and stations 75 and 76 were in the inner shelf towards the Magellan Strait (a narrow channel which communicates the South Atlantic to the South Pacific oceans, surrounded by fluvial-glacial Fjords and regulated by strong tides). The oxygen concentration of the FKLD stations was high with 6.4 ±0.3 ml.l^{-1}, consequent of the high phytoplankton biomass (Chl*a*, 2.90 ±1.56 mg.m^{-3}) characteristic of the productive waters of the Patagonian Large Marine Ecosystem (PLME) (WATSON et al., 2003; FERREIRA et al., 2009; LUTZ et al., 2010).

When the ACC passes through the Drake Passage a branch of the current is deflected northwards contouring the Malvinas Islands and Argentinean shelfbreak up to the Brazil-Malvinas Confluence Zone (BMCZ) (35-45^{o}S), were it meets the Brazilian Current and deflects back southwards forming two eastward branches: one that will form the STF and another that forms the SAF (Figure 6.2) (STRAMMA, 2001; PIOLA; MATANO, 2001; MATANO et al., 2010). One the most distinctive features of the FKLD is the high Chl*a* plume which accompanies the ~ 200 m shelfbreak isoline up to the BMCZ, as may be observed in Figure 6.2 (MATANO et al., 2010). This high Chl*a* plume is likely generated by the shelfbreak upwelling of nutrient enriched Subantarctic waters carried northward by the Malvinas Current (MC). The forces that drive this upwelling are still not clearly understood, but there are evidences that they may be related to frictional intrusions of the MC on the continental shelf, generating an alongshore pressure gradient and cross-shelf divergence (MATANO et al., 2010). The frontal zone of the upwelled cold and less saline HNLC Subantarctic waters, mixing with the warmer and iron enriched coastal waters, promotes a stabilized near-surface

water column which enables and sustains this high phytoplankton shelfbreak bloom (mostly composed of diatoms, dinoflagellates and coccolithophores) throughout spring and summer (GARCIA et al., 2008). This high Chl*a* plume may have impacts on the biological productivity beyond the FKLD, in the Southwestern Atlantic, as it is advected eastward by the ACC into the SAF (MATANO et al., 2010), as observed in Figure 6.2 (reaching up to ≈ 40^{o}W, near St 46).

The mid and inner shelf circulation pattern of the Patagonian Shelf is influenced by combined effects of strong westerlies, high amplitude tides (~ 12 m), low salinity discharges (at the north portion with the large size La Plata River) and onshelf intrusions of the MC bringing HNLC Subantartic waters (MATANO et al., 2010). The interactions between these forces promote upwelling cells that also carry high biological productivity. Upstream of the Malvinas Islands a permanent, but weak eddy is formed by the MC deflection, associated with the fast changing continental slope from narrow to very wide (MATANO et al., 2010). Stations 59, 61 and 65 were undertaken just across this area, which was likely influenced by this productive upwelling cell, with the Chl*a* ranging from 1.8-5.2 mg.m^{-3} (Figure 6.1d and 6.2).

Westward towards the inner shelf stations 72, 75 and 76 where more influenced by the tidal fronts and mixing zones which can also uplift enriched waters carried by the MC cross-shelf intrusions (MATANO et al., 2010). The mixing of the HNLC Subantarctic waters with continental iron enriched sources with sediment resuspension, coastal erosion, and glacial runoffs discharged from the Magellan Strait, promote high phytoplankton growth in this southern sector of the Patagonian Shelf (MATANO et al., 2010). St 76 was the closest to the Magellan opening and Chl*a* was the highest with 4.8 mg.m^{-3} (although the salinity still indicated the dominance of marine waters, with 33). The tidal frontal zone also promotes a shallow stratification of the upper layer which favors phytoplankton growth and maintenance. The greatest bloom of the southern sector of the Patagonian Shelf, occurs usually during spring (November) (LUTZ et al., 2010), after the northern early spring bloom (September) (Figure 6.3), and when the waters are most stratified by the upper layer heat flux (MATANO et al., 2010).

Besides of the coastal-continental contributions of nutrient inputs, the depositioning of aerosol dusts, especially transporting volcanic material from the Patagonian Andes,

which have their strongest bursts during summer (mostly February), may also be some important sources of inorganic nutrients and minerals that promote the high productivity on the Patagonian Shelf (GAIERO et al., 2003). As previously discussed, aerosol dust is not likely a direct strong contributor to primary production in oceanic waters, however in the presence of volcanic material this may contribute for pathways to transform the mineral dusts in soluble bioavailable iron (LONGHURST, 2007).

The high Chl*a* encountered for the FKLD stations during the end of the austral summer, was thus characteristic of the southern FKLD for the studied (LUTZ et al., 2010), presenting patches of high phytoplankton biomass (>1 $mg.m^{-3}$). These phytoplankton blooms act as a major CO_2 sink along the inner shelf and shelfbreak (BIANCHI et al., 2009). The dominant phytoplankton groups during the summer blooms are usually composed of diatoms, haptophytes, cryptophytes, dinoflagellates and nanoflagellates. Significant efforts have been made to study the dynamics of this coastal system with regional and global relevance for carbon cycling and biodiversity. The different oceanic and continental forces interacting in this region with high spatio-temporal dynamics result in a highly complex system which is very distinct from coastal regions elsewhere (LUTZ et al., 2010; FERREIRA et al., 2013).

Stations 117-134 were located on the Southeast Pacific Ocean, in the southern sector of the Chile-Peru Current Coastal Province (HUMB). This province is influenced by the equatorial-ward Chile-Peru (Humboldt) Current, bringing cold Subantarctic waters up to the shelfbreak and inner shelf (LONGHURST, 2007). The mean temperature of the stations was 14.9 ± 0.1 ^{o}C, denoting a transition of Subtropical and Subantarctic waters. The mean salinity was 33.5 ±0.4, indicating dominance of marine waters, with some influence of runoffs and river discharge. This influence was likely highest for the first stations adjacent to the Chilean Fjords (117-127) (Figure 6.1) (VARGAS et al., 2011).

The oxygen concentration of the HUMB stations was 5.0 ±0.4 $ml.l^{-1}$, indicating well oxygenized waters, likely associated with the high productivity. The mean Chl*a* was 1.37 ±0.85 $mg.m^{-3}$ showing mostly enriched waters, however with a sharp gradient of higher Chl*a* for the stations closest to the shelfbreak (1.0-2.7 $mg.m^{-3}$) and lower for the offshore stations (0.42-0.56 $mg.m^{-3}$). Despite of being an eastern boundary coast, the southern Chile is dominated by unfavorable upwelling winds due to the strong and

persistent westerlies, suppressing the coastal upwelling (LONGHURST, 2007). Nonetheless, due to the narrow continental shelf and steep slope, the Chile-Peru Current passes very close to the coastline and there are evidences of intrusions of HNLC SASW waters into the upper layers of the shelfbreak and inner shelf, promoting phytoplankton blooms along the southern coast (ROMERO; HEBBELN, 2003). The Chilean coastal waters are known to be silica-limited, and hence more dominated by dino and nanoflagellates (LONGHURST, 2007). Sporadic diatom blooms may however occur related to the intrusions of SASW mixing with coastal iron and silica enriched waters (ROMERO; HEBBELN, 2003). The fluvial-glacial waters of the Chilean Fjords may also provide an important silica source for the stations adjacent to this system (VARGAS et al., 2011), favoring such blooms especially in the summer.

The last two stations of the MV1102 (St 133 and 134), actually reached the southern limit of the persistent upwelling cells of the Chilean coast, just off the coast of Concepción, within the *Punta Lavapies* (PL) upwelling cell (36^{o}S) (LONGHURST, 2007). The mean temperature of these two stations was similar to the adjacent stations, with 15.1 ±0.2^{o}C, however the salinity was a unit higher (34.3 ±0.01), indicating the emergence of more saline deeper waters up to the surface layer (Figure 6.1a-c). The Chl*a* was also somewhat higher with 2.56 ±0.28 mg.m^{-3} against 0.56±0.21 mg.m^{-3} for the adjacent stations, confirming the influence of upwelled enriched waters from the PL cell (Figure 6.1d). The strongest upwellings in the Central Chilean Coast actually occurs during the austral winter (LONGHURST, 2007), which may be why the T-S and Chl*a* differences from the southern stations were rather low, but still distinguishable.

In resume the MV1102 stations sampled during the austral summer of 2011 across the Southern Atlantic and Southeast Pacific encompassed 6 BGCP with highly distinct properties and biogeochemical processes governing the phytoplankton distribution: BENG (St 01), SATL (St 02-08), SSTC (St 09-19), SANT (St 21-57), FKLD (St 59-76) and HUMB (St 117-134). Since the two last stations of the HUMB were differentiated as being part of a persistent upwelling cell, this province was also sub-divided into the southern HUMB (HUMB(S)) (St 117-132) and the *Punta Lavapies* Upwelling Cell (PL) (St 133 and 134) for some analysis. The OC3M Chl*a* map averaged over the study period (18/02-13/03/11) did not captured the simultaneous spatial variability sampled

within the MV1102, nonetheless this temporal averaging was necessary to obtain a greater spatial coverage due to the extensive cloud coverage, typical of the Southern Ocean. There were certainly also other biases associated with the OC3M satellite product, such as, atmospheric under-corrections and uncertainties in the bio-optical model. Anyhow, the OC3M was reasonably coherent with the Chl*a* range measured at the stations (0.10-11mg.m^{-3}), and the satellite maps enabled complementary analyses not only of the spatial, but also temporal dynamics. Such analysis were fundamental to comprehend the main processes determining the phytoplankton distribution among and within the biogeochemical provinces. The following sub-sections present the distribution of the IOPs and their relations with the phytoplankton biomass and community structure, defined by the processes governing the dynamics of each BGCP.

6.3.1.2. Surface distribution of the IOPs

The surface distribution of the IOPs was in first order associated with the Chl*a* gradient, with the lowest IOP values in the oligotrophic waters of the SATL and the highest in the meso-eutrophic waters of the coastal provinces, i.e. BENG, FKLD and HUMB (Figures 6.1 and 6.5). Hence, the IOPs had a high dynamic range, with the $a_{phy}443$ varying from 0.008-0.304 m^{-1}; the a_d443 from 0.002-0.031 m^{-1}, a_s443 from 0.003-0.110 m^{-1}and $b_{bp}443$ from 0.002-0.006 m^{-1}. These ranges were approximate to the observed in other environments with similar trophic levels (indexed by Chl*a*) (GREEN; SOSIK, 2004; BRICAUD et al., 2004; HUOT et al., 2008; BRICAUD et al., 2010; LOISEL et al., 2010). There were however, also some particularities in the distribution of each IOP, due to more regional and local processes governing their distribution. For instance, the $a_{phy}443$ was highest in the productive waters of the FKLD, whereas the a_s443 was highest in the PL upwelling cell, and the a_d443 and $b_{bp}443$ in the BENG. These differences, that departed from the general covarying trend between the IOPs and Chl*a*, were likely related to variations in the phytoplankton community structure, the composition and size distribution of the bulk particle assemblage and the production and loss processes of the CDOM in the surface layers (BROWN et al., 2008; LOISEL et al., 2010; SZETO et al., 2011).

6.3.1.2.1. Absorption coefficients

The $a_{phy}443$ had a 0.93 correlation coefficient (r_s) with the Chl*a*, denoting a strong but not exact relation. The second order variations in the $a_{phy}443$ vs. Chl*a* relation are partly due to the biases in their measurements (which are here assumed to be minor on behalf of the analysis of the previous Chapter), and to the natural variability in the phytoplankton absorption capacity (a_{phy}*) (LOISEL et al., 2010). The a_{phy}*443 is dependent on the intracellular chlorophyll *a* concentration and the proportions of light-harvesting accessory pigments, which will vary with the phytoplankton specie, cell size and ecophysiological state, regulating photoacclimatation processes (SATHYENDRANATH; PLATT, 2007). This last is dependent on the phytoplankton health, age, water temperature, nutrient availability and light regime (BOUMAN et al., 2003, 2005). Hence, there are many factors determining the variability of the a_{phy}* across the ocean, with spatio-temporal dynamics acting simultaneously in different scales from the global to molecular level.

Some factors, however, have a strong tendency to covary in nature, as for instance, small pico phytoplankton groups tend to dominate more oligotrophic waters with high light penetration (e.g. in the subtropical gyres), having thus a lower intracellular Chl*a* and higher a_{phy}*. Whereas, larger micro phytoplankton groups, generally dominate well-mixed meso-eutrophic waters, e.g. in mid-high latitudes and productive coastal systems, and have thus a higher intracellular Chl*a* to enhance their bulk light absorption capacity (CIOTTI et al., 2002; UITZ et al., 2006). The higher intracellular Chl*a*, in turns causes a pigment self-shading effects, called "packaging effect", which diminishes their absorption capacity (per milligram of Chl*a*). According to Ciotti et al. (2002) 80 % of the a_{phy}* variability can be explained by such changes in dominant size classes, with the highest a_{phy}* being characteristic of pico-sized fractions, especially *Prochlorococcus* cells, and the lowest of micro assemblages of diatoms and dinoflagellates. Hence, the a_{phy}*443 may be in first order associated with the dominant PFT size structure and co-varying photoacclimatation properties, which are strongly tied to the trophic levels across the global ocean (CIOTTI et al., 2002; UITZ et al., 2006). A strong correlation coefficient was in fact obtained between the a_{phy}* and Chl*a* (r_s, -0.73) and the PFT

sized-fractions determined by the HPLC pigment ratio model (-0.60 for micro and 0.70 for pico), across the study region.

Some minor, but important variations in the $a_{phy}443$ vs. Chl*a* relation were, however, also present, and were likely caused by more regional and local variations of the dominant PFT. For instance, the higher $a_{phy}443$ in the FKLD compared to equivalent Chl*a* waters in the BENG and HUMB (e.g. 0.144 m^{-1} for 2.29 $mg.m^{-3}$ at St 75 against 0.087 m^{-1} for 2.36 $mg.m^{-3}$ at St 134), revealed a higher absorption capacity for the FKLD stations (e.g., $a_{phy}443^*$, 0.63 against 0.37 $m^2.mgChla^{-1}$, for the respective stations), likely due to a dominance of smaller phytoplankton groups, despite of the high Chl*a*. The HPLC fraction model actually indicated the dominance of micro cells for both the FKLD (e.g., 57% for St 75) and high Chl*a* stations of the BENG and HUMB (e.g., 65% for St 134). Nonetheless, the microscopy analysis also revealed a dominance of nano and pico-sized diatoms at the FKLD stations (i.e., 3.10^6 and 2.10^5 $cells.L^{-1}$ of pico diatoms at St 61 and St 76, respectively), which may explain the higher a_{phy}^* and consequently $a_{phy}443$, despite of having high Fuco* as mapped by the HPLC analysis. Zingore et al. (2010) also found significant contributions of pico-sized diatoms during a summer campaign across more inner shelf waters of the Patagonian region. They discussed this awkward abundance and dominance of smaller diatom groups in the high Chl*a* waters to a probable shift of dominance of smaller groups towards the mid-summer season, due to a greater capacity of smaller diatoms to develop in more stratified and lower silicate waters, after the spring blooms typically dominated by larger diatoms.

Some local photoacclimatation processes may have also caused some variations in the a_{phy} vs. Chl*a* relation, but these were likely minor. In resume, the first order variation of the $a_{phy}443$ was strongly governed by the Chl*a* gradient and co-varying PFTs and photoacclimatation processes, whereas the second order variations seemed to be linked to more local shifts in the dominant PFTs, which will be further discussed.

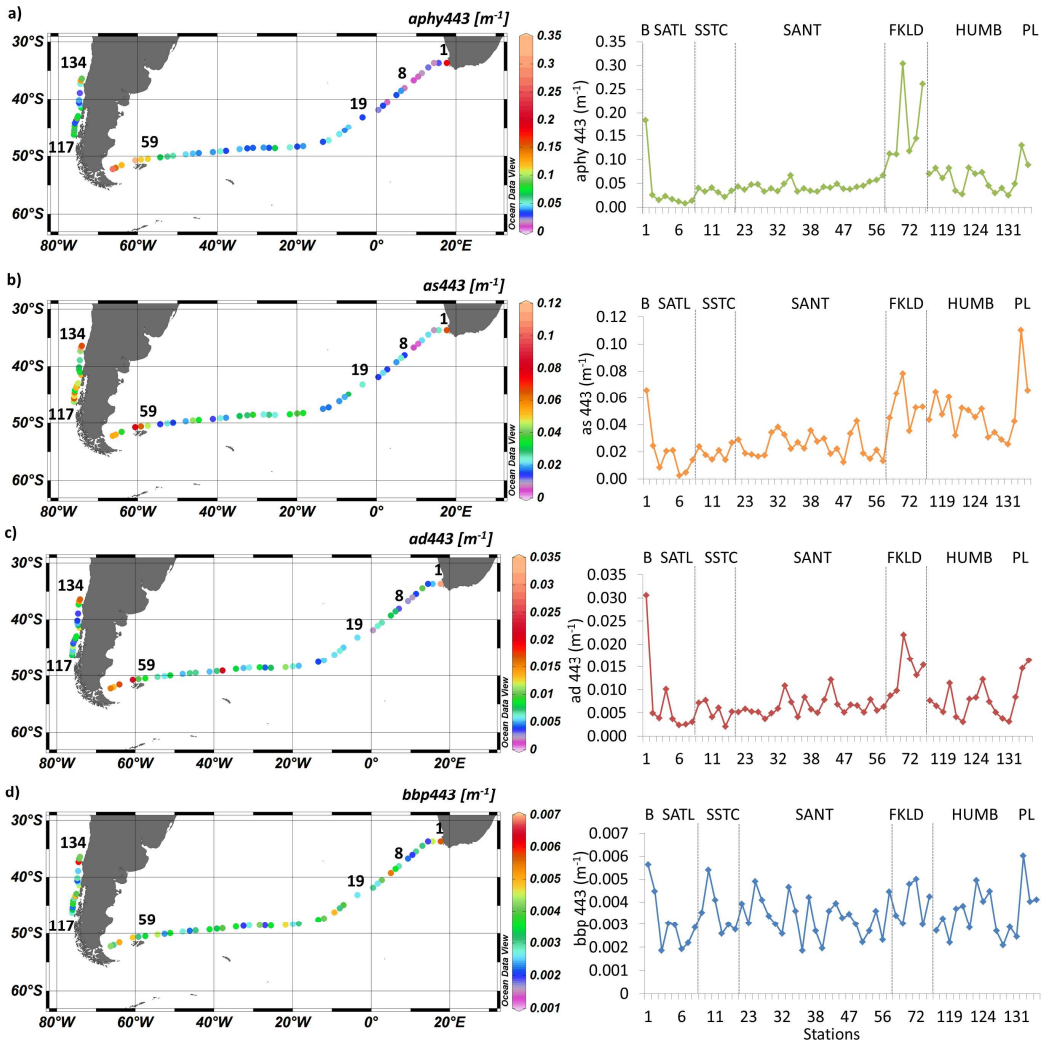

Figure 6.5 – Surface distribution of the IOPs: $a_{phy}443$ (a); a_s443 (b); a_d443 (c) and $b_{bp}443$ (d).

Regarding the CDOM distribution the higher a_s443 values were in the coastal provinces likely due to the co-varying exudation and degradation processes linked to the phytoplankton, microbial and zooplankton community (r_s, 0.60 with Chl*a*), as well as some external contributions from river flows, continental runoffs and deeper enriched upwelled waters (SIEGEL et al., 2002). This last may have been especially important for the PL stations which had the highest a_s443 values (Figure 6.5b). In the SATL province the lowest a_s443 values were likely associated with the low phytoplankton biomass, the "absence" of external sources, as well as the greater CDOM losses due to

the downwelling system and deeply stratified waters (LONGHURST, 2007), promoting intensive photodegradation processes, especially during summer (SIEGEL et al., 2002; SWAN et al., 2012). The SSTC and SANT provinces on the other hand, showed some distinct spatial patterns of the surface CDOM (Figure 6.5b), which were negatively correlated with the Chl*a* (-0.51), contrary to the expected global relation (MOREL; GENTILI, 2009). This awkward inverse relation between CDOM and Chl*a*, may be related to some different processes governing the major sources and sinks of both CDOM and phytoplankton biomass across these highly dynamic provinces of the Southern Atlantic.

In open ocean waters the main sources of CDOM are from degradation processes linked to the past and present phytoplankton community, including growth and decay cycles, phyto and zooplankton exudation, grazing, sloppy feeding, bacterial activity and viral lysis (SIEGEL et al., 2002). Some "external" sources may also come from adjacent enriched coastal waters advected by currents and upwelling cells bringing CDOM-rich deep waters to the surface layers (SIEGEL et al., 2002). The main sinking sources are the downwelling systems (such as the subtropical gyres) and photodegradation losses, which are more intensive in stratified waters with high solar incidence (i.e., at lower latitudes and during spring-summer seasons in mid-high latitudes) (SIEGEL et al., 2002; SWAN et al., 2012). The CDOM produced by the biological community during the mid-high latitudes spring-summer blooms are gradually depleted within periods of days and months within the surface layers, especially due to photodegradation processes (SWAN et al., 2012).

The photodegration processes however, are dependent on the vertical stability of the surface layer, which is highly dynamic in the Southern Ocean. According to Siegel et al. (2002), despite of the high biological production during the spring and summer blooms in the mid latitudes, the surface CDOM is generally low due to the shallower MLD and high solar incidence, whereas during fall-winter seasons CDOM may increase in the surface layers due to the deep vertical mixing and low solar incidence. Translating these relations to a spatial scale, a possible explanaition for the negative relation between Chl*a* and CDOM across the SSTC and SANT provinces, is the different effects of the eddy-induced upwelling cells, formed by the topographic effects, on the Chl*a* and

CDOM distribution. The strong vertical mixture at the upwelling core may be persistently bringing low-Chl*a* and high-CDOM waters to the surface layer, whereas at its borders, the upwelled nutrients spread out at more stabilized near-surface columns favorable for the development and mantainance of phytoplankton blooms, as well as for CDOM photodegradation. Hence, the upwelling cores could be characterized by low-Chl*a* high-CDOM waters, whereas its bordes would be of high-Chl*a* and low-CDOM. In fact, the low-Chl*a* high-CDOM stations were characterized by "cells" of 2-3 adjacent stations (Figure 6.5), which may indicate such effects of mesoscale processes related to active eddies. Meanderings formed between frontal zones typical of the SSTC and SANT, could also promote such near-surface stable environments, favoring phytoplankton growth (LONGHURST, 2007) and CDOM photodegration (SIEGEL et al., 2002), cohoboring for the negative CDOM and Chl*a* relations found for the austral summer across these provinces.

Another indirect effect that may also be causing such inverse CDOM and Chl*a* relations across the SSTC and SANT, is in respect to the temporal dynamics of the different timings of the phytoplankton blooming stages and the CDOM production. As shown in the previous section, the major and most extensive phytoplankton blooms occur during spring, whereas the summer second blooms occur in more spatially restricted waters. Hence, the high CDOM at the low-Chl*a* stations may also be associated with biodegradation products of the past spring blooms.

Across the FKLD there were also some inverse relations between Chl*a* and CDOM, especially at the inner shelf stations within the tidal mixing zone (St 72-76) (Figure 6.5). Besides of the high productivity of these stations the probably shallower stratified waters, may have promoted higher CDOM losses in the surface layer. The southern FKLD is actually known to have shallow stratifications during the summer season, due to thermal gradients and tidal fronts (MATANO et al., 2010). The HUMB stations, on the other hand, had a positive correlation between CDOM and Chl*a* (r_s, 0.67) and higher a_s443 values compared to the other provinces, which could be consequent of more vertically mixed waters, inhibiting greater CDOM losses, as well as some important contributions of the Chilean Fjords (VARGAS et al., 2011), and upwelled waters at the PL stations (Figure 6.5).

The detritus absorption coefficient (a_d443), on the other hand, had a positive correlation with the Chl*a* for all provinces (r_s, 0.74) (Figure 6.5a and b). The detritus usually has a closer relation with the phytoplankton biomass because it is an earlier stage of the decomposition processes of the cell debris, and it is more stable in the water column, whereas CDOM is a higher end degradation product, more related to the past assemblages, and highly reactive to photochemical processes (BRICAUD et al., 1981; BRICAUD et al., 1998; SIEGEL et al., 2002). The a_d443 and a_s443 had a 0.56 correlation coefficient, denoting some covariance, but also some independent variability likely due to the time lag between their production and the influence of different sinking and input sources.

The variability regarding the phytoplankton biomass and detritus production can be related to local variations in the biodegradation processes associated with the bacterial activity, zooplankton grazing, cell lysis and different stages of the phytoplankton blooming (from the initial growth to its decay), as well as, physical processes of current transport and vertical mixing (BRICAUD et al., 2010; SIEGEL et al., 2002). The first order spatial variability of the a_d443 was well explained by the Chl*a* gradient, but some local variations were observed at particular stations. Stations 04 and 07 of the SATL and 33 and 44 of the SANT for instance, had a high a_d443 proportion in respect to the Chl*a* (a_d443/Chl*a*, 0.02-0.06), which may have been associated with higher bacterial activity, zooplankton grazing and viral lysis. The BENG upwelling cell also had a slightly higher a_d443/Chl*a* (0.01), which could have also been related to a higher vertical mixture of the water column maintaining the detritus particles within the upper layer. Stations 65 and 76 of the FKLD, on the other hand, had much lower proportions (0.003 and 0.004), which could be related to the higher productivity and shallow stratification, with greater sinking rates of the detritus particles.

For a more comprehensive understanding of the relations between the biogenic absorption components (a_s, a_d and a_{phy}) and the variability of their proportions within the BGCPs, Figure 6.6 presents a ternary diagram showing the relative proportions of each component, with the stations grouped according to their province.

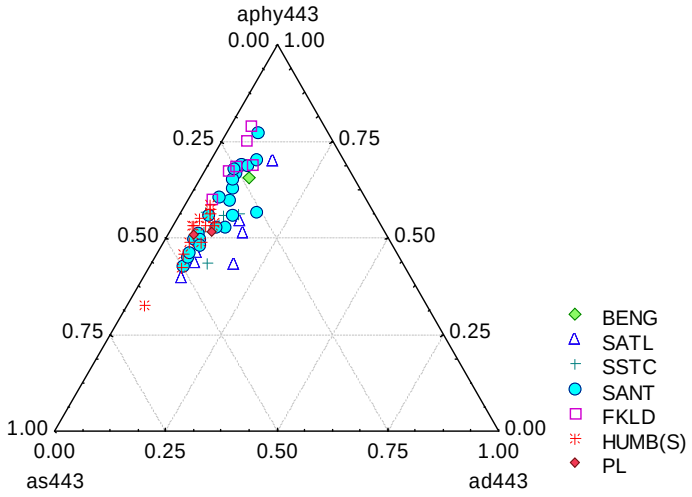

Figure 6.6 – Ternary diagram showing the proportions of $a_{phy}443$, a_s443 and a_d443, with the stations grouped according to the biogeochemical provinces.

The lowest contribution was for the a_d443 (9±3%), varying from 4-19%. The lowest a_d443% values were at the eutrophic stations of the FKLD and HUMB, where the phytoplankton absorption had its highest contribution, whereas the highest a_d443% stations were mostly at the oligotrophic waters of the SATL. The a_d443/a_p443 ratio (a_p corresponding to the total particulate matter) varied from 6-30%, with an average of 13±4%, and had a negative correlation with the Chl*a* (-0.57). These ranges and the negative relation with the phytoplankton biomass, was also observed by Bricaud et al. (2010) for the Southeast Pacific. Other works across different oceanic regions have also reported some different relations showing higher average values (25-30%) and no correlation with the Chl*a* (BRICAUD et al., 1998).

Some possible reasons for the negative relation between a_d443/a_p443 and the trophic state found in present work, and also discussed by Bricaud et al. (2010), could be: a) the time lag between the phytoplankton growth and debride production, with a faster biomass enhancement and slower detritus production in new nutrient enriched waters; b) the dominant phytoplankton size structure, with the production of larger and heavier debris with higher sinking rates for more eutrophic waters dominated by silicate PFTs (e.g. diatoms), especially in stratified environments; and c) the different biodegradation

activities, which may be higher in waters with a higher proportions of heterotrophic bacteria (HB*), such as the oligo-mesotrophic waters of the SATL, producing more light-weighed detritus in the surface layer (r_s, -0.80 between Chl*a* and HB*). According to Sathyendranath et al. (2009) there is a natural increase in the proportion of phytoplankton cells in respect to the rest of the living and non-living carbon (i.e., bacteria, zooplankton, detritus) for higher trophic levels, which also explains the generally negative relation between the carbon:Chl*a* ratio (C:Chl*a*) and Chl*a*. Besides this, the tendency of the shift of larger PFTs, with higher intracellular Chl*a*, to dominate more eutrophic waters, also provides a lower C:Chl*a* (SATHYENDRANATH et al., 2009), which may contribute to the higher a_{phy}% and lower a_d443%.

The a_s443 and a_{phy}443 proportions had an even higher variability within the BGCP, as observed in the *x* axes of Figure 6.6. The a_{phy}443 tended to dominate the biogenic absorption at most stations with an average of 56±10%, but there was a high dynamic range varying from 30-80%. The highest a_{phy}443 proportions were at the meso-eutrophic waters of the FKLD and SANT, with a positive correlation with the Chl*a* (r_s, 0.57). This supports the previous discussions of a greater contribution of phytoplankton absorption for more eutrophic waters, especially in stratified systems with higher CDOM photo-oxidation and detritus sinking rates.

The a_s443% had an average of 35±10%, with a high dynamic range varying from 16-64%, being highest at the HUMB coastal province, especially at St 122 (with 64%). This station was located just off a major opening of the Chilean Fjords and may have had some CDOM contribution of this adjacent estuarine system, although the station was located in deep offshore waters (2,375 m). The Chilean Fjords are characterized by organically enriched waters with inputs of continental runoffs and river flows of glacial-fluvial waters, enhanced by ice-melting and high precipitation rates during the austral spring and summer seasons, and may have some important contributions for the productivity of the southern coastal Chilean waters (ANTEZANA, 1999; VARGAS et al., 2011). The lowest a_s443% values were encountered in contrasting waters with both higher and lower Chl*a* of the FKLD, SANT and SATL provinces (Figure 6.6), which were likely associated with intensive photodegradation processes in the most stratified stations, independent of the Chl*a* level, as previously discussed.

Bricaud et al. (2010) found some similar ranges for the proportions of the biogenic absorption components with 10-20% for the a_d443%, 30-60% for $a_{phy}443$% and 40-50% for a_s443%. Their study was conducted within the upper layer of the Southeast Pacific encompassing the Subtropical Pacific Gyre and coastal Chilean upwelling areas, with a Chl*a* range approximate to the present work (although encompassing more ultraoligo-mesotrophic waters) (0.02-2 $mg.m^{-3}$). This denotes a coherency of the bio-optical relations for the two study regions, encompassing different BGCP across the Southern Atlantic and Pacific oceans.

The relations between the biogenic absorption components and the Chl*a* were also approximate to global mean fits presented in other works (Figure 6.7) (BRICAUD et al., 2004; MOREL; GENTILI, 2009; LOISEL et al., 2010), which also denotes a good consistency of the optical relations found in the present work. The $a_{phy}443$ and a_d443 had a linear relation with the Chl*a* as obtained by Bricaud et al. (2004), and the a_s443 had a power law relation, as in Morel and Gentili (2009) (Figure 6.7). The slower increase in CDOM for higher Chl*a*, could be associated with both the greater time lag between phytoplankton growth and CDOM production, as well as the higher effects of CDOM losses in more stratified highly productive waters (MOREL; GENTILI, 2009).

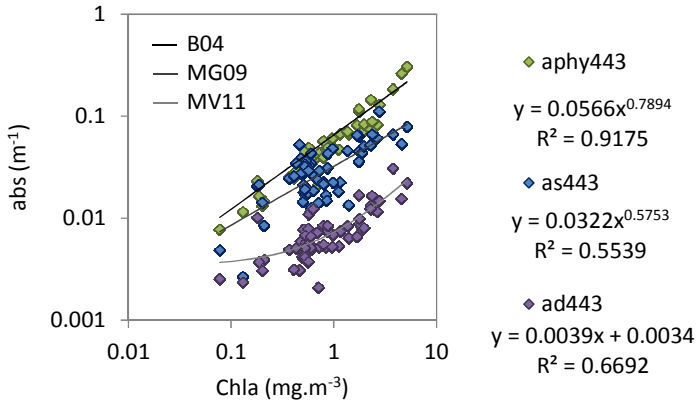

Figure 6.7 – Biogenic absorption coefficients, i.e., $a_{phy}443$, a_d443 and a_s443 vs. Chl*a*, showing the regression fits at the right, and the global fits of Bricaud et al., (2004) (B04 SI) and Morel and Gentili (2009) (MG09) in the graph. The MV11 line corresponds to the a_d443 linear fit for the MV1102 stations. (the axes are in log10 scale).

Despite of the reasonably strong covariation of the absorption coefficients with the Chl*a*, and the coherent trends compared to other global and regional data sets, there were also some significant dispersions (Figure 6.7), which reflected the impacts of the more specific variabilities, as discussed throughout this section, i.e., a_{phy}*, a_s% and a_d%. Such analysis regarding the sources of variability of the different biogenic components are fundamental to understand the processes governing their distribution to obtain important information of the regional and local biogeochemical processes.

Another important application of such analyses worth mentioning herein, is for the development and application of forward and inverse bio-optical models. For instance, the Case 1 and Case 2 classification scheme is extensively used to restrict the application of bio-optical models adjusted for either one of these water types. The ternary diagram of Figure 6.6 is often times used for such classification, being higher a_{phy}443% waters generically classified as Case 1, and higher a_s443% and a_d443% as Case 2 waters (MOBLEY et al., 2004). Controversially, lower Chl*a* open ocean waters across the SATL, SSTC and SANT, which would be typical Case 1 waters, had rather higher a_s443%, whereas highly productive coastal waters in optically complex systems, such as the BENG and FKLD, had higher a_{phy}443%. Another common mean to classify these water types is by analyzing how the absorption components covary, as by definition Case 1 waters should not only be dominated by phytoplankton absorption, but the other optical components (i.e., detritus and CDOM) should be essentially regulated by the phytoplankton community and have no external sources. Notwithstanding, the present work revealed highly complex CDOM and Chl*a* relations, showing both positive and negative correlations throughout the different BGCPs, as there were different processes governing their distribution in both dependent and independent ways. Photodegradation losses, upwelling sources and different phytoplankton bloom stages, for instance, seemed to have important impacts on the CDOM variability in both coastal and open ocean waters, as analyzed in other works (SIEGEL et al., 2002; SIEGEL; MARITORENA, 2005; MOREL; GENTILI, 2009; SWAN et al., 2012). Analyzing global data sets one may even obtain reasonably strong relations between the absorption components with the Chl*a*. However, when looking in detail the optical relations in more regional and local scales (and throughout different seasons), there may be in fact some significant deviations, as observed in the present work. In this context,

simplified Case 1 and 2 classification schemes may not be sufficient to explain the optical variability, as discussed by Mobley et al. (2004).

6.3.1.2.2. Particle backscattering coefficient

Regarding the surface distribution of the particle backscattering coefficient ($b_{bp}443$), this IOP had a smaller dynamic range, varying from 0.002-0.006 m^{-1}, but showed also some important variabilities associated with the variations in the particle assemblage (Figure 6.5d). There was a positive correlation with the Chl*a* (r_s, 0.57), denoting a first order variability likely governed by the trophic state across the BGCPs. The b_{bp} versus Chl*a* relation was approximate to global and regional fits obtained in other works and within their dispersions (MOREL and MARITORENA, 2001; HUOT et al., 2008; LOISEL et al., 2010) (Figure 6.8a). There seemed to be however, some tendency of higher $b_{bp}555$ values for lower Chl*a* and vice versa, which could be related to a tendency of higher b_{bp} "efficiency" for the particle assemblage sampled across the lower Chl*a* waters of the SATL, and lower b_{bp} for the more eutrophic waters, especially of the FKLD. The high dispersion of the b_{bp} vs. Chl*a* relation also revealed important effects of second order variability in the composition and size distribution of the particle assemblage, independent of the trophic level (Figure 6.8a).

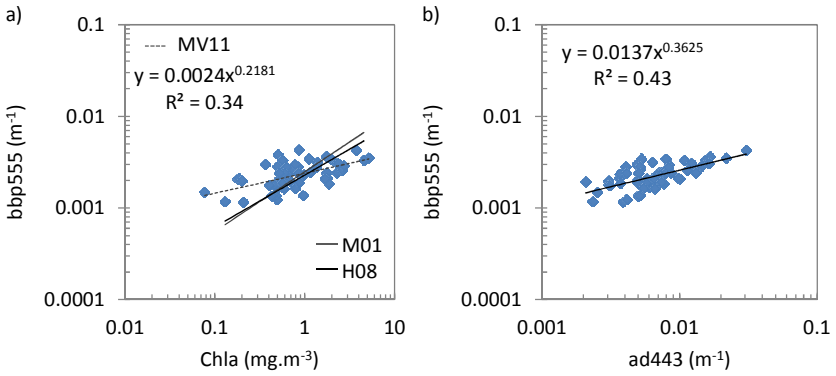

Figure 6.8 – Dispersions graphs of $b_{bp}555$ vs. Chl*a* (a) and a_d443 (b), with the MV1102 power law fits and the Morel and Maritorena (2001) (M01) and Huot et al., (2008) (H08) fits. (axes in log scale).

The relation between $b_{bp}555$ and a_d443 was somewhat stronger (r_s, 0.65) compared to the Chl*a*, with a lower dispersion (Figure 6.8b), pointing out two possible reasons: a) the detritus fraction may have a higher contribution to the bulk b_{bp} than the phytoplankton cells, due to some higher index of refraction and broader size range (STRAMSKI; KIEFER, 1991; STRAMSKI et al., 2001); and/or b) the detritus fraction may have a stronger covariation with the bulk carbon mass (including submicron detritus, virus, bacteria and phytoplankton cells), since the intracellular and bulk Chl*a* may vary with photoacclimatation processes, shifts in the dominant PFTs and variations in the proportions of phytoplankton cells in respect to the total living and non-living carbon (SATHYENDRANATH et al., 2009). An example of this variability can be observed comparing station 01 (BENG) that had higher a_d443 and $b_{bp}443$ values (0.03 and 0.0056 m^{-1}, respectively) with 3.8 $mg.m^{-3}$ of Chl*a*, and station 76 (FKLD) that had an even higher Chl*a* (4.6 $mg.m^{-3}$), but lower a_d443 and $b_{bp}443$ values (0.015 and 0.004 m^{-1}). The BENG station had a higher proportion of detritus absorption (a_d443%, 10%) and lower $a_{phy}443$% (65%), compared to the FKLD station (a_d443%, 6% and $a_{phy}443$%, 80%), which indicated a greater proportion of detritus particles in respect to the phytoplankton cells, and a probably higher C:Chl*a*. Hence, the higher $b_{bp}443$ at St 01 could have been related to the greater contribution of detritus particles to the bulk b_{bp}, as well as the co-varying submicron detritus and microbial community, which may be even stronger b_{bp} contributors (STRAMSKI et al., 2001). Anyhow, some high dispersion in the $b_{bp}555$ vs. a_d443 relation associated with more specific variations in the particle assemblage was still present.

To understand the main sources of oceanic b_{bp} is not a trivial task and there are still many discussions in respect to the particle types, shapes and size ranges that are effective contributors to b_{bp} across different BGCPs. There are contrasting works showing either a greater role of small submicron particles (i.e., detritus, bacteria and hydrosols) (STRAMSKI; KIEFER, 1991; STRAMSKI et al., 2001), while others show that larger particles (i.e., aggregates, nano and microplankton, > 3 μm), may also be significant contributors to the bulk b_{bp} (BOSS et al., 2009; DALL'OLMO et al., 2009; WHITMIRE et al., 2010). The former hypothesis is in accordance with Mie theory, which assumes homogenous spherical particles and a Junge-Type Particle Size Distribution (PSD) with an average -4 slope (for marine particles). According to these

assumptions, smaller particles should always be more abundant and have a higher b_{bp} efficiency (compared to particles with equivalent refractive index), as the increasing size tends to scatter light more towards the forward direction (and less backwards) (GORDON et al., 1975). Mie theory has been well applied to explain scattering processes in different mediums, such as the atmosphere, where water vapor molecules and aerosols are generally more spherical and homogeneous. In marine environments however, there is a much greater diversity of particles in terms of biogeochemical composition, with different refractive indices, size ranges and morphological structures, varying from tiny roundish particles to complex aggregates, colonial-type phytoplankton and elaborated frustules of large diatoms. Hence, simplified radiative transfer (RT) models are more likely to fail when it comes to explain more complex optical relations in non-homogenous mediums with a high diversity of particles, as in the oceans (DALL'OLMO et al., 2009).

Nevertheless, nature often times follows some general rules and different works have shown average PSDs in agreement with a Junge-Type function and a -4 slope, across the oceans. As small particles (i.e. colloids, virus and bacteria) also usually have an approximate spherical shape, such RT models have shown comparable results with some *in situ* measurements, and considered to fairly representing the scattering processes of ocean particles (STRAMSKI et al., 2001; GREEN; SOSIK, 2004). According to Stramski and Kiefer (1991), applying such models, submicron detritus particles (<0.6 μm) should be responsible for ~80% of the bulk b_{bp}, whereas the living microbial community should have solely up to 18% of contribution, being ~10% of HB (for Chl*a*<0.5 mg.m^{-3}). What would therefore explain the relation between the Chl*a* and b_{bp}, is a probably tight covariation between the phytoplankton biomass and the smaller particle assemblage of tiny submicron detritus, virus and bacteria, which are likely much more abundant and stronger contributors to b_{bp} (HUOT et al., 2008). Variations in the C:Chl*a* ratio, as well as the presence of highly backscattering particles with higher index of refraction, i.e., coccolith plates, bubbles and minerals, could then be significant sources of deviations in the b_{bp} vs. Chl*a* relation. Stramski et al. (2001) applied RT simulations adding the contribution of hydrosols (i.e., minerals and bubbles), and found that even in lower concentrations, minerals could dominate the b_{bp} signal (up to ~85%),

for oligotrophic waters (Chl*a*, 0.8 mg.m^{-3}). Its presence would thus, cause high dispersions in b_{bp} vs. Chl*a* relation.

Dall'Olmo et al. (2009) on the other hand, found some contrasting results comparing RT models with *in situ* fractional experiments carried out in the Equatorial Pacific. They made PSD and b_{bp} measurements in samples filtered through different pore sizes (i.e. 0.2, 0.7, 1, 3 and 5 μm) to verify the contribution of the different fractions to the bulk b_{bp}. The authors found a significant contribution of particles in the size range of phytoplankton assemblages (> 3 μm) (median, 50% for $b_{bp}470$) and a negligible contribution of the 0.2 μm fraction, with a rather stable PSD with a -3.49±0.37 slope. This was highly contrasting with the RT simulations provided by Stramski and Kiefer (1991), in which the submicron fraction (<0.6 μm) should contribute to ~80% of the bulk b_{bp}, and tiny submicron detritus <0.2 μm to ~50%. Dall'Olmo et al. (2009) discussed the unexpected high contributions of larger particles, as being due to the complex optical relations regarding their internal and external morphological structures, which would provide higher b_{bp} efficiencies for aggregates, nano and microplankton, than predicted by Mie theory. With this insight, they argued that b_{bp} could thus, be directly related to the phytoplankton carbon biomass and used to derive this biogeochemical parameter, which is of high interest for biogeochemical modelers.

Nonetheless, Dall'Olmo et al. (2009) also had some limitations in their experiments. The PSD measurements encompassed only the 2-8 μm range and were made with indirect measurements using the Coulter Counter Multisizer-3. Hence, the submicron PSD was unsampled and extrapolated using the power law function. Furthermore, there could have been some biases in their b_{bp} measurements since they used MiliQ 0.2 μm filtered water as a "transparent" background to determine the bucket wall reflection and apply the correction for such effects on the b_{bp} measurements. In the previous Chapter regarding the uncertainty analysis, it was shown however, that for the present work the bucket wall reflection was considered negligible, as the in-water profile measurements matched perfectly well with the bucket measurements of corresponding depths (even for the lowest Chl*a*, 0.10 mg.m^{-3}). Different testes of MiliQ filtered and non-filtered water also revealed some variable offsets from the theoretical pure seawater b_w curve (BUITEVELD et al., 1994; TWARDOWSKI et al., 2007), indicating the presence of

submicron particles, which are very difficult to completely eliminate even in the most purified water (Twardowski, M. S., personal communication). Hence, Dall'Olmo et al. (2009) could have somewhat overestimated the bucket wall reflection effects when using the MiliQ "transparent" background, consequently underestimating the 0.2 μm oceanic b_{bp}, which they considered negligible. Furthermore, even if the larger fraction has in fact a significant contribution to b_{bp}, the variability in the Chl*a* vs. b_{bp} relation remains to be explained, as well as the nature of the particles within each size range that are the most effective backscatters, e.g., if phytoplankton cells or detritus, hydrosols or even other unknown particles, and how these relations sustain across different BGCP.

A major challenge for these studies is the achievement of accurate *in situ* measurements of both the PSD and b_{bp}, especially regarding the submicron range. Most of the available instrumentations for PSD measurements e.g., Coulter Counter, flow cytometry and the Laser *In situ* Scattering and Transmissometry - LISST (Sequoia Scientific, Inc.), resolve only beyond 0.5-2 μm, and still very little is known regarding the PSD of the submicron range (GROUNDWATER et al., 2010). The separation and quantification of the carbon fractions of each living and non-living component is also a challenge for current techniques, limiting the knowledge of the exact contribution of each component to the bulk carbon mass (SATHYENDRANATH et al., 2009). The challenges in obtaining accurate b_{bp} are also important as analyzed and discussed in the previous Chapter. Hence, the above discussions so far presented have relied on limited indirect measurements and simplified theories, which are still too limited to adequately explain the complex optical relations across the different BGCP of the oceans.

In attempt to contribute to such discussions and verify the role of submicron (<0.7 μm) and larger particles to the bulk b_{bp}, as well as to identify some possible sources of variability in the b_{bp} and Chl*a* relation, throughout the BGCP of the MV1102, b_{bp} fractional experiments were performed in some FL (N =28) and CTD (N = 12) stations. The measurements were performed in a black bucket for filtered (GFF, 0.7 μm) and non-filtered samples and no correction for the bucket wall reflection was applied, as described in Chapter 3. To avoid extrapolation biases, the measured 420 and 590 bands were also used for the present analyses. The experiments for the CTD stations were performed at the Fl_{max} depth and the statistical relations were analyzed for both separate

and combined FL (1-4 m) and CTD (13-60 m) stations. Since the relations were the same with only slight differences in the degree of correlation, the results are presented for the combined stations (N = 40). However, since the experiments started only at St 25, they did not contemplate the oligotrophic waters of the SATL, which could have provided a more complete analysis for a higher Chl*a* range. Nonetheless, some interesting relations were observed for the meso-eutrophic waters of the SANT, FKLD and HUMB (with a Chl*a* range of 0.42 to 5.80 $mg.m^{-3}$), which pointed out some important possible factors determining the b_{bp} variability.

The contribution of the submicron fraction (<0.7 µm) to the bulk $b_{bp}443$ ($b_{bp}443$<0.7 µm%) was on average 33±8%, which was very close to the average obtained by Dall'Olmo et al. (2009) (32%), supporting their discussions regarding the significant role of larger particles. Notwithstanding, there was also some high variability in the contribution of the submicron fraction (20-60%), which was independent of the Chl*a* (r_s, 0.08), but negatively correlation to the bulk b_{bp} (r_s,-0.68). Hence, the variability in the submicron contribution was governed by other factors not associated with the trophic level, and the higher contribution of submicron particles provided lower bulk b_{bp} (whatever the Chl*a*). This was contrasting with the RT simulations provided by Stramski and Kiefer (1991), as smaller particles should in principle have higher b_{bp} contributions than larger particles.

The higher b_{bp} provided by the greater contributions of larger particles could be partly explained by the more complex optical relations regarding their morphological structures, as argumented by Dall'Olmo et al. (2009) and Whitmire et al. (2010). In fact, a couple of stations that had microscopy samples indicated some relations of higher b_{bp}>0.7 µm% with greater proportions of larger microplankton cells. St 46 in the SANT, for instance, had a higher contribution of larger particles for b_{bp} ($b_{bp}420$>0.7 µm%, 66%) and a higher concentration of micro diatoms ($1.2.10^6$ $cells.m^{-3}$), compared to other stations in the SANT and FKLD, that had lower b_{bp}>0.7 µm% and micro diatom concentration i.e., St 32, 61 and 76, with 49, 48 and 52% of $b_{bp}420$>0.7 µm%, and $8.0.10^4$, 0.0 and $2.5.10^5$ $cells.m^{-3}$ of micro cells, respectively. St 01 of the BENG did not contemplate the fractioned b_{bp} experiments but it had a higher $b_{bp}443$ compared to the FKLD stations with equivalent Chl*a*, which may have been caused by the greater

proportion of detritus particles, as previously discussed, but it could also be related to the higher concentration of micro cells ($7.8.10^6$ cells.m^{-3}) at this station. Of course, a greater number of stations would be required to confirm such trends. Anyway, one may still consider that these examples showed some evidences that the larger microplankton cells, and their co-varying detrital material, could be significant contributors to the fractioned b_{bp}>0.7 µm and bulk b_{bp}, supporting discussions of Dall'Olmo et al. (2009) and Whitimire et al., (2010).

On the other hand, the variability in the contribution of the larger fraction to the bulk b_{bp} was not correlated at all to the Chl*a* (r_s, 0.08). And as larger microplankton cells tend to be present in greater proportions in higher Chl*a* waters (UITZ et al., 2006), one could expect that such effects of greater contributions of micro cells to the bulk b_{bp}, could be higher for increasing Chl*a* waters. Even though the microscopy cell count revealed some significant deviations in respect to the proportions of micro cells obtained from the fractioned HPLC pigment model and the Chl*a*, as discussed for the FKLD stations, the other stations of the BENG and SANT showed a more coherent trend between the micro fraction of both microscopy and HPLC analysis, and with the Chl*a* (Figure 6.9).

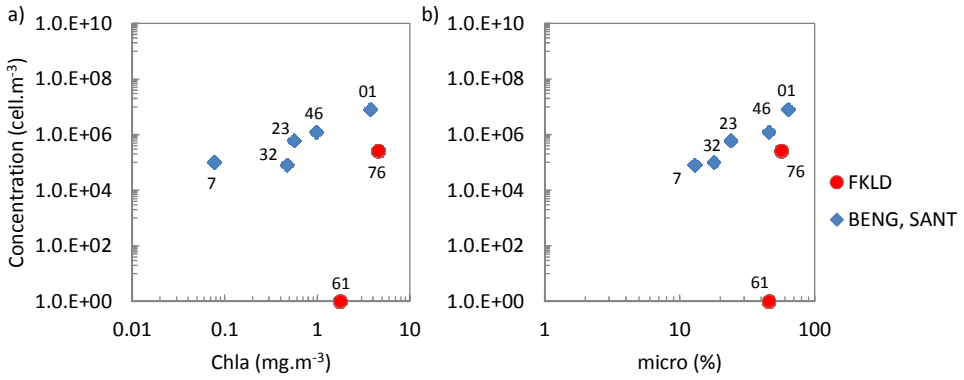

Figure 6.9 - Concentration of the microplankton cells (diatoms+dinoflagellates) obtained from the microscopy analysis versus the Chla (a) and the micro fraction obtained from the pigment ratios of the HPLC (b) (axes in log10 scale).

The small number of stations (N=7) is limiting to adequately analyze this trend however, since the stations encompassed different BGCP (BENG, SSTL, SANT and FKLD) with a high Chl*a* range (0.07-4.8 $mg.m^{-3}$), one may consider that this trend was reasonably valid for the sampled region. On this basis, one may assume that despite of some regional particularities (as in the FKLD), the HPLC fraction model may have fairly represented the general PFT size distribution across the study region, or at least indicated a trend of the different proportions of the sized PFTs. Hence, as the micro HPLC fraction had a strong positive correlation with the Chl*a* (across the entire study region, N=59) (r_s, 0.74), higher Chl*a* waters (with exception for the FKLD) likely had a general trend of higher proportions of larger micro cells (as for St 46 and 01). In this case, one could expect some greater effects of higher b_{bp}>0.7 µm contribution due to the increasing b_{bp} efficiency for the larger diatoms with more complex morphological structures. This however, did not seem to be much the case as b_{bp}>0.7 µm% was independent of the Chl*a* (r_s, 0.08) and HPLC micro fraction (r_s, 0.26).

Hence, other factors were likely as, or more important in determining the contribution of the different size fractions to the bulk b_{bp}. For instance, the different proportions of phytoplankton cells in respect to the bulk carbon mass, as previously discussed, was also probably important. The b_{bp}<0.7 µm%, was in fact negatively correlated to a_d443% (r_s, -0.44), indicating that the smaller fraction had a tendency of greater contributions where there were lower proportions of larger detritus (>0.7 µm), which may be stronger b_{bp} contributors than phytoplankton cells, due to their greater abundance (STRAMSKI; KIEFER, 1991; STRAMSKI et al., 2001). Thus, greater proportions of larger detritus particles would provide a higher b_{bp}>0.7 µm%, whereas greater proportions of phytoplankton cells would provide lower b_{bp}>0.7 µm%. This may have contributed for the lower b_{bp}>0.7 µm% at St 76 (56%) which had the highest a_{phy}443 (80%) and lowest a_d443% (6%). Whereas, the higher b_{bp}443 for the BENG station, may have also been related to the higher a_d443% (10%). The proportion of phytoplankton cells to the bulk carbon generally co-varies with the trophic state, tied to the phytoplankton growth and decay processes. Nonetheless, some local variations also occur associated with the vertical stability of the upper layer, zooplankton grazing, sloppy feeding, viral lysis, among others (SATHYENDRANATH et al., 2009). Hence, the stations with higher

local variations in the detritus and phytoplankton proportions may have had some impacts on the varying proportions of the different size fractions to the bulk b_{bp}.

The presence of particle types with high indices of refraction was also most likely a significant source of variability in the contribution of the b_{bp}. Particles composed of inorganic minerals, even in relatively low concentrations could cause significant impacts in the bulk b_{bp} (STRAMSKI et al., 2001). For instance, calcite carbonate coccoliths plates detached from coccolithophores, have high b_{bp} efficiencies and can enhance the oceanic b_{bp} even in low-medium concentrations. The coccolithophores themselves may be also strong contributors to the b_{bp} (although less than the coccoliths plates) (GORDON et al., 2009). The study region of the Southern Atlantic and Southeast Pacific, is known to have widely distributed coccolithophore species (BOECKEL et al., 2006). The HPLC analysis revealed some significant presence of calcareous haptophytes throughout all the BGCPs, especially in the SSTC and HUMB, although in probably medium to low abundances (maximum HF'19*, 0.14 at St 122). No significant correlation was found between the biomarker pigment ratios (HF'19*) and b_{bp}>0.7 µm% (r_s, 0.17), indicating that the coccolithophores were probably not a major source of b_{bp}>0.7 µm. However, this biomarker pigment is also present in other groups i.e., other haptophytes (Type 6 and 7) and dinoflagellates (Type 2) (WRIGHT, 2005), and it may not indicate solely the presence of calcareous haptophytes.

The microscopy analysis, on the other hand, showed that for the stations with higher proportions of calcareous haptophytes, there was a tendency of higher b_{bp} in respect to the total autotrophic cell concentration and Chl*a* (Figure 6.10). St 23 had the highest proportion of calcareous haptophytes (mainly *Emiliania huxleyi*) (70% of the cells from 3-20 µm, with 4.10^8 cell.m^{-3}) and the highest b_{bp} in respect to the total cell concentration and Chl*a* (Figure 6.10). St 32 had also a greater proportion of calcareous haptophytes (66%, with 1.10^8 cell.m^{-3}), as well as St 46 (45%, with 8.10^7 cell.m^{-3}), whereas St 07 was dominated by prochlorophytes (96%), St 61 by pico diatoms (99%) and St 76 by nano diatoms (55%). St 32 had actually a lower b_{bp}>0.7 µm% (50%), compared to the other stations with higher proportions of coccolithophores (70% and 66% for St 23 and 46), which may indicate that there were other important factors also regulating the b_{bp}

variability, such as the proportions of detritus (a_d443%, 0.7%, 0.9 and 10%, for St 32, 23 and 46) and the varying presence of other particles types, such as coccoliths.

Other particles that could be significant sources of oceanic b_{bp}, with high index of refraction (high-index particles) are the suspended minerals deposited from aeolian desert dusts (STRAMSKI et al., 2001). In the Southern Atlantic such sources may come from wind bursts from the Kalahari (Namibia) desert, off of the southwestern African coast (BHATTACHAN et al., 2012), and from the Patagonian desert, from the South American continent (GAIERO et al., 2003). Although these sources are more northern to the study region, they may still provide some amounts of suspended minerals, especially during episodic strong wind burst events across extensive areas (Figure 6.11). The wind bursts of the Kalahari desert can occur all year long and in the Patagonian Region the most frequent month is actually in February (GAIERO et al., 2003). These sources of aeolian dusts can be transported hundreds of kilometers off the coast fertilizing remote open ocean waters across the Southern Ocean and be suspended for long periods due to their low sinking rates (BHATTACHAN et al., 2012). Large scale currents could also act in redistributing these particles throughout the ocean basin.

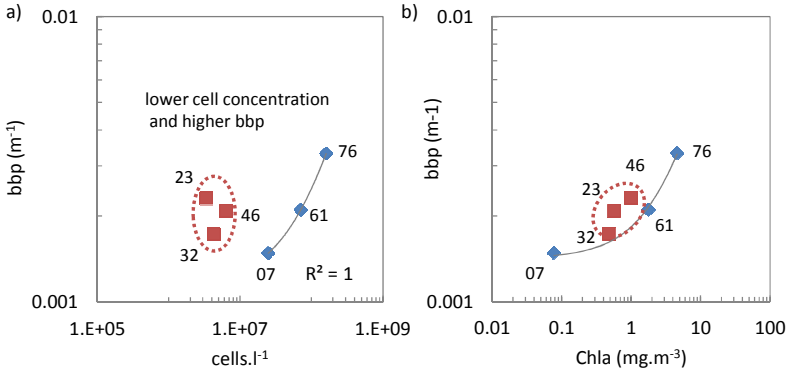

Figure 6.10 - b_{bp}555 vs. the total cell concentration of autotrophic cells (pico, nano and micro) obtained from flow cytometry and microscopy analysis. (axes in log10 scale).

For oligotrophic waters with lower concentrations of living cells and detrital particles, even low concentrations of suspended minerals may have significant impacts on the

bulk b_{bp} (STRAMSKI et al., 2001). This could be one of the reasons for the higher b_{bp} vs. Chl*a* relation at the SATL stations, compared to the global MM01 and South Pacific HUOT08 fits (Figure 6.8). Huot et al. (2008) also discussed that higher b_{bp} values could be encountered in the South Atlantic due to the presence of minerals from aeolian dust (compared to the Pacific). The meso-eutrophic stations of the FKLD however, had generally lower b_{bp} values in respect to the Chl*a* (Figure 6.8), which could indicate a minor contribution of such high-index particles in these waters with higher biogenic absorption and concentrations of living cells and organic detritus (with low mineral concentrations) (GAIERO et al., 2003).

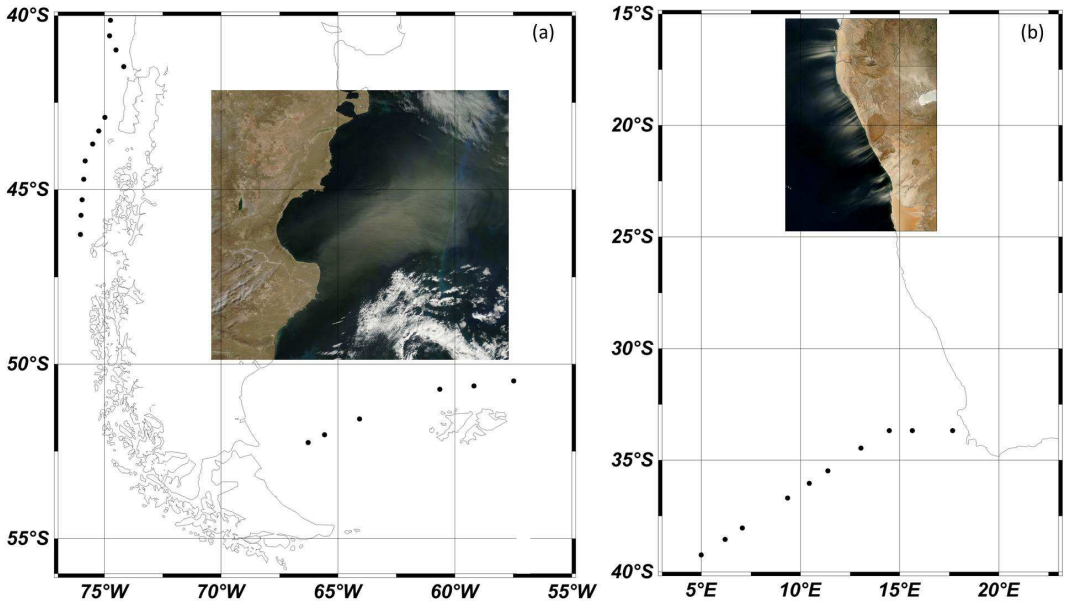

Figure 6.11 – Wind bursts of Aeolian desert dusts from the Patagonian Desert – MODISAqua true colour image (143) acquired in Jan 24th, 2010 (a) and the Namibia Kalahari Desert - MODISTerra (same composition) (1 km) (b). Credits for Jeff Schmatz (a) and Jacques Descloitres (b), MODIS Rapid Response Team, NASA, GSFC. The black dots are the MV1102 stations.

Another point is that the aeolian dusts can encompass a broad size range from small submicron particles to large-sized dusts (GROUNDWATER et al., 2010; BHATTACHAN et al., 2012), and could thus have impacts on both the smaller and

larger b_{bp} fractions (STRAMSKI et al., 2001). Hence, this still would not explain the variability in the contribution of the different fractions, unless some larger mineral particles were present at some stations (since the larger fraction was associated with higher b_{bp}). This would be more likely to happen at the stations closer to the continental sources, which was again not the case of the FKLD stations, since they had the lowest b_{bp420}>0.7 µm contribution, compared to the SANT and the HUMB stations (b_{bp420}>0.7 µm, 65±10%, 71±8% and 72±8%, respectively) (Figure 6.12). Further experiments and detailed analyses would be necessary to obtain more conclusive results of the role of aeolian mineral dusts in the study region. The present observations only show some indications that these particles may have had some contribution but were likely not the major sources of b_{bp} variability, at least for the meso-eutrophic stations of the FKLD.

The HUMB stations in the Southeast Pacific, on the other hand, could have had some influences of coastal minerals from runoffs, coastal erosion and resuspension, especially of fine suspended sediments, which can be advected far off the coast, due to their low sinking rates. Although, all stations were located off the shelfbreak (>200 m deep) they were still fairly near the coast. As previously mentioned, the Chilean Fjords provide organic-enriched fluvial-glacial waters to the Chilean southern coastal waters, especially during the austral summer with the maximum ice melting from the Andes (VARGAS et al., 2011). Figure 6.12b shows a true colour MODIS image acquired just before the MV1102 (02/19/2011). One may note the two major glacial ice-fields which feed the downstream rivers, the lakes and Fjord channels carried with sediments, nutrients and organic loads, denoted by the bright turquoise colours of these waters, on both sides of the Andes. There was not however, a well-defined spatial pattern of higher b_{bp}>0.7 µm% for the stations closer to the coastline or a major river sources (Figure 6.12a). Stations 123, 124 and 127 with higher b_{bp}>0.7 µm% (>77%), may have had some influence of coastal sediments due to their proximity to the Fjords, whereas other stations as close to the coast had some lower b_{bp}>0.7 µm% (e.g., St 117 with 63%), and other stations more distant had higher b_{bp}>0.7 µm% (St 120, 130-134, >75%) (Figure 6.11a). Hence, coastal sediments could have had some local influence on some stations, but did not seem to be a major source of b_{bp} variability for the HUMB province, as well.

The last two stations (St 132-134) within the PL upwelling cell had some higher $b_{bp}555$ (0.0030±0.0001 m^{-1}) and a_{d443}% (8±2%), compared to the FKLD stations with equivalent and even higher Chl*a* (with $b_{bp555,}$ 0.0029±0.0006 m^{-1} and a_{d443}%, 6±2%). The higher b_{bp} at the PL and BENG upwelling cells, compared to the stratified FKLD stations, could have been related to some greater proportions of detritus particles, and larger diatoms, as previously discussed (62% for micro HPLC for the PL stations, 64% for the BENG and 51% for the FKLD – having in mind that the FKLD were mostly of smaller diatoms, as shown in the microscopy samples). A common condition for the HUMB stations with greatest contribution of larger particles was in fact the higher a_d443% (>5%). This was the only parameter that actually showed a significant statistical correlation with the different proportions of the sized-fractions on the bulk b_{bp} (r_s, -0.44) for the entire study region. Hence, although all the other mentioned sources of b_{bp} variability likely played some roles across the different BGCPs, the variations in the proportions of the phytoplankton cells and non-algal detritus particles could have been one of the main sources of second order variability of the oceanic b_{bp}.

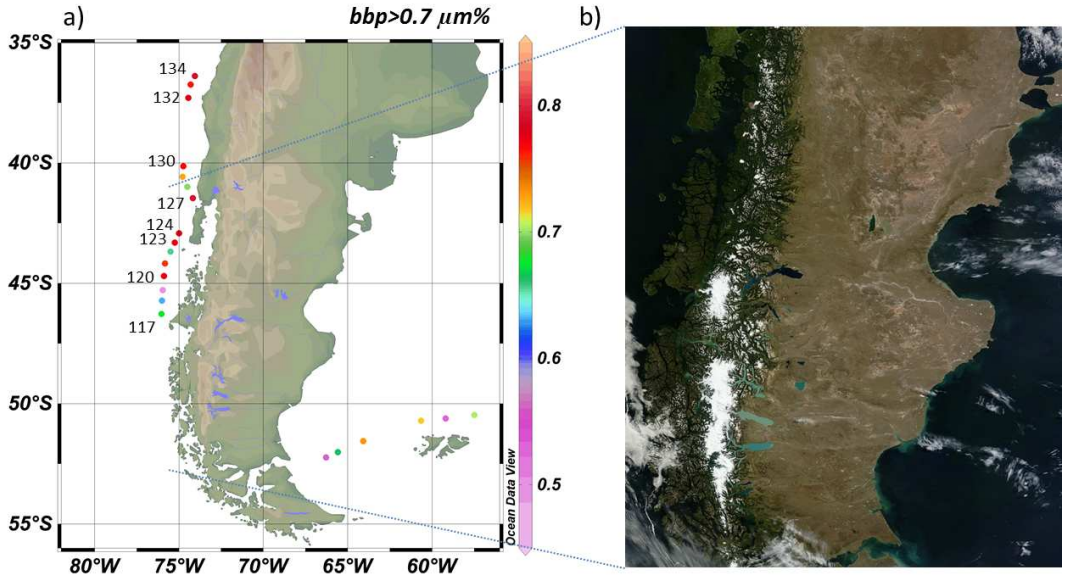

Figure 6.12 - Surface distribution of the contribution of the larger fraction to the bulk b_{bp} (b_{bp}>0.7 µm%) at the FKLD and HUMB provinces (a); and a MODISTerra true colour image (143) acquired previous to the MV1102 (Feb. 19th, 2011) (b), credits for Jeff Schmatz, MODIS Rapid Response Team, NASA, GSFC.

All of the different b_{bp} sources that may have caused some variations in the contributions of smaller and larger particles, i.e. larger aggregates and diatoms with complex morphologies, varying proportions of phytoplankton and detritus, and the presence of high-index particles such as, coccoliths and minerals, occur independently and with likely different levels of impacts, across the BGCPs. Thus, it is rather difficult to isolate the contribution of one or another source, without more detailed analysis on the composition and PSD of the particle assemblage. The present analysis indicate, however, that there are likely diverse sources acting simultaneously, which may explain the high variability in the contribution of the different size ranges and the dispersion in the b_{bp} vs. Chl*a* relation across the study region.

The impact of the variability of the contribution of each fraction to the bulk b_{bp}, on its relation with the Chl*a*, is shown in Figure 6.13. One may note how this variability was independent of the Chl*a* and how the higher submicron contributions provided lower bulk b_{bp} values, and vice-versa. Such impacts were similar for the b_{bp} vs. a_d relation (Figure 6.13b), which indicated that they were consistent for the bulk particle assemblage, and probably not solely due to the differences in the proportions of phytoplankton cells to the larger detritus (>0.7 μm). An insightful observation was that obtaining a separate fit for the two sets of higher and lower submicron contributions, it turned out that the stations with higher proportions of submicron particles actually provided a much stronger relation with the Chl*a*, showing a linear fit (R^2 0.81, N=20). Whereas the stations with higher proportions of larger particles provided a much greater dispersion (with a power law fit) (R^2 0.13, N=20) (Figure 6.13a and b).

Analyzing the b_{bp} of each fraction separately and their relations with the Chl*a*, the above observations are even more evident. Despite that the larger fraction (b_{bp}>0.7 μm) had a generally higher contribution to the bulk b_{bp} (mean, 70%), the relation between b_{bp}>0.7 μm and Chl*a* was highly dispersive (R^2, 0.28, for b_{bp}590), whereas the submicron fraction (b_{bp}<0.7 μm) had a stronger and linear relation (R^2, 0.51, for b_{bp}590) (Figure 6.14). This may indicate that what actually could be regulating the tight relation between the Chl*a* and b_{bp} is in fact the co-varying abundance of smaller submicron detritus and heterotrophic bacteria, as discussed by Huot et al. (2008). Submicron minerals could also be present, as suggested by Stramski et al. (2001), but as long as

there are somehow tied to the phytoplankton biomass for both the Southern Atlantic and Southeast Pacific. The contribution of larger particles, on the other hand, introduced a much higher dispersion, likely due to more complex optical relations regarding this fraction, with the varying particle types and more complex morphological structures. Hence, even though the larger fraction may have a significant contribution to the bulk b_{bp}, with such a high variability of the different sources, it may be rather difficult to directly relate b_{bp} with the phytoplankton carbon mass, as suggested by Dall'Olmo et al. (2009).

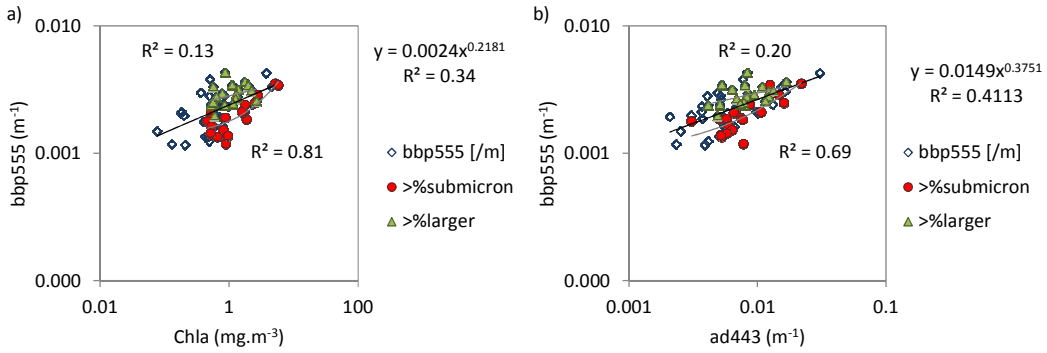

Figure 6.13 – Dispersion graphs of the $b_{bp}555$ vs. Chl*a* (a) and a_d443 (b) for all stations (N=59) (in blue diamonds) with the power law fit and R^2 in the upper right. The stations with the highest percentages of the submicron (<0.7 µm) and highest percentages larger particles are in the red and green dots, respectively (axes in log10 scale).

In Figure 6.14 one may also note that the submicron fraction had a higher contribution for the shorter band (420 nm), as smaller particles have increasing b_{bp} towards the shorter wavelengths. There were also some higher dispersion in the b_{bp} vs. Chl*a* relation for the shorter spectral band, especially regarding the larger fraction, which may be associated with a higher sensitivity of this band to variations in the particle assemblage of the most effective size range (likely of smaller particles).

The linear relation between the submicron b_{bp} and Chl*a* may be associated with the higher b_{bp} efficiency of these smaller particles, which would not change very much with the increasing trophic levels, hence b_{bp} can increase linearly with the particle

concentration. For the larger fraction however, the power law relation may be associated with a decreasing bulk b_{bp} efficiency with the increasing Chl*a*, which could be due to a tendency of higher proportions of larger particles for higher trophic levels (i.e., detritus and phytoplankton cells) (LOISEL et al., 2006; KOSTADINOV et al., 2009), as well as, the lower C:Chl*a* ratios, with higher proportions of phytoplankton cells, and higher intracellular Chl*a* (SATHYENDRANATH et al., 2009).

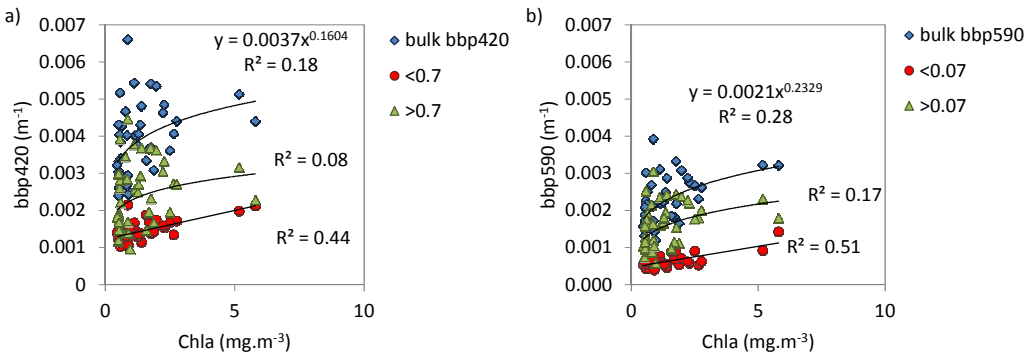

Figure 6.14 – Dispersion graphs of the $b_{bp}420$ (a) and $b_{bp}590$ (b) for the bulk, submicron (<0.7 µm) and larger particle assemblage, with the R^2 of the regression fits.

On the other hand, the slow increase in the submicron b_{bp} with Chl*a* and the generally higher b_{bp} of the larger fraction, could be explained by a lower relative concentration of submicron particles in respect to the larger fraction (>0.7 µm). Some studies that have used high resolution techniques with cameras and scanning electron microscope (SEM) to resolve the PSD for the submicron range, have revealed that there may be actually a decrease in the relative abundance of submicron particles in natural waters (GROUNDWATER et al., 2010; GRAHAM et al., 2012), which could be associated with a rapid tendency of the submicron detritus to aggregate into larger colloids (BOSS et al., 2009). This fast aggregation tendency may cause a natural deviation from the Junge type PSD function for the submicron range, even though for larger size ranges (>1 µm) measurements using different instruments (e.g. LISST, SEM, Coulter counter) have shown more coherency and accordance with the Junge type PSDs (with an approximate -4 slope) (DALL'OLMO et al., 2009; GROUNDWATER et al., 2010).

In the present work the above hypothesis regarding the submicron detritus could not be tested due to the lack of such high resolution PSD measurements. For the microbial and phytoplankton assemblage ranging from ~0.5 to 50 µm, the PSD could be analyzed using data from the flow cytometry and microscopy analyses. Figure 6.15 and Table 6.1 show the PSDs of the stations with the microbes and phytoplankton cells grouped according to their approximate average diameter (Ø). The flow cytometry analysis comprehended more stations across the study area, but only the ones shown in Figure 6.15 had microscopy data contemplating cells larger than 3 µm. The cells were divided according to the following groups: a) Ø≈0.5-0.6 µm: heterotrophic bacteria (HB), composed by High Nucleic Acid (HNA) and Low Nucleic Acid (LNA) cells; and *Prochlorococcus* cells, which were summed to this group due to their approximate diameter and co-varying distribution of higher proportions of HB with dominance of prochlorophytes (r_s , 0.60 between HB* and Proch%); b) Ø≈1.3 µm: *Synechococcus* cyanobacteria; c) Ø≈2-3 µm: picoeukaryotes, pico diatoms and prasinophytes; d) Ø≈5-10 µm: nano haptophytes (calcareous and non-calcareous), diatoms and dinoflagellates; and e) Ø≈50 µm: micro diatoms and dinoflagellates.

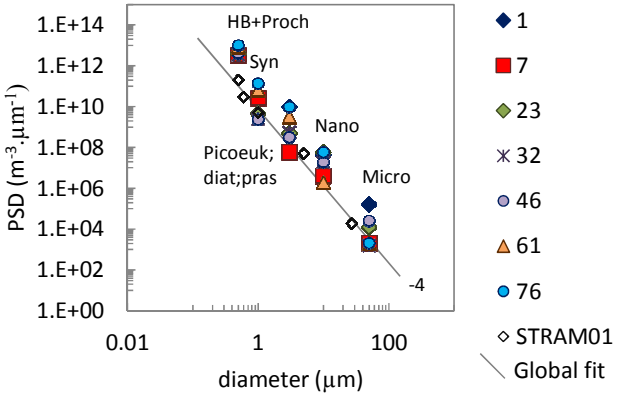

Figure 6.15 - PSD of the MV1102 stations with the cell concentrations normalized by the mean diameter of each group vs. the mean diameter. HB: heterotrophic bacteria; Proch: Prochlorococcus; Syn: Synechococcus; Picoeuk: picoeukaryotes; diat: diatoms; pras: prasinophytes; hapt: haptophytes; dino: dinoflagellates; STRAM01: Stramski et al. (2001). (axes in log10 scale).

Table 6.1 - Cell concentration (cells.m^{-3}) of the microbial and phytoplankton community.

St	Chl*a* (mg.m^{-3})	PSD ξ (-)	0.5-0.6µm HB+Proch	1.3 µm Syn	3 µm Picoeuk +diat+pras	10 µm Nano hapt+diat+dino	50 µm Micro diat+dino
1	3.78		-	-	1.0E+09*	4.1E+08	7.9E+06
7	0.08	4.38	1.6E+12	6.5E+08	1.7E+08	3.8E+07	1.0E+05
23	0.57	3.74	2.0E+12	4.4E+09	1.4E+09	5.7E+08	6.0E+05
32	0.47	4.13	1.7E+12	2.4E+09	1.6E+09	1.8E+08	8.0E+04
46	0.98	3.60	2.0E+12	2.3E+09	9.1E+08	1.9E+08	1.2E+06
61	1.77	4.73	4.0E+12	6.2E+10	9.2E+09	1.9E+07	0.0E+00
76	4.59	4.43	4.8E+12	1.3E+11	2.8E+10	5.7E+08	2.5E+05

HB: heterotrophic bacteria; Proch: Prochlorococcus; Syn: Synechococcus; Picoeuk: picoeukaryotes; diat: diatoms; pras: prasinophytes; hapt: haptophytes; dino: dinoflagellates. Obs.: St 01 did not have flow cytometry analysis (–, for no data) and the pico count (*) was just for pico diatoms.

The PSDs of the MV1102 stations were coherent and approximate to the global average (STRAMSKI, et al., 2001), as shown in Figure 6.15. The slopes varied from -3.6 to -4.4, with an average of 4.1±0.4. Dall'Olmo et al. (2009) found an average of 3.49±0.37 for the Equatorial Pacific, analyzing a smaller size range of 2-8 µm. For this same range the slope obtained for the MV1102 stations was somewhat lower (3.02±0.90), but still approximate, considering that the stations comprehended more meso-eutrophic waters (1.76±1.75 mg.m-3), which may have a tendency of higher proportions of larger cells (UITZ et al., 2006; LOISEL et al., 2006).

An important question to be addressed is in respect to how is the PSD of the bulk living and non-living assemblage, related to the amplitude and spectral variations of b_{bp}, and more specifically, what would be the effective size ranges and particle types determining such relations. According to Loisel et al. (2006) and Kostadinov et al. (2009), the b_{bp} slope (η) can be directly related to the PSD slope (ξ) since both are sensitive to changes in the size structure of the particle assemblage. Moreover, in oceanic environments the bulk assemblage should generally co-vary with the dominant PFT size structure and trophic state, i.e., as pico cells tend to dominate more oligotrophic waters, which have higher proportions of smaller particles, providing higher ξ and η, whereas micro groups dominate more eutrophic waters with higher proportions of larger particles (and lower ξ and η). Hence, they interpreted variations in the $b_{bp}555$ and η to co-varying changes in ξ and associated shifts in the proportions of the phytoplankton size fractions. Loisel et al. (2006) made a qualitative analysis of such

relations, whereas Kostadinov et al. (2009) made also some quantitative analyses using RT simulations. The last even proposed a model based on LUTs to derive the global distribution of PFTs, using satellite remotely sensed $b_{bp}555$ and η.

Such analyses, however, still lack of "ground truth" confirmations, since *in situ* PSD and b_{bp} measurements are still sparsely distributed in the global ocean. Moreover, Kostadinov et al. (2009) extrapolated their simulations to determine the distribution of phytoplankton-sized particles from 0.5-50 μm, using the η and ξ relations. Their global maps did show a coherent distribution with other PFT models, with the general trend of pico dominance in the oligotrophic gyres, nano in mesotrophic mid-latitudes and micro dominance in high-latitudes and coastal eutrophic waters (ALVAIN et al., 2006; UITZ et al., 2006; MOUW; YODER, 2010). Notwithstanding, according to Mie theory, nano sized particles larger than ~11 μm should have a non-selective scattering (with a spectrally invariable b_{bp}, in the visible spectral range). Moreover, as phytoplankton cells should be rather low b_{bp} contributors (AHN et al., 1992), such extrapolations would only be valid in the case of a tight covariation between the PSD of the effective b_{bp} contributors with the PFT distribution up to the micro range. Unless the phytoplankton cells are in fact strong b_{bp} contributors, as discussed by Dall'Olmo et al., (2009) and Whitmire et al. (2010), which did not seem to be much the case denoted by the highly dispersive relation between $b_{bp}>0.7$ μm and Chl*a*.

In the present work, it was possible to analyze the relations between the PSD of the living assemblage with the bulk and fractioned b_{bp}, to contribute for the above discussions and verify the consistency of such relations for the study region, in the austral summer of 2011. As previously shown, the average PSD of the stations analyzed for the 0.5-50 μm size range, was approximate to the global fit with a -4 slope (for both plankton and non-living particles) (STRAMSKI et al., 2001). Looking at each station separately, however, there was also some variability of the PSD slope, with different proportions of the microbial and phytoplankton sized groups at each BGCP.

In contrast to the global trend of lower ξ slopes for higher Chl*a* waters, with greater proportions of larger nano and micro cells (UITZ et al., 2006; KOSTADINOV et al., 2009), the PSD slopes of the 0.5-50 μm range, did not co-vary with the Chl*a* for all stations, as the meso-eutrophic FKLD stations were dominated by smaller pico and

nano diatoms. The BENG, SATL and SANT stations had a more coherent trend of decreasing ξ for higher Chl*a*, (ξ, 4.38 at St 07 to 3.60 at St 46), with the increasing proportions of nano (for St 23 and 32) and micro cells (for St 01 and 46) (Figure 6.15 and Table 6.1). The meso-eutrophic stations of the FKLD, on the other hand, had ξ slopes as high, or even higher, than the most oligotrophic station of the SATL (ξ, 4.7 and 4.4 for St 61 and 76), due to the dominance of smaller diatoms (Figure 6.15 and Table 6.1). St 61 was even dominated by a unique pico diatom, i.e., *Lennoxia faveolata*., which may be typical of the region for the summer season, as encountered in other cruises across the Patagonian Region, during the same season (ZINGONE et al., 2010). As previously discussed, the Patagonian mid and late summer blooms could be more dominated by smaller diatoms due to their greater capacity to develop in lower silicate and more stratified waters (ZINGONE et. al., 2010). Due to these regional and seasonal specificities of the FKLD, with high Chl*a* waters dominated by smaller pico and nano diatoms, the PSD slopes deviated highly from the expected global trend.

Despite of this variability in ξ, the b_{bp} slopes had a more stable covariation with the Chl*a*, with a diminishing trend for increasing Chl*a*, even for the FKLD stations, with 1.63 for St 61 and 1.08 for St 76, compared to 1.74 for St 07 (SATL). This indicated that the η slope was more sensitive to other changes in the particle assemblage more tied to the trophic gradient, rather than the shifts in the PFT dominance. Thus, even though the PSDs of the living assemblage within the 0.5-50 µm size range (PSD50 µm) had no correlation with the $b_{bp}555$ (r_s, -0.18), η (r_s, 0.14), nor Chl*a* (r_s, 0.25), the η still showed a strong negative correlation with the Chl*a* (r_s, -0.83). Despite of the low number of stations (N=7), with a questionable statistical significance, such relations show strong evidences that the b_{bp} slope was not sensitive to changes in the PSD of the living assemblage within the pico to micro size range. Testing these relations with the fractioned b_{bp}, there was also no correlation between ξ with the submicron $b_{bp}590$<0.7 µm (r_s, 0.60) or slope (η<0.7 µm) (r_s, 0.40), as well as for the larger fraction ($b_{bp}590$>0.7 µm, -0.30; η<0.7 µm, 0.00).

Observing the PSDs in more detail, one may note however, that despite that there was some high variability within the nano and micro range, the microbial and pico sized fractions showed a more coherent covariation with the Chl*a* for all the 7 stations. There

was a trend of higher proportions of HB and small *Prochlorococcus* cells (97% of the picoautotrophs) for the lower Chl*a* stations (St 07, 23 and 32), shifting to higher proportions of *Synechococcus* and especially, picoeukaryotes for the higher Chl*a* stations (i.e., St 01, 46, 61 and 76) (Figure 6.15 and Table 6.1). In fact, analyzing solely the PSD slope within the pico range (0.5-3 µm) (PSD3 µm), the ξ had a strong negative correlation with the Chl*a* (r_s,-0.83), some negative correlation with $b_{bp}555$ (r_s, -0.38) and positive with η (r_s, 0.31). These relations were even stronger for the submicron fraction with 0.90 for $b_{bp}590$<0.7 µm and 0.80 for η<0.7 µm, indicating a probably tight covariation between the tiny submicron particles with the pico-sized PSD, both co-varying with the Chl*a*.

Analyzing the entire flow cytometry data set (N=54), the above relations are still low, but somewhat significant, showing the negative correlation between PSD3 µm ξ and Chl*a* (r_s, -0.52) and $b_{bp}555$ (r_s, -0.30), and positive with η (r_s, 0.27). The higher PSD slopes were determined by greater proportions of HB (HB*) (r_s, 0.64) and prochlorophytes (Proch%) (r_s, 0.54), and lower picoeukaryotes (Picoeuk%) (r_s, -0.71), typical of the more oligotrophic and deeply stratified SATL waters (BOUMAN et al., 2011) (ξ, 7.27±0.23). Whereas the lowest ξ were in the most eutrophic waters of the FKLD, with higher proportions of picoeukaryotes (ξ, 5.35±0.38), and the mesotrophic stations of the SSTC, SANT and HUMB had average intermediate slopes (ξ, ~6.3), as shown in Figure 6.16.

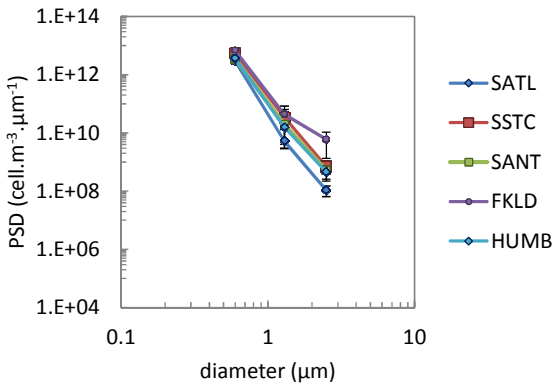

Figure 6.16 - Mean and SD of the PSD of the pico size range (0.5-3 µm) for each BGCP.

In respect to the fractioned b_{bp}, in the same manner that the submicron fraction had a tighter relation with the Chl*a*, it was also more associated with the changes in the PSD3 µm, than the larger fraction. The PSD3 µm ξ had a low but significant negative correlation with $b_{bp}590$<0.7 µm (r_s, -0.31) (for p<0.05) and a positive correlation with η<0.7 µm (r_s, 0.22), whereas the larger fraction had no correlation at all (r_s, -0.02 for $b_{bp}590$>0.7 µm and 0.11 for η>0.7 µm). This may be explained by both the direct contribution of HB to b_{bp}<0.7 µm determining its amplitude and spectral variations, as well as, the likely tighter covariation between the microbial and pico size structure with the distribution of the submicron detritus, which is probably a stronger b_{bp} contributor (STRAMSKI et al., 2001). The total HB concentration had in fact a positive correlation with b_{bp}<0.7 µm (r_s, 0.44), denoting a probably significant contribution of this microbial group to the submicron b_{bp}. The HNA group, which is composed of more active cells with a greater role in the detritus production (ZUBKOV; QUARTLY, 2003), had also a stronger correlation with b_{bp}<0.7 µm (r_s, 0.55), than the LNA group, composed of lower active and dead cells (ZUBKOV; QUARTLY, 2003) (r_s, 0.29), despite that both groups were present in equivalent proportions (~50%). This indicates the probably greater role of the submicron detritus on the b_{bp}, but also a tight covariation with the HB assemblage.

Hence, the amplitude and spectral variations of the submicron b_{bp} were more tied to the PSD of the microbial and pico-sized assemblage, as both co-varied with the trophic gradient and the proportions of submicron particles (i.e., of detritus and HB). Whereas, the b_{bp} variations of the larger fraction had much lower relations with both the PSD3 µm and PSD50 µm, despite that these size ranges embraced the particles within the analyzed fraction, likely due to the higher variability of the optical relations regarding the larger assemblage, i.e., with more complex morphological structures and varying particle types.

On the other hand, as the larger fraction had generally a stronger contribution to the bulk b_{bp}, the b_{bp} slope was also more determined by the spectral variations of the larger fraction (r_s, 0.60, against 0.36 for η<0.7 µm), which added more variabilities in the relations between the bulk b_{bp} η and PSD3 µm. Nonetheless, even with the greater optical variabilities regarding the larger fraction, there was still a general trend of the

η>0.7 µm to co-vary with the trophic state (r_s, -0.47), which guaranteed a reasonable correlation between the bulk η and Chl*a* (r_s, -0.47, for all stations with N=59). This correlation was however, not explained by the PSD3 µm or PSD50 µm, but rather other sources of variability which may be regarding the varying proportions of other particles (i.e. detritus aggregates and minerals), as well as the effects of the detritus and phytoplankton absorption in the shorter bands, diminishing the b_{bp} slope (LOISEL et al., 1998; MOREL; MARITORENA, 2001).

Analyzing the b_{bp} spectral variability in more detail, the submicron η<0.7 µm was always higher than the larger fraction (mean, 2.48 against 1.28 for η>0.7 µm) (in the 420-590 nm interval). This is expected according to Mie theory, with an increasing contribution of smaller particles at the shorter spectral bands and a more flatten spectra for larger particles. Figure 6.17 presents the mean and SD of the bulk and fractioned b_{bp} at the 4 spectral bands measured by the HS6 (420, 470, 590 and 700 nm). One may note how the submicron b_{bp} had lower amplitude and spectral variations through the entire study region, whereas the larger fraction had much higher variations, likely due to the more complex optical relations regarding this fraction. One may also note that despite that the larger fraction had generally greater influences on the bulk b_{bp}, the submicron fraction had also significant influences especially at the shorter bands (420 and 470 nm), even for the highest Chl*a* stations (Figure 6.17b).

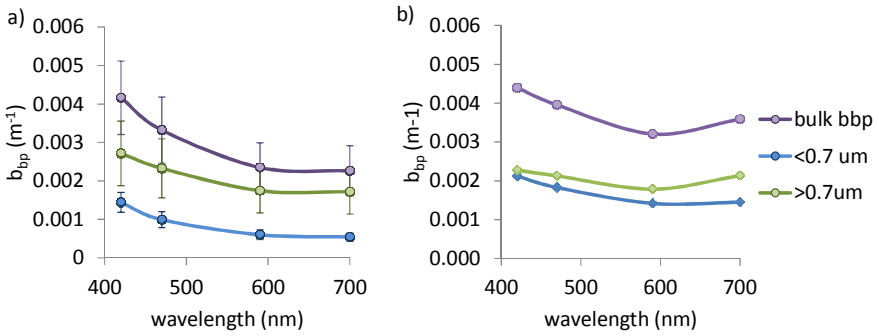

Figure 6.17 – Mean and SD of the b_{bp} measured at 4 spectral bands (420, 470, 590 and 700 nm) for the submicron (<0.7 µm) and larger (>0.7 µm) fractions and the bulk b_{bp} (a); and the fractioned bbp for St 76, with Chl*a* of 4.6 mg.m^{-3} (b).

Inelastic scattering of sun-induced fluorescence may also be a source of spectral variability of oceanic b_{bp}. In fact some stations with Chl*a* >2 mg.m^{-3} showed some features of higher b_{bp}700, which could be due to phytoplankton pigment fluorescence (chlorophylls and pheophytin), which has a broad emission band from 650 to beyond 700 nm (centered at ~685 nm) (HUOT et al., 2007). This may be noticed for St 76 in Figure 6.17b. Some stations also showed a slightly higher b_{bp}470, which could be due to CDOM fluorescence, which has a broad emission band (400-530 nm) centered at ~490 nm (HUOT et al., 2007). Such features were observed only for the larger fraction at the high Chl*a* stations, as the submicron measurements were made much after the water collection (after filtration) and in the dark. More spectrally resolved b_{bp} measurements could provide further detailed features associated with inelastic scattering and pigment absorption (AHN et al., 1992; HOUT et al., 2007). Nevertheless, for the OCR bands analyzed in the present study the power law fit between 420-590 nm was a reasonable approximation, as shown in the closure analysis of the previous Chapter, and the spectral slope for this interval should have minor effects of sun-induced fluorescence.

The η slope of the submicron fraction varied from 1.18-2.91 and had some negative relation with b_{bp}<0.7 μm (r_s, -0.50), as shown in Figure 6.18a. Whereas the larger fraction η>0.7 μm varied from 0.28 to 1.88 and had a much higher dispersion in relation to the b_{bp}>0.7 μm (r_s, -0.31) (Figure 6.18a). Nonetheless, as previously mentioned there was a reasonable relation between η>0.7 μm and Chl*a* (Figure 6.18b), which could be due to the effects of the detritus and phytoplankton absorption, diminishing the slope of the larger fraction for higher Chl*a* waters. As the submicron detritus has a negligible absorption (MITCHELL et al., 2003), this effect is not noticed for the submicron fraction.

The variability of the b_{bp} spectral dependency within the BGCP was thus, likely governed by the composition and PSD of the bulk particle assemblage, as well as, simultaneous effects of the biogenic particle absorption. The reasonable relation between the bulk η and Chl*a* (r_s, 0.47) was likely associated with the general covariation of both the PSD (especially in respect to the submicron and pico size range), and the biogenic absorption effects, with the Chl*a*. The dispersions and second order variations (in respect to the Chl*a*), were likely more associated with the varying contributions of

the different fractions at each spectral band, caused by more local variations in the composition of the particle assemblage, as discussed herein.

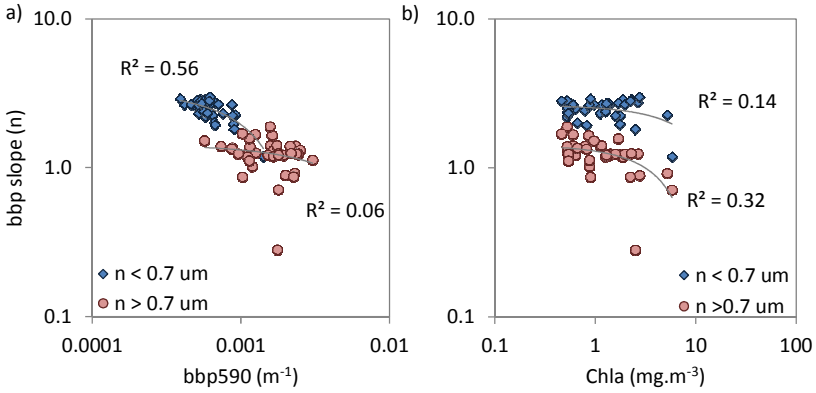

Figure 6.18 – The b_{bp} spectral slope (η) vs. $b_{bp}590$ (a) and Chl*a* (b), for the submicron (<0.7 µm) and larger (>0.7 µm) fractions. (axes in log10 scale).

In resume the present analyses revealed significant contributions of both the submicron and larger fractions to determine the bulk b_{bp} amplitude and spectral variations. The larger fraction showed some higher influences in the bulk b_{bp}, however also introducing some high dispersion in the relations with the trophic levels and PSD. This dispersion was likely caused by the more complex optical relations regarding the morphological structures of larger aggregates and phytoplankton cells, as well as, the varying proportions of detritus and algal cells, and the presence of high-index particles, such as coccoliths, deposited mineral dusts, advected sediments, and other unknown particles. The submicron fraction, on the other hand, had some lower influences on the bulk b_{bp}, but a tight covariation with the Chl*a*, likely due to the stronger relation between the trophic state and the submicron detritus and microbial abundance and size distribution. The lower contribution of the submicron fraction to the bulk b_{bp} and slow increase with Chl*a*, may be associated with a fast aggregation tendency of these tiny particles, diminishing their relative concentration in the submicron range.

Based on these analyses one may conclude that for the BGCP analyzed herein, the b_{bp} vs. Chl*a* relation was mainly governed by the tight relation between the submicron

detritus production and microbial and pico-sized community structure with the trophic state, as suggested by Huot et al. (2008), either than a direct contribution of larger phytoplankton cells. Larger particles may in fact have a more significant contribution to the bulk b_{bp} than predicted by Mie theory, as discussed by Dall'Olmo et al. (2009), nonetheless the complex optical relations regarding this fraction, with influences of different sources, makes it difficult to directly link their b_{bp} to the bulk carbon mass concentration. Another important point was that despite that the spectral variability has a reasonable correlation with Chl*a*, its variability was more associated with co-varying effects of biogenic absorption and the PSD of the microbial and pico-sized range regarding the living assemblage. Hence, PFT models based on ξ and η relations, as proposed by Kostadinov et al. (2009), would only work for waters in which there is a tight correlation between the PFTs and Chl*a*. But as there is not a direct link between η and the PFT distribution, for more complex environments such as the FKLD stations, with dominance of nano and pico diatoms in high Chl*a* waters, such model would fail to represent the PFT distribution.

6.3.1.2.3. Overall distribution of the IOPs

To synthetize the overall distribution of the bio-optical properties among the BGCP of the study region, Figure 6.19 and Table 6.2 show the mean and SD of the $b_{bp}(\lambda)$, $a_{cdm}(\lambda)$ and $a_{phy}(\lambda)$ for each BGCP. Since the present work is focused on bio-optical variations for ocean remote sensing applications and the models that will be analyzed herein retrieve solely the a_{cdm}, this term will be mainly used for further analysis. As the a_s443 proportion (35%) was much higher than a_d443 (9%), when adding these two components (a_{cdm}) the main variations can be interpreted as being mostly related to the CDOM variability.

Observing Figure 6.19 and Table 6.2 one may note the general first order variations of the IOPs were associated with the trophic levels of the BGCPs, but there were also some differences that were related to the more regional and local variabilities, as discussed throughout this section. The mean a_{phy} of the FKLD for instance, was very close to the BENG station (Figure 6.19c), which had a higher Chl*a* than the average FKLD stations, likely associated with the higher absorption capacity of the smaller pico and nano-sized diatoms of the FKLD. The $a_{cdm}443$ was also higher at the PL and BENG upwelling sites

compared to the approximate or even higher Chl*a* stations of the FKLD (e.g. 0.07 m^{-1} for St 76 with 4.8 $mg.m^{-3}$), likely associated with the higher CDOM sources in the coastal upwelling sites and higher CDOM photodegradation losses in the more stratified FKLD waters (Figure 6.19b).

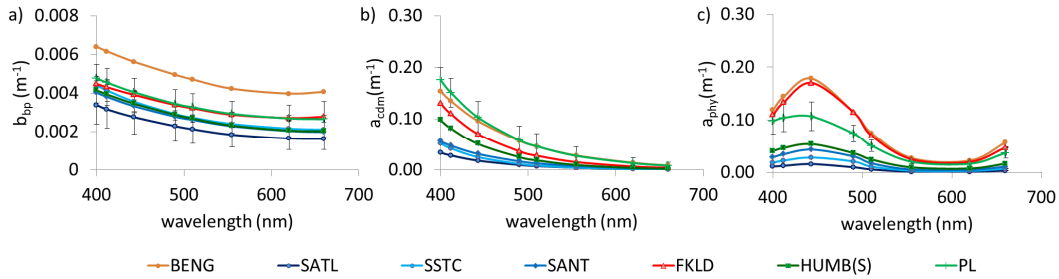

Figure 6.19 – Mean (±SD) of $b_{bp}(\lambda)$ (a), $a_{cdm}(\lambda)$ (b) and $a_{phy}(\lambda)$ (d), for each BGCP.

Table 6.2 – Mean and standard deviations of the surface Chl*a* and IOPs for each BGCP.

	Chl*a* ($mg.m^{-3}$)	$b_{bp}443$ (m^{-1})	$a_{cdm}443$ (m^{-1})	$a_{phy}443$ (m^{-1})
BENG (N=1)	3.78	0.006	0.096	0.184
SATL (N=7)	0.19 ±0.09	0.003 ±0.001	0.018 ±0.010	0.016 ±0.006
SSTC (N=6)	0.59 ±0.09	0.004 ±0.001	0.025 ±0.006	0.028 ±0.010
SANT (N=23)	0.71 ±0.25	0.003 ±0.001	0.031 ±0.009	0.043 ±0.010
FKLD (N=6)	2.90 ±1.57	0.004 ±0.001	0.069 ±0.017	0.174 ±0.085
HUMB(S) (N=14)	1.21 ±0.76	0.003 ±0.001	0.050 ±0.014	0.055 ±0.022
PL (N=2)	2.56 ±0.28	0.004 ±0.000	0.104 ±0.030	0.108 ±0.029

The $b_{bp}443$ had the highest variability in respect to the Chl*a* levels among the IOPs. The BENG station for instance, had a much higher $b_{bp}443$ values (St 01, 0.006 m^{-1}) than the FKLD with higher Chl*a* (e.g. St 76 with 4.59 $mg.m^{-3}$ and 0.004 m^{-1}). Such variability was likely due to more specific variations in particle assemblage i.e., likely with a higher proportion of detritus particles (a_d%, 10%) and larger phytoplankton cells (with more complex morphologies) (8.10^6 $cells.m^{-3}$, of micro diatoms) in the BENG (compared to 6% of a_d% and 3.10^5 $cells.m^{-3}$ of micro diatoms at St 76). As discussed, detritus particles may have some higher b_{bp} "efficiencies" than phytoplankton cells and a greater proportion in the probably more well-mixed upwelling site of the BENG,

contributing for a higher b_{bp}. Moreover, larger diatoms have more complex morphological structures with elaborated frustules and colonial type formations, which may also contribute to some higher bulk b_{bp} (DALL'OLMO et al., 2009; WHITMIRE et al., 2010).

6.3.1.3. Distribution of the specific IOPs

To support the above discussions and obtain new insights of the possible sources of IOP variability within each BGCP, analyses of the surface distribution of the specific IOPs i.e., a_{phy}*443, a_{cdm}/a_{nw} and b_{bp}*555, and bio-optical indices are presented herein.

6.3.1.3.1. Specific phytoplankton absorption coefficient

The surface distribution of the a_{phy}*443 (a_{phy}443/Chl*a*), was approximate to the Chl*a* and a_{phy}443 distributions (Figures 6.1, 6.5 and 6.20), showing an inverse relation of higher a_{phy}* for lower Chl*a* (r_s, -0.73) and a_{phy}443.

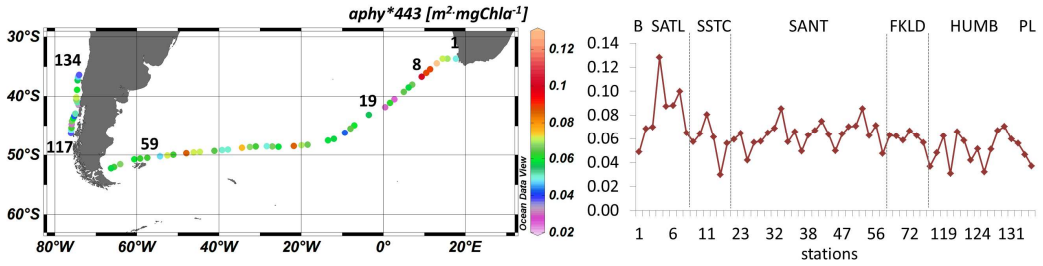

Figure 6.20 – Surface distribution of a_{phy}*443.

This relation is expected as pico cells with higher absorption capacities tend to dominate more oligotrophic waters, whereas micro cells tend to dominate more meso-eutrophic waters (CIOTTI et al., 2002; UITZ et al., 2006). Nonetheless, as shown in the previous section, there were some deviations from this trend for the FKLD stations, which had dominance of pico and nano-sized diatoms in higher Chl*a* waters, causing some variability in the a_{phy} vs. Chl*a* relation, with a higher a_{phy}*443 associated with these smaller groups. Besides of the PFT dominant size structure, some variations in the a_{phy}*

may be also caused by more regional and local variations of photoacclimatation processes. These processes are adaptive mechanisms of the phytoplankton cells to both protect from photodamage (in high-light conditions) and enhance the light absorption (in low-light conditions), by regulating the intracellular concentration of the chl*a* and accessory pigments (BOUMAN et al., 2003, 2005; BRICAUD et al., 1995, 2004). These processes generally co-vary with the dominant PFT, as pico cells which inhabit stratified high-light penetration waters, have more photoprotective pigments and lower intracellular Chl*a*, whereas micro cells in well-mixed environments have more photosynthetic pigments and higher intracellular Chl*a* (BOUMAN et al., 2005; BRICAUD et al., 2004). Nonetheless, seasonal and local variations associated with the light intensity and nutrient availability may cause some variations independent of the PFT size structure. For the MV1102 larger scale effects of seasonal and latitudinal variation of the solar intensity and photoperiod should have been minor, as all stations were collected in the end of the austral summer, and the latitudinal gradient was not so high (~33.7-52.2^{o}S). Finer scale variations regarding the time of collection, sampled depths and light attenuation, were likely minor as analyzed in further sub-sections. Hence, the PFT size structure was likely the dominant source of a_{phy}*443 variability.

The a_{phy}*443 values were mainly high throughout most of the study area, with a mean of 0.061 m^2.mgChla^{-1}, which may be in part due to the higher solar intensity and greater photoperiod of the austral summer, and to the greater proportions of smaller phytoplankton cells. The dominance of smaller nano and pico cells is actually typical of most of the Southern Atlantic in the end of the austral summer, when the early spring and summer blooms start to decay due to nutrient depletion (and grazing), (BOYD, 2002; LONGHURST, 2007), with exception for more localized eddy-induced blooms such as upstream of South Georgia and the coastal regions, i.e., BENG and HUMB.

Ciotti et al. (2002) measured pure pico and microplankton samples, obtaining a maximum average of a_{phy}*443 of 0.078 m^2.mgChla^{-1} for pico *Prochlorococcus* cells and a minimum of 0.012 m^2.mgChla^{-1} for a mixed culture of micro-sized diatoms and dinoflagellates. Figure 6.21 shows a comparison of the pico and micro endmember spectra obtained by Ciotti et al. (2002) and Ciotti and Bricaud (2006) with the MV1102, denoting the generally high specific absorption coefficient of the MV1102 stations.

The highest a_{phy}*443 were in the SATL (Figure 6.20) (mean, 0.087 m^2.mgChla^{-1}), which were dominated by pico cells (pico fraction, 60%) (Table 6.4), more specifically of *Prochlorococcus* (PROCH%, 82%). Prochlorophytes are the smallest picoautrotrophic groups (~0.5-0.6 µm) and have the highest a_{phy}*443 in natural environments (CIOTTI et al., 2002; CIOTTI; BRICAUD, 2006). Station 04 had the highest a_{phy}*443 with 0.128 m^2.mgChla^{-1}, close to the pico endmember of pure Prochlorophytes obtained by Ciotti and Bricaud (2006). This station had 0.18 mg.m^{-3} of Chl*a* with 67% of pico cells, being 94% of *Prochlorococcus*.

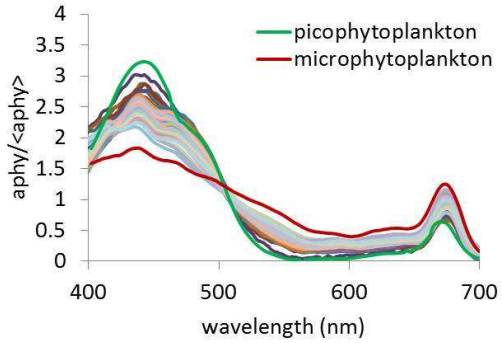

Figure 6.21 – Phytoplankton absorption spectra normalized by a_{phy}400-700 (<a_{phy}>) for the pico and micro endmembers (CIOTTI et al., 2002; CIOTTI; BRICAUD, 2006) and the MV1102 stations.

Table 6.3 – Mean and SD of the a_{phy}*443, HPLC size fractions (micro, nano and pico), Bricaud et al. (2004) size index (B04 SI) and Ciotti and Bricaud (2006) size index (CB06 SI), for each BGCP.

	a_{phy}*443 (m^2.mgChla^{-1})	Micro (%)	Nano (%)	Pico (%)	B04 SI	CB06 SI
BENG (N=1)	0.049	64	14	22	32.9	0.52
SATL (N=7)	0.087 ±0.022	12 ±6	28 ±6	60 ±11	8.2 ±3.5	0.89 ±0.14
SSTC (N=6)	0.049 ±0.017	13 ±3	52 ±9	35 ±11	9.4 ±1.6	0.74 ±0.07
SANT (N=23)	0.063 ±0.011	19 ±10	48 ±8	33 ±10	12.2 ±4.9	0.70 ±0.06
FKLD (N=6)	0.062 ±0.003	51 ±14	32 ±15	17 ±7	27.2 ±6.2	0.63 ±0.05
HUMB (N=14)	0.052 ±0.013	45 ±23	38 ±19	17 ±12	24.7 ±10.8	0.55 ±0.15
PL (N=2)	0.042 ±0.007	62 ±4	33 ±7	4 ±3	32.6 ±1.8	0.42 ±0.01

The lowest a_{phy}*443 values were at the BENG (0.049 m^2.mgChla^{-1}) and PL (0.042 ±0.007 m^2.mgChla^{-1}) upwelling sites, which had likely higher proportions of microplankton assemblages, given by both the HPLC pigment ratios (>60%) (Table 6.3) and microscopy analysis (8.10^6 cells.m^{-3}). These specific absorption values however, were still higher than the micro endmember obtained by Ciotti et al. (2002) (Figure 6.21), likely due to the mixed assemblages of the natural samples with important contributions of nano and pico groups (Table 6.3 and Table 6.4). The microscopy analysis of St 01, for instance, revealed a high concentration of pico and nano diatoms (1.10^9 and 1.10^8 cells.m^{-3}, respectively), which likely contributed for the higher specific absorption of this station, compared to the lower Chl*a* waters of the PL (Table 6.3).

The FKLD stations had the highest deviations from the global trend with an untypical higher a_{phy}*443 values (0.062±0.003 m^2.mgChla^{-1}) for high Chl*a* waters, due to the dominance of pico and nano diatom groups, as revealed by the microscopy analysis, i.e., 99% of pico at St 61 and 55% of nano at St 76 (Table 6.4). The HPLC pigment ratio model (VIDUSSI et al., 2001; UITZ et al., 2006) indicated higher proportions of micro cells for the FKLD stations (Table 6.3) (e.g., 46 and 57%, for St 61 and 76), due to the higher proportions of Fuco and Perid, which are biomarker pigments of diatoms and dinoflagellates (Equation 6.1c). In nature these groups are in fact usually within the micro size range, nonetheless they may also occur in smaller nano and pico sizes, depending on more local, regional and seasonal conditions of light, nutrient, temperature, water column stability and grazing pressure (ZIGNORE et al., 2011). As previously discussed, the austral summer seems to have more favorable conditions for the development of smaller groups across the Southern Atlantic and especial the FKLD, i.e., smaller diatoms may prevail for more silica or iron limited waters after the major spring blooms (ZINGORE et al., 2011). Moreover, Fuco is also present in other phytoplankton groups which are more typical of nano and pico sizes, such as haptophytes, crysophytes, raphydophytes (WRIGHT, 2005), and picoeukaryotes (KIRKHAM et al., 2011). Hence, the HPLC micro fraction can be overestimated by both varying diatom size ranges and the abundance of other smaller groups containing Fuco. Such overestimations were highest for the FKLD stations (Figure 6.9), but may also have occurred in other BGCPs, as pico diatoms were also abundant in the BENG, and nano diatoms and picoeukaryotes were abundant across the SANT (Table 6.4).

The SSTC and SANT provinces also had reasonably high a_{phy}*443 values (mean, 0.049 and 0.066 m^2.mgChla^{-1}) (Figure 6.20) related to the higher proportions of nano groups (nano fraction, 52 and 48%, respectively) (Table 6.3), mainly of haptophytes (calcareous and non-calcareous) (Table 6.4). Only stations 11 and 17 in the SSTC had much lower a_{phy}*443 values (0.024 and 0.030 m^2.mgChla^{-1}) (Figure 6.20), which could have been associated with changes in the nano groups, local photoacclimatation processes, or even some measurement biases. There was no clear evidence of a dominance of any particular group with changes in the pigment composition of these stations (compared to the adjacent), but an important note was that they were very close to a submerged seamount with high elevations (~300 m deep), which likely had some influence in the biological productivity and IOP characteristics of these stations.

Table 6.4 – Cell concentration (cell.m^{-3}) of the phytoplankton groups from the microscopy analysis.

St	Diatoms micro	Diatoms nano	Diatoms pico	Dino micro	Dino nano	Prasin	Hapto calcareous	Hapto non cal.
1	7.7E+06	9.9E+07	1.0E+09	2.2E+05	4.8E+07	2.1E+07	1.8E+08	8.3E+07
7	0	0	0	1.0E+05	9.4E+06	0	2.9E+07	0
23	5.8E+05	3.5E+07	0	2.0E+04	5.4E+07	1.1E+07	4.0E+08	7.4E+07
32	4.0E+04	6.1E+06	0	4.0E+04	3.5E+07	0	1.2E+08	2.1E+07
46	1.2E+06	8.9E+06	0	0	1.1E+07	0	8.4E+07	8.3E+07
61	0	0	2.8E+09	0	0	0	0	1.9E+07
76	4.0E+04	4.3E+08	2.0E+08	2.1E+05	0	1.7E+07	5.8E+06	1.3E+08

Dino: dinoflagellates; Prasin: Prasinophytes; Hapto: Haptophytes.

The stations with highest a_{phy}*443 values across the SSTC and SANT (Figure 6.20) were associated with the dominance of pico cells (r_s, 0.40 with the pico fraction), which were mainly composed of *Synechococcus* (SYN%, 82%). Ultra-nano Prasinophytes (green algae) (~3 μm) were also abundant at some stations with higher a_{phy}* (r_s, 0.30 with Prasin*) covarying with the pico dominance (see also Table 6.4 for Prasinophyte abundance in the SANT). The stations with lowest a_{phy}*443 were associated with the cells of higher productivity linked to the topographic effects, and probably eddy induced-nutrient upwelling cells, as previously discussed. Such stations had higher Chl*a*

(>0.7 mg.m^{-3}) and proportions of micro groups with 20-46% of the HPLC micro fraction i.e., St 21-26 (across the Mid-Atlantic Ridge), St 34-36 (across the Orcadas Rise), St 46 (up stream of South Georgia Is.) and St 54-57 (beginning of the Patagonian Shelf slope). For the HUMB, the highest a_{phy}* values were associated with the lower Chl*a* stations with dominance of nano and pico groups (mainly *Synechococcus* and picoeukaryotes) e.g., St 130 with 0.57 mg.m^{-3} of Chl*a*; 0.07 m^2.mgChl*a*$^{-1}$ of a_{phy}*443 and 42% of nano fraction. Whereas, the lower values were at the higher Chl*a* stations with higher proportions of micro groups, e.g., St 120 with 2.72 mg.m^{-3} of Chl*a*; 0.03 m^2.mgChl*a*$^{-1}$ of a_{phy}*443 and 85% of micro fraction.

In Figure 6.22 one may note the high covariation between the Chl*a* and the PFT fractions, with: higher proportions of pico groups (especially of Prochlorophytes) in low Chl*a* waters of the SATL; increasing proportions of nano groups (mainly Haptophytes) with increasing Chl*a* waters of the SSTC and SANT, and increasing proportions of micro diatoms and dinoflagellates for the highest Chl*a* waters of the BENG, SANT, FKLD and HUMB (r_s, -0.79 between pico and Chl*a* and 0.73 for micro). One should have in mind though that the HPLC fractions presented a general distribution of the main phytoplankton groups, but not truly the PFT size ranges.

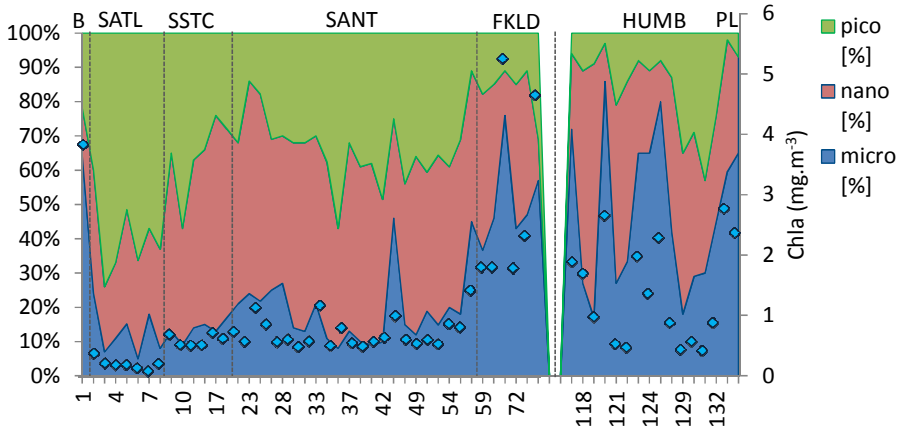

Figure 6.22 – Distribution of the percentage of the sized PFT fractions from the HPLC analysis: pico, nano and micro, and the TChl*a* concentration (blue diamonds).

Figure 6.23 shows the surface distribution of the dominant PFTs overlaid on the OC3M Chl*a* MODIS map averaged over the sampling period, showing the high spatial correlation between the HPLC dominant PFT fractions and the Chl*a* gradient.

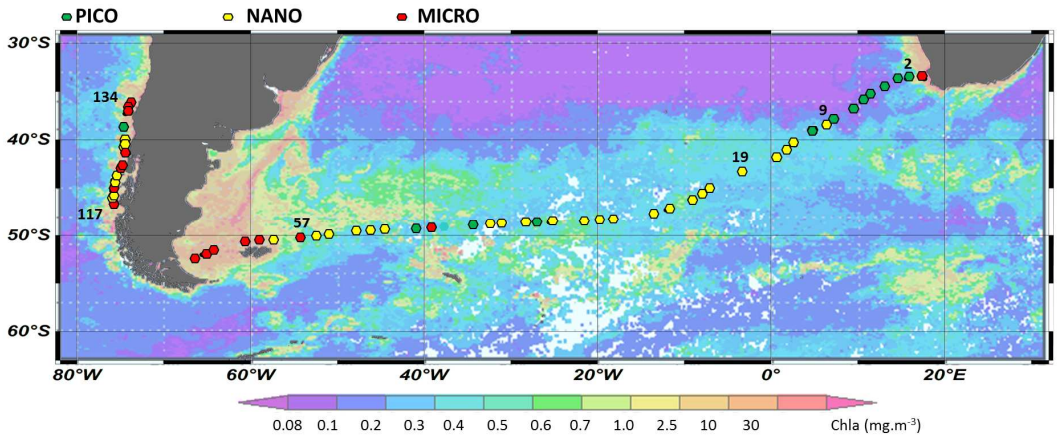

Figure 6.23 – Surface map of the OC3 Chl*a* MODIS composite averaged over the sampling period (02/20-03/14/2011), with the indication of the dominant PFT size fraction determined by the pigment HPLC analysis at each station.

A relevant reflection worthwhile presenting herein is regarding the remote sensing PFT models that relay on statistical global relations between the dominant HPLC PFT size fractions and the Chl*a* gradient (BREWIN et al., 2010; UITZ et al., 2006). Such models may reasonably represent the global transition of pico dominance in the oligotrophic gyres, nano dominance in the transitional and mid latitude zones and micro dominance in high latitudes and coastal eutrophic waters. Nonetheless, for more complex environments such as the FKLD, the biases would be both on the HPLC fraction determinations (used as input and model validation) and the PFT model performance (linking high Chl*a* to micro dominance). This highlights two important points: (i) that HPLC fraction models may provide a general distribution of the phytoplankton groups, but should not be blindly applied across different BGCPs. Microscopy analyses are still highly required to validate HPLC fraction models and have a more comprehensive analysis of the phytoplankton assemblage and size distribution. Hence, these are complementary analysis and one does not substitute the other (NAIR et al., 2008); and

(ii) the remote sensing PFT models that rely on the above mentioned statistical relations will not capture more specific regional variabilities on the phytoplankton size structure, and should be applied with this caution.

Remote sensing PFT models which rely on the specific optical properties of phytoplankton groups have the advantage to overcome the above limitations and detect variabilities independent of the Chl*a*. Nonetheless, due to the higher level of complexity to identify the second order optical variations associated with each dominant PFT, in waters with mixed assemblages and complex mixture of other optically active constituents (i.e., CDOM, detritus, minerals), these models have also shown limited accuracy. Comparing a climatological map of the distribution of the dominant PFTs for the month of February (1998-2008) using the Alvain et al. (2005; 2008) model (Figure 6.24) for instance, the model seemed to map well the dominance of *Prochlorococcus* in the SATL and higher *Synechococcus* abundance in the SSTC and SANT. Nonetheless, it also mapped a widely distributed dominance of diatoms across the SSTC and SANT, whereas more nano groups were actually found to be dominant during the MV1102 campaign.

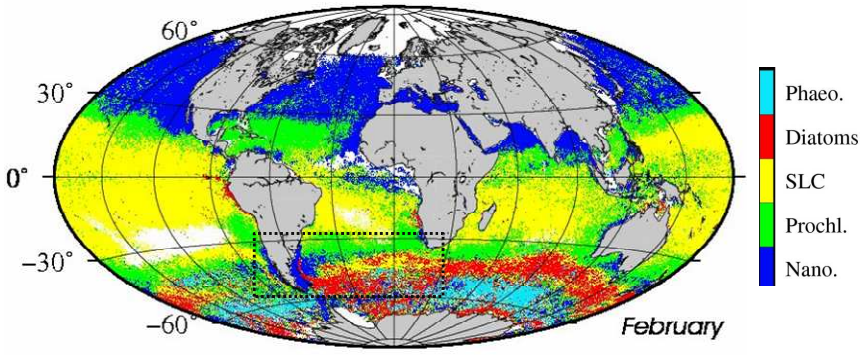

Figure 6.24 - A classified map of the climatology for February (SeaWiFS- 1998-2008 period, 9 km composite) for the dominant PFT groups using the Alvain et al. (2008) model. Phaeo. Refers to Phaeocystis; SLC to *Synechococcus* and Prochl. to *Prochlorococcus.*

Source: Alvain, S., personal communication.

The March climatological map actually shows a drastic decrease of diatom dominance shifting to an increasing dominance of *Synechococcus* and nano groups across the SSTC and SANT (ALVAIN et al., 2008), which is more in accordance with the MV1102 distribution. However, for the coastal provinces of the southern BENG, FKLD and HUMB, the differences remained for both month climatologies. The authors emphasize that the model is only reliable for Case 1 Waters, nonetheless as the sampled sectors of the coastal provinces had actually a rather lower a_{cdm}/a_{nw} (comparable to oceanic stations in the SANT), the biases due to higher CDOM content should be low for these provinces. The model mapped these BGPCs (BENG, FKLD and HUMB) as being dominated by nano groups (mainly Haptophytes) for the February and March climatologies, whereas there was a dominance of diatom groups in all three provinces.

One may argue about the temporal disconnection of the climatological series and the instantaneous collections of the MV1102 cruise, however, this general distribution of the PFT model was found to be similar throughout different years with a rather stable seasonal pattern for the macro regions (ALVAIN et al., 2005; 2008). Although finer scale variations are likely to occur, this comparison exercise was not for a model validation, but solely to contribute with some general discussions of the distribution of the PFTs across the study region during the sampled period, and the challenges to model these groups using satellite PFT bio-optical models.

The Ciotti and Bricaud (2006) size index (CB06 SI), adapted from Ciotti et al. (2002) for satellite applications, is based solely on the variations of the specific absorption phytoplankton coefficient and associated dominant PFT size fraction. As the a_{phy}*443 traced well the variability in the phytoplankton size structure independent of the Chl*a*, , the CB06 SI could be a reasonable alternative to map the PFT size structure variability for the study region, even for the complex FKLD. The model uses the pico and micro endmembers as shown in Figure 6.21, and with a linear mixing model, retrieves the index that varies from 0-1, indicating the proportion of pico cells (being 1 correspondent to 100% pico and 0 to 100% micro). The CB06 SI had a strong positive correlation with the pico HPLC fraction (r_s, 0.76), with the highest values at the SATL (0.89) and the lowest at the BENG and PL (0.52 and 0.42, respectively) (Table 6.3). The FKLD stations had a higher index (0.63) than the other coastal provinces, indicating its

sensitivity to the dominance of smaller diatoms groups. When analyzing the index one should have in mind though, that pico dominance may not always correspond to prochlorophytes and cyanobacteria, but also diatoms which have highly different biogeochemical and ecological roles. As an index it is also only a rough indicator of the dominant PFT size structure, and there may be some variations caused the complex mixture of diverse natural assemblages and local photoacclimatation processes, as previously discussed.

Figure 6.25 shows the relations between the a_{phy}*443 with the Chl*a*, CB06 SI and B04 SI, for each BGCP to resume the relations discussed throughout this section.

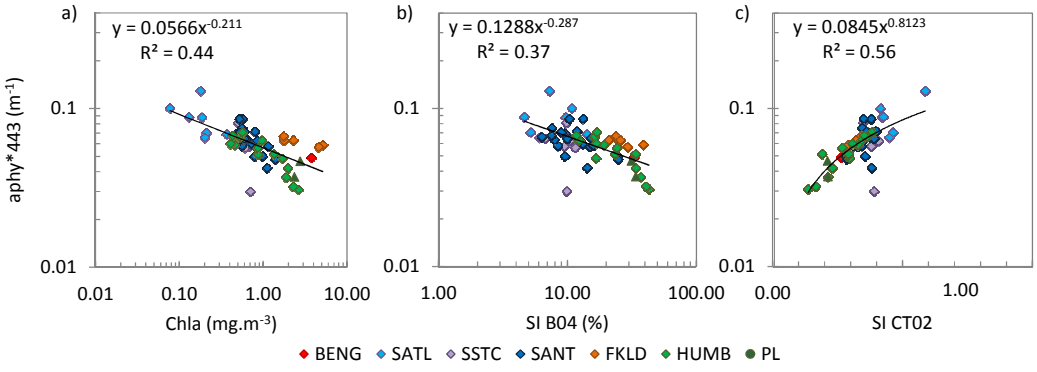

Figure 6.25 – Dispersion graphs of the a_{phy}*443 vs. Chl*a* (a); the CB06 size index (b); and the B04 size index (c).

One may note the general negative covarying trend of between a_{phy}*443 and Chl*a* and some more specific variations within the BGCPs (Figure 6.25a). The two stations with highest dispersion were St 04 at the SATL (with highest a_{phy}*443) and St 17 of the SSTC (with the lowest a_{phy}*443). As previously discussed, these two stations did not present indications of shifts in the dominant PFT, being similar to the adjacent stations, but may have been more influenced by some local photoacclimatation processes. The intermediate Chl*a* stations of the SSTC, SANT and HUMB had a closer relation of the a_{phy}*443 with the Chl*a*, and at the lower end of the graph for the higher Chl*a* stations (Figure 6.25a), there was a division of the FKLD station with higher a_{phy}*443 and the

HUMB stations with lower a_{phy}*443, likely due to the greater contribution of smaller diatoms in the FKLD and larger in the HUMB. The BENG station also showed a somewhat higher a_{phy}*443, compared to the HUMB stations with equivalent Chl*a*, which may have been associated with the significant proportions of nano and pico diatoms also at this station (Table 6.4).

In respect to the B04 SI, this index varies form 0-50 and indicates the increasing proportions of larger nano and micro cells (BRICAUD et al., 2004), unifying the HPLC PFT fractions in one index value (Equation 6.2). One may note the trend of higher proportions of larger nano and micro groups (haptophytes, diatoms and dinoflagellates) to have lower a_{phy}*443 (Figure 6.25b), but also a significant dispersion caused by the deviations in the "true" PFT size structure and the HPLC model fractions, and some local photoacclimation processes. The CB06 SI index on the other hand, had a much tighter relation with the a_{phy}*443, being more close to the "true" size ranges independent of the different groups of cyanobacteria, chlorophytes, haptophytes or diatoms. Taking out St 17 the r^2 of the CB06 SI fit is even much higher (0.70) (Figure 6.25c). Hence, the CB06 SI seemed to be a reasonable size index to represent the predominant variability in the a_{phy}*443 and associated dominant PFT size structure throughout the study region.

6.3.1.3.2. Coloured organic matter absorption variability (a_{cdm}/a_{nw})

Regarding the variations in the proportions of the a_{cdm} with the total biogenic (non-water) absorption (a_{cdm}/a_{nw}443, equivalent to a_{cdm}%), there was some high spatial variability within the provinces, but showing an overall negative relation with the Chl*a* (r_s, -0.57). The lowest values were in the most productive coastal waters of the FKLD and BENG (~0.3), whereas the highest values were in the oligo-mesotrophic waters of the SATL, SSTC, SANT and HUMB (Figure 6.26 and Table 6.5).

As shown in the previous section the CDOM absorption (which dominates the a_{cdm} signal), has a power-law relation with the Chl*a*, whereas a_{phy}443 and a_d443 have a linear relation (Figure 6.7). The fast increase of the a_{phy}443, and slower increase of CDOM with Chl*a*, provides a trend of higher a_{phy}443% and lower a_s% for increasing Chl*a*. This

trend is related to the higher proportions of phytoplankton cells and with higher intracellular Chl*a* for more productive waters (SATHYENDRANATH. et al., 2009).

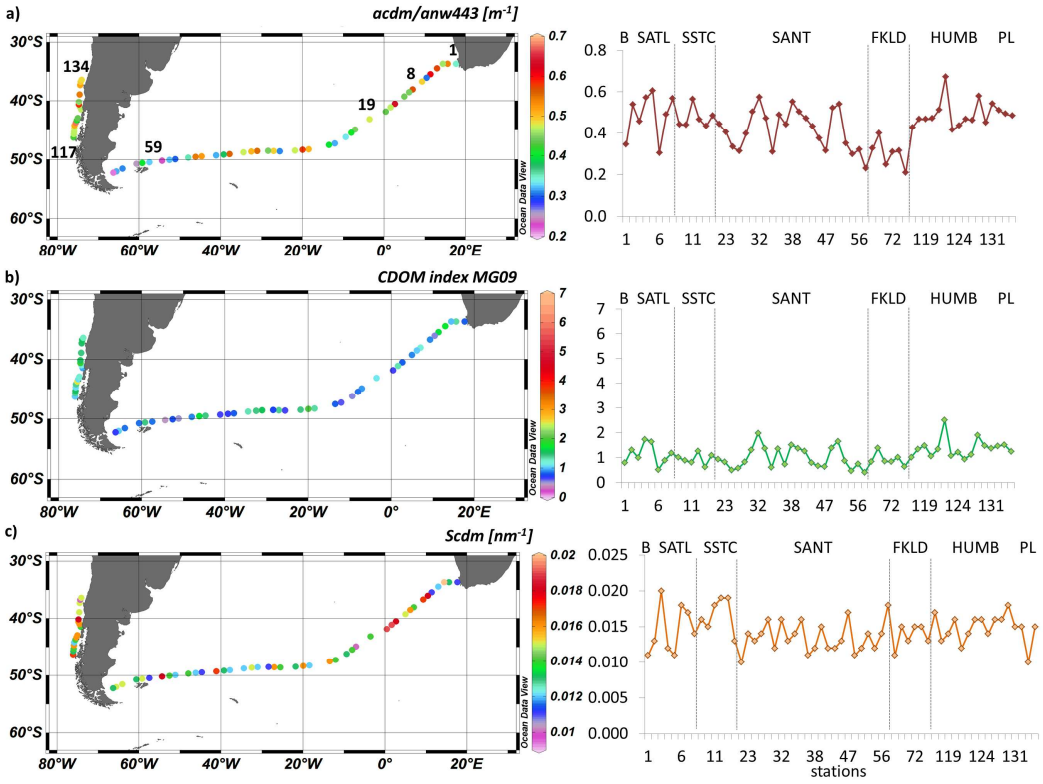

Figure 6.26 – Surface distribution of the $a_{cdm}/a_{nw}443$ (a), CDOM index (b) and S_{cdm} (c).

Table 6.5 – Mean and SD of the specific properties of the CDM distribution: a_{cdm}/a_{nw}, CDOM index and the spectral slopes (S) of the a_{cdm}, a_s and a_d, for each BGCP.

	$a_{cdm}/a_{nw}443$	CDOM index	S_{cdm} (nm^{-1})	S_{cdom} (nm^{-1})	S_d (nm^{-1})
BENG	0.343	0.79	0.011	0.012	0.009
SATL	0.504 ±0.102	1.18±0.43	0.015±0.003	0.019±0.008	0.010±0.001
SSTC	0.481±0.076	0.94±0.22	0.017±0.002	0.019±0.003	0.010±0.001
SANT	0.422±0.100	0.98±0.43	0.014±0.002	0.015±0.003	0.011±0.002
FKLD	0.300±0.066	0.92±0.25	0.014±0.002	0.015±0.002	0.009±0.002
HUMB	0.491±0.069	1.38±0.41	0.015±0.002	0.016±0.002	0.011±0.001
PL	0.488±0.006	1.37±0.19	0.013±0.003	0.014±0.005	0.011±0.001

The CDOM production has a time lag with the phytoplankton growth and decay cycles, and may also have significant losses due to photodegradation processes during its

production (SIEGEL et al., 2002), which would explain its slower increase with the Chl*a*. Nonetheless, there is still a generally strong covariation between the a_{cdm} and a_{cdm}% with the Chl*a* (r_s, 0.63 and 0.57, respectively), as the CDM production and losses are directly or indirectly tied to the phytoplankton productivity. In this manner, despite that the $a_{cdm}/a_{nw}443$ ratio contains information of the variability of the CDM proportions in respect to the phytoplankton biomass, it is still well correlated to the Chl*a*, which makes it more difficult to detect independent variations caused by more regional and local sources i.e., current advection, upwelling cells, continental inputs, downwelling and photodegradation losses, which are likely the main causes of deviations for the global OCR models (MOREL; GENTILI; 2009). The CDOM index (MG09 CI), on the other hand, is strongly related to the $a_{cdm}/a_{nw}443$ ($r_{s,}$ 0.81), but has a more independent variation in respect to the Chl*a* ($r_{s,}$ -0.31), indicating the dispersion of the CDOM absorption in respect to its global relation with Chl*a*. This index may thus, be a finer indicator of the CDOM second order variability than the $a_{cdm}/a_{nw}443$ ratio used in other works (LOISEL et al., 2010; SZETO et al., 2011).

Hence, despite that the CDOM index had generally a tight correlation with the $a_{cdm}/a_{nw}443$, it smoothed out the variations linked to the Chl*a* gradient, and evidenced more the local variations, which was highest across the SANT (Figure 6.26b). The BENG and FKLD had slightly lower index values (>1), whereas the HUMB coastal province had the highest values (1.37±0.4) (Table 6.5), probably associated with the greater continental contributions in this province, from the Chilean Fjords, and the upwelling sources at the PL. Whereas, the FKLD stations had likely more stratified conditions promoting higher photodegradation losses.

The SSTC and SANT had average values closer to 1 (Table 6.5), however, with a highly variable spatial pattern, which was negatively correlated to the Chl*a* (r_s, -0.75). This distribution was likely associated with the high spatial-temporal dynamics of the phytoplankton blooming stages and eddy-induced upwelling cells of these provinces, as discussed in the previous sections. The higher CDOM index values were at the low-Chl*a* "cells", which were likely associated with sources of past phytoplankton spring and early summer blooms and strong upwelling sites with well-mixed waters and emergence of deeper high-CDOM HNLC waters to surface. Whereas, the adjacent

stations with high-Chl*a* low-CDOM waters, were likely associated with the frontal mixing zones with new nutrient injections and more stable near-surface water columns, sustaining a longer duration of the summer phytoplankton blooms (LONGHURST, 2007), and enabling more CDOM photodegradation losses.

For a more comprehensive analysis of the spatial distribution of the CDOM and its variability in respect to the Chl*a*, MODIS ocean colour products averaged over the MV1102 sampling period for the Chl*a* (OC3M), $a_{cdm}443$ (QAA) and CDOM index (MG09) are shown in Figure 6.27. Instantaneous match-ups were not possible due to the intensive cloud coverage during the sampling period, as previously stated. Nonetheless, these averaged maps could also provide some important information to complement the *in situ* analysis, for further interpretations of the bio-optical relations and the processes governing their distribution. As mentioned for the OC3M, the $a_{cdm}443$ also showed a coherent spatial distribution with the *in situ* stations with approximate values. The *in situ* $a_{cdm}443$ varied from 0.005 to 0.125 m^{-1}, being lowest at the SATL (0.018 m^{-1}), SSTC and SANT (0.03 m^{-1}), and highest for the coastal productive provinces of the BENG (0.1 m^{-1}), FKLD (0.07 m^{-1}) and HUMB (0.05 m^{-1}), which was reasonably approximate to the MODIS QAA values across the provinces (Figure 6.27b). The MODIS CDOM index also seemed to be coherent with the *in situ* data, showing some higher values, but with a coherent spatial variability (Figure 6.27c).

Comparing the OC3M with the $a_{cdm}443$ maps, one may note the high spatial covariation between the phytoplankton biomass and CDM content, as obtained for the *in situ* set (r_s, 0.60). Despite that these waters are highly dynamic, some typical features were observed for both the *in situ* and MODIS ocean colour maps i.e., the lowest Chl*a* and $a_{cdm}443$ values for the oligotrophic SATL, the intermediate values for the SSTC and SANT, and the highest for the coastal productive provinces, with a sharp gradient demarking the shelf break limit of these provinces (Figure 6.27a and b). Regarding the CDOM index, some interesting features were the generally higher values at the waters adjacent to the productive systems, denoting some influences of current advections of higher CDOM waters to adjacent less productive waters i.e., at the borders of the coastal provinces and at the frontal zones of the Subtropical Front (STF) and Subantarctic Front (SAF). After the meeting of the equatorward Malvinas Current with the poleward

Brazilian Current at the Brazil-Malvinas Confluence Zone (BMCZ), the mean flow travels back southeastwards to the Southern Atlantic carrying highly productive and organically enriched waters from the South American shelves (MATANO et al., 2010). In this process there seems to be some accumulation of higher CDOM waters in the Argentina Abyssal Plain, which is advected eastward across the STF and SAF fronts by the South Atlantic Current (Figure 6.27). Hence, besides of the mesoscale processes of upwelling cells and vertical mixture, some larger scale circulation processes may also be governing second order variations in the CDOM distribution across the SANT and SSTC provinces.

As previously mentioned, some temporal dynamics of the phytoplankton blooming cycles and CDOM production across the SANT may also have caused some variability in the distribution of the CDOM index. As the CDOM is produced by both the current living phytoplankton assemblage and covarying zoo and bacterioplankton, and the degradation products of the past assemblage, there are some temporal differences in the phytoplankton growth and major CDOM production (SIEGEL; MARITORENA, 2005). As the major and most extensive phytoplankton blooms across the SANT occurs typically in the spring (November) (Figure 6.3) and diminishes to more localized blooms throughout the summer (January-February), the CDOM content likely has its highest production post-blooms (~1-2 months after) (SIEGEL; MARITORENA, 2005). Nonetheless, as it is being produced, CDOM is also being advected, downwelled and photodegradated, and is thus rapidly diminished throughout the productive seasons (SIEGEL et al., 2002; SWAN et al., 2012). Moreover, the Southern Atlantic is also influenced by high ultraviolet radiation (UV) incidence during spring, which may enhance the photodegradation processes (SIEGEL et al., 2002). Hence, the study period (Feb-March) comprehended high CDOM production by present and past phytoplankton, but also intensive photodegradation losses in the surface layer, across the Southern Atlantic. The higher CDOM index waters across the SANT were thus, likely associated with past phytoplankton bloom degradation products, strong upwelling cells of deeper CDOM-rich waters, and some accumulation of CDOM advected from highly productive shelves systems, especially in the STF and SAF frontal zones.

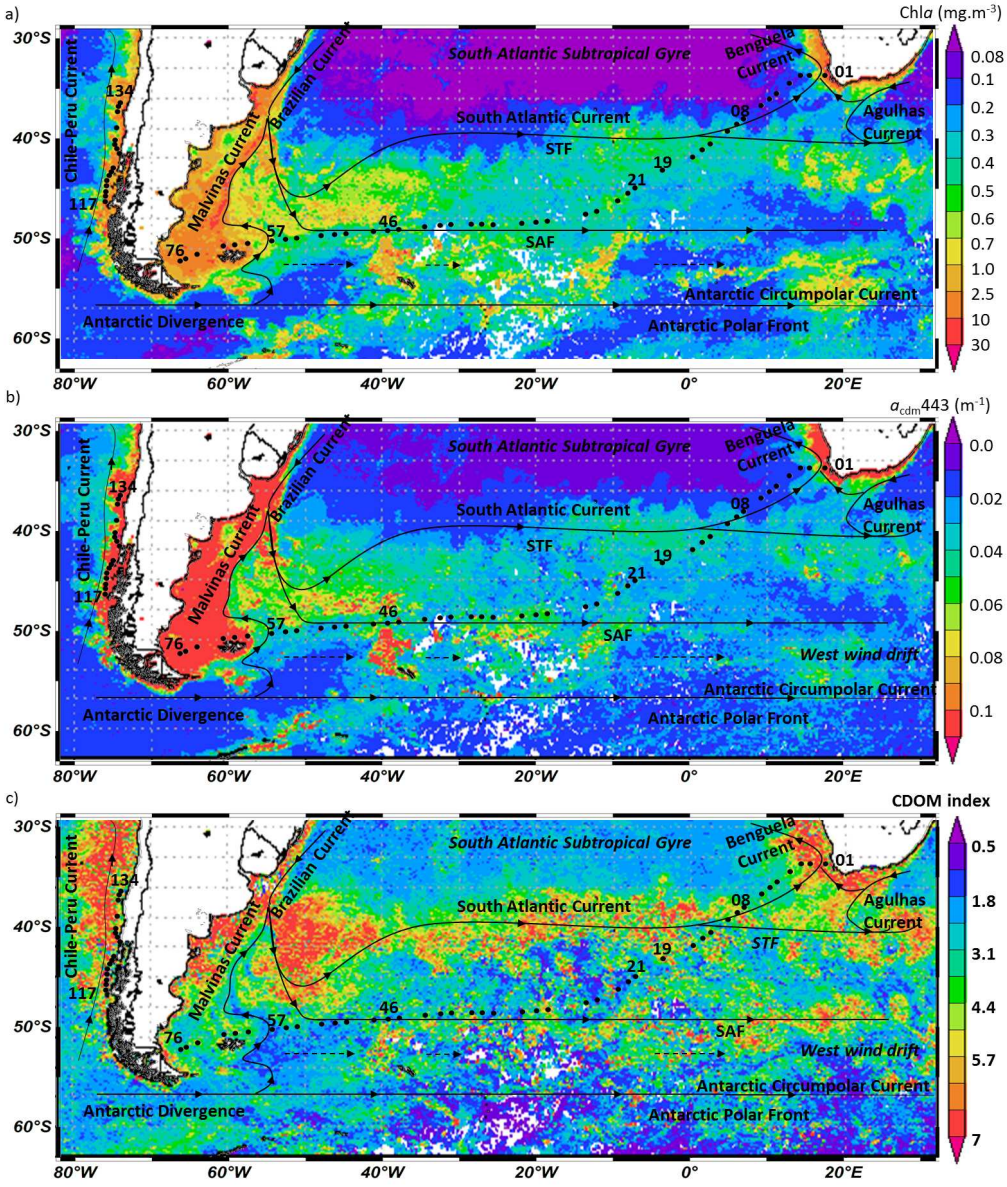

Figure 6.27 – OC3M (a), $a_{cdm}443$ (b) and CDOM index (c) maps using MODIS 8-day composites (4 km) averaged over the MV1102 sampling period (02/18-03/14/11). Stations in black dots and currents according to Stramma and England (1999).

For a final analysis of the CDOM second order variability across the study region, Figure 6.28 shows the relation between the $a_{cdm}/a_{nw}443$ and CDOM index with the Chl*a* for the different BGCPs. Both indices had a negative relation with the Chl*a* indicating a trend of higher CDOM proportions for lower Chl*a* waters, and vice versa. Nonetheless,

as the CDOM index was less correlated to the Chl*a*, it also highlighted some different trends for each province. The SATL followed a gradient of slightly higher CDOM index for the stations of the gyral borders, likely due to the influences of the adjacent productive BGCPs, of the BENG and the SSTC (as shown in Figure 6.27c). The stations located more towards the core of the SATL (St 06 and 07) had much lower CDOM indices, likely due to the greater distance of the adjacent provinces and more intensive photodegradation processes within these deeply stratified waters.

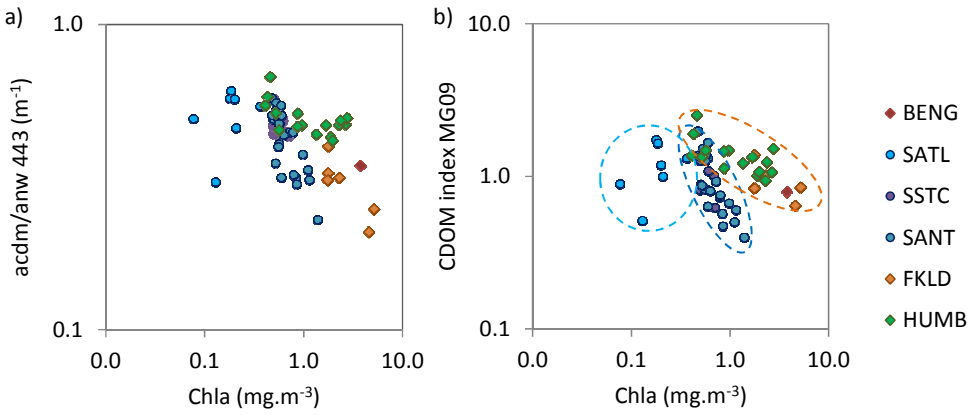

Figure 6.28 – $a_{cdm}/a_{nw}443$ and the CDOM index (b) versus Chl*a* for each BGCP.

The SSTC and SANT stations showed a negative relation with the Chl*a* (r_s, -0.75) with a fast decrease of the CDOM index for increasing Chl*a* waters, likely associated with the well-mixed low-Chl*a* high-CDOM "cells" and more stratified higher-Chl*a* lower-CDOM "cells (Figure 6.28b). The coastal provinces, on the other hand, showed some also tight relation with the Chl*a*, but with a slower decrease of the CDOM index for increasing Chl*a* (Figure 6.28b), which was likely associated with the high productivity of these stations and likely some influences of continental sources i.e., river discharger, runoffs, coastal erosion, and coastal upwellings. The highest index was at St 122 which was one of the lowest Chl*a* stations of the HUMB (0.46 $mg.m^{-3}$), and may have had influence of the Chilean Fjords and adjacent productive coastal waters (Figure 6. 27). Stations 133 and 134 of the PL upwelling site, also showed a shift of higher CDOM

index compared to the stations with equivalent or higher Chl*a*, denoting some sources of CDOM-rich upwelled waters e.g., St 127, with Chl*a* of 2.2 $mg.m^{-3}$ had an index of 0.9, whereas St 133 with 2.7 $mg.m^{-3}$ had an index of 1.5.

The lower CDOM index at the most productive stations of the FKLD were likely associated with the lower continental inputs at these stations and higher vertical stability promoting greater photodegradation CDOM losses. The major continental inputs of this coastal province, the La Plata River, is pushed northward by the Malvinas Current and thus, has minor (are no) influence in the southern FKLD (RIVAS, 2010). The southern FKLD is also known to have shallow stratified water columns throughout the spring and summer seasons (MATANO et al., 2010; LUTZ et al., 2010), which may favor more intensive photodegradation processes, as will be further discussed.

The BENG station showed an index approximate to the FKLD stations (Figure 6.28), which may be associated with the low continental inputs with minor river sources and precipitation, typical of the region (HARDMAN-MOUNTFORD et al., 2003), allied to the intensive CDOM photodegradation losses in the surface layers. The Cape Peninsula Upwelling Cell is characterized by dynamic pulses of strong upwelling events (SHILLINGTON; REASON, 2006). After such events that bring nutrient enriched waters to the surface, phytoplankton blooms develop in a more stable water column, which may be also more favorable for CDOM photodegradation losses, which was likely the condition of St 01.

According to Siegel et al. (2002) the main sources of CDOM variability in the open ocean are due to variations in the biological cycle of phytoplankton growth and decay and covarying microbial activity, photodegradation processes, which are more intensive in stratified systems and higher latitudes during summer, as well as physical forces of current transport and upwelling cells. The coastal provinces may also have some influences of continental CDOM inputs. All of these processes seemed to have significant effects on the CDOM variability across the Southern Atlantic Southeast Pacific, during the MV1102 cruise in the end of the austral summer.

Another bio-optical parameter that may also provide some important information regarding the CDOM distribution in terms of its origin (marine or continental) and

photochemical reactions, is the spectral slope (S) of the absorption coefficient. The variability of this parameter is also important for ocean colour applications as most semi-analytical (SA) models need to parameterize the S spectral slope to retrieve the CDM absorption. Hence, some analyses of the S_{cdm} distribution are also presented.

The CDM spectral slope ranged from 0.010-0.020 nm^{-1}, with a mean of 0.0144 nm^{-1}, showing some distinct spatial patterns across the study region. It was highest in the SATL, SSTC and HUMB and lowest in the BENG and PL upwelling cells, while the SANT and FKLD had more evenly distributed intermediate values (Figure 6.26c and Table 6.5). This range is compatible to other published values for regional and global data sets, with some slight variations. Roesler et al. (1989) obtained a range of 0.008-0.023, with a mean of 0.018 nm^{-1} for measured a_s in globally distributed oceanic waters. Carder et al. (1999) and Maritorena et al. (2002), on the other hand, obtained global fits of 0.0225 nm^{-1} and 0.0206 nm^{-1}, respectively, using *in situ* and IOP simulated data sets (IOCCG, 2006), whereas Lee et al. 2002 obtained an average of 0.015 nm^{-1} for the NOMADv2.

The CDM spectral slope is usually used as a constant in SA ocean colour models, nonetheless there may be some significant spatio-temporal variability depending on complex interactions involving land/sea exchanges, the productivity and state of the phytoplankton community, the microbial activity and photoreactive processes (MARITORENA et al., 2002; SWAN et al., 2012). As the a_{cdm} is mainly determined by the CDOM contribution, the S_{cdm} is also mainly regulated by S_{cdom}. Analyzing each component separately, the S_d had a much lower variability, and was evenly distributed across the entire study region, with an average of 0.010 m^{-1} (ranging from 0.007-0.014 nm^{-1}) (Table 6.5). The S_{cdom} had a much greater range, varying from 0.010-0.033 nm^{-1}, and a high spatial variability, proximate to the S_{cdm} distribution (Figure 6.26c). The highest values were in the SATL and SSTC (mean, 0.019 m^{-1}), and the lowest in the BENG and PL upwelling sites (mean, 0.0120 and 0.0135) (Table 6.5).

The distribution of the S_{cdm} did not reveal a pattern of different values for the coastal and open ocean provinces, or related to the CDOM index, which could link its variability to the different CDOM sources and loss processes. Nonetheless, there was some negative correlation between the spectral slope and the absorption coefficient

($a_{cdm}443$), which was consistent for both the CDOM and detritus components (r_s, -0.30). The trend of higher slopes for lower CDM waters could be associated with more intensive photodegradation processes (SWAN et al., 2012), especially for the most stratified conditions such as for the SATL core stations (St 06 and 07), and also probably some SSTC stations (St 11, 13 and 17), which had the highest S_{cdom} slopes (Figure 6.29).

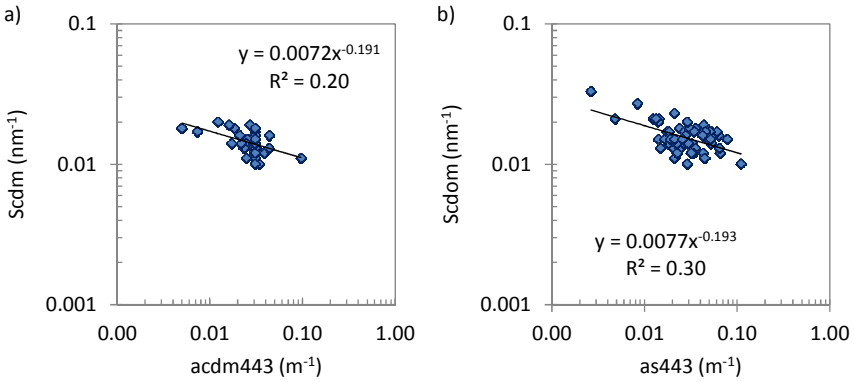

Figure 6.29 – CDM (a) and CDOM (b) spectral slopes (S) vs. their absorption coefficients (acdm443 and as443).

The relations between the a_s spectral slope with the CDOM origin, chemical structure, and biological and photochemical degradation, are still not very well known, as there are complex inter-relations acting simultaneously in natural systems. Hence, it is difficult to obtain strong covariations likely associated with any of the processes regarding the CDOM sources and losses. Further works are needed to understand better these relations and obtain further information of the CDOM variability across different BGCPs. An important point to highlight though is that there may be in fact a high variability of the S_{cdm} which needs to be accounted in ocean colour models. The use of a constant value may degrade the IOP retrievals and omit important bio-optical variability with information of the biogeochemical processes.

*6.3.1.3.3. Specific particle backscattering coefficient (b_{bp}*555)*

The particle backscattering coefficient normalized by the Chl*a* (b_{bp}*555, b_{bp}555/Chl*a*) can be used as an indicator of the b_{bp} "efficiency" of the bulk particle assemblage in respect to the Chl*a*. This index provides information on how much greater or lower is the bulk b_{bp} per unit of mgChl*a*, which may be linked to the varying contribution of the particles types and size ranges. Hence, its variability may provide some information on the composition and PSD of the particle assemblage (LOISEL et al., 2010).

According to Mie theory the b_{bp} efficiency should be highest for smaller and/or high-index particles and lowest for larger and/or low-index particles. Nonetheless as previously discussed, natural complexities of mixed assemblages with varying sizes, refractive indices and morphological structures, add higher-level complexities to these relations. As shown in the present work, both the submicron and larger fractions (>0.7 μm) had significant contributions to the bulk b_{bp}, the first with a tight linear covariation with the Chl*a*, and the second with a dispersive power law relation (Figure 6.14). The linear relation of the submicron fraction was likely due to an invariant b_{bp} "efficiency" of this range. Whereas the power law relation of the larger fraction was likely due to a trend of decreasing b_{bp} "efficiency" for higher Chl*a*, with increases in the proportions of larger particles (LOISEL et al., 2006), and low b_{bp} contributors i.e., more phytoplankton cells (with also high intracellular Chl*a*) and less detritus. The high dispersion associated with the larger fraction was however, also likely associated with the varying contributions of larger high-index particles i.e., coccoliths and minerals (STRAMSKI et al., 2001), as well as some possible effects of more complex morphological structures of aggregates and micro diatoms (DALL'OLMO et al., 2009). Such sources varied independently with the Chl*a* across the BGCPs and caused the greater dispersions in the b_{bp} vs. Chl*a* relation. Hence, there were both Chl*a*-dependent and independent sources regulating the b_{bp} variability associated with different PSD and particle types. To provide some more insights on such variability across the study region, analysis of the distribution of the b_{bp}*555 are presented herein.

The b_{bp}*555 had a spatial distribution strongly related to the Chl*a* gradient (Figure 6.30a), with a negative correlation (r_s, -0.86). As the bulk b_{bp}555 increased with the Chl*a* in a power law function, the b_{bp}*555 decreased in an inverse manner (Figure

6.31a). The number of HB cells per milligram of Chl*a* (HB*) also had a strong negative correlation with the Chl*a* (r_s,-0.89), with a very similar pattern as the b_{bp}*555, showing a strong linear relation (r_s, 0.84) (Figure 6.31). The b_{bp}*555 also had a positive correlation with the PSD3 µm ξ (r_s, 0.49) and a_d% (r_s, 0.56), indicating higher b_{bp} "efficiencies" associated with greater contributions of smaller microbes and picoautotrophs, and covarying submicron particles, as well as the greater proportions of detritus in respect to the phytoplankton cells (with likely higher C:Chl*a*). The highest b_{bp}*555 values were thus at the oligotrophic waters of the SATL (0.011±0.004 m^2.mgChla^{-1}) with greater proportions of microbes (HB*) and small *Prochlorococcus* cells (82±20%) (Table 6.5), and higher a_d443%. Whereas, the lowest b_{bp}*555 values were at the most eutrophic stations of the BENG, FKLD and PL (mean, 0.001 m^2.mgChla^{-1}) (Figure 6.30), with lower HB* and higher proportions of larger pico-sized cells of *Synechococcus* and picoeukaryotes (r_s, -0.56) (Table 6.6), and lower a_d%443.

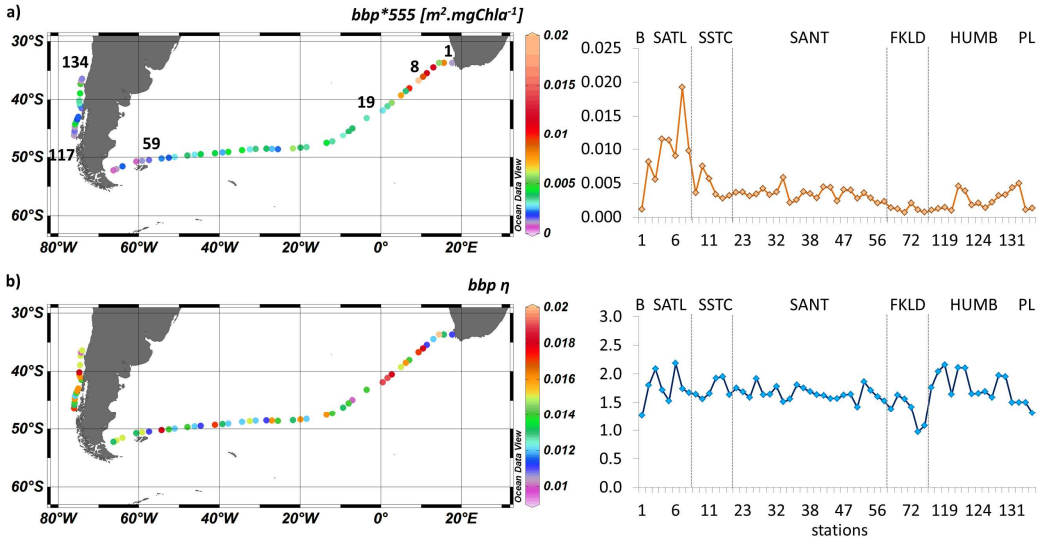

Figure 6.30 – Surface distribution of the specific b_{bp} (b_{bp}*555) (a) and spectral slope η (b).

Besides of the submicron and pico-sized PSD ξ and the varying proportions of phytoplankton cells and detritus particles, another source that may indirectly cause some impacts on the b_{bp}*555, which is also associated with changes in the C:Chl*a* ratio, is the variability of intracellular Chl*a* (SATHYENDRANATH et a., 2009). In fact, the a_{phy}*

which may indicate this source of variability, had a positive correlation with b_{bp}* (r_s, 0.63). Hence, the higher b_{bp}*555 for lower Chl*a* waters was also likely associated with the lower intracellular Chl*a* of the pico cells typical of these waters.

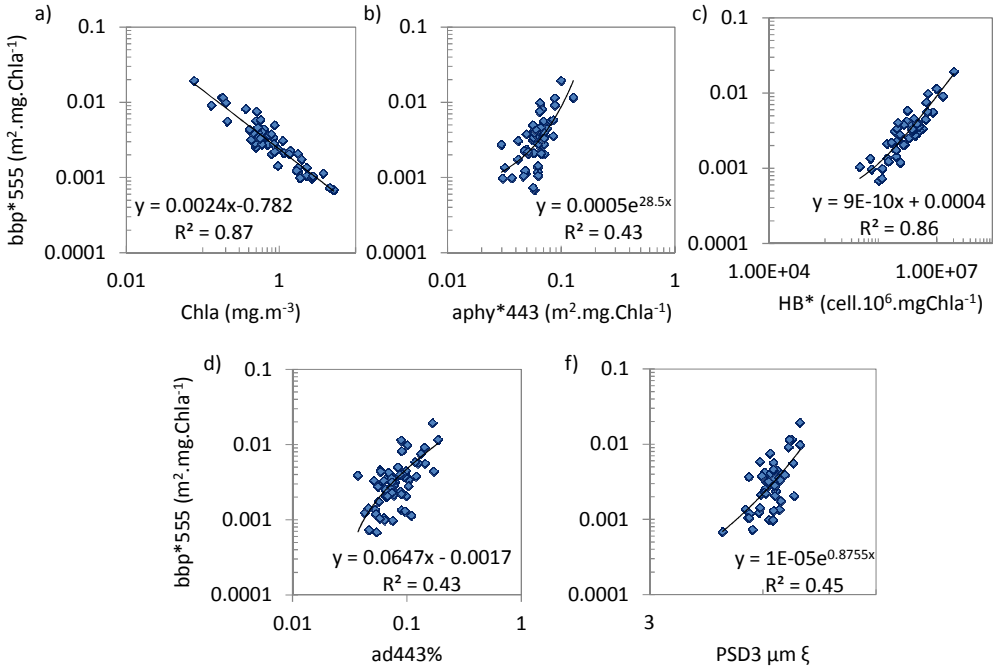

Figure 6.31 – Dispersion graphs of the specific b_{bp} (b_{bp}*555) vs. the Chl*a* (a), a_{phy}*443 (b), HB* (c), a_d443% (d) and PSD3 µm ξ (f).

As all these indices are correlated to the Chl*a*, it is rather difficult to detect to what extent one determines the other, or are indirectly covarying. In attempt to verify if the relations between the specific b_{bp} and the greater proportions of smaller cells sustain independently of the variations in the a_d%433 and a_{phy}*443, the b_{bp}/a_d443 ratio was also analyzed. The correlation coefficients were somewhat lower but still significant with a negative correlation of b_{bp}/a_d443 with Chl*a* (r_s, -0.51) and a_d443 (r_s, -0.76), and positive with HB* (r_s, 0.44) and PSD 3 um ξ (r_s, 0.31). Hence, this indicates that both the varying proportions of smaller particles, including detritus, HB and proclorophytes, as well as, the shifts in the C:Chl*a*, associated with the varying abundance of

phytoplankton cells, and intracellular Chl*a*, were likely important sources determining the b_{bp}* distribution across the study region.

The b_{bp}*555 had also a weak positive correlation with the b_{bp} spectral slope (r_s, 0.29) (Figure 6.30). The η had a negative correlation with the Chl*a* (r_s, -0.47) likely related partly to the PSD of the submicron and pico-sized particles (r_s, 0.27 with the PSD3 µm ξ) and partly to the effects of the biogenic absorption (r_s, -0.58 with a_d443 and 0.50 with a_{phy}443), as discussed in the previous section. These sources of b_{bp} variability generally covaried with the trophic levels however, there were also some independent variations of η and b_{bp}*555, which indicated significant effects of some different sources. Whereas the b_{bp}*555 was strongly correlated to the Chl*a* gradient, by both direct and indirect sources (of the PSD and C:Chl*a* ratio), the η slope was less correlated, showing stronger effects of the independent sources of variability, such as the varying presence of high-index larger particles. Such sources may have in fact caused an inverse relation between the b_{bp}*555 and η, as the greater contribution of larger high-index particles would provide a higher b_{bp}*555 but lower η.

Table 6.6 – Mean and SD of the b_{bp}*555, the b_{bp} spectral slope (η), proportion of heterotrophic bacteria (HB*) and percentage of Prochlorococcus (PROCH), Synechococcus (SYN) and Picoeukaryotes (EUK) (within the picoautotrophs), for each BGCP.

	b_{bp}*555 (m^2.mgChla^{-1})	η	HB* (cell.10^6.mgChla^{-1})	PROCH (%)	SYN (%)	EUK (%)
BENG	0.001	1.260	-	-	-	-
SATL	0.011 ±0.004	1.818±0.23	11,546,966	82±20	18±20	0.8±0.5
SSTC	0.004 ±0.002	1.729±0.17	5,527,590	11±5	83±11	6±6
SANT	0.003 ±0.001	1.656±0.12	3,182,386	0.1±0.2	80±19	20±19
FKLD	0.001 ±0.001	1.340±0.26	1,384,434	0±0	68±29	32±29
HUMB	0.003 ±0.001	1.809±0.24	2,285,367	7±14	86±17	7±6
PL	0.001 ±0.004	1.403±0.14	892,006	0±0	77±29	23±29

To verify the consistency of these relations, and the effects of the variability of the b_{bp}*555 and η on the b_{bp}555 vs. Chl*a*, Figure 6.32 shows the dispersion graphs with the stations grouped to corresponding higher and lower values for each parameter (25% highest and lowest). The highest b_{bp}*555 values mapped well the stations with higher

b_{bp} "efficiencies" of both lower and intermediate Chl*a* waters, and vice versa (Figure 6.32a). Nonetheless, as the sources of higher b_{bp}*555 were different for the lower and intermediate Chl*a* waters, the first being caused by greater contributions of smaller particles and the second by greater contributions of high-index larger particles, the b_{bp}*555 alone could not separate these different sources.

Regarding the higher and lower η values, its distribution was also strongly determined by the Chl*a* gradient. The most dispersive stations, however, had in fact inverse relations of b_{bp}* and η (Figure 6.32b and c). Hence, using both the b_{bp}* and η parameters one may distinguish the different sources of b_{bp} variability: a) a first order variability of covarying b_{bp}* and η values linked to the Chl*a* gradient, with direct and indirect effects of the PSD shifts, C:Chl*a* and biogenic absorption; and b) a second order variability associated with the varying abundance of larger high-index particles, causing inverse b_{bp}* and η relations i.e., higher b_{bp}* and lower η values in the presence of larger high-index particles and lower b_{bp}* and higher η for greater contributions of low-index submicron and pico-sized particles (Figure 6.32c).

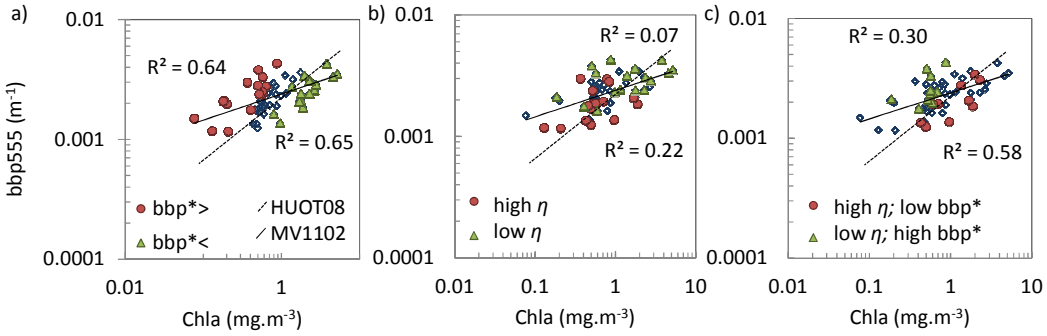

Figure 6.32 –b_{bp} vs. the Chl*a*, highlighting the stations with the highest and lowest b_{bp}*555 (a), η spectral slopes (b) and with inverse b_{bp}*555 and η relations (c). The HUOT08 is the Huot et al. (2008) fit and the MV1102 is the fit for the present work. The R^2 values correspond to the fits of the subsets of higher and lower respective values.

6.3.1.4. Effects of the variations in the local time

Variations in the photosynthetic active radiation (PAR) of each sampling site due to the different times of collection, latitudes and cloud coverage, may also cause some sources of variability in the bio-optical relations and surface distribution of the specific IOPs, which may be minor, but somewhat significant. The local PAR may cause some variations in the photoacclimatation processes of the phytoplankton assemblage, in the intensity of the CDOM photodegradation processes and composition and PSD of the living and non-living assemblage, associated with vertical migration processes and diel cycles, i.e., zooplankton grazing, microbial activity, phytoplankton productivity, respiration and growth, among others. Such sources of variability were not the focus of the present work and only limited analyses can be performed. Nonetheless, in attempt to verify the significance of such sources and possible mis-leading interpretations regarding the spatial variability of the bio-optical relations of the specific IOPs, i.e., the a_{phy}*, a_{cdm}/a_{nw} (and CDOM index) and b_{bp}*, some brief analyses are presented herein.

As previously mentioned the latitudinal gradient of the sampled region was not so high (~33.7-52.2^{o}S) and this effect was considered minor. The cloud coverage may have had some effects, however as most of the stations were held under mostly overcast conditions, with only a few clear sky days (see Table 5.1), it would be rather difficult to evaluate such effects comparing stations with similar conditions of Chl*a* levels, PFTs and CDOM content, but different sky conditions. Moreover, as the study region is generally subjected to persistent cloud coverage, such conditions may be considered prevalent for most of the stations and also have minor effects on the variability of the bio-optical properties sampled throughout the study region.

The effects of the variations in the local time of collection was however, likely an important source of variability which was possible to verify since there was a synchronized collection time along the transect. The collection times were approximately at: 6, 12 and 19:00, with also some intermediate stations at: 9, 16 and 21:00. The stations were thus grouped into: early morning, noon and evening-night stations for analysis of the impacts of this variability. Figure 6.33 shows the means and SDs of the Chl*a* and specific IOPs within each group of collection. The Chl*a* was evenly distributed with no statistical difference between the groups (p<0.05, for the Analysis of

Variance (ANOVA)), showing that all the optical ranges of water types were well represented within each group.

There seemed to be some trend of higher a_{phy}*443 and b_{bp}*555, and lower CDOM index values for the evening-night group (Figure 6.33). The higher a_{phy}*443 could be associated with a slight decrease in the intracellular Chl*a* of the phytoplankton cells, or some vertical migration of the PFT groups, at the end of the day. The higher b_{bp}*555 at the evening group could be associated with the accumulation of diurnal processes of growth and carbon fixation, causing shifts of higher proportions of smaller particles, whereas the early morning lower b_{bp}*555 could be associated with nocturnal processes of respiration and losses of cellular material, cellular division and grazing, increasing the proportions of larger particles (KHIEREDDINE; ANTOINE, 2013). The lower evening CDOM index could be associated with the greater photodegradation loss occurred during the day, and the higher morning index due to the accumulation of night-time exudation and degradation processes.

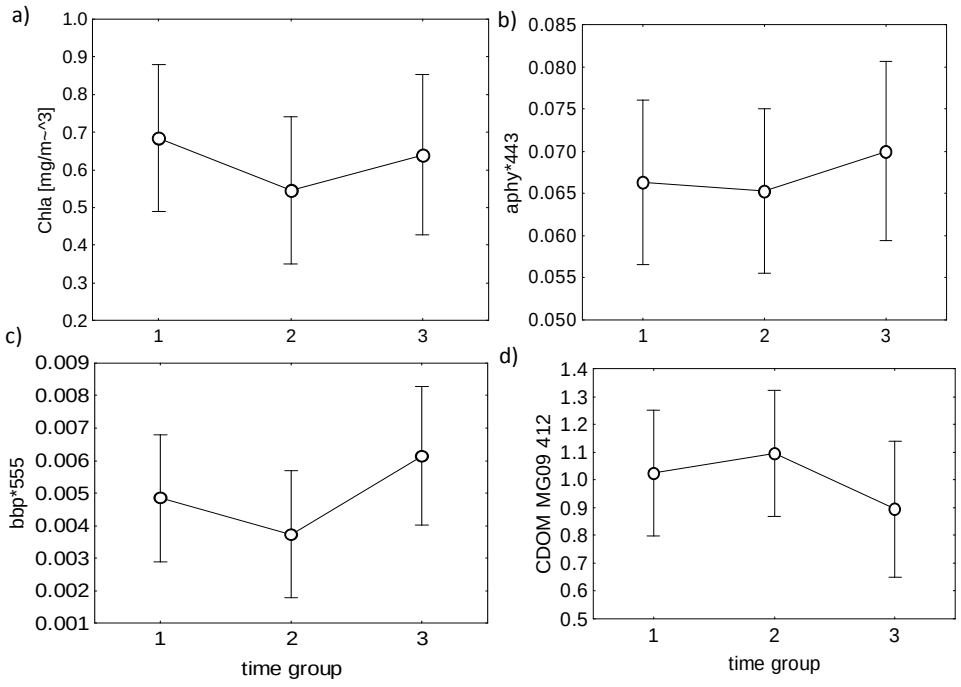

Figure 6.33 - Mean and SD of the Chl*a* (a), a_{phy}*443 (b), b_{bp}*555 (c) and CDOM index (d), for the early morning (1), noon (2) and evening-night (3) stations.

These differences however, were not statistically significant, applying the ANOVA test (p<0.05), which denoted minor effects of these sources, compared to the much greater horizontal spatial variability of the specific IOPs across the study region. This supports the analysis and discussions presented so far regarding the major sources of bio-optical variability across the surface layer of the study region. Nonetheless, it is pertinent to highlight the importance to consider such sources of variability, as there may be some significant impacts, especially when looking into finer scale variabilities.

6.3.1.5. Vertical distribution of the IOPs and bio-optical indices

The vertical distribution of the IOPs was also analyzed for the radiometric (CTD) stations (N=19) in attempt to verify the representativity of the surface depths (1-4 m) within the first optical depth ($\delta \sim 1/K_d490$), and to analyze the bio-optical relations within the upper layer (~100 m) for further discussions regarding the processes governing the distribution of the IOPs.

Figure 6.34 shows cross section maps of each IOP interpolated for the entire transect to illustrate the main vertical and horizontal distributions. The oceanic stations were mostly homogeneous within the first optical depth (33-11.5 m) and upper most layer (~50 m), across the SATL, SSTC and SANT, whereas the coastal stations of the FKLD and HUMB, had more attenuating waters (δ, 4-15 m) and shallower optical stratifications. Even though these coastal stations had some sharp surface IOP variability, the surface depths were still fairly representative of the first optical depth as shown in Figure 6.34 (and also analyzed in the previous Chapter). Hence, even for these stations the surface depths used in the analysis of the horizontal distribution of the IOPs, were considered reasonably representative for remote sensing applications.

The SATL stations had the most deeply stratified waters as expected for this oligotrophic province, with the Fl_{max} reaching ~80 m at St 06, covarying with the IOP peaks (Figure 6.34). The SSTC stations (St 09-19), with intermediate Chl*a* levels, had higher IOP values in the upper most layers (up to 50-80 mm) generally following the Chl*a* profile with an Fl_{max} ranging from 1-35 m. The SANT stations (St 23-56) had a similar pattern as the SSTC stations, with the Fl_{max} ranging from 20-50 m. Some differences in the vertical distribution of the IOPs were however, also observed. The

$a_{phy}443$ and $b_{bp}443$ followed a pattern more tied to the Chl*a* distribution, whereas the $a_{cdm}443$ had some independent variations, generally with a more homogenous profile within the upper layer or with a sub-surface peak bellow the $a_{phy}443$ and $b_{bp}443$ peaks.

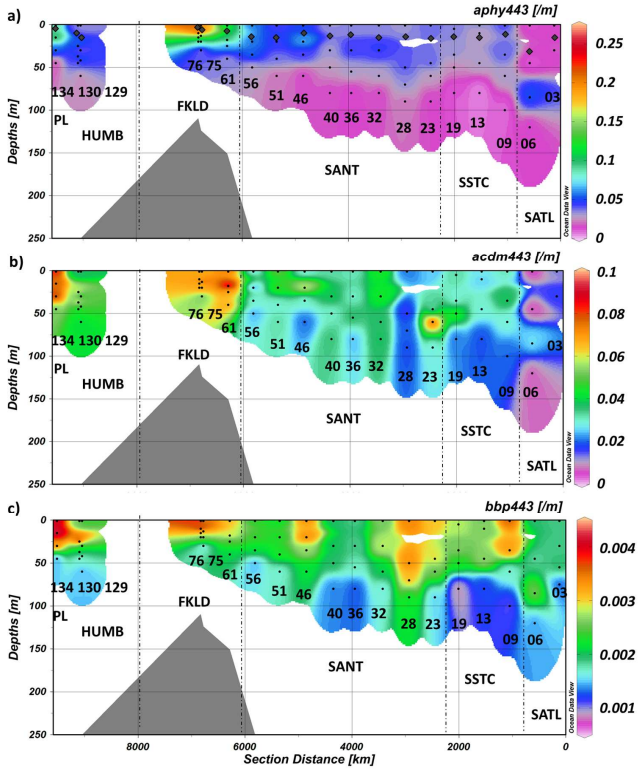

Figure 6.34 – Vertical distribution of the IOPs across the MV1102 stations: $a_{phy}443$ (a); $a_{cdm}443$ (b) and $b_{bp}443$ (c), for the radiometric stations (N=19). The black dots correspond to the sampled depths and the diamonds to the first optical depth (in (a)).

The higher-Chl*a* stations of the SANT (e.g. St 46 and 28) showed some more pronounced optical stratifications for all the IOPs, which could be associated with the more stabilized near-surface frontal zones, sustaining higher phytoplankton blooms throughout the summer season, adjacent to well-mixed stronger upwelling cells, as discussed in the previous sections. The shallow optically stratified FKLD stations also showed a distribution coherent with other works across the FKLD during spring and summer seasons (MATANO et al., 2010; LUTZ et al., 2010), and with the present

discussions, with high phytoplankton biomass and likely more intensive surface CDOM photodegradation processes. The HUMB province had contrasting optical waters with a surface Chl*a* ranging from 0.43 $mg.m^{-3}$ (St 129) to 2.36 $mg.m^{-3}$ (St 134), denoting the sharp gradient across the coastal productive waters and the offshore clear oceanic waters. The most productive station at the PL upwelling site (St 134) had higher IOP values within the upper ~30 m generally following the Chl*a* distribution (Figure 6.34).

Regarding the specific IOPs, the a_{phy}*443 was generally higher within the upper layer (<50 m) and lower for greater depths (Figure 6.35). These differences were mainly associated with the variations in the phytoplankton community structure, with distinct vertical distributions for the different PFTs (UITZ et al., 2006), and to some local photoacclimatation processes. The higher a_{phy}*443 in the upper most layers followed the general trend of higher proportions of pico and nano groups (r_s, 0.54), shifting to lower a_{phy}*443 at greater depths, with the increasing proportions of nano and micro groups (r_s, 0.60) (Figure 6.36). The highest values at surface depths were also likely influenced by some local photoacclimatation processes to adapt to higher light levels, shifting to lower a_{phy}443* at higher-depths with low-light levels (HOEPFFNER; SATHYENDRANATH, 1992; BRICAUD et al., 1995, 2004).

The b_{bp}*443 showed an inverse distribution of the a_{phy}443, denoting the strong negative relation with the Chl*a* (r_s, -0.82), also observed for the horizontal distribution (Figures 6.34 and 6.35). The CDOM index, on the other hand, had more independent variations in respect to the a_{phy}443 and Chl*a* (r_s, -0.22), denoting stronger effects of other sources regulating its vertical variability. The index was generally more vertically homogeneous, and showed some lower values at the most surface depths likely associated with more intensive photodegradation losses, whereas the higher values at greater depths were likely associated with the lower Chl*a*, higher biodegradation of sinking particles, and upwelling of deep CDOM-rich waters.

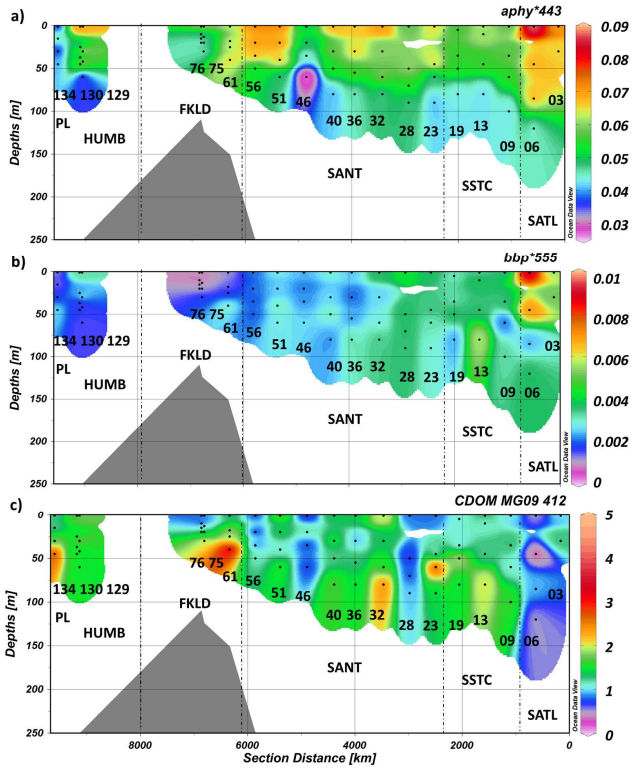

Figure 6.35 – Vertical distribution of the specific IOPs: a_{phy}*443 (a), b_{bp}*555 (b) and CDOM index (c) for the radiometric stations (N=19).

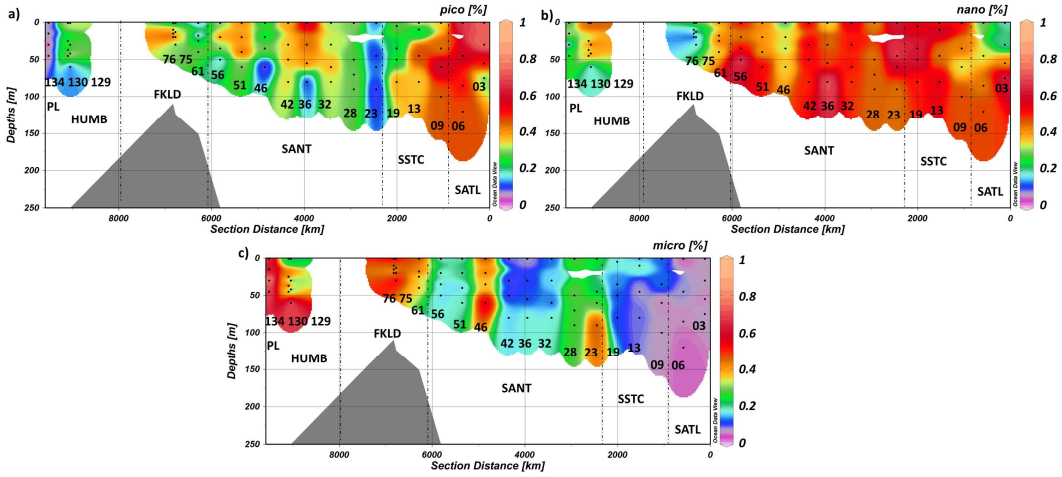

Figure 6.36 – Vertical distribution of the phytoplankton size fractioned PFTs (pico, nano and micro) determined by HPLC pigments ratios.

The lowest CDOM index throughout the entire upper layer, was at the SANT (St 03 and 06), denoting the intensive photodegradation processes of the deeply stratified clearest-water province. The high-Chl*a* stations of the SANT (St 28, 46 and 56) also had lower CDOM index values, likely associated with the more stratified conditions of these stations. Whereas the adjacent low-Chl*a* higher-CDOM stations (St 32-42 and 51) were likely associated with more well-mixed waters with CDOM-rich upwellings and post spring-bloom biodegradation products. The higher Chl*a* stations of the SANT had in fact higher proportions of nano and micro groups as shown in Figure 6.36, which are more typical of near-surface stabilized productive waters, adjacent to nutrient renewal sources of upwelling cells and coastal systems (BOYD, 2002; LONGHURST, 2007). Whereas, the low-Chl*a* higher-CDOM stations were dominated by pico (*Synechococcus* and picoeukaryotes) and nano groups (Figure 6.36), typical of the well-mixed HNLC waters of the SANT (BOYD, 2002).

For a closer analysis of vertical distribution of the bio-optical properties and indices within each BGCP, some stations are shown with a more detailed analysis. Figure 6.37 shows the vertical profile of St 06 of the SATL, denoting the deep Chl*a* maximum peak beyond 80 m. All the IOPs covaried with the Chl*a* distribution, as well as the total HB concentration. The a_{phy}*443 had a tight covariation with the PFT fractions, decreasing with depth as the proportion of nano fraction increased, independent of the Chl*a*. Some minor photoacclimatation processes also likely contributed for the highest a_{phy}*443 at surface. The b_{bp}*555 practically mimicked the inverse Chl*a* profile, linked to the higher proportions of smaller particles for lower Chl*a* waters and higher C:Chl*a*. The CDOM index was fairly homogenous and lower than 1, likely associated with the lower phytoplankton living stock and intensive photodegradation processes.

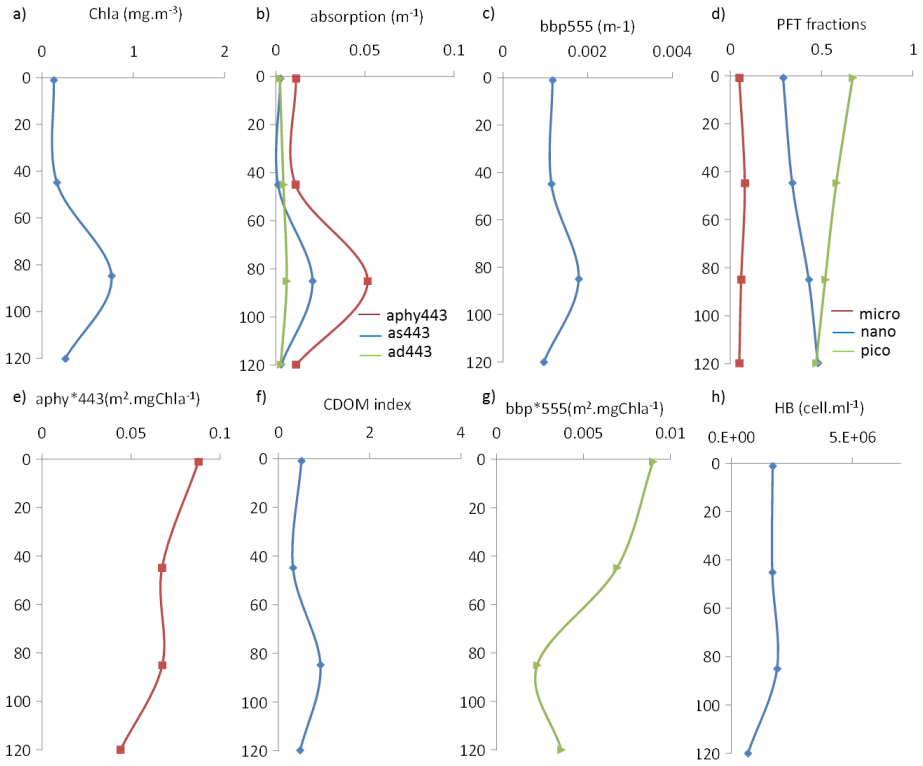

Figure 6.37 – Vertical profiles of the bio-optical parameters at St 06 (SATL): Chl*a* (a); biogenic absorption coefficients (b); backscattering coefficient (c); HPLC PFT fractions (d); the specific phytoplankton absorption coefficient (e); CDOM index (f); the specific backscattering coefficient (g); and the total concentration of heterotrophic bacteria (HB) (h). The dots correspond to the sampled depths.

As the SSTC and SANT stations are more spatio-temporally dynamic systems, defined by strong seasonal cycles and influence of mesoscale processes, there were some greater differences in the vertical distribution of the IOPs, showing some independent relations. As previously discussed, these BGCPs were characterized by intermittent "cells" of lower-Chl*a* higher-CDOM waters dominated by nano and pico groups. Figure 6.38 shows an example of St 32 with such conditions. One may note the generally homogenous distribution of the IOPs, PFTs and HB, and especially of the a_s443. This last even showed some independent distribution in respect to the other IOPs, cohobating with the discussions of well-mixed waters and influences of "extra" CDOM sources from past phytoplankton blooms and upwelled waters.

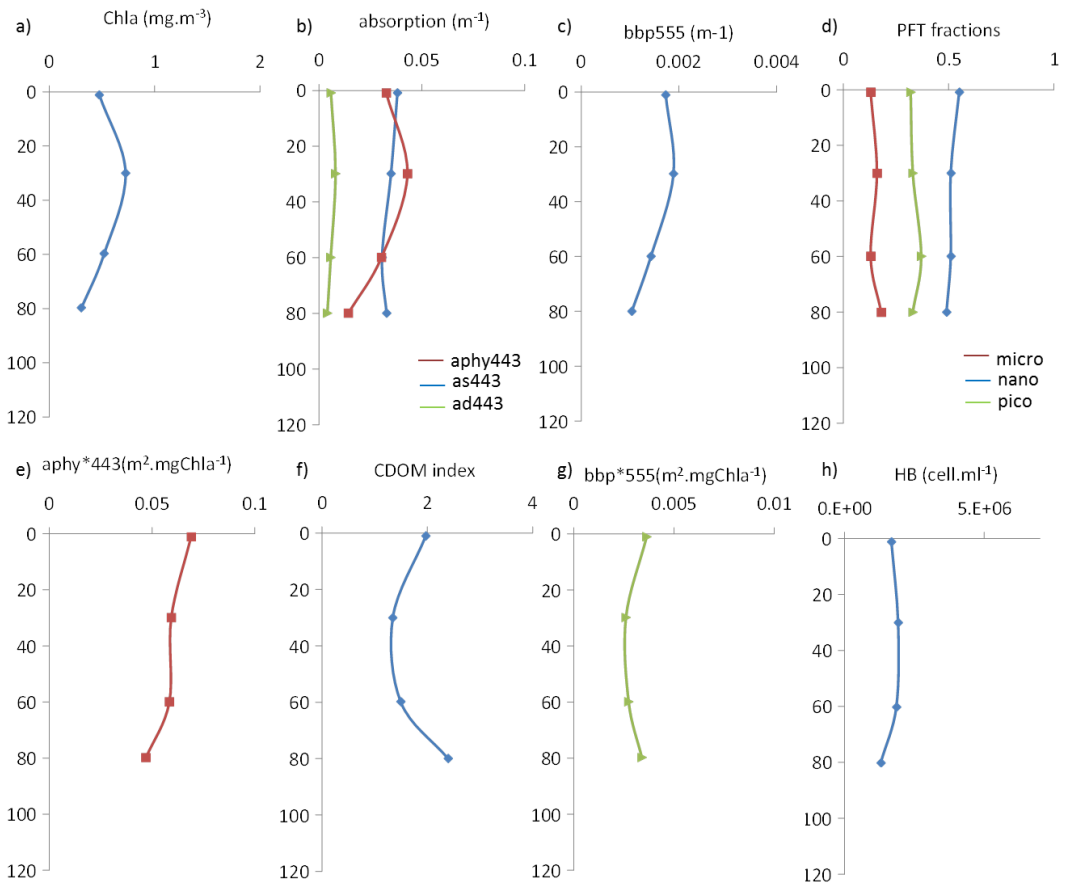

Figure 6.38 - Vertical profiles of the bio-optical parameters at St 32 (SANT): Chl*a* (a); biogenic absorption coefficients (b); $b_{bp}555$ (c); HPLC PFT fractions (d); a_{phy}*443 (e); CDOM index (f); $b_{bp*}555$ (g); and HB (h).

The higher-Chl*a* lower-CDOM "cells", with greater proportions of micro groups, on the other hand, had a tight covariation of the a_s443, and other IOPs, with the Chl*a*, and showed more optically stratified profiles (Figure 6.39). The covarying pattern of the a_s443 with the Chl*a*, supports the previous discussion related to the longer bloom duration of these productive waters, as well as the higher CDOM photodegradation losses of more stratified waters and lower influence of external upwelling CDOM-rich sources.

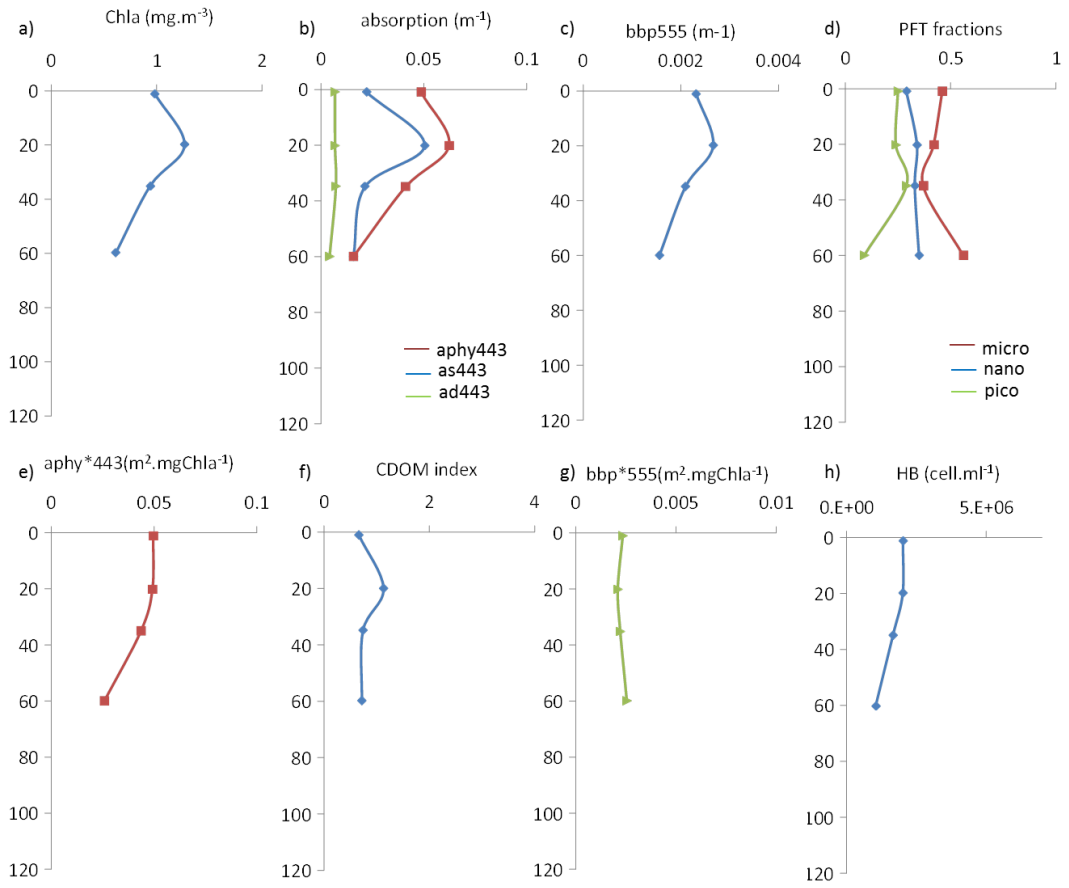

Figure 6.39 - Vertical profiles of the bio-optical parameters at St 46 (SANT): Chl*a* (a); biogenic absorption coefficients (b); $b_{bp}555$ (c); HPLC PFT fractions (d); a_{phy}*443 (e); CDOM index (f); $b_{bp*}555$ (g); and HB (h).

Figure 6.40 shows an example of a FKLD station, denoting the shallow optical stratification and the tight covariation between the IOPs and Chl*a*. The a_{phy}* showed a monotonic decrease with depths, following the increasing proportions of micro cells with likely also some effects of local photoacclimation processes (Figure 6.40). The CDOM index had the lowest value at the surface depths indicating some higher effects of photodegradation.

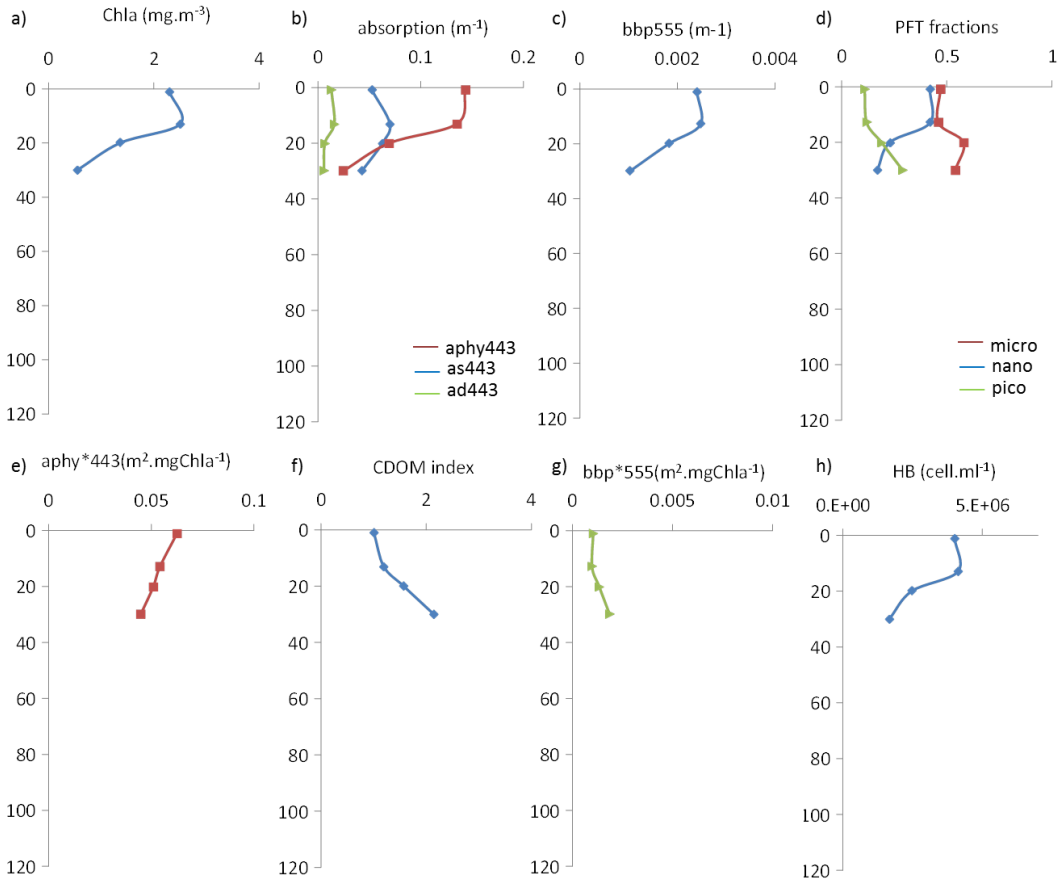

Figure 6.40 - Vertical profiles of the bio-optical parameters at St 75 (FKLD): Chl*a* (a); biogenic absorption coefficients (b); $b_{bp}555$ (c); HPLC PFT fractions (d); a_{phy}*443 (e); CDOM index (f); $b_{bp*}555$ (g); and HB (h).

The HUMB stations were characterized by two typical conditions of: lower Chl*a* with nano and pico dominance; and higher Chl*a* with greater proportions of micro and nano groups and shallower optically stratified waters. For both cases the IOPs generally covaried with the Chl*a* profile, with exception for the a_s443 which showed some independent distribution and a more homogenous profile, likely related to the greater influence of "external" sources of continental inputs, coastal upwelling and advection from more productive waters. Hence, the CDOM index was generally higher for all of the HUMB stations (with both higher and lower Chl*a*). The a_{phy}*443 showed the same pattern as for all the other provinces, strongly determined by the PFT distribution, i.e., lower at greater depths with greater proportions of micro groups. A different pattern that

was more evident at St 129, was regarding the $b_{bp}443$ distribution, which showed some independent variations in respect to the Chl*a*, and more tied to the a_d443 and HB distributions (Figure 6.41). This cohobates for the discussions regarding the stronger contributions of other particles, i.e., detritus, microbes, hydrosols, to the bulk b_{bp}.

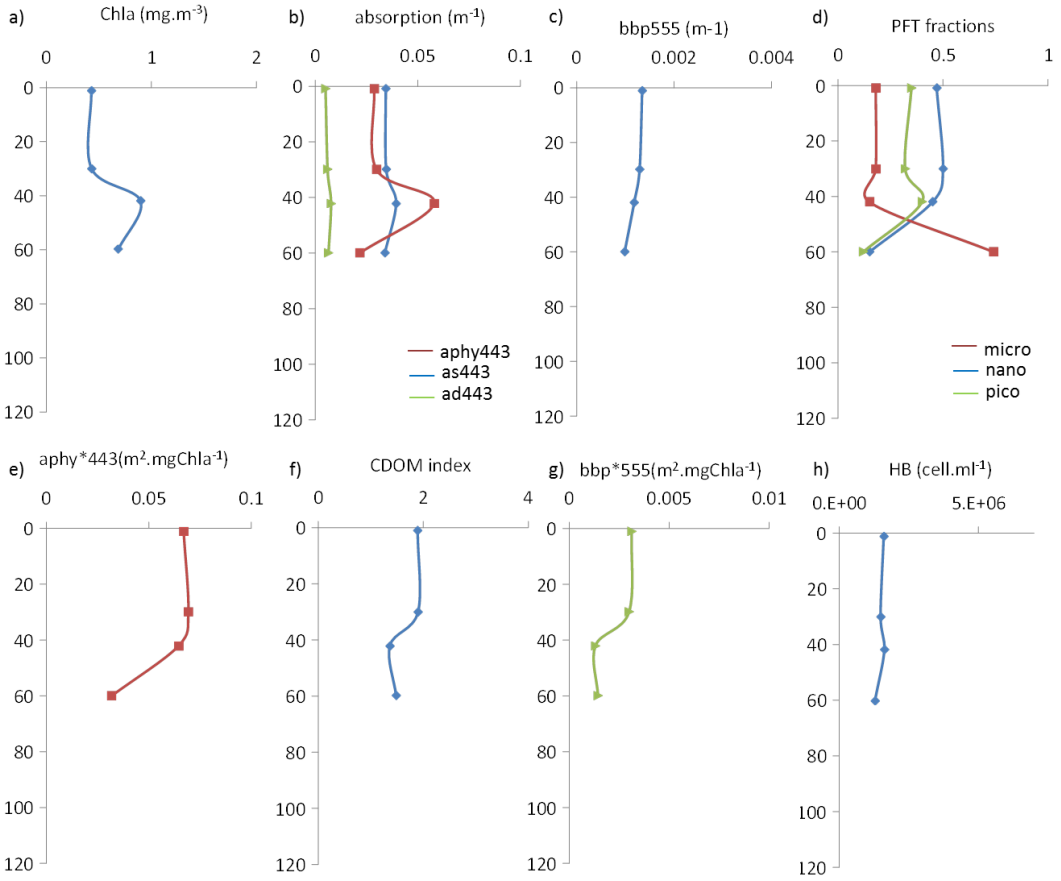

Figure 6.41 - Vertical profiles of the bio-optical parameters at St 129 (HUMB): Chl*a* (a); biogenic absorption coefficients (b); $b_{bp}555$ (c); HPLC PFT fractions (d); a_{phy}*443 (e); CDOM index (f); $b_{bp*}555$ (g); and HB (h).

The vertical distribution of the IOPs and bio-optical indices showed some similar relations as observed for the surface horizontal distribution across the study region. The present analysis contributed to some discussions regarding the possible sources determining the bio-optical variability across the different BGCPs, highlighting the

following relations: a) the strong covariation of the a_{phy}* with the sized PFTs, (independent of the Chl*a*), and some minor effects of local photoacclimatation; b) the lower CDOM index, especially at the surface depths for more stratified waters, with more intensive photodegradation processes (for both higher and lower Chl*a* waters), and the higher CDOM index for more homogenous water columns with "external" sources of past phytoplankton blooms, upwelling cells and continental inputs; and c) the generally strong positive covariation of b_{bp} and Chl*a*, however, determined by the covarying contribution of other particle types, i.e., submicron and larger detritus, microbes and hydrosols.

6.3.2. Implications of the bio-optical variability for the OC4v6 model

The empirical Maximum Band Ratio (MBR) OC4v6 model (O'REILLY, 1998; O'REILLY et al., 2000) retrieves the surface Chl*a* using a polynomial function with the MBR of: R_{rs}443/555; R_{rs}490/555 and R_{rs}510/555 (Equation 3.14). The choice of the MBR is to optimize the performance of the model for a high Chl*a* dynamic range (0.02-100 mg.m^{-3}), as the signal-to-noise ratio diminishes for the shorter spectral bands as Chl*a* increases (due to the higher absorption and lower R_{rs}). The empirical model has generally a good performance for Case 1 waters, but there is also some significant dispersion which may be associated with the spatio-temporal variations of the specific IOPs across different BGCPs (MOORE et al., 2009; SZETO et al., 2011). To verify the impacts of the bio-optical variability across the Southern Atlantic and Southeast Pacific for the OC4v6 model, its performance was analyzed using the RTE R_{rs} and comparing the modeled and measured Chl*a* (Chl*a*3).

The overall performance of the OC4v6 for the study region was reasonably good with a r^2 of 0.90, a RMSE of 0.34 mg.m^{-3} and a RPD* of 22%, which is lower than the uncertainty level recommend by standard OCR programs (35% for Chl*a*) (ESAIAS et al., 1998; O'REILLY et al., 2000; MUELLER et al., 2003). There was no overall trend of under or overestimations (RPD, -0.7%) nevertheless, when looking at each BGCP separately there were some significant differences likely related to the distribution of the specific IOPs within each province (Figure 6.42).

The SATL stations had the highest overestimations with a 47% RPD (Figure 6.42), especially for stations 04 and 05 which had high values for all the specific IOPs, e.g., St 04 had an a_{phy}*443 of 0.128 m^2.mgChla^{-1} (the highest obtained for the MV1102), a b_{bp}*555 of 0.011 of m^2.mgChla^{-1} and a CDOM index of 1.72. As all the SATL stations were dominated by small *Prochlorococcus* cells (PROCH, >90%), what mainly distinguished these 2 stations were not only the high a_{phy}* and b_{bp}* values, but also the higher CDOM index, which was much lower for the adjacent stations (>0.80, especially for St 06 and 07 at the SATL core). Hence the combining effects of the specific IOPs may either enhance the dispersions when they covary positively, or have compensation effects, when they have inverse relations.

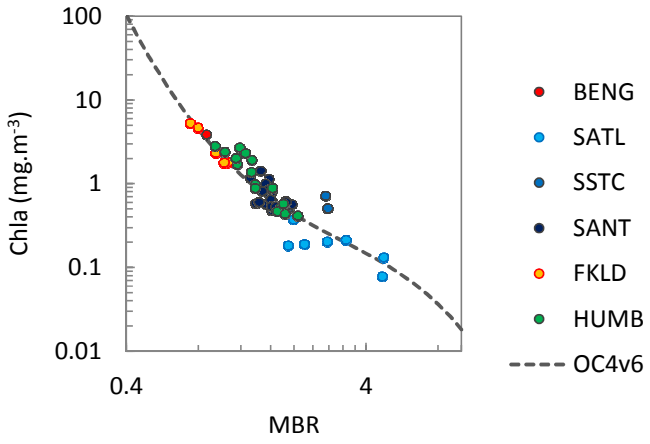

Figure 6.42 –Maximum Band Ration (MBR) (R_{rs}443;490;510/555) vs. Chl*a* for each BGCP, indicating the OC4v6 global fit by the dashed line.

The highest underestimations were at the SSTC province (-21.6% RPD) (Figure 6.42), especially for stations 11 and 17, which had much lower specific IOPs. Station 17 had the lowest a_{phy}*443 for the entire cruise, with 0.029 m^2.mgChla^{-1}, which may be associated with some local photoacclimatation processes, as previously discussed. The b_{bp}*555 was also very low with 0.0027 m^2.mgChla^{-1}, as well as the CDOM index with 0.61, all contributing for the OC4v6 underestimation.

The SANT province had closer matches to the OC4v6 fit with both under and overestimations (0% RPD and 20% RPD*) (Figure 6.42), likely related to the higher bio-optical spatial variability of this province. The underestimations were associated with the "cells" of higher-Chl*a* (with lower a_{phy}* and b_{bp}*) and lower-CDOM, whereas the overestimations were for the "cells" of lower-Chl*a* and higher-CDOM index.

Despite of the optical complexity of the coastal FKLD waters (LUTZ et al., 2010; FERREIRA et al., 2013), this province actually had the best match for the OC4v6, showing only some slight overestimations (5% RPD and 6% RPD*) (Figure 6.42). The higher a_{phy}*443 (0.06 ±0.003 m^2.mgChla^{-1}) characteristic of the small pico and nano-sized diatoms abundant at these stations, was likely the main cause of the model overestimations. The lower b_{bp}* (0.0012 ±0.001 m^2.mgChla^{-1}) and CDOM index (0.92±0.25), on the other hand, compensated some of the spectral MBR variations, enhancing the OC4v6 performance.

The HUMB coastal province had a trend of more underestimations (-15.2% RPD) (Figure 6.42), due to the lower a_{phy}*443 (0.047 ±0.009 m^2.mgChla^{-1}), with likely greater proportions of larger micro diatoms and dinoflagellates (53% of the HPLC fraction) and lower b_{bp}* (0.0019 ±0.0008 m^2.mgChla^{-1}). The slightly higher CDOM index of this coastal province (1.37±0.3), also compensated some of the MBR spectral variations, diminishing the OC4v6 underestimations.

Analyzing the effects of each specific IOP separately, one may see even more clearly how the highest values of the specific IOPs i.e., a_{phy}*443, b_{bp}*555 and a_{cdm}/a_{nw}443 (and CDOM index), caused overestimations for the OC4v6 model, whereas the lowest values caused underestimations (Figures 6.43 and 6.44 and Table 6.7). The quartile of lowest a_{phy}*443 values (D1) (0.043±0.008 m^2.mgChla^{-1}) had a -32% RPD, whereas the highest values (D2) (0.081±0.016 m^2.mgChla^{-1}) had a 29% RPD, between the modeled and measured Chl*a* (Figures 6.43a and 6.44a, and Table 6.7).

The spectral effects of the a_{phy}*443 on the MBR is regarding the higher absorption, for a given Chl*a*, that diminishes the R_{rs} of the shorter spectral bands (R_{rs}443;490;510), consequently diminishing the band ratios (with R_{rs}555) (and vice versa). Hence, the a_{phy}*443 variability causes an effect of "greener" waters for higher values, and "bluer"

waters for lower a_{phy}*443 (LOISEL et al., 2010). Since the a_{phy}*443 is strongly determined by the phytoplankton size structure, which generally covaries with the trophic state (Chl*a*), the first order variability of the a_{phy}*443 will not have significant impacts on the MBR global empirical fit. Nonetheless, when there are more regional or local variations in the PFT distribution and/or photoacclimatation processes, as discussed throughout the work, this may cause some impacts on the OC4v6 performance.

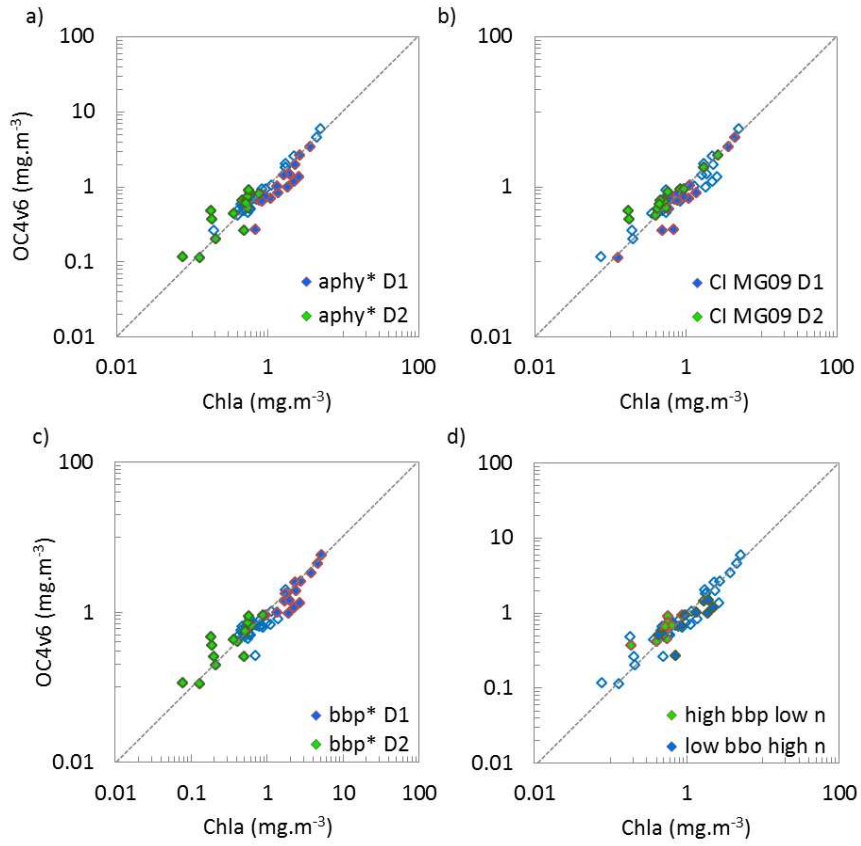

Figure 6.43 –Measured Chl*a* vs. modeled OC4v6, indicating the lowest (D1) and highest (D2) quartile for the: a_{phy}*443 (a); CDOM index (CI MG09) (b); b_{bp}*555 (c); and the stations with inverse relations for b_{bp}*555 and the spectral slope (η) (d).

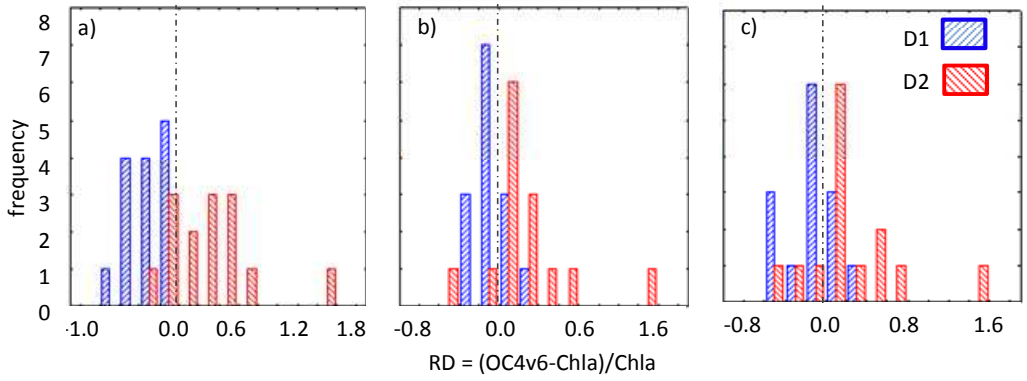

Figure 6.44 – Histograms of the frequency distribution of the RD (Relative Difference) (of the measured Chl*a* and modeled OC4v6) for the lowest (D1) and highest (D2) quartile of each specific IOP: a_{phy}*443 (a); CDOM index (CI MG09) (b); b_{bp}*555 (c).

Table 6.7 - Mean values and the RPD (measured Chl*a* vs. OC4v6) for the quartile of the stations with the 25% lowest (D1) and highest (D2) specific IOPs, i.e., a_{phy}*443, b_{bp}*555, acdm/anw and CDOM index. (N= 15 for each quartile).

		D1	D2
a_{phy}*443	Mean (m^2.mgChla^{-1})	0.043±0.008	0.081±0.016
	RPD (%)	-32	29
a_{cdm}/a_{nw}443	Mean	0.30±0.041	0.57±0.043
	RPD (%)	-9	28
CDOM index	Mean	0.63±0.13	1.62±0.31
	RPD (%)	-23	26
b_{bp}*555	Mean (m^2.mgChla^{-1})	0.001±0.000	0.008±0.004
	RPD (%)	-17	26

Regarding the variability in the proportions of CDM in respect to the bulk biogenic absorption, there was also a trend of overestimations (28% RPD) for higher values (D2) and underestimation for lower values (-9%) (D1) (Figures 6.43b and 6.44b, and Table 6.7). Since the a_{cdm}/a_{nw}443 ratio was strongly correlated to the Chl*a*, as shown in the previous sections, the CDOM index separated better the effects of the second order CDM variability on the OC4v6 model, showing higher underestimations for the lowest values (-23% RPD) and overestimations for the highest (26% RPD) (Table 6.7). The spectral effects of the variability in the proportions of CDM has a similar effect as the a_{phy}*443, with a higher absorption for higher CDM, diminishing the R_{rs} at the shorter

blue bands, and diminishing the MBR (and vice versa) (LOISEL et al., 2010). Hence, the waters are "greener" for higher CDM proportions and "bluer" for lower CDM.

The impacts of the a_{phy}* variability on the MBR model showed to be somewhat higher than the CDM proportions for the study region (Table 6.7). Nonetheless, this was likely due to the higher dynamic range of the second order variations of the a_{phy}*. The spectral variations of the a_{cdm}, however, may have greater effects on the MBR for equivalent ranges of variability (LOISEL et al., 2010). This may be observed by decomposing the total absorption coefficient (a) at the 443 and 555 nm spectral bands and comparing the relative contributions of the $a_{cdm}555/a443$ and $a_{phy}555/a443$ ratios (Figure 6.45). As one may note, for the Chl*a* range of 0.3 to 3.0 mg.m^{-3} the $a_{cdm}555/a443$ is generally higher than the $a_{phy}555/a443$. Analyzing a global *in situ* data set (NOMADv2) and simulated IOP, Loisel et al. (2010) obtained higher $a_{cdm}555/a443$ ratios by a factor of 3.6 to 1.9 than the $a_{phy}555/a443$ ratios, for the same Chl*a* range. Hence, variations in the $a_{cdm}555/a443$ ratio may have greater impacts on the MBR for the same range of variation as for the $a_{phy}555/a443$. Moreover, as the CDM variability is generally less correlated to the Chl*a*, this source may cause some higher dispersion for the OC4v6, when analyzing global data (MOREL; GENTILI, 2009).

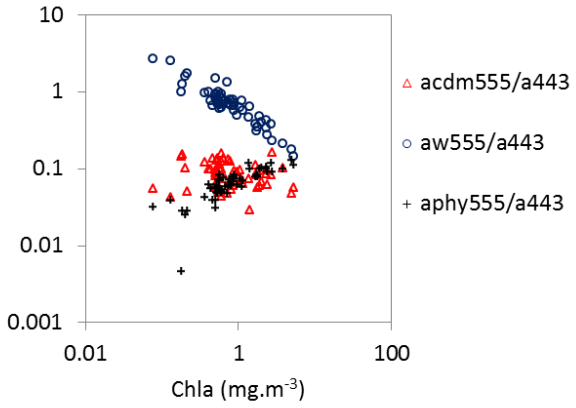

Figure 6.45 – a_w555/a_t443, $a_{cdm}555/a_t443$ and $a_{phy}555/a_t443$ ratios as function of the Chl*a*.

The b_{bp}*555 variability also showed significant impacts on the MBR model, with underestimations for the lowest values (D1) (0.001±0.000 m^2.mgChla^{-1}) with a -17% RPD, and overestimations for the highest (D2) (0.008±0.004 m^2.mgChla^{-1}) with 26% RPD (Figures 6.43c and 6.44c and Table 6.7). As shown in the previous sections, the b_{bp}*555 was highly correlated with the Chl*a* likely associated with the trend of higher proportions of smaller particles and higher C:Chl*a* ratios, with higher proportions of probably stronger b_{bp} contributors i.e. detritus, microbes and hydrosols, and phytoplankton cells with lower intracellular Chl*a*. Local independent variations in these relations, as well as the varying presence of "larger" (>0.7 μm) high-index particles, were likely the main sources of second order variability causing dispersions in the OC4v6 model. Hence the b_{bp}*555 alone was not so efficient to map the major dispersions in the MBR. An alternative to map the major sources of second order b_{bp} variability, was by identifying the stations with inverse relations between the b_{bp}*555 and b_{bp} spectral slope (η), in which higher b_{bp}*555 and lower η would indicate the presence of larger high-index particles i.e., coccoliths and minerals, and lower b_{bp}*555 and higher η would indicate higher proportions of smaller low-index particles i.e., submicron detritus and microbes. When mapping the stations with such inverse relations, only the independent-Chl*a* dispersions related to the b_{bp} variability were identified, with higher-b_{bp}*555 lower-η stations causing overestimations (20% RPD, N=10), and low-b_{bp}*555 high-η causing underestimations for the OC4v6 (-24% RPD, N=10) (Figure 6.43d).

The spectral effects of the higher b_{bp} for a given Chl*a* (b_{bp}*555) on the MBR, cause the same effect of "greener" waters, diminishing the MBR (as for the higher a_{phy}* and CDOM index), however in a different manner. As the biogenic absorption dominates more the R_{rs} signal of the shorter bands, the variations in the b_{bp}, causes greater impacts on the longer green-red spectral bands. Hence, the higher b_{bp}*555 values increases more the green R_{rs} band (R_{rs}555), especially when associated with larger high-index particles with lower η slopes, diminishing the MBR and overestimating the OC4v6 (LOISEL et al., 2010). For lower b_{bp}*555 waters, especially with higher η slopes, the effect is the inverse, with lower R_{rs}555 enhancing the MBR. Hence, higher proportions of larger high-index particles cause OC4v6 overestimations, whereas higher proportions of smaller low-index particles cause underestimations.

In resume the present analysis revealed that the second order variations of the specific IOPs i.e., a_{phy}*443, CDOM index and b_{bp}*555, caused some important impacts on the OC4v6 performance for the BGCPs of the Southern Atlantic and Southeast Pacific. The highest values caused spectral effects that diminished the MBR, causing overestimations for the OC4v6 model, whereas the lower values caused the inverse, with underestimations. This was coherent with similar analysis presented in other works analyzing the impacts of the bio-optical variability on the OC4, using global data (NOMADv2) (LOISEL et al., 2010; SZETO et al., 2011). Nonetheless, as the specific IOPs had some independent variations within the BGCP, there were also some compensation effects lowering the OC4 dispersion for the study region (in the sampled period).

According to Szeto et al. (2011), the impacts of the bio-optical variability on the OC4v6 may be grouped by oceanic basins as there may be some prevailing specific optical characteristics within each basin, associated with dominant larger scale biogeochemical processes (Figure 3.4). In their analysis the Atlantic Ocean had an overall tendency to be overestimated by the OC4v6, which they discussed as being related to higher CDM proportions, as it is a more narrow oceanic basin with important inputs of large size rivers, e.g., the Amazon and La Plata rivers, and higher a_{phy}*443, more dominated by smaller PFTs. The Southern Ocean, on the other hand, may have a tendency to be underestimated as there are lower CDM proportions, with higher photodegradation processes, and lower a_{phy}*443 values due to the greater dominance of larger micro PFTs. The Pacific basin, also may have a tendency to be underestimated, likely due to lower CDM proportions and lower a_{phy}*443. Nevertheless, although Szeto et al. (2011) analyzed a comprehensive data set of the NOMADv2 (N=2,365), the points were highly concentrated in some specific regions, especially in coastal provinces of the northern hemisphere, and some restricted to some seasons. The Pacific Ocean also has high concentrations of points near the Californian, Japanese and Chinese coasts, which are productive waters that may in fact have lower a_{phy}*443 with more dominance of micro PFTs. A couple of points are spread in the Equatorial and Subtropical open ocean waters, but they are much fewer. For the Atlantic basin, there is a high concentration of points near the North American coastal waters and in the surroundings of the Amazon river discharge, which are likely higher CDM waters. The North Atlantic is also known

to have extensive blooms of coccolithophores, which may contribute for higher b_{bp}* values, and for the OC4v6 overestimations. The Southern Ocean points are highly concentrated in the surroundings of the Antarctic Peninsula (Werdell Sea), and the majority were taken during the austral spring and summer seasons, when there are likely higher CDOM photodegradation processes and diatoms blooms (with lower a_{phy}*443). Hence, even though Szeto et al. (2011) found consistent trends across the basins and suggest such dominant conditions, they do call attention for the uneven spatio-temporal distribution of the points, which may cause mis-leading interpretations when extrapolating to the entire basin.

In the present work the BGCPs showed some dominant trends which were somewhat comparable to the analysis provided by Szeto et al. (2011), with more overestimations for the southern Atlantic and underestimations for the Southeast Pacific. Nonetheless, the second order variations of the specific IOPs also showed some high spatial variability and the combined effects of the simultaneous interactions of the properties, resulted in either higher or lower dispersions for the OC4. As the relations are also temporally dependent following the seasonal cycle of phytoplankton blooms, CDM production and photodegradation, surface layer stratification and mixing processes, as well as, the continental inputs of glacial-fluvial waters at ice-melting and rain fall seasons, further analysis of the the bio-optical variability within the oceans need to account for such temporal dynamics. Hence, a class-based approach defining dynamic optical water types, such as proposed by Moore et al. (2009; 2012), may be more adequate to encompassed the spatio-temporal variations across the different BGCPs and ocean basins.

6.3.3. Correlation and grouping analysis: class-based approach

To synthetize the bio-optical variability and the relations with the distribution of the phytoplankton groups and microbial assemblage across the study region, as well as the impacts on the OC4v6 MBR model, a Spearman correlation analysis is shown in Table 6.8. All the specific IOPs were negatively correlated to the Chl*a*, with generally higher values for lower Chl*a* waters and lower for higher Chl*a*. There were however, some particularities for each specific IOP related to the different sources of second order variabilities, as shown and discussed throughout the previous sections.

As the b_{bp}*555 had the strongest correlation with Chl*a* (r_s, -0.86) it had similar inverse relations with all the other bio-optical indices, either by direct or indirect relations, i.e., higher b_{bp}*555 for greater proportions of pico cells and microbes (r_s, 0.84 for HB* and r_s, 0.44 for PROCH%) and likely lower C:Chl*a* ratios, for lower Chl*a* waters, and vice-versa. The b_{bp}*555 also had some correlation with the OC4v6 RPD (r_s, -0.44), denoting the impacts of this property on the MBR. Such impacts, however, may have been more significant for covarying effects of the a_{phy}*443, as these properties were also strongly correlated (r_s, 0.63). Hence, the OC4v6 overestimations were greater for lower Chl*a* waters and the underestimations for higher Chl*a* waters (r_s, -0.51), due to the covarying effects of the b_{bp}*555 and a_{phy}*443 on the MBR.

The b_{bp} spectral slope (η) was less correlated to the Chl*a* (r_s, -0.47), indicating some greater effects of independent sources of variations, regarding the composition and size distribution of the particle assemblage, with varying proportions of smaller low-index and larger high-index particles. There was no significant correlation with the OC4v6 RPD, nevertheless, as previously shown, when analyzing the b_{bp}*555 and η together, these two properties provided more information on the variability of the particle assemblage and their impacts on the MBR model (Figure 6.43).

The a_{phy}*443 had the strongest correlation with the OC4v6 RPD (r_s, 0.72), denoting the significant impacts of the second order variations of this property on the MBR OC4v6 model deviations. The CB06 SI size index had a positive correlation with a_{phy}*443 (r_s, 0.70) and pico fraction (r_s, 0.76) (and negative with micro (r_s, -0.80), denoting a reasonable indicator of the PFT size distribution. The pico fraction was positively correlated to both Zea* (r_s, 0.70) and Prasin* (r_s, 0.68), indicating the significant contribution of *Synechococcus*, Prochlorophytes and Prasinophytes for the pico fraction. The nano fraction was mainly represented by Haptophytes (both calcareous and non-calcareous), with a strong correlation with 19'HF (r_s, 0.95). The micro fraction was mostly represented by diatoms (r_s, 0.70) and much minor by dinoflagellates (r_s, 0.00). The a_{phy}*443 was not so strongly correlated to the micro fraction (r_s, -0.59) as the pico, likely due to the variability in the size distribution of the diatoms, especially at the FKLD stations, with pico and nano-sized diatoms.

The CDOM index (MG09 CI) had a much weaker correlation with the Chl*a* (r_s, -0.33) than the $a_{cdm}/a_{nw}443$ (r_s, -0.57), as this index was more related to second order variations in the proportions of CDM in respect to the current phytoplankton biomass. Hence, as previously shown, the MG09 CI was also more related to the OC4v6 deviations (r_s, 0.57) than the $a_{cdm}/a_{nw}443$ (r_s, 0.47), highlighting the impacts of this source of variability in the MBR model.

Table 6.8 - Spearman Rank Correlation coefficients for the specific IOPs, OC4v6 RPD, Chl*a* and the microbial and PFT indices. The values in bold are significant for $p<0.05$.

	Chl*a*	aphy*	CB06	bbp*	bbp η	acdm*	MG09	Sacdm	RPD	micro	nano	pico	ξ 3um
Chl*a*	1.00												
aphy*443	**-0.73**	1.00											
CB06 SI	**-0.74**	**0.70**	1.00										
bbp*555	**-0.86**	**0.63**	**0.66**	1.00									
bbp η	**-0.47**	0.16	**0.38**	**0.29**	1.00								
acdm*443	**-0.57**	**0.31**	0.19	**0.44**	0.24	1.00							
MG09 CI	**-0.32**	**0.28**	0.04	0.13	0.14	**0.81**	1.00						
Sacdm	-0.15	-0.04	0.11	0.01	**0.28**	-0.12	-0.12	1.00					
RPD OC4v6	**-0.51**	**0.72**	**0.45**	**0.44**	-0.08	**0.47**	**0.57**	**-0.33**	1.00				
micro%	**0.74**	**-0.59**	**-0.80**	**-0.64**	-0.36	**-0.28**	-0.07	-0.03	**-0.37**	1.00			
nano%	-0.17	0.07	0.24	0.12	0.28	0.10	0.06	-0.13	0.02	**-0.40**	1.00		
pico%	**-0.79**	**0.70**	**0.76**	**0.73**	0.17	**0.27**	0.04	-0.01	**0.48**	**-0.82**	-0.04	1.00	
PSD ξ 3um	**-0.52**	**0.38**	**0.34**	**0.49**	0.27	**0.32**	0.12	0.11	0.15	-0.27	-0.27	**0.40**	1.00
Zea*	**-0.69**	**0.63**	**0.66**	**0.66**	0.21	**0.41**	**0.32**	0.05	**0.60**	**-0.60**	0.01	**0.70**	**0.34**
Prasin*	**-0.76**	**0.56**	**0.66**	**0.75**	**0.41**	**0.32**	0.08	0.03	**0.41**	**-0.68**	0.16	**0.68**	**0.31**
HF'19*	-0.19	0.11	**0.35**	0.17	**0.28**	0.04	-0.01	-0.08	0.01	**-0.51**	**0.95**	0.08	-0.24
Chlc1,2	**0.77**	**-0.68**	**-0.66**	**-0.66**	-0.25	**-0.36**	-0.14	-0.08	**-0.44**	**0.70**	0.13	**-0.89**	**-0.42**
Perid	-0.14	-0.23	-0.10	**0.26**	0.33	**0.27**	0.14	0.10	-0.25	0.00	**0.38**	-0.16	0.05
HB*	**-0.89**	**0.70**	**0.75**	**0.84**	**0.33**	**0.44**	0.22	0.12	**0.51**	**-0.73**	0.13	**0.75**	**0.59**
Proch%	**-0.44**	0.20	**0.38**	**0.44**	**0.25**	**0.37**	0.10	0.25	0.05	**-0.30**	-0.28	**0.34**	**0.50**
Syn%	0.07	-0.07	-0.17	-0.08	0.04	0.14	0.27	-0.09	0.07	-0.02	**0.30**	-0.09	-0.01
Picoeuk%	**0.54**	**-0.38**	**-0.44**	**-0.55**	-0.24	**-0.48**	**-0.33**	-0.06	**-0.37**	**0.47**	0.15	**-0.50**	**-0.60**

For an overall analysis of the bio-optical relations within the BGCPs, Figure 6.46 shows a Principal Components Analysis (PCA) with the a_{phy}*443, b_{bp}*555, η and CDOM index as active variables and the CB06 SI, PFT fractions, Chl*a* and ξ PSD3 μm as (non-active) supplementary variables. The stations are overlaid on the vectorial PCA graph, identified by their BGCP, to show their distribution in respect to the main variables determining their optical characteristics.

The a_{phy}*443 and b_{bp}*555 explained most of the bio-optical variability, with 0.87 and 0.84 coefficients for Factor 1, which explained 47% of the variance. These specific IOPs were strongly related to the trophic levels (Chl*a*) and PFT distribution, delineating the main transition of the oligotrophic waters, with higher proportions of microbes and pico cells (especially Prochlorophytes), to the mesotrophic waters, with greater contributions of nano groups (mainly Haptophytes), and the eutrophic waters, with greater contributions of larger sized diatoms (with lower a_{phy}* and b_{bp}*). The CDOM index and η explained a lower percentage of the bio-optical variability, with stronger coefficients for Factor 2 (-0.64 and -0.63, respectively), which explained 26% of the variance. These specific IOPs, however, were also important to explain some significant second order optical variabilities associated with the varying composition and size distribution of the particle assemblage and CDM proportions, across the BGCPs.

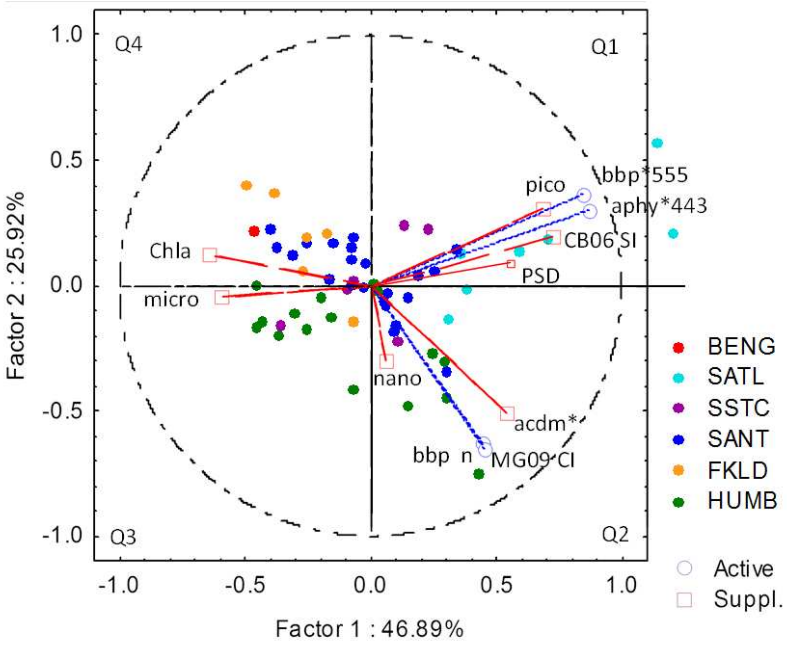

Figure 6.46 – Principal Components Analysis (PCA) with the a_{phy}*443, b_{bp}*555, η and CDOM index as active variables and the CB06 SI, PFT fractions, Chl*a* and ξ PSD3 µm as (non-active) supplementary variables, and the stations identified by their BGCP.

Together these 4 optical variables i.e, a_{phy}*, b_{bp}*, CDOM index and η, could explain the dominant modes of first and second order variability, identifying the "groups" of stations distributed in the quadrants of the PCA graph (Figure 6.46). Quadrant 1 (Q1) encompassed the stations with highest a_{phy}* and b_{bp}* values, which were characteristic of the most oligotrophic stations of the SATL, SSTC and SANT, with greater proportions of small microbes and pico cells. The η slope and CDOM index were more variable for this group, as some stations had higher η and lower CDOM, e.g., at the SATL core (St 06 and 07), while other stations had lower η likely due to the presence of high-index particles (e.g., coccoliths), and higher CDOM due to influences of adjacent productive waters, e.g., at the SATL borders. Quadrant 2 (Q2) encompassed the stations with the highest η and CDOM index, characteristic of the oligo-mesotrophic waters dominated by nano groups, with greater contributions of low-index submicron particles and some "external" CDOM sources i.e., past blooms, upwelling cells and current advection of adjacent productive waters. Such stations were characteristic of the low-Chl*a* and high-CDOM waters of the SANT and HUMB provinces.

Quadrant 3 (Q3) encompassed the stations with the lowest a_{phy}*443 and b_{bp}*555 values, characteristic of the meso-eutrophic waters with greater contributions of larger diatoms, at the HUMB province. These stations also had some higher CDOM index values, likely related to the contribution of some continental sources and coastal upwelling. Quadrant 4 (Q4) encompassed the stations with the lowest η and CDOM index values, characteristic of the meso-eutrophic waters of the SANT and FKLD, with more optically shallow stratifications, promoting more intensive CDOM photodegradation losses (the high-Chl*a* low-CDOM "cells" of the SANT and FKLD). The lowest η values at these stations were likely determined by the strong biogenic absorption of these productive waters, and maybe also some greater proportions of larger particles (e.g., detritus and coccoliths). The slightly higher a_{phy}*443, which also differentiated these stations from the productive HUMB stations, were likely associated with greater contributions of the smaller pico and nano-sized diatoms, especially for the FKLD stations.

As the specific IOPs explained well the first and second order bio-optical variability across the study region, showing strong relations with the PFT distribution and particle

assemblage, as well as and regional/local biogeochemical processes regulating the CDM distribution, these variables were used for a K-means Cluster Analysis to separate the stations into Regional Specific Optical Water Types (R-SOWT). For purposes of OCR applications all the specific IOPs used for the classification scheme should be obtainable by OCR models. Hence, the CB06 SI was used in place of the a_{phy}*443. The other specific IOPs and indices i.e., MG09 CDOM index, η and b_{bp}*555, may all be derived by empirical and SA OCR models. Two classifications were obtained and compared in respect to their relevance to identify optical water types: with 4 and 5 classes (4-Class and 5-Class).

The 4-Class scheme separated the stations in the following groups (Figure 6.47): Cluster 1 (C1): stations with the highest CB06 SI, b_{bp}*555 and η values, and lower MG09 CDOM index, grouping all the stations of the SATL province, characteristic of the mostly stratified oligotrophic waters dominated by Prochlorophytes; Cluster 2 (C2): stations with higher η and CDOM index, characteristic of the oligo-mesotrophic waters of the SSTC, SANT and HUMB, with mixed pico and nano assemblages, higher contributions of low-index small particles and with "external" CDOM sources and less photodegradation losses, characteristic of well-mixed waters; c) Cluster 3 (C3): with lower CDOM index and η, characteristic of the mesotrophic waters of the SANT with mixed assemblages of nano and micro groups, characteristic of the more productive stratified cells; and d) Cluster 4 (C4): with the lowest values for all indices i.e., CB06 SI, b_{bp}*555, η and CDOM index, characteristic of the most productive stations of the BENG, FKLD and HUMB, with greater proportions of diatoms and more near-surface stable waters, with higher CDOM photodegradation.

The 5-Class scheme basically separated an additional class for the meso-eutrophic stations differentiating the stations with the lowest CB06 SI and some higher CDOM index, correspondent to the HUMB stations, with greater contributions of larger diatoms and coastal CDOM sources (C4) (correspondent to Q3 in Figure 6.46). The Cluster 5 comprehended the stations with higher CB06 SI and lower CDOM index of the BENG and FKLD provinces, with greater proportions of pico and nano-sized diatoms and shallower stratifications (correspondent to Q4 in Figure 6.46) (Figure 6.48).

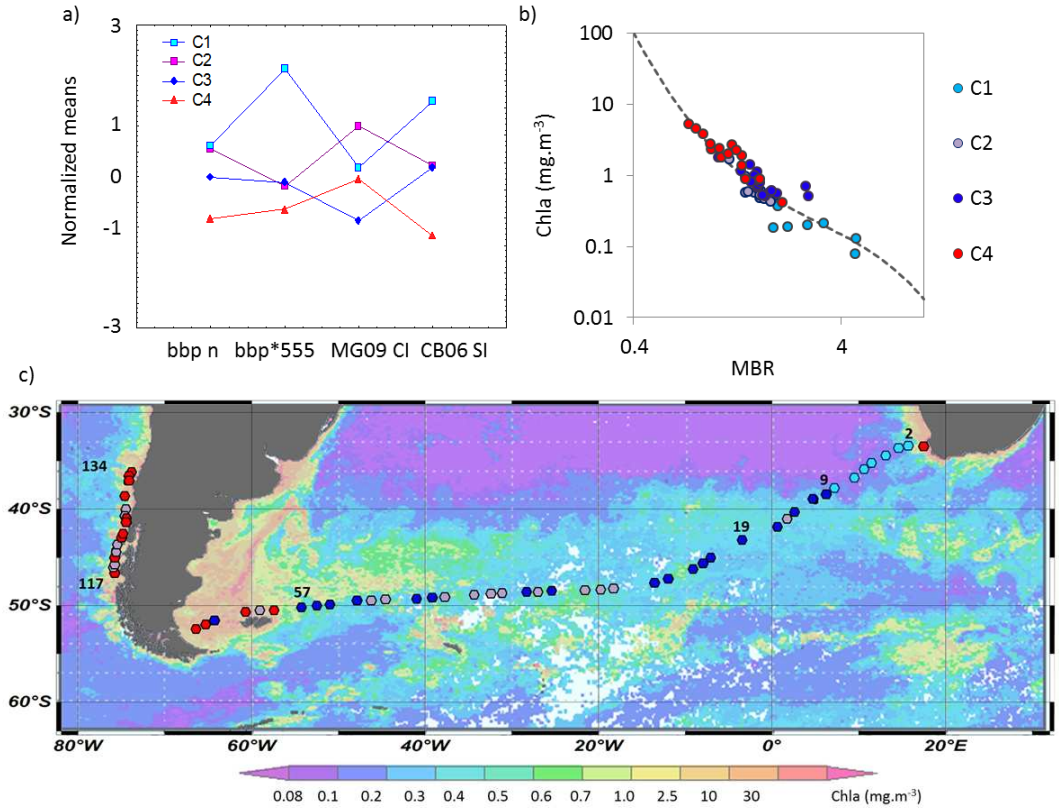

Figure 6.47 – Normalized means of the specific IOPs i.e., η, b_{bp}*555, CB06 size index and MG09 CDOM index, for each R-SOWT 4-Class (a); MBR vs. Chl*a* graph for each class (b) and surface map of the classes overlaid on the OC3M averaged over the sampling period (02/18-03/14/11).

Despite that the R-SOWT classes had a trend of increasing the mean Chl*a* levels, from classes 1-4(5), determined by the dominant variability of the b_{bp}* and CB06 SI, which covaried with the trophic levels, the classes had overlapping Chl*a* ranges, denoted by the high Chl*a* SDs of both the 4-Class and 5-Class schemes (Tables 6.9). This indicates the effective separation of both the first and second order bio-optical variability for both schemes. The classes also separated well the variability related to the OC4v6 deviations, especially for the 5-Class scheme (Figure 6.48 and Table 6.9): C1: with the highest overestimations (47% RPD), especially due to the higher a_{phy}* (0.087±0.022 $m^2.mg.m^{-3}$) and b_{bp}* (0.0106±0.004 $m^2.mg.m^{-3}$); C2: with some overestimation (12% RPD) due to the combined effects of higher CDOM index (1.48±0.36), a_{phy}* and b_{bp}*; C3: with underestimations (-21% RPD) due to the combined effects of lower CDOM index

(0.69±0.16), a_{phy}* and b_{bp}*; C4: with underestimations (-22% RPD) due to the lower a_{phy}*443 (0.046±0.011 $m^2.mg.m^{-3}$) and b_{bp}* and C5: with slight overestimations (1.3% RPD) due to the higher a_{phy}*443 (0.060±0.007 $m^2.mg.m^{-3}$), but also compensated by lower CDOM index.

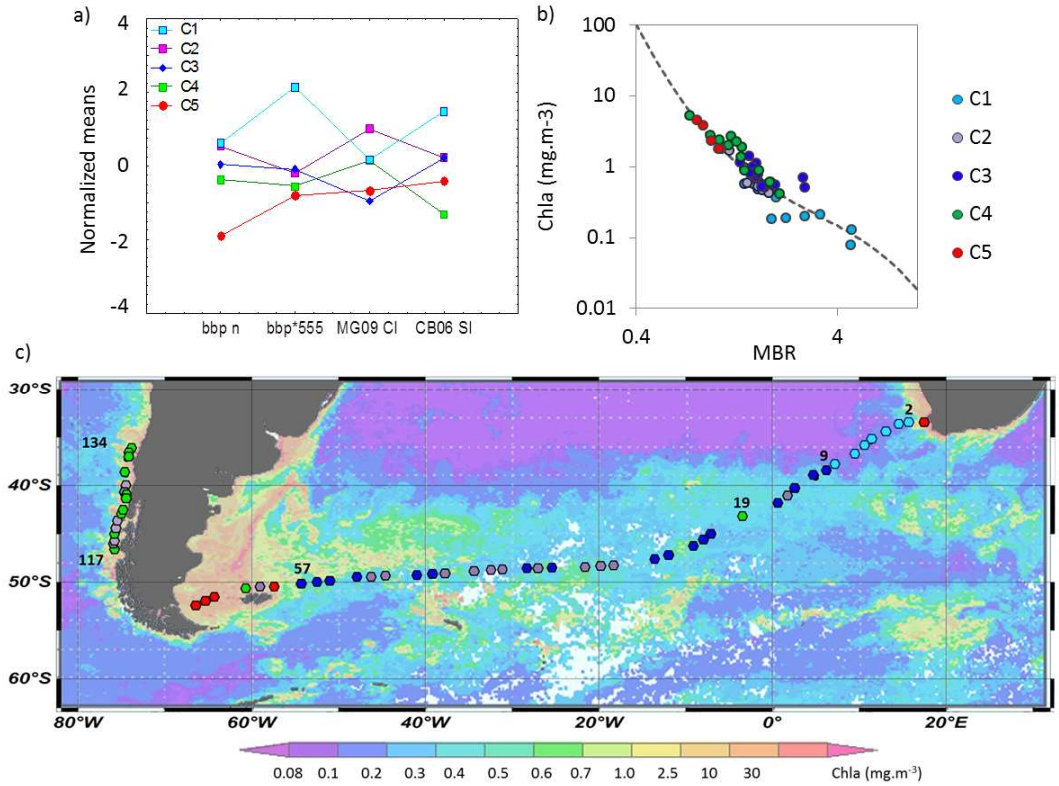

Figure 6.48 – Normalized means of the specific IOPs i.e., η, b_{bp}*555, CB06 size index and MG09 CDOM index, for each R-SOWT 5-Class (a); MBR vs. Chl*a* graph for each class (b) and surface map of the classes overlaid on the OC3M averaged over the sampling period (02/18-03/14/11).

The 4-Class scheme was effective to synthetized the general bio-optical variability across the study region, grouping the optical water types with the major variations. The 5-Class scheme on the other hand, made also an important separation for the meso-eutrophic waters, identifying different PFT sized distributions and CDOM sources and losses. Hence, it separate relevant biogeochemical information and also resolved better the impacts of the variability on the OC4v6.

Table 6.9 - Mean and standard deviation of the specific IOPs and indices and the relative percent difference (RPD) for the OC4v6 model, for each class of the 5-Class cluster analysis.

	Chl*a*	a_{phy}*443	CB06 SI	MG09 CI	b_{bp}*555	η	RPD
C1	0.19±0.09	0.087±0.022	0.90±0.14	1.18±0.43	0.0106±0.004	1.82±0.23	47.1
C2	0.69±0.40	0.066±0.008	0.70±0.05	1.48±0.36	0.0033±0.001	1.79±0.23	12.0
C3	0.79±0.26	0.059±0.014	0.70±0.07	0.69±0.16	0.0035±0.001	1.69±0.13	-20.6
C4	1.93±1.31	0.046±0.011	0.47±0.11	1.16±0.21	0.0020±0.001	1.58±0.12	-21.8
C5	2.84±1.28	0.060±0.007	0.61±0.06	0.82±0.13	0.0013±0.000	1.22±0.19	1.3

Cluster 1 (C1) N= 7; Cluster 2 (C2) N= 18; Cluster 3 (C3) N= 17; Cluster 4 (C4) N= 12; Cluster 5 (C5) N= 5. Chl*a* (mg.m^{-3}), a_{phy}*443 and b_{bp}*555 (m^2.mgChl*a*$^{-1}$), RPD (%).

The Optical Water Type (OWT) approach of Moore et al., (2009, 2012) was based on a clustering analysis of R_{rs}(0-) spectra, using the 6 spectral bands correspondent to the MODIS sensor. Applying the OWT for the present study the stations were grouped into 4 OWT, correspondent to the Types 2, 3, 4 and 5, which were somewhat close to the 4-Class R-SOWT classes defined in the present study. For a comparison solely regarding the different approaches of using either R_{rs} spectra or the specific IOPs to classify the optical water types (not considering the global range of the OWT and different clustering techniques), a K-means regional R_{rs} grouping was applied for the stations of the present work (referred as OWT*). Figure 6.49a shows the mean R_{rs} spectra of each OWT* class, which were very similar to the original OWT classes (Figure 3.3).

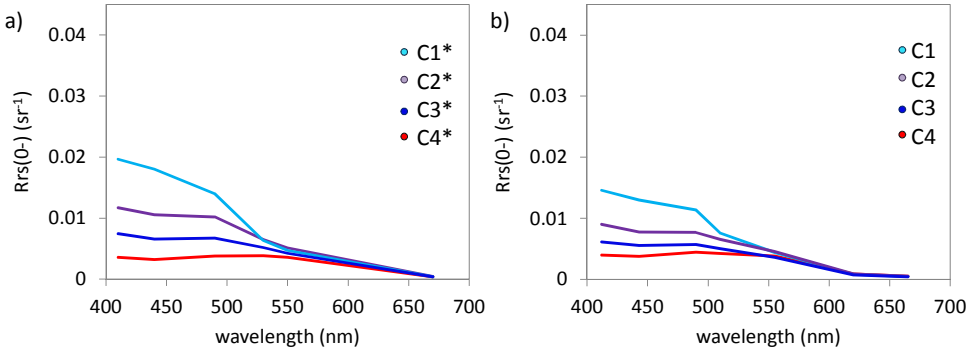

Figure 6.49 – Mean R_{rs} of the OWT* classes (a) and of the R-SOWT 4-Class approach (b).

Comparing the OWT* and R-SOWT classes, there were some differences between the mean R_{rs} of the correspondent classes of the R-SOWT 4-Class approach, in both amplitude and spectral shape (Figure 6.49). The OWT* approach separated the main spectral variations associated with the first order variability of the IOPs, and even though the classes had some overlapping Chl*a* levels (MOORE et al., 2009), the variability related to the specific IOPs were not so well distinguished, as for the R-SOWT approach. Figure 6.50a shows the MBR versus Chl*a* for the OWT*, and one may note how the classes were more distributed according to the Chl*a* gradient with both over and underestimations for all classes. Applying a 5-Class scheme for the R_{rs} OWT*, the classes followed the same trend of overlapping Chl*a* levels, however still strongly determined by the Chl*a* gradient (Figure 6.50b). Table 6.10 shows the mean and SD of the Chl*a*, specific IOPs and OC4v6 RPD for the OWT* 5-Class approach. The values are much different than the R-SOWT 5-Class (Table 6.9), and it is evident how the OWT* classes were more distributed according to the first order IOP gradient, and how the OC4v6 deviations were minimized for all classes as there were both over and underestimations (maximum of 17% for C1* and minimum of -11% for C5*).

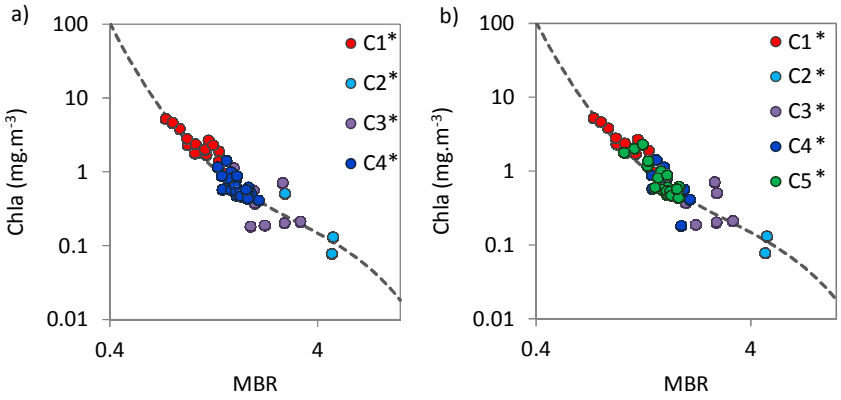

Figure 6.50 – MBR vs. Chl*a* for the OWT* 4-Class (a) 5-Class (b) approaches.

Table 6.10 - Mean and standard deviation of the specific IOPs and indices and the relative percent difference (RPD) for the OC4v6 model, for each class of the 5-Class OWT* cluster analysis.

	Chl*a*	a_{phy}*443	CB06 SI	MG09 CI	b_{bp}*555	η	RPD
C1*	0.10±0.04	0.094±0.008	0.84±0.02	0.70±0.27	0.0141±0.007	1.96±0.31	17.2
C2*	0.38±0.20	0.066±0.018	0.81±0.08	1.06±0.34	0.0072±0.003	1.75±0.21	4.4
C3*	0.70±0.28	0.064±0.019	0.71±0.14	0.95±0.40	0.0043±0.002	1.69±0.17	1.1
C4*	0.86±0.54	0.062±0.012	0.65±0.12	1.28±0.47	0.0028±0.001	1.69±0.17	0.9
C5*	2.64±1.26	0.051±0.012	0.54±0.13	1.09±0.29	0.0011±0.000	1.52±0.35	-11.9

Cluster 1 (C1*) N= 2; Cluster 2 (C2*) N= 7; Cluster 3 (C3*) N= 17; Cluster 4 (C4*) N= 21; Cluster 5 (C5*) N= 12. Chl*a* ($mg.m^{-3}$), a_{phy}*443 and b_{bp}*555 (m^2.mgChl*a*), RPD (%).

The classification of optical water types based solely on R_{rs} spectra has the advantage of using "direct" OCR from either *in situ* or satellite measurements, with likely lower uncertainty levels and the availability of extensive data bases globally distributed. Hence, this allows more comparisons across different BGCP and applications of robust classification schemes for globally distributed classes such as the OWT proposed by Moore et al. (2009; 2012). Nonetheless, although the OWT classes had some overlaping Chl*a* ranges, likely encompassing some second order variations, the 4 classes of biogenic dominated waters (MOORE et al., 2012) had equally distributed spectral R_{rs} intervals mainly determined by the first order IOP variations, linked to the Chl*a* gradient. Hence, the second order optical variations which are the main sources of the OC4v6 deviations, and may be associated with the PFT distribution, CDM variability and particle assemblage, were not so well identified in the OWT scheme. The R-SOWT scheme on the other hand, was able to separate the classes grouping both first and second order optical variabilities, which were related to specific characteristics linked to the PFT distribution, the composition and size distribution of the bulk particle assemblage and processes governing the CDOM variability. The R-SOWT scheme was also more efficient to identify the impacts of the bio-optical variability on the OC4v6 MBR model, grouping better typical water types with specific properties that either covaried positively enhancing the deviations, or negatively compensating some spectral effects.

6.3.4. Class based approach: applications for OCR products

In attempt on to verify the application of the class-based approach to enhance OCR semi-analytical models, some tests were applied for the QAA and GSM models, comparing their performance with the global fits and the regional class-specific parameterizations of the a_{phy}*, η and S_{cdm}, using the R-SOWT and OWT* 5-Class approaches.

6.3.4.1. QAA (LEE et al., 2002)

The Quasi-Analytical Algorithm (QAA) (LEE et al., 2002) (Equations 3.16-20) is a SA model which has the advantage to estimate the η and S_{cdm} using empirical fits with the $r_{rs}443/555$ ratio and *in situ* measurements obtained from the NOMADv2. Nonetheless, they are also constrained by the range of the input data sets, which may not encompass all of the optical variabilities within different BGCPs. The most critical case is for the η which was fitted with only 80 points to represent the global distribution.

Table 6.11 shows the η and S_{cdm} values determined by the QAAv5 and the mean measured values, for each class of the R-SOWT and OWT* approaches. The QAAv5 underestimated the η values for all classes, especially for the meso-eutrophic C4 and C5, for which the measured η were 1.583 and 1.223, and the derived QAAv5 were 1.078 and 0.707, respectively. The η values had a high range of variability for the study region, varying from 0.973 to 2.182. The QAAv5 estimations followed the same general trend of decreasing slopes for higher Chl*a* waters, however showing some high dispersion with 0.36 r^2, and a tendency of underestimation (-21% RPD). The differences between the modeled and measured values were likely associated with the uncertainties intrinsic to the empirical model and of the data set used to adjust the fit (of both R_{rs} and η). Uncertainties regarding the present data and possible natural η variations with a trend of higher values for the study region and sampled period, are also some possible sources of deviations between the modeled and measured values.

The S_{cdm} estimated by the QAAv5 model had more approximate values to the measured, as the range of variability of this parameter was much lower varying from 0.010-0.020 sr^{-1}. Nonetheless, there were still some differences with a trend of overestimation of the

QAAv5 S_{cdm} with 15% RPD. The QAAv5 overestimated the S_{cdm} values for all classes, with exception for the OWT* C1* (composed of the two most oligotrophic stations i.e., St 06 and 07). There was no covariation between the modeled and measured values with a r^2 of 0.10. Hence, even though this parameter had apparently lower differences between the modeled and measured, the dispersion was high.

Besides of the relatively high regional optical variability of the η and S_{cdm} shown for the study region, which likely caused significant deviations in the QAAv5 estimates, the empirical fits are solely based on one band ratio, which is likely subjected to spectral variations that result from combined effects of second order variations of the different IOPs, as discussed for the MBR model. Hence, even though the QAAv5 has a more flexible scheme to account for some of the spatio-temporal variations in the specific IOPs, the model performance is still limited to the "global" relations used to parameterize the empirical fits, and hence subjected to second order variations.

Table 6.11 – Mean values for the $b_{bp}(\eta)$ and CDM (S_{cdm}, nm^{-1}) spectral slopes determined by the QAAv5 model and measured for each R-SOWT and OWT* class.

	R-SOWT					OWT*			
	QAA η	QAA S_{cdm}	η	S_{cdm}		QAA η	QAA S_{cdm}	η	S_{cdm}
C1	1.750	0.016	1.818	0.015	C1*	1.958	0.015	1.961	0.018
C2	1.361	0.016	1.789	0.014	C2*	1.690	0.016	1.751	0.016
C3	1.447	0.016	1.685	0.015	C3*	1.416	0.016	1.687	0.014
C4	1.078	0.016	1.583	0.015	C4*	1.324	0.016	1.690	0.014
C5	0.707	0.017	1.223	0.013	C5*	0.850	0.016	1.524	0.014

Applying the class-specific parameterizations using the mean measured values of η and S_{cdm} for the R-SOWT and OWT* classes, both schemes enhanced the overall QAA retrievals, with similar performances. The $a_{phy}443$ retrievals were very close to the measured values for all three approaches: the global QAAv5 (r^2, 0.98 and 17.1% RPD*) and the regional R-SOWT (r^2, 0.98 and 16.8% RPD*) and OWT* parameterizations (r^2, 0.98 and 17.9% RPD*). The QAAv5 actually had a very good performance for the $a_{phy}443$ using the global fit, approximate to the regional parameterizations. The $a_{cdm}443$ on the other hand, had much better retrievals using the class-based approaches, with

0.60 r^2 and 23.4% RPD* for the R-SOWT compared to 0.39 r^2 and 30.2% RPD* for the QAAv5. The $b_{bp}443$ was also somewhat enhanced for the class-based approaches with 0.86 r^2 and 10.2% RPD* for the R-SOWT compared to 0.78 r^2 and 10.9% RPD* for the QAAv5 (Figure 6.51 and Table 6.12).

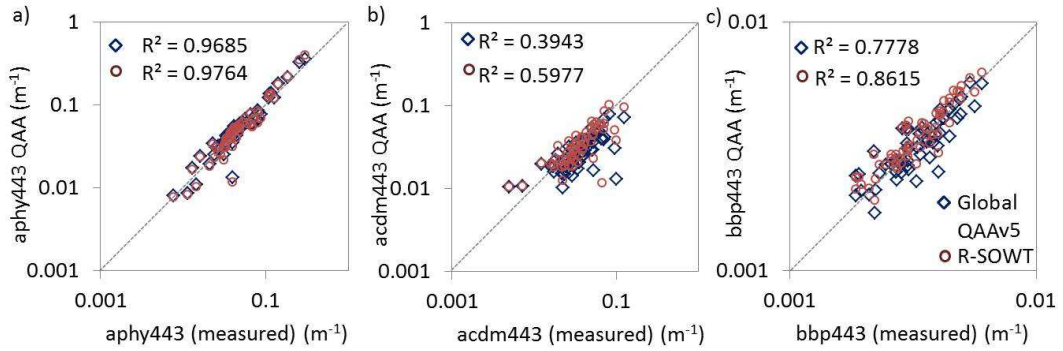

Figure 6.51 – Measured versus modeled $a_{phy}443$ (a), $a_{cdm}443$ (b) and $b_{bp}443$ (c) for the QAA model using the global fit (QAAv6) and the R-SOWT regional class-based parameterizations.

Table 6.12 - Absolute percent difference (RPD*, %) between measured and modeled IOPs i.e., $a_{phy}443$, $a_{cdm}443$ and $b_{bp}443$, for the QAA model, using the QAAv5 global fit and the regional class specific parameterizations i.e., R-SOWT and OWT* approaches. The values are for each BGCP and the entire study region (All).

	$a_{phy}443$			$a_{cdm}443$			$b_{bp}443$		
	QAAv5	RSOWT	OWT*	QAAv5	RSOWT	OWT*	QAAv5	RSOWT	OWT*
BENG	17.6	19.2	23.6	68.1	46.7	41.6	18.6	6.9	0.4
SATL	29.7	28.2	29.2	39.3	36.3	29.7	24.6	26.3	25.9
SSTC	20.8	22.1	21.3	15.9	19.8	15.6	4.4	6.9	7.7
SANT	17.0	14.3	14.0	30.4	20.5	20.6	5.0	7.2	6.7
FKLD	20.3	23.3	26.0	63.5	40.8	36.9	9.4	11.4	14.7
HUMB	9.1	10.7	14.0	16.5	15.3	18.9	15.9	8.6	7.9
All	**17.1**	**16.8**	**17.9**	**30.2**	**23.4**	**22.7**	**10.9**	**10.2**	**10.1**

Regarding the performances of the QAA for each BGCP, the R-SOWT approach showed no difference for the $a_{phy}443$ retrievals, but had lower underestimations for the $a_{cdm}443$ (-4.1%, compared to 19.5% for the QAAv5) and $b_{bp}443$ (5.5% compared to -

2.2% for QAAv5), especially for the most eutrophic provinces of the BENG, FKLD and HUMB (Table 6.12). Hence, the most significant enhancement of the QAA using the regional class-based approaches was for the $a_{cdm}443$ and in minor degree for the $b_{bp}443$, especially for higher biogenic absorbing waters. The $a_{phy}443$ QAA retrievals are already reasonably good using the global fit, for all the BGCPs analyzed in present work, with a high dynamic range of Chl*a* levels.

6.3.4.2. GSM01 (MARITORENA et al., 2002)

The Garver-Siegel-Maritorena version 1 (GSM01) model uses parameterized global means for the specific IOPs to simultaneously derive the Chl*a* and IOPs in the inversion scheme (Equation 3.15). The specific IOPs (eigenvectors) were obtained from *in situ* and simulated data sets using an optimization technique for the best fit (MARITORENA et al. 2002). The global parameterizations used in the GSM01 are: 0.05583 m^2.mgChla^{-1} for a_{phy}*443, 0.0206 (nm^{-1}) for S_{cdm} and 1.0337 for η.

The average a_{phy}*443 values for each of the R-SOWT classes ranged from 0.087 m^2.mgChla^{-1} (C1) to 0.046 m^2.mgChla^{-1} (C4), and the average for the entire study region was 0.0619 m^2.mgChla^{-1}, which is slightly higher than the GSM01 global fit (Table 6.9). This may have been related to the generally smaller phytoplankton groups for the summer period, especially of the Southern Atlantic, as discussed in the previous sections. The η values were also higher for all the R-SOWT classes with averages ranging from 1.233 (C5) to 1.818 (C1) (Table 6.11). The η values of the GSM01 fit were obtained from simulated IOP data, as there are very few *in situ* data available, and thus higher biases are actually expected for this parameter (MARITORENA et al., 2002). The S_{cdm} was the only parameter that was lower than the average values of study region and R-SOWT classes (ranging from 0.014-0.018 nm^{-1}) (Table 6.11).

As the IOPs are simultaneously derived using the IOP eigenvectors and spectral R_{rs} (412, 443, 490, 510, 555 and 670 nm), the uncertainties in one or another parameter may propagate to all the retrieved IOPs. Hence, the adequate parameterization of the specific IOPs is a critical step for the good performance of the GSM inversion scheme (IOCCG, 2006).

As for the QAA analysis, the R-SOWT and OWT* approaches had very similar performances with practically the same r^2 and RPDs for the modeled and measured parameters (Table 6.12 and 6.13). The regional class-based parameterizations showed some enhancement in the retrievals of the GSM for all provinces, especially for the $b_{bp}443$ (Figure 6.52 and Table 6.13). For the Chl*a* retrievals the GSM01 global fit had a reasonably good performance (r^2, 86 and RPD* 27.8%). The regional class-based approach was somewhat better with an r^2 of 0.81 and RPD* of 23.7%. This was closer to the overall performance of the empirical OC4v6 for the study region (22% RPD*). The R-SOWT showed less underestimations of the Chl*a* with -6.6% RPD compared to -7.4% for the global fit. The lower underestimations were especially for the SSTC province with -13% RPD for the R-SOWT compared to -41% for the GSM01. For the FKLD there were also much lower overestimations with the R-SOWT, with 8% RPD compared to 48% for the global fit. These higher differences for the SSTC and FKLD were because of the higher variability in the a_{phy}* for these provinces, with lower values for the SSTC (especially St 11 and 17) and higher for the FKLD. Hence, even though the regional class-based approach did not show a global major enhancement in the Chl*a* retrievals of the GSM, for optical classes with higher variability in the a_{phy}* the enhancement was much higher. In such cases, the R-SOWT approach was also more accurate than the OWT*, as it mapped classes which separated by these second order variabilities in the a_{phy}*443, e.g., separating the higher a_{phy}*443 of the FKLD stations (Table 6.13).

For the $a_{cdm}443$ the regional class-based approach was also somewhat better than the global GSM01, with a 0.82 r^2 compared to 0.72 for the global fit. The overall RPD* was slightly lower using the R-SOWT approach, with 25.7% compared to 26.4% for the global fit. There were some lower overestimations, especially for the most eutrophic provinces, and more underestimations (-22% RPD compared to -16% for the GSM01). The $b_{bp}443$ on the other hand, was the parameter which was most affected by the regional class-based parameterizations with values much closer to the measured. The R-SOWT approach had a 0.85 r^2 and 9.5% RPD* for the retrieved $b_{bp}443$ values, compared to 0.65 r^2 and 34.7% RPD* for the GSM01 (Figure 6.52 and Table 6.13).

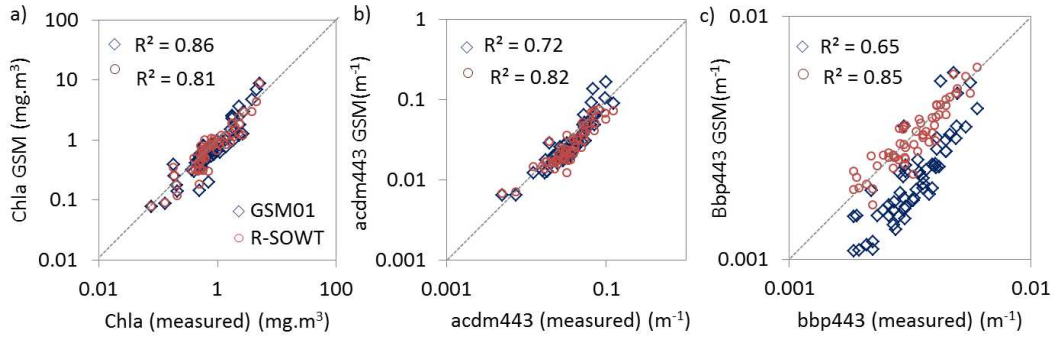

Figure 6.52 – Measured versus modeled $a_{phy}443$ (a), $a_{cdm}443$ (b) and $b_{bp}443$ (c) for the GSM model using the global fit (GSM01) and the R-SOWT regional class-based parameterizations.

Table 6.13 - Absolute percent differences (RPD*, %) between the measured and modeled parameters i.e., Chl*a*, $a_{cdm}443$ and $b_{bp}443$, for the GSM model, using the GSM01 global fit and the regional class-specific parameterizations of the R-SOWT and OWT* approaches.

	Chl*a*			$a_{cdm}443$			$b_{bp}443$		
	GSM01	RSOWT	OWT*	GSM01	RSOWT	OWT*	GSM01	RSOWT	OWT*
BENG	23.7	22.2	3.2	7.7	29.5	24.2	5.2	14.4	2.1
SATL	35.2	32.6	47.8	26.2	15.2	23.0	23.1	16.5	16.8
SSTC	40.7	40.2	26.4	27.0	21.4	23.5	39.2	3.6	4.1
SANT	21.3	15.2	18.6	25.5	33.8	33.0	41.4	7.0	6.4
FKLD	48.3	19.7	23.7	39.6	22.3	20.2	11.6	12.4	13.6
HUMB	21.7	27.3	32.6	23.7	21.4	17.2	38.9	10.8	9.6
All	**27.8**	**23.7**	**26.9**	**26.4**	**25.7**	**25.1**	**34.7**	**9.5**	**8.9**

In resume the $a_{phy}443$ of the QAA and Chl*a* of the GSM were not so affected by the class-based regional parameterizations in the overall performance, as they had reasonably good matches using the global fits. However, looking into a case by case analysis, the GSM for instance was much better using the regional class parameterizations for the provinces with highest a_{phy}* variability such as the SSTC and FKLD. As the QAA retrieves the $a_{phy}443$ using a step-by-step equation system, with R_{rs} band ratios, it does not require a parameterized eigenvector (a_{phy}*443), which may explain the good performance of this model for the $a_{phy}443$ across all of the BGCPs.

The $a_{cdm}443$ was more problematic for the QAAv5, with higher dispersion and underestimations. In this case the regional class-specific parameterizations of the S_{cdm} was more important for the better performance of the model. Even using more adjusted values with the empirical model, the S_{cdm} values were still much different from the measured values for the optical classes of the study region. The GSM on the other hand, had a reasonably good match for the $a_{cdm}443$ even using the global fit of S_{cdm}, which was somewhat higher than the average values for the R-SOWT classes.

The most problematic parameter for the GSM01 was the $b_{bp}443$, which had high dispersion and underestimations. For this case, the R-SOWT approach significantly enhanced the $b_{bp}443$ retrievals for the BGCPs. The measured η values were higher than the global fit of the simulated IOP data set used in the GSM01, which could be due to a trend of higher slopes for the study region, with greater contributions of smaller particles, or biases in the simulated data. Further *in situ* b_{bp} measurements across different BGCPs may provide more insights regarding global and regional variabilities of this parameter, which remains poorly known.

The regional class-based approach was thus efficient to enhance the retrieval of OCR products using class-specific parameterizations for SA models, especially for BGCPs with more complex optical characteristics. Both the R-OWT and OWT* approaches showed overall similar performances, however the R-OWT was somewhat better for these particular cases of higher optical variabilities, such as for the FKLD stations which had higher a_{phy}*443, associated with the dominance of pico and nano-sized diatoms in highly productive waters.

6.4. Final Considerations

The present Chapter presents a comprehensive analysis of the bio-optical variability across the Southern Atlantic and Southeast Pacific, for the end of the austral summer of 2011. The main goals were to identify the sources of variability associated with the trophic gradient, PFT distribution, bulk particle assemblage and CDM variability, as well as to verify the impacts on ocean colour models. A class-based approach was proposed to define Regional Specific Optical Water Types (R-SOWT) gathering

relevant biogeochemical information and applied for the enhancement of OCR products for the study region.

The sampled transect of the MV112 encompassed 6 biogeochemical provinces with highly differing optical waters and biogeochemical roles, relevant for regional and global carbon cycles, i.e., the BENG, SATL, SSTC, SANT, FKLD and HUMB. These provinces comprehend extensive unsampled regions of global *in situ* data bases, which may compromise the performance of OCR products and limit the comprehension of the actual variability and dynamic of the biogeochemical processes, which are mainly studied using satellite OCR data for these remote regions of the Southern globe. Hence, the present work contributed with bio-optical information across these provinces for a better understanding of the bio-optical variability, its relations with biogeochemical parameters, and means to enhance OCR products for the study region.

The IOPs i.e., $a_{phy}443$, $a_{cdm}443$ and $b_{bp}555$, had a distribution generally determined by the trophic gradient, with a first order variability strongly related to the Chl*a*. Looking into each BGCP however, some variabilities related to more specific optical properties were also observed. The analysis of the distribution of the specific IOPs enabled the identification of such minor variabilities, independent of the trophic levels, namely second order variations. The a_{phy}*443 was strongly associated with the phytoplankton size fractions, which generally covaried with the Chl*a* and HPLC fractions, with higher values for the oligotrophic waters of the SATL dominated by *Prochlorococcus* cells, and lower values for higher Chl*a* waters dominated by micro diatom groups. Some minor but important second order variations were, however, also present and related to different shifts in the phytoplankton size structure, as well as some local photoacclimation processes. The productive waters of the FKLD had the most evident example of such variability with high Chl*a* waters dominated by pico and nano-sized diatoms with high a_{phy}*443. The HPLC pigment model could not map this variability as it defines the PFT sized groups essentially by the biomarker pigment ratios. Hence, the high Fuco* of the FKLD stations mapped the dominance of micro diatoms, which in reality were pico and nano-sized. This highlights the importance to use complementary analysis such as microscopy and flow cytometry, which may elucidate such variabilities in the actual size distribution of the PFTs.

Furthermore, it was shown that PFT remote sensing models that rely on statistical relations between the HPLC PFT fractions, and OCR Chl*a* retrievals, may have serious biases for more optically complex regions that depart from the global trends of micro dominance in higher Chl*a* waters, nano in intermediate and pico in low Chl*a* waters. Even though there was a general trend of such distribution for the Southern Atlantic and Southeast Pacific, there were some important regional and local variabilities, and higher proportions of nano and pico-sized diatoms were observed for different stations across the BENG, SANT and especially FKLD. This may have been a more typical condition for the study region in the end of the austral summer, as smaller groups are more competitive for nutrient limiting waters, post spring and early summer blooms (BOYD, 2002; ZIGNORE et al., 2011). The Ciotti and Bricaud (2006) size index model (CB06) was strongly associated with the a_{phy}*443 first and second order variations, and could thus map the higher indices related to smaller phytoplankton groups, independent of the Chl*a* and HPLC fractions. Hence, this index was able to map the second order variations related to the a_{phy}*443 and PFT distribution for the study region.

Regarding the variability of the CDM proportions in respect to the phytoplankton biomass, the CDOM index was more efficient to map the second order variations, as the a_{cdm}/a_{nw} ratio was strongly correlated to the Chl*a*, likely due to the covarying effects of higher proportions of phytoplankton cells and with higher intracellular Chl*a* for higher Chl*a* waters, and CDOM photodegradation losses for stratified productive waters. The sources of CDM variability across the study region were associated with different processes governing "external" sources and photodegradation losses. The lowest CDOM indices were at the most oligotrophic and deeply stratified waters of the SATL core, and the highest values were at the coastal HUMB province, with more productive waters, continental influences and upwelling sources. Cells of lower-Chl*a* with higher CDOM index well characteristic of the SANT province, and were related to well-mixed upwelling cells and past phytoplankton spring and summer blooms degradation products. These well mixed waters were likely associated with eddy-induced upwelling cells formed by local topographic effects changing the mean ACC flow in the surroundings of submerged elevations e.g., the South Georgia Islands, Islas Orcadas and Mid-Atlantic Ridge. Adjacent to these cells, near-surface stabilized water columns with new nutrient inputs, likely promoted higher phytoplankton blooms, sustained

throughout summer, and with higher CDOM photodegradation processes, characterizing the cells of higher-Chl*a* and lower-CDOM index of the SANT. The SSTC higher CDOM index values may have been influenced also by larger scale circulation patterns with advection of the productive waters of the Southwestern Shelves Systems accumulating in the STF. The BENG and FKLD stations had lower CDOM indices for the surface waters, related to the minor continental contributions at these stations and higher CDOM photodegradations processes for the more shallow optically stratified waters. In resume, the CDM first and second order sources of variability within the different BGCPs were tied to spatio-temporal dynamics of the past and current phytoplankton assemblage, the water column stability, and presence of "external" sources from upwelling cells, current advection and continental influences.

The sources of b_{bp} variability were more complex and difficult to trace. Nonetheless, the analysis of the present work revealed some insightful results regarding the possible sources of first and second order variability of the b_{bp} across the BGCPs of the study region. The fraction experiments revealed that larger particles (> 0.7 μm) may be in fact significant contributors to the bulk oceanic b_{bp}. Nonetheless, the contributions of these larger particles were highly variable and had a dispersive relation with the Chl*a*. The submicron particles likely composed of smaller detritus and microbes on the other hand, had generally lower b_{bp} contributions, but a very tight covariation with the Chl*a*. Hence, what may actually be regulating the relation of the bulk b_{bp} with the Chl*a*, is the covarying presence of submicron detritus particles and microbes. Whereas larger high-index particles i.e., coccoliths and minerals, or complex morphological structures of aggregates and diatom frustules, cause higher dispersions in the b_{bp} vs. Chl*a* relation, with more independent sources of variability and complex optical relations.

The b_{bp}*555 was used as an index to map the second order variations associated with the composition and size distribution of the particle assemblage. Nonetheless, this index was strongly correlated to the Chl*a*, likely related to both direct and indirect effects of shifts in the PSD of submicron and pico-sized particles, with greater proportions of smaller particles in lower Chl*a* waters, and higher C:Chl*a* ratios, with lower proportions of phytoplankton cells and dominance of PFTs with lower intracellular Chl*a*. The minor second order variations caused by the varying presence of larger high-index particles

and smaller low-index particles, which were likely the main causes of deviations in the b_{bp} vs. Chl*a* relation, were thus not so well identified solely with the b_{bp}*555. The b_{bp} spectral slope (η) was also sensitive to changes to the PSD of the submicron and pico-sized assemblage, nonetheless, it was also highly influenced by other sources strongly related to the Chl*a* gradient, such as the biogenic absorption diminishing the slope for higher Chl*a* waters. The combined analysis of the b_{bp}*555 and η however, enabled more comprehensive analysis of the first and second order b_{bp} variability across the study region. The positive covariations of the b_{bp}*555 and η were linked to the first order variability with greater proportions of smaller particles of lower Chl*a* waters, whereas the inverse relations of these parameters identified the main sources of second order variability, as larger high-index particles had likely higher b_{bp}*555 and lower η (and vice versa).

The impacts of the bio-optical variability on the OC4v6 for the study region were comparable with previous works carried out for different BGCPs and ocean basins. The combined effects of higher specific IOPs i.e., a_{phy}*443, b_{bp}*555 and CDOM index, promoted OC4v6 overestimations, which were highest for the SATL, whereas the lower specific IOPs caused underestimations, especially for the SSTC and HUMB provinces. Nonetheless, as the specific IOPs had some independent variations, inverse relations also caused compensation effects lowering the OC4v6 biases, such as for the FKLD stations, which had higher a_{phy}*443, but lower CDOM index, and had thus a good OC4v6 match.

The analysis presented by Szeto et al. (2011) regarding the dominant modes of second order variability for each oceanic basin, were comparable with the analysis of the present work for the Southern Atlantic and Southeast Pacific. The present analysis, however, also revealed a high spatial (and likely temporal) variability of the specific IOPs within the different BGCPs. In this manner a class-based approach defining dynamic bio-optical water types seemed more appropriate to synthetize the bio-optical variability, as well as to identify the actual impacts of the variability on the OC4v6, which varied for the different provinces.

The Regional Specific Optical Water Types (R-SOWT) proposed in the present work to defined classes according to the specific IOPs i.e., CB06 SI, MG09 CI, b_{bp}*555 and η,

was effective to group the first and second order optical variabilities of the study region into 4 and/or 5 classes, gathering relevant information of the PFT distribution, bulk particle assemblage and CDM variability. Comparing with the OWT approach of Moore et al. (2009) based on R_{rs} spectra, the R-SOWT approach separated better the classes associated with the second order variability of the specific IOPs, whereas the OWT classes were more determined by the first order IOP variations linked to the Chl*a* gradient. The R-SOWT was also more effective to identify the OC4 deviations related to the specific IOPs, and to enhance the retrieval of OCR products for the study region, applying class-specific parameterizations for the QAA and GSM models. The R-SOWT and OWT* regional classes had similar overall performances for the enhancement of the OCR retrievals, nonetheless, for some specific classes with higher second order variations, such as for the FKLD, the R-SOWT approach was more effective.

The R-SOWT class-based approach provided thus, means to synthetized and first and second order bio-optical variability, defining classes associated with the specific IOPs and covarying PFT distribution, composition and PSD of the particle assemblage and CDM variations. These classes defined well the OC4v6 deviations for the study region and were effective to enhance the retrieval of OCR products using class-specific parameterizations for SA models. This scheme however, was representative of the Southern Atlantic and Southeast Pacific for the end of the austral summer. Further works are needed to analyze the distribution of the bulk and specific IOPs during other seasons for the same region and other BGCPs. The main bio-optical relations were actually close to the relations obtained in other works for regional and global data sets. Nonetheless, the sources of second order variability may have some higher spatial-temporal variations which need further investigations.

The R-SOWT approach also used specific IOPs and bio-optical indices which are obtainable by OCR empirical and SA models, and may thus be further applied for satellite data, testing its applicability across the study region and elsewhere. The classification scheme could be applied such as described by Moore et al. (2009) for the OWT, using Fuzzy K-Means membership functions to map the water types. These are some the suggestions for future works.

7 GENERAL CONCLUSIONS AND FINAL REMARKS

The present work contributed with analysis of the ocean colour variability across the Southern Atlantic and Southeast Pacific using a comprehensive *in situ* data set collected during the MV1102 campaign, in the austral summer of 2011. The first part of the work was regarding the uncertainty analysis of the radiometric and bio-optical measurements. Such analysis were important to identify the main sources of uncertainties and means to obtain more accurate measurements for further analysis of the bio-optical variability and applications for OCR modeling.

All of the different approaches used for the R_{rs} measurements, including the above-water ASD and in-water HOCR, PRR and TriOS, showed some significant biases and environmental noises which were minimized with correction and quality control schemes applied to each data set. The above-water ASD showed some higher biases associated with the sea surface sky reflection, especially for partially cloudy conditions. For the in-water approaches the winched TriOS showed the highest biases related to platform shading effects and the bio-optical stratification, due to the greater depths used to extrapolated the L_u and E_d subsurface values. The free-falling profilers showed some minor biases, but still with some significant environmental effects, especially due the high illumination variation conditions with partially clouded skies, as well as the focus and defocusing effects of the downwelling rays due to the wavy facets. As the environmental conditions were mostly adverse with strong winds, currents and waves, and partially cloudy skies, the noises were high for all approaches and had different impacts on the amplitude and spectral variations of the measured R_{rs}. Hence, the averaging of the different approaches (INS) provided a reasonable mean to obtain more accurate *in situ* R_{rs} measurements, normalizing the main spectral noises and biases of the different approaches and environmental effects.

The averaged INS still showed some significant differences with the modeled RTE and MM01 R_{rs} (18-34%). Some uncertainties were also associated with the modeled R_{rs}, nonetheless as the differences were higher for the most adverse environmental conditions, while the stations with more uniform skies (clear or overcast) and lower winds and waves, showed very close matches, the measured R_{rs} had certainly the highest

biases. As most of the spectral biases were correlated, the band ratios significantly minimized the differences. Hence, OCR models that relay on band ratios, such as the OC4v6, had minor impacts of the INS uncertainties. The biases that remained generally caused higher OC4 underestimations, as the main sources of environmental noises caused higher R_{rs} for the shorter spectral bands, increasing the MBR i.e., sky radiance sea surface reflectance, different proportions of diffuse and direct light and illumination variations during the casts. OCR SA models that relay on spectral R_{rs}, i.e., QAA and GSM, had some higher impacts of the R_{rs} uncertainties, with underestimations of the biogenic absorption coefficients (and Chl*a*) and overestimations of the b_{bp}, caused by the same spectral effects previously mentioned. Such impacts of the INS uncertainties, however, were still lower than the intrinsic errors of the inversion schemes.

The *in situ* R_{rs} measurements showed thus, significant uncertainty levels related to instrumental and environmental biases with impacts on OCR models. Such biases may be significant sources of dispersions for the OCR models, as they rely on *in situ* data for their parameterizations and further applications on satellite data. The bio-optical measurements also showed some important uncertainties with impacts for OCR modeling. The fluorimetric and HPLC Chl*a* measurements showed the highest differences, and the spectrofluorimetric method with 100% methanol solution for the pigment extraction, was considered the most accurate approach. Particle backscattering measurements may also have some significant uncertainty levels and biases due to the nature of the indirect measurements (extrapolating βv measurements for the entire backward hemisphere). Hence, these data sets, as well as the CDOM and particulate absorption coefficients, need to be treated very carefully to obtain accurate measurements.

Some data collection, processing schemes and quality controls were proposed to enhance the measurements of both R_{rs} and the bio-optical properties, obtained by each approach and integrating the approaches, as for the INS. Such schemes may be suggested for further recommendations in standard OCR protocols. This is relevant for the improvement of R_{rs} and bio-optical *in situ* collections with the acquisition of more accurate data to be used in OCR programs, for *in situ* satellite validation, bio-optical modeling and analysis of the bio-optical variability across the oceans.

Making use of more accurate data, the analysis of the bio-optical variability in the second part of the work provided information regarding the main sources of first and second order variations of the optical properties associated with the distribution of important biogeochemical parameters across the Southern Atlantic and Southeast Pacific. The bulk IOPs were in first order associated to the Chl*a* gradient across the different biogeochemical provinces of the study region, i.e., BENG, SATL, SSTC, SANT, FKLD and HUMB. More regional and local variabilities were associated with second order variations of the specific IOPs, i.e., a_{phy}*443, b_{bp}*555, η and CDOM index. These indices presented some positive, negative and independent variations related to the different processes governing their distribution within each province. The a_{phy}*443 was predominantly governed by shifts in the dominant size fraction of the phytoplankton assemblage, with higher values for dominance of pico groups (including pico diatoms) and lower for dominance of micro groups. The first was typical of the oligotrophic waters of the SATL and the last of the eutrophic waters of the HUMB. The FKLD stations showed the highest second order variations of the a_{phy}*443 with higher values associated with the dominance of pico and nano-sized diatoms in high Chl*a* waters. The CDOM variability was governed by different spatio-temporal processes governing the sources and losses in the surface waters. The major sources were from current and past phytoplankton blooms, upwelling cells, current advection and continental influences, whereas the losses were mainly due to bio- and photodegradation processes especially in stratified waters of both oligotrophic (SATL) and eutrophic waters (BENG and FKLD). There was a general negative relation of the CDOM index with the Chl*a*, which was especially marked for the SSTC and SANT. These provinces had some distinct optical spatial distribution characterized by well mixed "cells" of lower-Chl*a* and higher-CDOM index and productive cells with likely more near surface stable waters with higher-Chl*a* and lower CDOM-index.

The b_{bp}555* and η parameters were able to identified the first and second order variations of the bulk b_{bp}. Their positive relations were related to direct and indirect effects of shifts in the submicron and pico-sized PSD, C:Chl*a* ratios and effects of the biogenic absorption, with higher values for lower Chl*a* waters with greater proportions of smaller particles, higher C:Chl*a* and lower biogenic absorption (and vice versa). The inverse relations between b_{bp}555* and η, on the other hand, indicated the sources of

second order variability of b_{bp}, with higher $b_{bp}555^*$ and lower η indicating the presence of larger high-index particles i.e., coccoliths and minerals, and lower $b_{bp}{}^*555$ and higher η indicating higher proportions of smaller low-index particles i.e., submicron detritus and microbes. This last was actually the fraction that had the tightest relation with the Chl*a*, whereas the larger high-index particles were likely the major sources of dispersions in the b_{bp} vs. Chl*a* relation.

The covarying specific IOPs caused either overestimations (especially for the SATL) or underestimations (for HUMB) with the OC4v6 model, showing similar effects as stated in other works across different regions. Some independent variations of the specific IOPs, however, also caused some compensation effects of the spectral MBR variations, showing a reasonably good performance of the OC4v6 even for more optically complex, waters as in the FKLD (with higher *a*phy* and lower CDOM).

The R-SOWT approach synthetized well the dominant modes of first and second order bio-optical variabilities across the Southern Atlantic and Southeast Pacific defining 5 classes associated with the specific IOPs and covarying PFT, compositions and PSD of the particle assemblage and CDM variability. The R-SOWT approach defined well the main OC4v6 biases for the study region, related to each class, and was efficient to enhance the retrievals of OCR products using class-specific parameterizations for SA models i.e., QAA and GSM.

Future works may concern further analysis of spatio-temporal variations of the distribution of the bulk and specific optical properties for the Southern Atlantic and Southeast Pacific, as well as for other ocean regions encompassing different BGCPs. The application of the proposed regional class-based approach on satellite imagery using OCR products of the specific IOPs and indices, to obtain maps of dynamic optical water types (such as proposed by Moore et al. (2009; 2012)), is also recommended for further works. This may serve as a new OCR product defining classes with relevant biogeochemical information and provide means for the application of class-specific parameterized SA models to obtain more accurate OCR products for the study region.

8 REFERENCES

AHN, Y. H.; BRICAUD, A.; MOREL, A. Light backscattering efficiency and related properties of some phytoplankters. **Deep-Sea Research**, v. 39, n. 11/12, p. 1835–1855, 1992.

AIKEN, J. et al. The Atlantic Meridional Transect: overview and synthesis of data. **Progress in Oceanography**, v. 45, n. 3-4, p. 257–312, abr. 2000.

AIKEN, J. et al. Validation of MERIS reflectance and chlorophyll during the BENCAL cruise October 2002: preliminary validation of new demonstration products for phytoplankton functional types and photosynthetic parameters. **International Journal of Remote Sensing**, v. 28, n. 3-4, p. 497–516, fev. 2007.

AIKEN, J. et al. Phytoplankton pigments and functional types in the Atlantic Ocean: A decadal assessment, 1995–2005. **Deep Sea Research Part II: Topical Studies in Oceanography**, v. 56, n. 15, p. 899–917, jul. 2009.

ALVAIN, S. et al. A species-dependent bio-optical model of case I waters for global ocean color processing. **Deep Sea Research Part I: Oceanographic Research Papers**, v. 53, n. 5, p. 917–925, maio. 2006.

ANTEZANA, T. Hydrographic features of Magellan and Fuegian inland passages and adjacent Subantarctic waters. **Scientia Marina**, v. 63, p. 23–34, 1999.

ANTOINE, D. et al. Assessment of uncertainty in the ocean reflectance determined by three satellite ocean color sensors (MERIS, SeaWiFS and MODIS-A) at an offshore site in the Mediterranean Sea (BOUSSOLE project). **Journal of Geophysical Research**, v. 113, n. C7, p. C07013, 11 jul. 2008.

ANTOINE, D. et al. Variability in optical particle backscattering in contrasting bio-optical oceanic regimes. **Limnology and Oceanography**, v. 56, n. 3, p. 955–973, 2011.

ANTOINE, D. et al. Underwater radiance distributions measured with miniaturized multispectral radiance cameras. **Journal of Atmospheric and Oceanic Technology**, p. 120809055559000, 8 ago. 2012.

ASTORECA, R. et al. Development and application of an algorithm for detecting Phaeocystis globosa blooms in the Case 2 Southern North Sea waters. **Journal of plankton research**, v. 31, n. 3, p. 287–300, mar. 2009.

AUSTIN, R. W. The remote sensing of spectral radiance from below the ocean surface. In: JERLOV, N. G.; NIELSEN, E. S. (Eds.). **Optical Aspects of Oceanography**. San Diego, CA: Academic Press, 1974. p. 317–344.

BAILEY, S. W. et al. Sources and assumptions for the vicarious calibration of ocean color satellite observations. **Applied optics**, v. 47, n. 12, p. 2035–45, 20 abr. 2008.

BAILEY, S. W.; WERDELL, P. J. A multi-sensor approach for the on-orbit validation of ocean color satellite data products. **Remote Sensing of Environment**, v. 102, n. 1-2, p. 12–23, maio. 2006.

BHATTACHAN, A. et al. The Southern Kalahari: a potential new dust source in the Southern Hemisphere? **Environmental Research Letters**, v. 7, n. 2, p. 024001, 1 jun. 2012.

BIANCHI, A. A. et al. Annual balance and seasonal variability of sea-air CO 2 fluxes in the Patagonia Sea: Their relationship with fronts and chlorophyll distribution. **Journal of Geophysical Research**, v. 114, n. C3, p. 1–11, 25 mar. 2009.

BOECKEL, B. et al. Coccolith distribution patterns in South Atlantic and Southern Ocean surface sediments in relation to environmental gradients. **Deep Sea Research Part I: Oceanographic Research Papers**, v. 53, n. 6, p. 1073–1099, jun. 2006.

BORRIONE, I.; SCHLITZER, R. Distribution and recurrence of phytoplankton blooms around South Georgia, Southern Ocean. **Biogeosciences Discussions**, v. 9, n. 8, p. 10087–10120, 2 ago. 2012.

BOSS, E.; SLADE, W.; HILL, P. Effect of particulate aggregation in aquatic environments on the beam attenuation and its utility as a proxy for particulate mass. **Optics express**, v. 17, n. 11, p. 9408–20, 25 maio. 2009.

BOUMAN, H. et al. Temperature as indicator of optical properties and community structure of marine phytoplankton: implications for remote sensing. **Marine Ecology Progress Series**, v. 258, p. 19–30, 2003.

BOUMAN, H. et al. Dependence of light-saturated photosynthesis on temperature and community structure. **Deep Sea Research Part I: Oceanographic Research Papers**, v. 52, n. 7, p. 1284–1299, jul. 2005.

BOUMAN, H. A. et al. Water-column stratification governs the community structure of subtropical marine picophytoplankton. **Environmental Microbiology Reports**, v. 3, n. 4, p. 473–482, 17 ago. 2011.

BOYD, P. W. Environmental factors controlling phytoplankton processes in the Southern Ocean. **Journal of Phycology**, v. 861, n. October 2001, p. 844–861, 2002.

BREWIN, R. J. W. et al. A three-component model of phytoplankton size class for the Atlantic Ocean. **Ecological Modelling**, v. 221, n. 11, p. 1472–1483, jun. 2010.

BRICAUD, A. et al. Variability in the chlorophyll-specific absorption coefficients of natural phytoplankton: Analysis and parameterization. **Journal of Geophysical Research**, v. 100, n. C7, p. 13321–13332, 1995.

BRICAUD, A. et al. Variations of light absorption by suspended particles with chlorophyll a concentration in oceanic (case 1) waters: Analysis and implications for bio-optical. **Journal of Geophysical Research**, v. 103, n. C13, p. 31033–31,044, 1998.

BRICAUD, A. et al. Natural variability of phytoplanktonic absorption in oceanic waters: Influence of the size structure of algal populations. **Journal of Geophysical Research**, v. 109, n. C11, p. 1–12, 2004.

BRICAUD, A. et al. Retrieval of pigment concentrations and size structure of algal populations from their absorption spectra using multilayered perceptrons. **Applied optics**, v. 46, n. 8, p. 1251–60, 10 mar. 2007.

BRICAUD, A. et al. Light absorption properties and absorption budget of Southeast Pacific waters. **Journal of Geophysical Research**, v. 115, n. C8, p. C08009, 7 ago. 2010.

BRICAUD, A.; MOREL, A.; PRIEUR, L. Absorption by dissolved organic matter of the sea (yellow substance) in the UV and visible domains. **Limnology and oceanography**, v. 26, n. 1, p. 43–53, 1981.

BROWN, C. et al. The origin and global distribution of second order variability in satellite ocean color and its potential applications to algorithm development. **Remote Sensing of Environment**, v. 112, n. 12, p. 4186–4203, 15 dez. 2008.

BUITEVELD, H.; HAKVOORT, J. H. M.; DONZE, M. The optical properties of pure water. In: SPIE Ocean Optics 12, 1994, Bergen, Norway, **Proceedings** Bergen SPIE, 1994, doi:10.1117/12.190060.

CAPELLO, M. et al. The composition and distribution of the particulate matter in the Strait of Magellan (Chile) during the 1991 and 1995 Italian campaigns. **Polar Biology**, v. 34, n. 9, p. 1335–1347, 6 mar. 2011.

CARDER, K.L., CHEN, F.R., LEE, Z.P., HAWES, S.K., KAMYKOWSKI, D., Semianalytic Moderate-Resolution Imaging Spectrometer algorithms for chlorophyll-a and absorption with bio-optical domains based on nitrate- depletion temperatures. **Journal of Geophysical Research**, 104: 5403-5421. 1999.

CHANG, G.; BARNARD, A.; ZANEVELD, J. R. V. Optical closure in a complex coastal environment: particle effects. **Applied optics**, v. 46, n. 31, p. 7679–92, 1 nov. 2007.

CIOTTI, A. M.; BRICAUD, A. Retrievals of a size parameter for phytoplankton and spectral light absorption by colored detrital matter from water-leaving radiances at SeaWiFS channels in a continental shelf region off Brazil. **Limnology and Oceanography: Methods**, v. 4, p. 237–253, 2006.

CIOTTI, A. M.; LEWIS, M. R.; CULLEN, J. J. Assessment of the relationships between dominant cell size in natural phytoplankton communities and the spectral shape of the absorption coefficient. **Limnology and Oceanography**, v. 47, n. 2, p. 404–417, 2002.

DALL'OLMO, G. et al. Significant contribution of large particles to optical backscattering in the open ocean. **Biogeosciences**, v. 6, n. 6, p. 947–967, 5 jun. 2009.

DESCHAMPS, P.-Y. et al. SIMBAD: a field radiometer for satellite ocean-color validation. **Applied optics**, v. 43, n. 20, p. 4055–69, 10 jul. 2004.

DEVRED, E. et al. A two-component model of phytoplankton absorption in the open ocean: Theory and applications. **Journal of Geophysical Research**, v. 111, n. C3, p. C03011, 2006.

DOERFFER, R., HEYMANN, K., SCHILLER, H. Case 2 water algorithm for the medium resolution imaging spectrometer (MERIS) on ENVISAT. In: **Proceedings of the ENVISAT validation workshop**, 9-13 December 2002, ESA report. 2002.

DORON, M. et al. Spectral variations in the near-infrared ocean reflectance. **Remote Sensing of Environment**, v. 115, n. 7, p. 1617–1631, jul. 2011.

DOXARAN, D.; CHERUKURU, R. C. N.; LAVENDER, S. J. Estimation of surface reflection effects on upwelling radiance field measurements in turbid waters. **Journal of Optics A: Pure and Applied Optics**, v. 6, n. 7, p. 690–697, 1 jul. 2004.

DOXARAN, D.; FROIDEFOND, J.-M.; CASTAING, P. Remote-sensing reflectance of turbid sediment-dominated waters. Reduction of sediment type variations and changing illumination conditions effects by use of reflectance ratios. **Applied optics**, v. 42, n. 15, p. 2623–34, 20 maio. 2003.

DUCKLOW, H.; STEINBERG, D.; BUESSELER, K. Upper Ocean Carbon Export and the Biological Pump. **Oceanography**, v. 14, n. 4, p. 50–58, 2001.

FALKOWSKI, P. G.; BARBER, R. T.; SMETACEK, V. Biogeochemical Controls and Feedbacks on Ocean Primary Production. **Science**, v. 281, n. 5374, p. 200–206, 10 jul. 1998.

FERREIRA, A.; GARCIA, V. M. T.; GARCIA, C. A. E. Light absorption by phytoplankton, non-algal particles and dissolved organic matter at the Patagonia shelf-break in spring and summer. **Deep Sea Research Part I: Oceanographic Research Papers**, v. 56, n. 12, p. 2162–2174, dez. 2009.

FERREIRA, A., GARCIA, C. A. E., DOGLIOTTI, A. I., GARCIA, V. M. T. Bio-optical characteristics of the Patagonia Shelf break waters: Implications for ocean color algorithms. **Remote Sensing of Environment**, 136, pp. 416–432, doi:10.1016/j.rse.2013.05.022

FINKEL, Z. V. et al. Phytoplankton in a changing world: cell size and elemental stoichiometry. **Journal of Plankton Research**, v. 32, n. 1, p. 119–137, 28 out. 2009.

FLATAU, P. J.; PISKOZUB, J.; ZANEVELD, J. R. V. Asymptotic light field in the presence of a bubble-layer. **Optics express**, v. 5, n. 5, p. 120–123, 1999.

FOUGNIE, B. et al. Reduction of skylight reflection effects in the above-water measurement of diffuse marine reflectance. **Applied optics**, v. 38, n. 18, p. 3844–56, 20 jun. 1999.

FROUIN, R.; SCHWINDLING, M.; DESCHAMPS, P. Spectral reflectance of sea foam in the visible and near-infrared: In situ measurements and remote sensing implications. **Journal of Geophysical Research**, v. 101, n. C6, p. 14361–14371, 1996.

GAIERO, D. M. et al. Iron and other transition metals in Patagonian riverborne and windborne materials: geochemical control and transport to the southern South Atlantic Ocean. **Geochimica et Cosmochimica Acta**, v. 67, n. 19, p. 3603–3623, out. 2003.

GARCIA, V. M. T. et al. Environmental factors controlling the phytoplankton blooms at the Patagonia shelf-break in spring. **Deep Sea Research Part I: Oceanographic Research Papers**, v. 55, n. 9, p. 1150–1166, set. 2008.

GERNEZ, P.; ANTOINE, D. Field characterization of wave-induced underwater light field fluctuations. **Journal of Geophysical Research**, v. 114, n. C6, p. C06025, 27 jun. 2009.

GORDON, H. et al. A semianalytic radiance model of ocean color. **Journal of Geophysical Research**, v. 93, n. 8, p. 10,909–10,924, 1988.

GORDON, H. R. et al. Light scattering by coccoliths detached from Emiliania huxleyi. **Applied optics**, v. 48, n. 31, p. 6059–73, 1 nov. 2009.

GORDON, H. R.; BROWN, O. B.; JACOBS, M. M. Computed relationships between the inherent and apparent optical properties of a flat homogeneous ocean. **Applied optics**, v. 14, n. 2, p. 417–27, 1 fev. 1975.

GORDON, H. R.; DING, K. Self-shading of in-water optical instruments. **Limnology and Oceanography**, v. 37, n. 3, p. 491–500, 1992.

GORDON, H. R.; MCCLUNEY, W. R. Estimation of the depth of sunlight penetration in the sea for remote sensing. **Applied optics**, v. 14, n. 2, p. 413–6, 1975.

GORDON, H. R.; MOREL, A. Y. **Remote assessment of ocean color for interpretation of satellite visible imagery:** a review. Washington, D. C.: American Geophysical Union, 1983. v. 4p. 114

GREEN, R. E.; SOSIK, H. M. Analysis of apparent optical properties and ocean color models using measurements of seawater constituents in New England continental shelf surface waters. **Journal of Geophysical Research**, v. 109, n. C3, p. C03026, 2004.

GROUNDWATER, H. et al. A method for determining oceanic particle size distributions and particle composition using scanning electron microscopy coupled with energy dispersive spectroscopy. **Proceedings of SPIE**, v. 7729, p. 77290E–77290E–12, 2 jun. 2010.

HARDMAN-MOUNTFORD, N. J. et al. Ocean climate of the South East Atlantic observed from satellite data and wind models. **Progress in Oceanography**, v. 59, n. 2-3, p. 181–221, out. 2003.

HAYNES, J. M. et al. Major Characteristics of Southern Ocean Cloud Regimes and Their Effects on the Energy Budget. **Journal of Climate**, v. 24, n. 19, p. 5061–5080, out. 2011.

HENRIQUES, M.; SILVA, A.; ROCHA, J. Extraction and quantification of pigments from a marine microalga : a simple and reproducible method. In: MÉNDEZ-VILAS, A. (ed.). **Communicating current research and educational topics and trends in applied microbiology**. [S.l: s.n.]. p. 586–593. 2007.

HIRATA, T. et al. An absorption model to determine phytoplankton size classes from satellite ocean colour. **Remote Sensing of Environment**, v. 112, n. 6, p. 3153–3159, jun. 2008.

HIRATA, T. et al. An inherent optical property approach to the estimation of size-specific photosynthetic rates in eastern boundary upwelling zones from satellite ocean colour: An initial assessment. **Progress in Oceanography**, v. 83, n. 1-4, p. 393–397, dez. 2009.

HOEPFFNER, N.; SATHYENDRANATH, S. Bio-optical characteristics of coastal waters: absorption spectra of phytoplankton and pigment distribution in the western North Atlantic. **Limnology and oceanography**, v. 37, n. 8, p. 1660–1679, 1992.

HOLM-HANSEN, O. et al. Fluorimetric determination of chlorophyll. **J. Cons. Cons. Int. Explor. Mer**, v. 30, p. 3–15, 1965.

HOOKER, S. et al. An evaluation of above-and in-water methods for determining water-leaving radiances. **Journal of Atmospheric and Oceanic Technology**, v. 19, p. 486–515, 2002.

HOOKER, S. et al. The third seawifs HPLC analysis round-robin experiment (seaharre-3). **NASA technical report**, n. December, 2009.

HOOKER, S. B. **Algorithm updates for the fourth SeaWiFS data reprocessing**., v. 22, p. 74, 2003. Tech. Report No. NASA/TM-2003.

HOOKER, S. B. et al. Above-water radiometry in shallow coastal waters. **Applied optics**, v. 43, n. 21, p. 4254–68, 20 jul. 2004.

HOOKER, S. B.; MARITORENA, S. An Evaluation of Oceanographic Radiometers and Deployment Methodologies. **Journal of Atmospheric and Oceanic Technology**, v. 17, p. 811–830, 2000.

HOOKER, S.; MOREL, A. Platform and environmental effects on above-water determinations of water-leaving radiances. **Journal of Atmospheric and Oceanic Technology**, p. 187–205, 2003.

HOEGH-GULDBERG, O. AND BRUNO, J. F., The Impact of Climate Change on the World's Marine Ecosystems, **Science**, vol. 328, no. 5985, pp. 1523-1528, 2010.

HUOT, Y.; BROWN, C. A.; CULLEN, J. J. Retrieval of phytoplankton biomass from simultaneous inversion of reflectance, the diffuse attenuation coefficient, and Sun-induced fluorescence in coastal waters. **Journal of Geophysical Research**, v. 112, n. C6, p. C06013, 20 jun. 2007.

HUOT, Y.; MOREL, A.; TWARDOWSKI, M. Particle optical backscattering along a chlorophyll gradient in the upper layer of the eastern South Pacific Ocean. **Biogeosciences**, v. 5, p. 495–507, 2008.

IOCCG. **Remote Sensing of Ocean Colour in Coastal and Other Optically-Complex Waters**. 3. ed. Dartmouth, Canada: Reports of the International Ocean-Colour Coordinating Group, 2000. 140 p.

IOCCG. **Remote sensing of inherent optical properties:** fundamentals, tests of algorithms, and applications. 5. ed. Dartmouth, Canada: Reports of the International Ocean-Colour Coordinating Group. 2006, 124 p..

IOCCG. **Atmospheric correction for remotely-sensed ocean- colour products**. 10. ed. Dartmouth, Canada: Reports of the International Ocean-Colour Coordinating Group, 2010. 2010, 78 p.

JERLOV, N. G. **Optical oceanography**. [S.l.] Elsevier Oceanography Series 5, 1968. 194 p.

KAHRU, M.; MITCHELL, B. G. Spectral reflectance and absorption of a massive red tide off southern California. **Journal of Geophysical Research**, v. 103, n. C10, p. 21601–21609, 1998.

KHEIREDDINE, M. ; ANTOINE, D. Diurnal variability of particulate matter from observations of beam attenuation and backscattering coefficients in the Northwestern Mediterranean sea (BOUSSOLE site). In: OCEAN OPTICS CONFERENCE, 21., 2012, Glasgow. **Ocean optics book of abstracts**. Glasglow, Scotland, 2012.

KIRKHAM, A. R. et al. Analysis of photosynthetic picoeukaryote community structure along an extended Ellett Line transect in the northern North Atlantic reveals a dominance of novel prymnesiophyte and prasinophyte phylotypes. **Deep Sea Research Part I: Oceanographic Research Papers**, v. 58, n. 7, p. 733–744, jul. 2011.

KLUNDER, M. B. et al. Dissolved iron in the Southern Ocean (Atlantic sector). **Deep Sea Research Part II: Topical Studies in Oceanography**, v. 58, n. 25-26, p. 2678–2694, dez. 2011.

KORB, R. E.; WHITEHOUSE, M. Contrasting primary production regimes around South Georgia, Southern Ocean: large blooms versus high nutrient, low chlorophyll waters. **Deep Sea Research Part I: Oceanographic Research Papers**, v. 51, n. 5, p. 721–738, maio. 2004.

KOSTADINOV, T. S.; SIEGEL, D. A.; MARITORENA, S. Retrieval of the particle size distribution from satellite ocean color observations. **Journal of Geophysical Research**, v. 114, n. C9, p. C09015, 18 set. 2009.

KOWALCZUK, P., DURAKO, M. J., COOPER, W. J., WELLS, D., SOUZA, J. J. Comparison of radiometric quantities measured in water, above water and derived from SeaWiFS imagery in the South Atlantic Bight, North Carolina, USA. **Continental Shelf Research**, 26(19), 2433–2453. 2006. doi:10.1016/j.csr.2006.07.024.

KRUEGER, S. et al. Ocean circulation patterns and dust supply into the South Atlantic during the last glacial cycle revealed by statistical analysis of kaolinite/chlorite ratios. **Marine Geology**, v. 253, n. 3-4, p. 82–91, ago. 2008.

KWINT, R.; KRAMER, K. DMS Production by Plankton Communities. **Marine Ecology Progress Series**, v. 237, p. 227–237, 1995.

LE QUERE, C. Reply to Horizons Article "Plankton functional type modelling: running before we can walk" Anderson (2005): I. Abrupt changes in marine ecosystems? **Journal of Plankton Research**, v. 28, n. 9, p. 871–872, 13 jun. 2006.

LE QUÉRÉ, C. et al. Impact of climate change and variability on the global oceanic sink of CO 2. **Global Biogeochemical Cycles**, v. 24, n. 4, p. 1–10, 26 out. 2010.

LEATHERS, R.; DOWNES, T.; MOBLEY, C. Self-shading correction for oceanographic upwelling radiometers. **Optics express**, v. 12, n. 20, p. 4709–18, 4 out. 2004.

LEE, Z. et al. Euphotic zone depth: Its derivation and implication to ocean-color remote sensing. **Journal of Geophysical Research**, v. 112, n. C3, p. C03009, 16 mar. 2007.

LEE, Z. et al. Robust approach to directly measuring water-leaving radiance in the field. **Applied optics**, v. 52, n. 8, p. 1693–701, 10 mar. 2013.

LEE, Z.; CARDER, K. L.; ARNONE, R. A. Deriving inherent optical properties from water color: a multiband quasi-analytical algorithm for optically deep waters. **Applied optics**, v. 41, n. 27, p. 5755–72, 20 set. 2002.

LEE, Z.; CARDER, K. L.; DU, K. Effects of molecular and particle scatterings on the model parameter for remote-sensing reflectance. **Applied optics**, v. 43, n. 25, p. 4957–64, 1 set. 2004.

LEWIS, M. R. et al. Quantitative estimation of the underwater radiance distribution. **Journal of Geophysical Research**, v. 116, p. C00H06, 15 out. 2011.

LOISEL, H. et al. Spectral dependency of optical backscattering by marine particles from satellite remote sensing of the global ocean. **Journal of Geophysical Research**, v. 111, n. C9, p. C09024, 2006.

LOISEL, H.; LUBAC, B.; DESSAILLY, D. Effect of inherent optical properties variability on the chlorophyll retrieval from ocean color remote sensing: an in situ approach. **Optics Express**, v. 18, n. 20, p. 20949–20959, 2010.

LOISEL, H.; MOREL, A. Light scattering and chlorophyll concentration in case 1 waters: A reexamination. **Limnology and Oceanography**, v. 43, n. 5, p. 847–858, 1998.

LOISEL, H.; STRAMSKI, D. Estimation of the inherent optical properties of natural waters from the irradiance attenuation coefficient and reflectance in the presence of Raman scattering. **Applied optics**, v. 39, n. 18, p. 3001–11, 20 jun. 2000.

LONGHURST, A. **Ecological geography of the sea**. 2. ed. [S.l.] Academic Press, 2007. p. 560

LUTZ, V. A. et al. Primary production in the Argentine Sea during spring estimated by field and satellite models. **Journal of Plankton Research**, v. 32, n. 2, p. 181–195, 28 nov. 2010.

MAFFIONE, R. A; DANA, D. R. Instruments and methods for measuring the backward-scattering coefficient of ocean waters. **Applied optics**, v. 36, n. 24, p. 6057–67, 20 ago. 1997.

MARANÓN, E. et al. Basin-scale variability of phytoplankton biomass , production and growth in the Atlantic Ocean. **Deep-Sea Research Part I**, v. 47, p. 825–857, 2000.

MARIE, D.; SIMON, N.; VAULOT, D. Phytoplankton cell counting by flow cytometry. In: **Algal culturing techniques**. Oxford: Elsevier, 2005, p. 1–17.

MARITORENA, S.; SIEGEL, D. A; PETERSON, A. R. Optimization of a semianalytical ocean color model for global-scale applications. **Applied optics**, v. 41, n. 15, p. 2705–14, 20 maio. 2002.

MATANO, R. P.; PALMA, E. D.; PIOLA, A. R. The influence of the Brazil and Malvinas Currents on the Southwestern Atlantic Shelf circulation. **Ocean Science**, v. 6, n. 4, p. 983–995, 30 nov. 2010.

MATSUOKA, A. et al. Tracing the transport of colored dissolved organic matter in water masses of the Southern Beaufort Sea: relationship with hydrographic characteristics. **Biogeosciences**, v. 9, n. 3, p. 925–940, 6 mar. 2012.

MCCLAIN, C. R. A Decade of Satellite Ocean Color Observations*. **Annual Review of Marine Science**, v. 1, n. 1, p. 19–42, jan. 2009.

MCCLAIN, C. R.; FELDMAN, G. C.; HOOKER, S. B. An overview of the SeaWiFS project and strategies for producing a climate research quality global ocean bio-optical time series. **Deep Sea Research Part II: Topical Studies in Oceanography**, v. 51, n. 1-3, p. 5–42, jan. 2004.

MERCIER, H.; ARHAN, M.; LUTJEHARMS, J. R. . Upper-layer circulation in the eastern Equatorial and South Atlantic Ocean in January–March 1995. **Deep Sea Research Part I: Oceanographic Research Papers**, v. 50, n. 7, p. 863–887, jul. 2003.

MITCHELL, B. Algorithms for determining the absorption coefficient for aquatic particulates using quantitative filter technique, In: SPIE 1302, Ocean Optics, 10 1990, Orlando, Fl. **Proceedings of SPIE**. Orlando: SPIE,1990. v. 1302. doi: 10.1117/12.21440 Volume 1302.

MITCHELL, B. et al. Determination of spectral absorption coefficients of particles, dissolved material and phytoplankton for discrete water samples. **Ocean optics protocols**, v. 4, p. 39–60, 2002.

MITCHELL, B.; KAHRU, M. Algorithms for SeaWiFS standard products developed with the CalCOFI bio-optical data set. **CALCOFI reports**, v. 39, p. 133–147, 1998.

MOBLEY, C. et al. Optical Modeling of Ocean Waters: Is the Case 1-Case 2 Classification Still Useful? **Oceanography**, v. 17, n. 2, p. 62–67, jun, 2004.

MOBLEY, C. D. Estimation of the remote-sensing reflectance from above-surface measurements. **Applied optics**, v. 38, n. 36, p. 7442–55, 20 dez. 1999.

MOBLEY, C. D. **Light and water radiative transfer in natural waters**. Academic Press, 2004. ISBN-10: 0125027508. ISBN-13: 978-0125027502. CD edition ed. 593p., 2004.

MOBLEY, C. D.; SUNDMAN, L. K.; BOSS, E. Phase function effects on oceanic light fields. **Applied optics**, v. 41, n. 6, p. 1035–50, 20 fev. 2002.

MOORE, J. K. et al. SeaWiFS satellite ocean colour data from the Southern Ocean. **Geophysical Research Letters**, v. 26, n. 10, p. 1465–1468, 1999.

MOORE, J. K.; ABBOTT, M. R. Phytoplankton chlorophyll distributions and primary production in the Southern Ocean. **Journal of Geophysical Research**, v. 105, n. C12, p. 28709, 2000.

MOORE, T. S.; CAMPBELL, J. W.; DOWELL, M. D. A class-based approach to characterizing and mapping the uncertainty of the MODIS ocean chlorophyll product. **Remote Sensing of Environment**, v. 113, n. 11, p. 2424–2430, 16 nov. 2009.

MORAN, M. A.; ZEPP, R. G. Role of photoreactions in the formation of biologically compounds from dissolved organic matter. **Limnology and Oceanography**, v. 42, n. 6, p. 1307–1316, 1997.

MOREL, A. Optical Properties of Pure Water and Pure Sea Water. In: JERLOV, N. G.; NIELSEN, E. S. (Eds.). **Optical Aspects of Oceanography**. Lodon and New York: Academic Press, 1974. p. 1–24.

MOREL, A. In-water and remote measurements of ocean color. **Boundary-Layer Meteorology**, v. 18, p. 177–201, 1980.

MOREL, A. et al. Optical properties of the "clearest" natural waters. **Limnology and oceanography**, v. 52, n. 1, p. 217–229, 15 jan. 2007.

MOREL, A.; ANTOINE, D. Heat Rate within the Upper Ocean in Relation to its bio-optical state. **Journal of Physical Oceanography**, v. 24, p. 1652–1665, 1993.

MOREL, A.; ANTOINE, D.; GENTILI, B. Bidirectional reflectance of oceanic waters: accounting for Raman emission and varying particle scattering phase function. **Applied optics**, v. 41, n. 30, p. 6289–306, 20 out. 2002.

MOREL, A.; BRICAUD, A. Theoretical results concerning light absorption in a discrete medium, and application to specific absorption of phytoplankton. **Deep Sea Research Part A. Oceanographic Research**, v. 28, n. 11, p. 1375–1393, 1981.

MOREL, A.; GENTILI, B. Diffuse reflectance of oceanic waters: its dependence on Sun angle as influenced by the molecular scattering contribution. **Applied optics**, v. 30, n. 30, p. 4427–4438, 1991.

MOREL, A.; GENTILI, B. Diffuse reflectance of oceanic waters. II Bidirectional aspects. **Applied Optics**, v. 32, n. 33, 1993.

MOREL, A.; GENTILI, B. A simple band ratio technique to quantify the colored dissolved and detrital organic material from ocean color remotely sensed data. **Remote Sensing of Environment**, v. 113, n. 5, p. 998–1011, maio. 2009.

MOREL, A.; GENTILI, B.; MOREL, ANDRÉ; GENTILI, B. Diffuse reflectance of oceanic waters. III. Implication of bidirectionality for the remote-sensing problem. **Applied Optics**, v. 35, n. 24, p. 4850–4862, 1996.

MOREL, A.; MARITORENA, S. Bio-optical properties of oceanic waters- A reappraisal. **Journal of Geophysical research**, v. 106, p. 7163–7180, 2001.

MOREL, A.; PRIEUR, L. Analysis of Variations in Ocean Colour. **Limnology and Oceanography**, v. 22, n. 4, p. 709–722, 1977.

MOUW, C. B.; YODER, J. A. Optical determination of phytoplankton size composition from global SeaWiFS imagery. **Journal of Geophysical Research**, v. 115, n. C12, p. 1–20, 7 dez. 2010.

MUELLER, J. L.; FARGION, G. S.; MCCLAIN, C. R. **Ocean optics protocols for satellite ocean color sensor validation -** revision 4, Volume III : Radiometric Measurements and Data Analysis Protocols, NASA technical Report, Greenbelt, Maryland, NASA. NASA/TM-2003-21621/Rev-Vol III, 2003.

NAIR, A. et al. Remote sensing of phytoplankton functional types. **Remote Sensing of Environment**, v. 112, n. 8, p. 3366–3375, ago. 2008.

O'REILLY, J., MARITORENA, S., MITCHELL, G., et al. Ocean color chlorophyll algorithms for SeaWiFS. **Journal of Geophysical Research**, v. 103, n. C11, p. 24937–24–953, 1998.

O'REILLY, J. E. et al. **SeaWiFS postlaunch calibration and validation analyses.,** Maryland, USA, 2000. v. **11, Part 3**.

OHDE, T.; SIEGEL, H. Derivation of immersion factors for the hyperspectral TriOS radiance sensor. **Journal of optics A: pure and applied optics**, v. 12, p. 3–6, 2003.

PARK, J. et al. Variability of SeaWiFs chlorophyll-a in the southwest Atlantic sector of the Southern Ocean: Strong topographic effects and weak seasonality. **Deep Sea Research Part I: Oceanographic Research Papers**, v. 57, n. 4, p. 604–620, abr. 2010.

PARK, Y.-J.; RUDDICK, K. Model of remote-sensing reflectance including bidirectional effects for case 1 and case 2 waters. **Applied optics**, v. 44, n. 7, p. 1236–49, 1 mar. 2005.

PIOLA, A.; AIRES, B.; MATANO, A. Brazil and Falklands (Malvinas) currents. In: STEELE, J. H.; HORPE, S. A.; TUREKIAN, K. K (eds.). **Ocean currents:** a derivative of encyclopedia of ocean science**.** Academic Press, 2001. p. 340-349.

PISKOZUB, J. et al. Small-scale effects of underwater bubble clouds on ocean reflectance: 3-D modeling results. **Optics express**, v. 17, n. 14, p. 11747–52, 6 jul. 2009.

PITCHER, G.; BERNARD, S.; NTULI, J. Contrasting Bays and Red tides in the Southern Benguela Upwelling System. **Oceanography**, v. 21, n. 3, p. 82–91, 2008.

PLATT, T.; SATHYENDRANATH, S. Spatial structure of pelagic ecosystem processes in the global ocean. **Ecosystems**, v. 2, p. 384–394, 1999.

POPE, R.; FRY, E. Absorption spectrum (380-700 nm) of pure water. II. Integrating cavity measurements. **Applied optics**, v. 36, n. 33, p. 8710–8723, 1997.

RAITSOS, D. E. et al. Identifying four phytoplankton functional types from space: An ecological approach. **Limnology and Oceanography**, v. 53, n. 2, p. 605–613, 2008.

RAVEN, J. A., CALDEIRA, K, ELDERFIELD, H., Ocean acidification due to increasing atmospheric carbon dioxide, **Royal Society London**, Policy document 12/05, pp. 60. 2005.

REYNOLDS, A. S., HUSZAR, V. KURK, C., NASELLI-FLORES, L., MELO, S., Review: Towards a functional classification of the freshwater phytoplankton. **Journal of Plankton Research**, vol. 24, pp. 417-428. 2002.

RIVAS, L. A. Spatial and temporal variability of satellite-derived sea surface temperature in the southwestern Atlantic Ocean. **Continental Shelf Research**, v. 30, n. 7, p. 752–760, abr. 2010.

ROESLER, C.S., PERRY, M.J., CARDER, K.L. Modeling in situ phytoplankton absorption from total absorption spectra in productive inland marine waters. **Limnology and Oceanography**. 34: p. 1510-1523. 1989.

ROESLER, C.; PERRY, E M. J., *In situ* phytoplankton absorption, fluorescence emission, and particulate backscattering spectra determined from reflectance, **Journal of Geophysical Research**, v. 100, pp.13279-13294. 1995.

ROMERA-CASTILLO, C. et al. Production of chromophoric dissolved organic matter by marine phytoplankton. **Limnology and Oceanography**, v. 55, n. 3, p. 1466–1466, 2010.

ROMERO, O. E.; HEBBELN, D.; WEFER, G. Temporal and spatial variability in export production in the SE Pacific Ocean: evidence from siliceous plankton fluxes and surface sediment assemblages. **Deep Sea Research Part I: Oceanographic Research Papers**, v. 48, n. 12, p. 2673–2697, dez. 2001.

ROMERO, O.; HEBBELN, D. Biogenic silica and diatom thanatocoenosis in surface sediments below the Peru–Chile Current: controlling mechanisms and relationship with productivity of surface waters. **Marine Micropaleontology**, v. 48, n. 1-2, p. 71–90, maio. 2003.

RUDORFF, N.; KAMPEL, M. Orbital remote sensing of phytoplankton functional types: a new review. **International Journal of Remote Sensing**, v. 33, n. 6, p. 1967–1990, 20 mar. 2012.

RUDORFF, N. M.; FROUIN, R. J.; KAMPEL, M. Ocean color variability in the southern Atlantic and southeastern Pacific. In: R. Frouin et al., (Eds.)**Proceedings of SPIE**. dez. 2012.

SARTHOU, G. et al. Growth physiology and fate of diatoms in the ocean: a review. **Journal of Sea Research**, v. 53, n. 1-2, p. 25–42, jan. 2005.

SATHYENDRANATH, S., L. LAZZARA, AND L. PRIEUR. Variations in the spectral values of specific absorption of phyto plankton. **Limnology and Oceanography**. 32: p. 403–415. 1987.

SATHYENDRANATH, S. et al. Discrimination of diatoms from other phytoplankton using ocean-colour data. **Marine Ecology Progress Series**, v. 272, p. 59–68, 2004.

SATHYENDRANATH, S. et al. Carbon-to-chlorophyll ratio and growth rate of phytoplankton in the sea. **Marine Ecology Progress Series**, v. 383, p. 73–84, 14 maio. 2009.

SATHYENDRANATH, S.; PLATT, T. Spectral effects in bio-optical control on the ocean system. **Oceanologia**, v. 49, n. 1, p. 5–39, 2007.

SCHOEMANN, V. et al. Phaeocystis blooms in the global ocean and their controlling mechanisms: a review. **Journal of Sea Research**, v. 53, n. 1-2, p. 43–66, jan. 2005.

SHI, W.; WANG, M. An assessment of the black ocean pixel assumption for MODIS SWIR bands. **Remote Sensing of Environment**, v. 113, n. 8, p. 1587–1597, ago. 2009.

SHILLINGTON, F.; REASON, C. 4 Large scale physical variability of the Benguela Current Large Marine Ecosystem (BCLME). **Large marine Ecossystems**, v. 14, p. 15–30, 2006.

SIEBURTH, J. M., SMETACEK, V., & LENZ, J., Pelagic ecosystem structure: Heterotrophic compartments of the plankton and their relationship to plankton size fractions, **Limnology and Oceanography**, v. 23, pp. 1256−1263. 1978.

SIEGEL, D. A.; MARITORENA, S. Independence and interdependencies among global ocean color properties: Reassessing the bio-optical assumption. **Journal of Geophysical Research**, v. 110, n. C7, p. 1–14, 2005.

SIEGEL, D. A.; MARITORENA, S.; NELSON, N. B. Global distribution and dynamics of colored dissolved and detrital organic materials. **Journal of Geophysical Research**, v. 107, n. C12, p. 1–14, 2002.

SMITH, R.; BAKER, K. Analysis of ocean optical data. In: SLATER, P. N. (Ed.). **Ocean Optics VIII**, 1986. SPIE Proccedings

STEINBERG, D. et al. Production of chromophoric dissolved organic matter (CDOM) in the open ocean by zooplankton and the colonial cyanobacterium Trichodesmium spp. **Marine Ecology Progress Series**, v. 267, p. 45–56, 2004.

STRAMMA, L. Current systems in the Atlantic Ocean. **Encyclopedia of Ocean Sciences**, p. 589–598, 2001.

STRAMMA, L.; ENGLAND, M. On the water masses and mean circulation of the South Atlantic Ocean. **Journal of Geophysical Research**, v. 104, p. 20863–20883, 1999.

STRAMSKA, M.; DICKEY, T. Short-term variability of the underwater light field in the oligotrophic ocean in response to surface waves and clouds. **Deep-Sea Research Part I**, v. 45, p. 1393–1410, 1998.

STRAMSKI, D. et al. Relationships between the surface concentration of particulate organic carbon and optical properties in the eastern South Pacific and eastern Atlantic Oceans. **Biogeosciences**, v. 5, n. 1, p. 171–201, 14 fev. 2008.

STRAMSKI, D.; BRICAUD, A; MOREL, A. Modeling the inherent optical properties of the ocean based on the detailed composition of the planktonic community. **Applied optics**, v. 40, n. 18, p. 2929–45, 20 jun. 2001.

STRAMSKI, D.; KIEFER, D. A. Light scattering by microorganisms in the open ocean. **Progress in Oceanography**, v. 28, p. 343–383, 1991.

STRAMSKI, D.; TEGOWSKI, J. Effects of intermittent entrainment of air bubbles by breaking wind waves on ocean reflectance and underwater light field. **Journal of Geophysical Research**, v. 106, n. December, p. 345–360, 2001.

SUBRAMANIAM, A. et al. Bio-optical properties of the marine diazotrophic cyanobacteria Trichodesmium spp. I. Absorption and photosynthetic action spectra. **Limnology and Oceanography**, v. 44, n. 3, p. 618–627, 1999.

SWAN, C. M. et al. The effect of surface irradiance on the absorption spectrum of chromophoric dissolved organic matter in the global ocean. **Deep Sea Research Part I: Oceanographic Research Papers**, v. 63, p. 52–64, maio. 2012.

SZETO, M. et al. Are the world's oceans optically different? **Journal of Geophysical Research**, v. 116, n. July, p. C00H04, 4 out. 2011.

TOOLE, D. A et al. Remote-sensing reflectance determinations in the coastal ocean environment: impact of instrumental characteristics and environmental variability. **Applied optics**, v. 39, n. 3, p. 456–69, 20 jan. 2000.

TREES, C.; KENNICUTT, M.; BROOKS, J. Errors associated with the standard fluorimetric determination of chlorophylls and phaeopigments. **Marine Chemistry**, v. 17, p. 1–12, 1985.

TWARDOWSKI, M. S. et al. Optical backscattering properties of the “clearest” natural waters. **Biogeosciences**, v. 4, n. 6, p. 1041–1058, 29 nov. 2007.

UITZ, J. et al. Vertical distribution of phytoplankton communities in open ocean: An assessment based on surface chlorophyll. **Journal of Geophysical Research**, v. 111, n. C8, 2006.

VAN HEUKELEM, L.; THOMAS, C. S. Computer-assisted high-performance liquid chromatography method development with applications to the isolation and analysis of phytoplankton pigments. **Journal of chromatography. A**, v. 910, n. 1, p. 31–49, 23 fev. 2001.

VARGAS, C. A. et al. Allochthonous subsidies of organic matter across a lake–river–fjord landscape in the Chilean Patagonia: Implications for marine zooplankton in inner fjord areas. **Continental Shelf Research**, v. 31, n. 3-4, p. 187–201, mar. 2011.

VERNET, M.; LORENZEN, C. J. **The presence of chlorophyll b and the estimation of phaeopigments in marine phytoplankton**. Oxford University Press, 1987.

VOSS, K. J. et al. The spectral upwelling radiance distribution in optically shallow waters. **Limnology and Oceanography**, v. 48, n. 1_part_2, p. 364–373, 2003.

WASMUND, N.; TOPP, I.; SCHORIES, D. Optimising the storage and extraction of chlorophyll samples. **Oceanologia**, v. 48, n. 1, p. 125–144, 2006.

WATSON, R. et al. Mapping Fisheries onto Marine Ecosystems for Regional , Oceanic and Global Integrations. In: HEMPEL, G.; SHERMAN, K. (Eds.). **Large marine Ecosystems of the World**. Elsevier B.V., 2003. p. 375–395.

WELSCHMEYER, N. Fluorometric analysis of chlorophyll a in the presence of chlorophyll b and pheopigments. **Limnology and Oceanography**, v. 39, n. 8, p. 1985–1992, 1994.

WERDELL, P. J. et al. Regional and seasonal variability of chlorophyll-a in Chesapeake Bay as observed by SeaWiFS and MODIS-Aqua. **Remote Sensing of Environment**, v. 113, n. 6, p. 1319–1330, 15 jun. 2009.

WERDELL, P. J. et al. Generalized ocean color inversion model for retrieving marine inherent optical properties. **Applied optics**, v. 52, n. 10, p. 2019–37, 1 abr. 2013.

WERDELL, P. J.; BAILEY, S. W. An improved in-situ bio-optical data set for ocean color algorithm development and satellite data product validation. **Remote Sensing of Environment**, v. 98, n. 1, p. 122–140, set. 2005.

WESTBERRY, T. K.; SIEGEL, D. An improved bio-optical model for the remote sensing of Trichodesmium spp. blooms. **Journal of Geophysical Research**, v. 110, n. C6, p. C06012, 2005.

WHITMIRE, A. et al. Spectral backscattering properties of marine phytoplankton cultures. **Optics Express**, v. 18, n. 14, p. 1680–1690, 2010.

WRIGHT, S. **Analysis of phytoplankton populations using pigment markers on pigment analysis of Antarctic microorganisms**. Kingston, Australia, 2005.

ZANEVELD, J. R.; BARNARD, A.; BOSS, E. Theoretical derivation of the depth average of remotely sensed optical parameters. **Optics express**, v. 13, n. 22, p. 9052–61, 31 out. 2005.

ZEHR, J.; WATERBURY, J.; TURNER, P. Unicellular cyanobacteria fix N~ 2 in the subtropical North Pacific Ocean. **Nature**, v. 715, n. May 2000, p. 25–28, 2001.

ZIBORDI, G.; BERTHON, J.; D'ALIMONTE, D. An Evaluation of Radiometric Products from Fixed-Depth and Continuous In-Water Profile Data from Moderately Complex Waters. **Journal of Atmospheric and Oceanic Technology**, v. 26, n. 1, p. 91–106, jan. 2009.

ZIBORDI, G.; FERRARI, G. M. Instrument self-shading in underwater optical measurements: experimental data. **Applied optics**, v. 34, n. 15, p. 2750–4, 20 maio. 1995.

ZINGONE, A. et al. The importance and distinctiveness of small-sized phytoplankton in the Magellan Straits. **Polar Biology**, v. 34, n. 9, p. 1269–1284, 23 dez. 2010.

ZUBKOV, M.; QUARTLY, G. Ultraplankton distribution in surface waters of the Mozambique Channel-flow cytometry and satellite imagery. **Aquatic Microbial Ecology**, v. 33, p. 155–161, 2003.